



## Copyright Undertaking

This thesis is protected by copyright, with all rights reserved.

**By reading and using the thesis, the reader understands and agrees to the following terms:**

1. The reader will abide by the rules and legal ordinances governing copyright regarding the use of the thesis.
2. The reader will use the thesis for the purpose of research or private study only and not for distribution or further reproduction or any other purpose.
3. The reader agrees to indemnify and hold the University harmless from and against any loss, damage, cost, liability or expenses arising from copyright infringement or unauthorized usage.

### IMPORTANT

If you have reasons to believe that any materials in this thesis are deemed not suitable to be distributed in this form, or a copyright owner having difficulty with the material being included in our database, please contact [lbsys@polyu.edu.hk](mailto:lbsys@polyu.edu.hk) providing details. The Library will look into your claim and consider taking remedial action upon receipt of the written requests.

**EXPLORING EFFECT OF MEDIUM  
COUPLING ON ULTRASONIC LAMB  
WAVES IN ENGINEERING STRUCTURES  
AND SYNTHESISED SOFT TISSUE-BONE  
PHANTOMS**

**CHEN JIANGANG**

**Ph.D**

**The Hong Kong**

**Polytechnic University**

**2011**

*To my most beloved dad, mom, and Jiawei*

**The Hong Kong Polytechnic University**



**Department of Mechanical Engineering**

**Exploring Effect of Medium Coupling on  
Ultrasonic Lamb Waves in Engineering  
Structures and Synthesised Soft Tissue-bone  
Phantoms**

**CHEN Jiangan**

**A thesis submitted in partial fulfilment of the requirements for the  
degree of Doctor of Philosophy**

**September 2010**

# CERTIFICATE OF ORIGINALITY

I hereby declare that this thesis is my own work and that, to the best of my knowledge and belief, it reproduces no material previously published or written, nor material that has been accepted for the award of any other degree or diploma, except where due acknowledgement has been made in the text.

\_\_\_\_\_ (Signature)

CHEN Jiangang (Name of student)

# ABSTRACT

Lamb waves, the modality of elastic waves propagating in thin plate/shell-like structures, have been the core of intensive researches towards developing various nondestructive evaluation (NDE) techniques for engineering structures and quantitative ultrasound (QUS) techniques for human bone assessment, by taking advantage of their superb capability of sensing material deterioration and geometric changes in the medium in which they are travelling. However, a number of engineering structures work in liquid environments, as typified by boat/submarine hulls, offshore platforms and petroleum pipelines; and on the other hand human bones are covered with soft tissues. These surrounding media such as fluid and soft tissues have very distinct elastic properties from those of engineering structures and bone structures principally accommodating wave propagation, leading to perceivable coupling effect and modulating wave propagation characteristics, to different extents for different modes. Without appropriate rectification of such a coupling effect, accuracy of NDE and QUS techniques can be impaired considerably. Therefore to calibrate and compensate for the coupling effects arising from surrounding media remains of significance but challenge.

In this thesis work, the above-addressed coupling effect has been investigated and calibrated quantitatively. Calibration results have been used to compensate for medium coupling effects in engineering NDE and medical QUS. Investigations were divided into the following five parts:

Firstly, analytical description of propagation characteristics of Lamb waves in a two-layer medium (a solid plate coupled with a layer of fluid) was briefed. The dispersion properties of different wave modes in this coupled medium were observed to be markedly different from those of their counterparts in a free solid plate. This observation entailed the necessity of quantitative interrogation and calibration of coupling effect of coupled medium on wave propagation.

Secondly, the coupling effect of a fluid medium (pure water) on Lamb waves in engineering structures (typified by aluminium plates) was investigated through three-dimensional (3D) finite element (FE) simulation and experimental validation. With quantitative knowledge of the coupling effect from the surrounding fluid media, traditional Lamb-wave-based NDE approaches were rectified when used to evaluate a through-thickness hole and chemical corrosion in submerged aluminium plates, with the assistance of a probability-based diagnostic imaging technique. The identification results articulated the necessity of rectification and compensation for the medium coupling effect when applying Lamb-wave-based damage identification to structures with coupled media.

Thirdly, expanding the above study to a bio-medical application, the coupling effect arising from a layer of soft tissues on Lamb waves in mimicked human long bone was canvassed. A series of soft tissue-bone phantoms was fabricated, each consisting of a soft phase (mimicking coupled soft tissues) and hard phase (imitating bone). Ultrasonic tests were carried out on these phantoms in which the effect of soft tissues of different thicknesses and elastic properties on Lamb wave propagation was examined in a range reflecting normal to pathological conditions of soft tissues of

human beings. Study conducted has established quantitative relationships between the manifestation of the captured ultrasound signal (e.g., changes in propagation velocity and signal magnitude) and diversity of coupled soft tissues.

Fourthly, bearing in mind that real human long bones are tube-like structures, the coupling effect of soft tissues on propagation of cylindrical Lamb waves (the form of Lamb waves in tube-like structures) was evaluated using cylindrical bone phantoms made of acrylic tubes coupled with the soft phase layer. Such a way of modelling is deemed to offer closer similarity to real bone-soft tissue system. The propagation velocity and signal intensity of two fundamental cylindrical Lamb wave modes were interrogated and calibrated when the coupled soft medium had different thicknesses and elastic moduli. The results indicated more prominent coupling effect on the concerned waves in tubes than that in plate models.

Monitoring of the healing processes of bone fracture is an important application of QUS-based bone assessment in the clinic. However during the practical application, the coupling effect from soft tissues is often ignored. Without differentiating the influence due to degradation of bone from that contributed by coupled soft tissues, the accuracy in determination of healing progress of bone fracture may be comprised. In this part, the fundamental Lamb modes in fractured bone phantoms at different healing stages were examined via 3D FE simulation and experimental validation. With the previously obtained quantitative calibration of the coupling effect of soft tissues on concerned wave modes, prediction of a particular healing stage of a mimicked fractured bone was conducted. The results indicated that the estimate of the healing progress of bone fracture based on propagation of Lamb waves might be

inaccurate without compensation for the coupling effect of soft tissues.

In summary, the coupling effects arising from surrounding fluid/soft tissues on propagation characteristics of Lamb waves were examined systematically in this thesis work via numerical simulation and experimental validation. The results revealed that there was prominent influence of the coupling medium on wave propagation, to different extents for different wave modes, indicating that calibration and rectification of such coupling effects are an essential factor that should be taken into account in both NDE applications and clinical QUS-based bone evaluation.

# LIST OF PUBLICATIONS

## Refereed Journal Papers

1. **Chen, J.**, Su, Z. and Cheng, L. 2010. Identification of corrosion damage in submerged structures using fundamental anti-symmetric Lamb waves, *Smart Materials and Structures*, 19(1):015004(12pp).
2. **Chen, J.**, Su, Z. and Cheng, L. 2010. Coupling effect of soft medium on characteristics of ultrasonic Lamb waves: Part I – Development of analysis tool and application in nondestructive evaluation (NDE), *Ultrasonics* (submitted).
3. **Chen, J.**, Su, Z. and Cheng, L. 2010. Coupling effect of soft medium on characteristics of ultrasonic Lamb waves: Part II – Parametric studies and application in quantitative ultrasound (QUS), *Ultrasonics* (submitted).

## Refereed International Conference Papers

4. **Chen, J.**, Su, Z. and Cheng, L. 2010. Identification of corrosion damage in submerged structures using anti-symmetric Lamb wave mode, in *Proceedings of the 5<sup>th</sup> European Workshop on Structural Health Monitoring*, Jun., Naples, Italy.

5. **Chen, J.**, Su, Z. and Cheng, L. 2010. Influence of soft tissues on propagation of ultrasonic Lamb waves in synthesised soft tissue-bone phantoms, in *Proceedings of the 6<sup>th</sup> World Congress on Biomechanics*, Aug., Singapore.
6. **Chen, J.**, Su, Z. and Cheng, L. 2009. Exploring influence of coupled fluid layer on propagation of Lamb waves in bone phantoms: Modeling and experiment, in *Proceedings of the 3<sup>rd</sup> International Conference on Mechanics of Biomaterials & Tissues*, Dec., Clearwater Beach, USA, pp. 99.
7. **Chen, J.**, Su, Z. and Cheng, L. 2009. Influence of media coupling on Lamb waves in bone phantoms, in *Proceedings of the 4<sup>th</sup> Asia-Pacific Conference on Biomechanics* (AP Biomech 2009, A supplement of Journal of Biomechanical Science and Engineering), edited by David, T. and Tanaka, M., Apr., Christchurch, New Zealand, pp. 236-237.
8. **Chen, J.**, Zheng, YP, Ling, HY. 2007. Development of ultrasound platform for the evaluation of the plantar soft tissue properties, in *Proceedings of the 6<sup>th</sup> International Conference and Imaging of Tissue Elasticity*, Nov., New Mexico, USA, pp.99.

# ACKNOWLEDGMENT

I would like to begin the acknowledgement by thanking my supervisor, Dr. Zhongqing Su, who is my best role model of an outstanding scholar. For all my progress in accomplishing this thesis I am indebted to his extraordinary supervision. No matter what difficulties and obstructions I have met, he has never hesitated to bestow trust in me and has persevered in granting me generous support, which really means a lot to me. I am also grateful to Professor Li Cheng, my co-supervisor, who is a distinguished scholar with encyclopaedic knowledge. I have learned a lot from him, which substantially benefits the development of my future professional career.

During my work at the Consortium for Sound and Vibration Research (CSV) in the Department of Mechanical Engineering (ME), the Hong Kong Polytechnic University (HK POLYU), I have been blessed with the opportunity to work with many brilliant people. My sincere gratitude is given to all of them. Particular thanks go to Mr. Chao Zhou, Mr. Hao Xu, Dr. Rongping Fan, who provided me with the utmost and indispensable assistance. In addition, current and past members of the CSV, Dr. Long Yu, Mr. Kam-keung Tong, *etc.*, provided important helps to me in smoothing the progress of this study. My appreciation is also bestowed on colleagues in ME, HK POLYU, such as Mr. Zhengang Liu and Mr. Hao Jiang.

I am forever thankful to Professor Jue Wang, Xi'an Jiaotong University, P. R. China, who supervised my study leading to a Master's degree and set me on the path of biomedical engineering. I appreciate everything that she did for me, especially

providing me every opportunity to enrich my research experience.

My final acknowledgment should be reserved for my family: for my parents, who have raised me and inspired me to follow my dreams; for my wife, who has always had absolute confidence in me and supported me all the time. They cherished me at every great moment, and were also there for me through every difficult time. They all deserve far more credit than I can ever give them.

# TABLE OF CONTENTS

<b>ABSTRACT .....</b>	<b>II</b>
<b>LIST OF PUBLICATIONS .....</b>	<b>VI</b>
Refereed Journal Papers .....	VI
Refereed International Conference Papers .....	VI
<b>ACKNOWLEDGMENT .....</b>	<b>VIII</b>
<b>TABLE OF CONTENTS .....</b>	<b>X</b>
<b>LIST OF FIGURES.....</b>	<b>XIII</b>
<b>LIST OF TABLES.....</b>	<b>XVIII</b>
<b>NOMENCLATURE .....</b>	<b>XIX</b>
General Symbols.....	XIX
Abbreviations.....	XXII
<b>CHAPTER 1 Introduction.....</b>	<b>1</b>
1.1 Research Background .....	1
1.1.1 Coupling Effect in Nondestructive Evaluation (NDE) .....	1
1.1.2 Coupling Effect in Clinical Quantitative Ultrasound (QUS) .....	3
1.2 Objectives and Scope of the Thesis .....	6
1.3 About this Thesis .....	8
<b>CHAPTER 2 The State of the Art of NDE and QUS .....</b>	<b>10</b>
2.1 Introduction .....	10
2.2 Lamb-wave-based Damage Identification: <i>A Review of Methodology</i> .....	12
2.2.1 Plate-like Structures .....	13
<i>Using Lowest-order Symmetric Lamb Mode (<math>S_0</math>)</i> .....	15
<i>Using Lowest-order Anti-symmetric Lamb Mode (<math>A_0</math>)</i> .....	16
2.2.2 Tube-like Structures .....	18
<i>Using Longitudinal Modes</i> .....	19
<i>Using Torsional Modes</i> .....	21
2.3 QUS .....	23
2.3.1 Implementations.....	23
<i>Axial Transmission</i> .....	24
<i>Transverse Transmission</i> .....	26
<i>Pulse-echo</i> .....	26
2.3.2 Hypotheses .....	27

<i>Plate Model</i> .....	27
<i>Tube Model</i> .....	28
2.4 Medium Coupling Effect .....	29
2.4.1 Introduction .....	29
2.4.2 Coupling Issues in NDE .....	29
2.4.3 Coupling Issues in QUS .....	30
2.5 Concluding Remarks .....	32
<b>CHAPTER 3 Fundamentals of Guided Waves</b> .....	<b>34</b>
3.1 Introduction .....	34
3.2 Waves in Thin Plate Structures .....	35
3.3 Waves in Tubular Structures .....	37
3.4 Stoneley and Scholte Waves .....	39
3.5 Waves in Fluid-solid-coupled Media .....	40
3.6 Leaky Lamb Waves .....	48
3.7 Concluding Remarks .....	50
<b>CHAPTER 4 Coupling Effect of Fluid on Lamb Waves and Application to Identification of Damage in Submerged Structures</b> .....	<b>52</b>
4.1 Introduction .....	52
4.2 Coupling Effect of Fluid on Lamb Wave Propagation .....	53
4.2.1 Three-dimensional (3D) Finite Element (FE) Modelling and Simulation .....	53
4.2.2 Experimental Validation .....	58
4.2.3 Signal Processing and Results .....	60
4.3 Application to Identification of Damage in Submerged Structures .....	68
4.3.1 Probability-based Diagnostic Imaging .....	68
4.3.2 Identifying a Through-thickness Hole in a Submerged Aluminium Plate .....	72
4.3.3 Evaluating Corrosion Damage in a Submerged Aluminium Plate .....	82
4.4 Concluding Remarks .....	88
<b>CHAPTER 5 Coupling Effect of Soft Tissues on Lamb Waves in Synthesised Soft Tissue-bone Phantoms (<i>Plate Model</i>)</b> .....	<b>90</b>
5.1 Introduction .....	90
5.2 Fabrication of Synthesised Soft Tissue-bone Phantoms .....	91
5.2.1 Sample Preparation .....	91
5.2.2 Mechanical Property Testing of Artificial Silicon Rubber (ASR) .....	98
5.3 Analysis Method .....	101
5.3.1 3D FE Modelling and Simulation .....	101
5.3.2 Experimental Validation .....	104
5.3.3 Signal Processing .....	107
5.4 Results and Observations .....	108

5.4.1	Influence of Thickness of Coupled Soft Media .....	108
	98% Glycerin ( <i>Level I</i> ) .....	108
	ASR ( <i>Level II</i> ) .....	113
5.4.2	Influence of Elastic Properties of Coupled Soft Media .....	118
5.5	Discussion.....	121
5.6	Concluding Remarks .....	127
<b>CHAPTER 6 Coupling Effect of Soft Tissues on Lamb Waves in Synthesised Soft Tissue-bone Phantoms (<i>Tube Model</i>) .....</b>		<b>129</b>
6.1	Introduction .....	129
6.2	Fabrication of Synthesised Soft Tissue-bone Phantoms.....	130
6.3	Dispersion Properties of Lamb Waves in Tube .....	131
6.4	Analysis Method .....	136
6.4.1	3D FE Modelling and Simulation .....	136
6.4.2	Experimental Validation.....	137
6.5	Results and Discussion .....	138
6.6	Plate Model vs. Tube Model.....	151
6.7	Concluding Remarks .....	153
<b>CHAPTER 7 Application to Precision Enhancement of QUS-based Monitoring of Mimicked Healing Progress of Bone Fracture .....</b>		<b>154</b>
7.1	Introduction .....	154
7.2	Monitoring of Healing Progress of Mimicked Bone Fracture.....	156
7.2.1	Preparation of Fractured Bone Phantoms .....	156
7.2.2	Results and Discussion.....	158
7.3	Effect of Soft Tissues on Monitoring of Healing Progress of Mimicked Bone Fracture.....	166
7.3.1	Sample Preparation .....	167
7.3.2	Results and Discussion.....	168
7.4	Application to Prediction of Mimicked Bone Healing by Considering Coupling Effect .....	175
7.4.1	Prediction Without Consideration of Coupling Effect.....	177
7.4.2	Prediction With Consideration of Coupling Effect .....	178
7.5	Concluding Remarks .....	180
<b>CHAPTER 8 Conclusions and Future Research Recommendations .....</b>		<b>182</b>
8.1	Concluding Remarks .....	182
8.2	Research Recommendations.....	185
<b>APPENDIX .....</b>		<b>188</b>
<b>REFERENCE .....</b>		<b>190</b>

# LIST OF FIGURES

<b>Fig. 1.1.</b> QUS-based bone assessment: (a) axial transmission, (b) transverse transmission and (c) pulse-echo schemes .....	4
<b>Fig. 2.1.</b> Rationale of Lamb-wave-based damage evaluation (A: transmitter, B: defect, C: receiver, D: receiver) .....	11
<b>Fig. 2.2.</b> Dispersion curves of Lamb waves in a free aluminium plate ( $C_L = 6500 \text{ m/s}$ , $C_T = 3150 \text{ m/s}$ , $C_L$ : velocity of longitudinal wave, $C_T$ : velocity of transverse wave; dotted rectangle: non-dispersion region) [47] .....	14
<b>Fig. 2.3.</b> Particle motion in (a) $S_0$ and (b) $A_0$ .....	14
<b>Fig. 2.4.</b> Dispersion curves of cylindrical Lamb waves in a steel pipe (inner diameter: 150 mm, thickness: 50 mm) .....	19
<b>Fig. 2.5.</b> Mode shapes of (a) $L(0,1)$ and (b) $L(0,2)$ in a steel pipe (inner diameter: 76 mm, thickness: 5.5 mm) at an excitation frequency of 70 kHz.....	21
<b>Fig. 2.6.</b> Dispersion curves of torsional modes in a steel pipe (outer diameter: 60 mm, thickness: 3.5 mm) [64] .....	22
<b>Fig. 2.7.</b> Mode shape of $T(0,1)$ in a 3-inch pipe at 45 kHz (radial and axial displacements being zero) [59].....	23
<b>Fig. 2.8.</b> Illustration of Lamb waves propagating either (a) separately in bone and soft tissue or (b) in the combination of bone and soft tissue [100] .....	32
<b>Fig. 3.1.</b> Cylindrical Lamb waves in a pipe section, activated by an actuator at A and received by a sensor at B, showing six helical propagation paths [118]. .....	39
<b>Fig. 3.2.</b> Illustration of an interface wave travelling at an interface of two media .....	40
<b>Fig. 3.3.</b> Schematic of a fluid-solid-coupled medium .....	41
<b>Fig. 3.4.</b> Dispersion curves of (a) $S_0$ and (b) $A_0$ in water-aluminium-coupled medium (phase velocity vs. frequency) (T: thickness of water layer) calculated using the developed code .....	46
<b>Fig. 3.5.</b> Calculated dispersion curves of (a) $S_0$ and (b) $A_0$ in water-aluminium-coupled medium (group velocity vs. frequency) (T: thickness of water layer) ...	47
<b>Fig. 3.6.</b> Dispersion curves of the $A_0$ mode in an aluminium plate coupled with a layer of pure water (a: thickness of water layer) [22].....	50
<b>Fig. 4.1.</b> Schematic of transmitter and receiver allocation for examining Lamb waves propagating in fluid-solid coupled medium (distance between transmitter and receiver: 175 mm) .....	54
<b>Fig. 4.2.</b> Schematic of ‘TIE’ constraint for simulating the interface of fluid-solid-coupled media.....	56
<b>Fig. 4.3.</b> A five-cycle <i>Hanning</i> window-modulated sinusoid toneburst at a central frequency of 150 kHz .....	57
<b>Fig. 4.4.</b> FE model for fluid-solid-coupled medium containing a piezoelectric wave transmitter and receiver .....	58
<b>Fig. 4.5.</b> (a) Setup and (b) photo of experimental validation .....	59
<b>Fig. 4.6.</b> Raw Lamb wave signals at the interface in the absence and presence of a fluid layer of 4 mm in thickness (FT: fluid layer thickness).....	61
<b>Fig. 4.7.</b> HT-processed wave signals at the interface in the absence and presence of fluid layers of different thicknesses (FT: fluid layer thickness) .....	62

<b>Fig. 4.8.</b> Group velocities of (a) $S_0$ and (b) $A_0$ in aluminium plate coupled with a fluid layer versus thickness of fluid layer, obtained via FE simulation and experiment .....	64
<b>Fig. 4.9.</b> Stress distribution of Lamb wave propagating in a fluid-solid-coupled medium, showing energy leakage of the $A_0$ mode (for comparison, stress distributions displayed in the fluid layer and in the aluminium plate are not of the same scale; the darker the greyscale the higher the stress).....	66
<b>Fig. 4.10.</b> Dispersion curves of Lamb waves in an aluminium plate in the absence and presence of a fluid layer (4 mm in thickness) obtained via (a) FE simulation and (b) experiment.....	67
<b>Fig. 4.11.</b> Relative positions of transmitter, receiver and damage for a sensing path .	70
<b>Fig. 4.12.</b> Locus of roots to Equation 4.3 established by a sensing path, indicating possible locations of damage in the structure.....	72
<b>Fig. 4.13.</b> An aluminium plate containing a through-thickness hole for validation of the approach (unit: m).....	74
<b>Fig. 4.14.</b> HT-processed wave signals captured via sensing path $T_3$ - $R_3$ in the aluminium plate containing a through-thickness hole, in the absence and presence of fluid layers of different thicknesses, obtained via (a) experiment and (b) FE simulation (FT: fluid layer thickness) .....	75
<b>Fig. 4.15.</b> A probability greyscale image of damage established by sensing path $T_1$ - $R_1$ when the fluid layer was 4 mm in thickness (the darker the greyscale the higher the probability of the presence of damage) .....	76
<b>Fig. 4.16.</b> Identification results for a through-thickness hole in the aluminium plate coupled with fluid layers of different thicknesses: (a1 and a2) without rectification (a1: experimental result; a2: simulation result) when the fluid layer is 4 mm in thickness; (b1 and b2) without rectification (b1: experimental result; b2: simulation result) when the fluid layer is 7 mm in thickness; (c1 and c2) with compensation for the coupling effect (c1: experimental result; c2: simulation result) when the fluid layer is 4 mm in thickness; and (d1 and d2) with compensation for the coupling effect (d1: experimental result; d2: simulation result) when the fluid layer is 7 mm in thickness (white or black circle: actual damage) .....	78
<b>Fig. 4.17.</b> Aluminium plate containing corrosion damage (unit: m) .....	84
<b>Fig. 4.18.</b> HT-processed wave signals captured via sensing path $T_3$ - $R_3$ in aluminium plate containing corrosion damage in the absence and presence of fluid layers of different thicknesses, obtained via experiment (FT: fluid layer thickness).....	85
<b>Fig. 4.19.</b> Identification results for corrosion damage in aluminium plate coupled with fluid layer of different thicknesses: (a) without rectification when the fluid layer is 4 mm in thickness; (b) without rectification when the fluid layer is 7 mm in thickness; (c) with compensation for the coupling effect when the fluid layer is 4 mm in thickness; and (d) with compensation for the coupling effect when the fluid layer is 7 mm in thickness (white or black circle: actual corrosion).....	86
<b>Fig. 5.1.</b> Photos of production of ASR: (a) mixing silicon gel, firm agents and oil; (b) produced ASR layers .....	95
<b>Fig. 5.2.</b> Comparison of effects of different gluewater on gluing silicone rubber onto acrylic plate .....	97
<b>Fig. 5.3.</b> Setup for compression testing of fabricated ASR (MTS® Alliance RT/50 platform) .....	99
<b>Fig. 5.4.</b> Stress-strain relationship of the fabricated ASR (ROS: 1.6) obtained from	

compression testing .....	100
<b>Fig. 5.5.</b> Schematic of transmitter and receiver allocation in FEM for (a) glycerin and (b) ASR scenarios .....	103
<b>Fig. 5.6.</b> Photos of experimental setup for (a) glycerin and (b) ASR scenarios .....	105
<b>Fig. 5.7.</b> Experimental setup for (a) glycerin and (b) ASR scenarios.....	106
<b>Fig. 5.8.</b> (a) Pre-processed <i>in vitro</i> signals in phantoms in the absence (Sample No. 1#) and presence of a layer of 98% glycerin 4 mm in thickness (Sample No. 2#) at an excitation frequency of 100 kHz; and (b) HT-processed results of signals shown in (a) (signal being normalised relative to amplitude extremum of the signal in No. 1# sample).....	109
<b>Fig. 5.9.</b> Group velocities of FAS and SAS in phantoms (Samples No. 1#–2#) obtained through simulation and experiment vs. thickness of coupled 98% glycerin layer (excitation frequency: 100 kHz).....	111
<b>Fig. 5.10.</b> Stress field as a result of wave propagation in phantom (Sample No. 2#) coupled with a layer of 98% glycerin 2 mm in thickness, showing that energy associated with SAS leaks from hard to soft medium but that associated with FAS is confined in hard medium (note: for convenience of comparison, the displayed stress fields in the soft and hard media are not of the same scale; the darker the greyscale the higher the stress).....	112
<b>Fig. 5.11.</b> HT-processed <i>in vitro</i> signals in phantoms in the absence (Sample No. 3#) and presence of a layer of ASR of different thicknesses (Samples No. 4#, 6#, 7#, 10# and 11#) at an excitation frequency of 75 kHz (ST: thickness of soft medium (ASR); signal normalised relative to amplitude extremum of the signal in No. 3# sample) .....	115
<b>Fig. 5.12.</b> Group velocities of FAS and SAS in phantoms (Samples No. 3#–11#) obtained through simulation and experiment vs. thickness of coupled ASR layer (excitation frequency: 75 kHz).....	116
<b>Fig. 5.13.</b> Magnitudes of FAS and SAS in phantoms (Samples No. 3#–11#) vs. thickness of coupled ASR layer (excitation frequency: 75 kHz; signal magnitude normalised relative to amplitude extremum of the signal in No. 3# sample)....	116
<b>Fig. 5.14.</b> Stress field as a result of wave propagation in phantom (Sample No. 6#) coupled with a layer of ASR 3.4 mm in thickness, showing that energies associated with both FAS and SAS leak from hard to soft medium (note: for convenience of comparison, the displayed stress fields in the soft and hard media are not of the same scale; the darker the greyscale the higher the stress) .....	118
<b>Fig. 5.15.</b> Group velocities of FAS and SAS in phantoms (Samples No. 12#–22#) obtained through simulation and experiment vs. elastic modulus of the coupled ASR layer (excitation frequency: 75 kHz). .....	120
<b>Fig. 5.16.</b> Magnitudes of FAS and SAS in phantoms (Samples No. 12#–22#) vs. elastic modulus of coupled ASR layer (excitation frequency: 75 kHz; signal magnitude normalised relative to amplitude extremum of signal in No. 3# sample) .....	121
<b>Fig. 5.17.</b> Dispersion curves of FAS and SAS in phantoms in the absence (Sample No. 1#) and presence of a layer of 98% glycerin 4 mm in thickness (Sample No. 2#) obtained through (a) 3D FE simulation and (b) experiment.....	122
<b>Fig. 5.18.</b> Dispersion curves of FAS and SAS in phantoms in the absence (Sample No. 3#) and presence of a layer of ASR 3.4 mm in thickness (Sample No. 6#) obtained through (a) 3D FE simulation and (b) experiment.....	123
<b>Fig. 5.19.</b> Magnitudes of FAS and SAS in (a) a phantom in the absence of soft medium (Sample No. 3#) and (b) a phantom in the presence of a layer of ASR	

3.4 mm in thickness (Sample No. 6#) vs. excitation frequency (signal magnitude normalised relative to amplitude extremum of the signal in No. 3# sample at excitation frequency of 150 kHz) .....	126
<b>Fig. 6.1.</b> Dispersion curves of cylindrical Lamb waves at frequencies from 0 to 500 kHz calculated by <i>DISPERSE</i> <sup>®</sup> .....	132
<b>Fig. 6.2.</b> Mode shapes of (a) $L(0,2)$ , (b) $F(1,3)$ , (c) $L(0,1)$ , (d) $F(1,1)$ and (e) $F(1,2)$ calculated by <i>DISPERSE</i> <sup>®</sup> .....	134
<b>Fig. 6.3.</b> Schematic of experimental setup (wedge between transducer and tube is zoomed in) (distance of transmitter and receiver is 108 mm).....	138
<b>Fig. 6.4.</b> Signals captured from a free acrylic tube at an excitation frequency of 100 kHz: (a) time domain signal and (b) HT-processed result of signal in (a) .....	139
<b>Fig. 6.5.</b> Dispersion curves of (a) FAS and (b) SAS captured from No. 1# Sample via experiment and FE simulation (for comparison, wave modes calculated by <i>DISPERSE</i> <sup>®</sup> are also included in the figures, labelled $L(0,2)$ and $F(1,3)$ in (a); $F(1,2)$ , $L(0,1)$ and $F(1,1)$ in (b)).....	141
<b>Fig. 6.6.</b> Signals captured from an acrylic tube in the absence and presence of a layer of ASR at an excitation frequency of 100 kHz: (a) time domain signal and (b) HT-processed result of signal in (a).....	143
<b>Fig. 6.7.</b> Group velocities of FAS and SAS captured from an acrylic tube in the absence and presence of a layer of ASR of different thickness at an excitation frequency of 100 kHz .....	144
<b>Fig. 6.8.</b> Group velocities of FAS and SAS captured from an acrylic tube in the absence and presence of a layer of ASR of different elastic modulus at an excitation frequency of 100 kHz .....	145
<b>Fig. 6.9.</b> Dispersion curves of ((a) and (b)) FAS and ((c) and (d)) SAS captured from an acrylic tube in the absence and presence of a layer of ASR ((a) and (c) FE simulation; (b) and (d) experiment).....	146
<b>Fig. 6.10.</b> Magnitudes of FAS and SAS captured from an acrylic tube in the (a) absence and (b) presence of a layer of ASR vs. excitation frequency.....	149
<b>Fig. 6.11.</b> Magnitudes of (a) FAS and (b) SAS captured from an acrylic tube in the absence and presence of a layer of ASR vs. excitation frequency .....	150
<b>Fig. 7.1.</b> Schematic of ultrasonic measurement of mimicked fractured bone phantom .....	157
<b>Fig. 7.2.</b> Stress-strain relationship of ASR obtained from a mechanical compression test (open circles: experimental data; solid line: linear regression of experimental data) .....	158
<b>Fig. 7.3.</b> Wave signals captured from an intact phantom and a fractured phantom with callus width 3 mm: (a) raw signals and (b) their HT-processed results .....	159
<b>Fig. 7.4.</b> Velocities of FAS and SAS at different healing stages from both experiment and FE simulation (at 100 kHz).....	161
<b>Fig. 7.5.</b> Relative reductions in velocities of FAS and SAS at different healing stages of mimicked bone fracture via (a) FE simulation (b) experiment .....	162
<b>Fig. 7.6.</b> Magnitudes of FAS and SAS vs. callus width via (a) FE simulation and (b) experiment (excitation frequency of 100 kHz).....	164
<b>Fig. 7.7.</b> Relative reductions in magnitude of FAS and SAS at different healing stages of mimicked bone fracture via (a) FE simulation and (b) experiment .....	165
<b>Fig. 7.8.</b> Experimental setup.....	167
<b>Fig. 7.9.</b> Signals captured from bone fracture phantom with callus 2 mm in width in the absence and presence of ASR: (a) raw signals and (b) their HT-processed	

results.....	168
<b>Fig. 7.10.</b> Group velocities of FAS and SAS captured from fractured bone phantoms of different callus widths in the absence and presence of ASR via (a) FE simulation and (b) experiment.....	172
<b>Fig. 7.11.</b> Signal intensities of (a) FAS and (b) SAS captured from fractured bone phantoms of different callus widths in the absence and presence of ASR .....	173
<b>Fig. 7.12.</b> Influence of coupled ASR on (a) FAS and (b) SAS with callus of different widths .....	174
<b>Fig. 7.13.</b> Different configurations of bone fracture phantoms: (a) An intact bone phantom; (b) a fractured bone phantom with callus width 2 <i>mm</i> ; (c) a fractured bone phantom as in (b) but with a layer of ASR and (d) an intact phantom as same as that in (a) with a layer of ASR .....	176
<b>Fig. 7.14.</b> HT-processed results of wave signals captured from Phantom-1 and Phantom-3.....	178

# LIST OF TABLES

<b>Table 4.1.</b> Material properties of aluminium and fluid for studying the coupling effect of fluid on Lamb wave propagation .....	55
<b>Table 5.1.</b> Description of synthesised soft tissue-bone phantoms.....	92
<b>Table 5.2.</b> Elastic moduli of synthesised ASR .....	101
<b>Table 6.1.</b> Description of synthesised soft tissue-bone phantoms.....	131
<b>Table 6.2.</b> Relative reductions in velocities of FAS and SAS in phantoms coupled with ASR relative to those in free phantoms in terms of plate and tube models at excitation frequency of 100 kHz .....	152

# NOMENCLATURE

## General Symbols

$S_0$	Lowest-order symmetric Lamb wave mode
$A_0$	Lowest-order anti-symmetric Lamb wave mode
$S_i$	Symmetric Lamb modes ( $i=0, 1, 2, \text{etc.}$ )
$A_i$	Anti-symmetric Lamb modes ( $i=0, 1, 2, \text{etc.}$ )
$L(0,m)$	Longitudinal cylindrical Lamb modes ( $m=1,2,3, \text{etc.}$ )
$T(0,m)$	Torsional cylindrical Lamb modes ( $m=1,2,3, \text{etc.}$ )
$F(n,m)$	Flexural cylindrical Lamb modes ( $m,n=1,2,3, \text{etc.}$ )
$\lambda$	Lamé constant
$\nu$	Poisson's ratio
$\phi$	Scalar potential
$\psi_j$	Vector potential
$e_{ijk}$	Permutation symbol
$c_L$	Phase velocity of longitudinal wave in solid
$c_T$	Phase velocity of shear wave in solid
$c_F$	Phase velocity of bulk wave in fluid
$\rho$	Density of solid
$\rho_F$	Density of fluid

$K$	Wavenumber in solid
$K_F$	Wavenumber in fluid
$\sigma_{zz}$	Normal component of stress in solid
$\sigma_{zz}^F$	Normal component of stress in fluid
$u_{zz}$	Normal component of displacement in solid
$u_{zz}^F$	Normal component of displacement in fluid
$\sigma_{xz}$	Tangential component of stress in solid
$G$	Characteristic matrix for coupled media
$\lambda_{wave}$	Wavelength of a wave mode of interest
$V_{group}$	Group velocity
$f(t)$	Time domain signal
$H(t)$	Hilbert transform of $f(t)$
$K_B$	Bulk modulus
$t_{T-D-R}$	Time of flight of incident wave propagating from transmitter to damage and then to receiver
$t_{T-R}$	Time of flight of incident wave propagating directly from transmitter to receiver
$L_{D-R}$	Distance between damage centre and receiver
$L_{T-R}$	Distance between transmitter and receiver
$\sigma_{ij}$	Standard variance
$\rho_{bone}$	Density of human bone
$\rho_{acrylic}$	Density of acrylic

$E_{bone}$	Elastic modulus of human bone
$E_{acrylic}$	Elastic modulus of acrylic
$\nu_{bone}$	Poisson's ratio of human bone
$\nu_{acrylic}$	Poisson's ratio of acrylic
$\rho_{glycerin}$	Density of glycerin
$K_{glycerine}$	Bulk modulus of glycerine
$E_{ASR}$	Elastic modulus of ASR
$\rho_{ASR}$	Density of ASR
$\rho_{soft\ tissue}$	Density of human soft tissue
$\rho_{ICT}$	Density of initial connective tissue
$E_{ICT}$	Elastic modulus of initial connective tissue
$V_{no\ fracture\ -without\ ASR}$	Velocity of second-arrival signal (SAS) in an intact bone phantom without any artificial silicon rubber (ASR)
$V_{no\ fracture\ -with\ ASR}$	Velocity of SAS in an intact bone phantom with ASR
$V_{fracture\ -without\ ASR}$	Velocity of SAS in a fractured bone phantom without ASR
$V_{fracture\ -with\ ASR\ (in\ vitro)}$	Velocity of SAS in a fractured bone phantom with ASR

# Abbreviations

3D:	Three-dimensional
ASR:	Artificial silicon rubber
BMD:	Bone mineral density
BUA:	Broadband ultrasound attenuation
CDF	Cumulative distribution function
DXA:	Dual-energy X-ray absorptiometry
FAS:	First-arrival signal
FT:	Fluid layer thickness
HT:	Hilbert transform
ICT:	Initial connective tissue
NDE:	Nondestructive evaluation
PFT	Product of excitation frequency and plate thickness
QUS:	Quantitative ultrasound
RFS	Ratio of firming agent to silicon gel
ROS:	Ratio of oil-to-silicon gel
SAS:	Second-arrival signal
SNR	Signal-to-noise ratio
SOS:	Speed of sound
TEM:	Tissue equivalent material
ToF:	Time-of-flight

# **CHAPTER 1      Introduction**

## **1.1 Research Background**

### **1.1.1 Coupling Effect in Nondestructive Evaluation (NDE)**

An engineering structure for long-term operation should ideally meet the requirements of durability, safety, serviceability and sustainability. However, during the service, its performance may be undermined due to various kinds of damage, such as corrosion, crack and delamination. Under such a circumstance, the structure has large potential to collapse if periodic maintenances and inspections are not applied. With the attempt to identify damage in a structure at an early stage so as to prevent its further failure occurrence, nondestructive evaluation (NDE) techniques have been entailed over the years, exemplified by radiography, shearography, magnetic resonance imagery, laser interferometry, acoustic holography, infrared thermography, acoustic emission and eddy current [1, 2].

In particular, some structures are working in humid or moisturised environments, or even submerged in fluid, as typified by offshore platforms, boat/submarine hulls, and pipework submerged. Such sorts of working conditions can raise some additional issues during the application of the abovementioned NDE techniques, such as the difficulty in manipulating transducers in a fluid environment or inaccurate image reconstruction due to influence from surrounding fluid. As a result, traditional NDE techniques, although they have obtained great success in a huge number of applications, become unwieldy when applied to structures with coupled medium or submerged in fluid. To ensure the applicability of these techniques, most of them require termination of a normal service of the structure to be inspected and removal of the insulation layers, if any, incurring high cost in terms of labour and disruption to the service. Driven by the above, some special alternatives have been developed, such as magnetic particle inspection [1, 2] and magnetic flux leakage technique [3, 4]. However the major demerits of these available techniques are their inability to inspect nonferrous materials.

Lamb waves, the form of guided elastic waves in thin plate/shell-like structures, have been intensively examined over the past few decades, to serve as a promising means for developing cost-effective NDE techniques [5-9], because of their superb capabilities including low attenuation even when propagating in structures submerged, strong penetration, fast propagation, omnidirectional dissemination, convenience of activation and acquisition, inexpensive implementation, low energy consumption and,

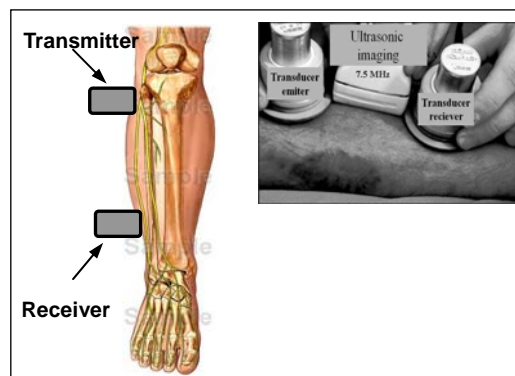
most importantly, high sensitivity to structural damage and material inhomogeneities even when they are small in size or lie beneath the surface. With these merits, Lamb waves have great potential to be used in detecting damage in submerged structures.

However, most current efforts in using ultrasonic Lamb waves for detecting damage in structures coupled with other types of media ignore the coupling effect of surrounding media such as fluid on the propagation of Lamb waves, potentially leading to compromised evaluation precision. It has been reported that Lamb waves are very sensitive to the presence of surrounding media and changes in their properties [10, 11]. This can create difficulty in delivering correct identification without appropriate rectification. The calibration and rectification of such coupling effects on Lamb wave propagation are thus relevant.

### **1.1.2 Coupling Effect in Clinical Quantitative Ultrasound (QUS)**

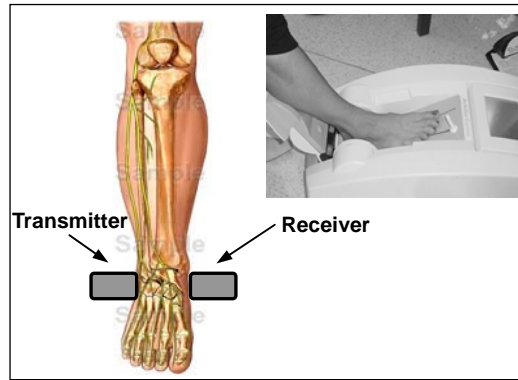
The coupling effect encountered in engineering NDE aforementioned is also a concern in clinical QUS. In the clinic, QUS is widely used for assisting in the diagnosis of some bone-related diseases, and in particular those as a result of deterioration of bone material property and geometry, e.g., osteoporosis (the consequence of asymptomatic bone loss earlier in cancellous and later in cortical bone, especially in regions with dominant skeletal sites, e.g., spine, distal radius and hip).

QUS is now competing with traditional radiation-based bone mineral density (BMD) (*i.e.*, *bone densitometry*, such as dual-energy X-ray absorptiometry (DXA) - the ‘gold standard method’ for clinical osteoporosis diagnosis). QUS outperforms densitometry in some aspects including (i) potential to render rich information including various elastic properties and geometric features of bone, contrasting BMD which is inherently limited to bone density and geometry alone; (ii) no health risk to operators and patients for not using ionizing radiation; and (iii) low energy consumption, good portability and inexpensive implementation. To clinically implement QUS, one can use (i) axial transmission, (ii) transverse transmission or (iii) pulse-echo scheme [12-21], as illustrated in Fig. 1.1, with the first one being the most promising thanks to its capacity to send ultrasound waves not only along axis of the bone but also across the bone thickness.

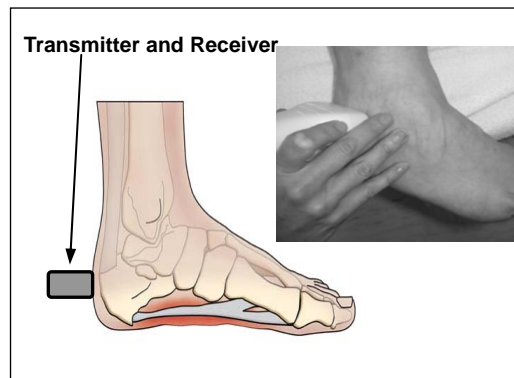


(a)

**Fig. 1.1.** QUS-based bone assessment: (a) axial transmission, (b) transverse transmission and (c) pulse-echo schemes



(b)



(c)

**Fig. 1.1. Cont.**

The existing QUS techniques in today's clinic, whichever scheme is used, are substantially based on canvassing the ultrasonic waves propagating in bone. By benchmarking a healthy colony, changes in captured wave signals can be linked to pathological degradation in bone. For example, the speed-of-sound (SOS) of the captured signals can serve as an indicator for various symptoms in bone, while broadband-ultrasound-attenuation (BUA) of ultrasonic waves can be used to predict hip fracture [12].

However, in spite of its wide applications QUS technique has been increasingly

challenged in terms of the accuracy and precision that it can offer. One of the main reasons is many existing QUS techniques do not properly consider the coupling effect from coupled soft tissues (skin, muscle, marrow, *etc.*) on ultrasonic waves propagating in bone [11, 22, 23]. Without differentiating the influence due to degradation of bone from that contributed by coupled soft tissue, the accuracy in determination of bone assessment can be comprised. Quantitative calibration of such a coupling effect becomes crucial but challenging.

In the work of this thesis, bearing in mind that it is of great necessity to calibrate and rectify the coupling effect exerted either by fluid in NDE for engineering structures and by soft tissues in QUS for bone assessment, comprehensive interrogation was accomplished in the hope of quantitatively exploring the coupling effect arising from coupled media on wave propagation in engineering structures and mimicked bone phantoms.

## **1.2 Objectives and Scope of the Thesis**

In recognition of the problems of today's NDE when applied to submerged structures and QUS in clinical practice, the objectives of the work described in this thesis are as follows:

- (i) to analytically study the wave propagation in a fluid-coupled medium;

- (ii) to experimentally and numerically examine the coupling effects arising from the fluid in NDE and soft tissues in QUS;
- (iii) to develop a three-dimensional (3D) finite element (FE) modelling technique for simulating wave propagation in a medium comprised of multi-phase;
- (iv) to calibrate and rectify the coupling effect of fluid/soft tissue on characteristics of Lamb waves in engineering structures/bone phantoms;
- (v) to perform identification of damage in submerged structures by taking into account the coupling effect arising from surrounding fluid; and
- (vi) to enhance the precision of QUS when used for predicting healing progress of fractured bones under the influence coupled soft tissues.

Based on the above objectives, the scope of the work introduced in this thesis includes:

- (i) wave propagation in coupled media;
- (ii) 3D FE modelling and simulation of wave propagation;
- (iii) ultrasonic Lamb wave generation and acquisition;
- (iv) signal processing and identification algorithm; and
- (v) fabrication of synthesised phantoms of bone and soft tissue.

## 1.3 About this Thesis

This thesis comprises eight chapters, organised as follows:

Chapter 2 provides a comprehensive literature review about the coupling effect on the propagation of ultrasonic Lamb waves in engineering structures and human bones, with engineering and clinical application backgrounds, respectively. Succedent to an introduction of the rationale of NDE and QUS, a variety of methods in Lamb-wave-based NDE and QUS are described.

Chapter 3 concerns the fundamentals of elastic waves in a free medium and a medium consisting of multi-phase, with the assistance of analytical interrogation. In particular, Lamb waves in fluid-coupled media are examined, serving as the basis for the following exploration of the coupling effect of coupled media (fluid, soft tissue, *etc.*) on Lamb wave propagation.

In Chapter 4, the coupling effect of fluid (pure water) on Lamb wave propagation in an aluminium plate is particularly focused on. Such a coupling effect is calibrated for different thicknesses of the fluid layer. Results are then applied to rectify a traditional Lamb-wave-based NDE approach when used for identifying corrosion in submerged structures.

As a clinical counterpart of the work reported in Chapter 4 that focused on an engineering application, Chapters 5 and 6 investigate the coupling effect of mimicked soft tissues on Lamb wave in synthesised bone phantoms. As a first level approximation, bone is modelled using a plate model, in Chapter 5, while is then simulated using a tube-like model, in Chapter 6, for a closer approximation to the reality.

As an application of the results arising from the above work, the calibrated relationships between variety in soft tissues and manifestation of captured signals is applied to improve the accuracy and precision of QUS when used for monitoring the mimicked healing progress of fractured bones, which is elaborated in Chapter 7.

At last, Chapter 8 presents concluding remarks arising from this work and recommendations for future work.

# **CHAPTER 2            The State of the Art of NDE and QUS**

## **2.1 Introduction**

Lamb waves are considered as a promising candidate for developing various NDE techniques and clinical QUS [18, 22, 24-38], because of their ability to propagate a long distance in a structure with low attenuation, fast propagation velocity, and most importantly, high sensitivity to damage. Having propagated for a specific distance in the structure under inspection or the bone under assessment, a captured Lamb wave signal contains rich information concerning abnormalities in the structure (e.g., crack, discontinuity, corrosion or delamination) or in the bone (e.g., osteoporosis-related thickness reduction or material loss). Abnormality produces unique scattering characteristics in Lamb waves. Interrogation of the differences between the captured and baseline wave signals (from undamaged structures or healthy bone) can lead to qualitative or quantitative evaluation of abnormalities through appropriate identification algorithms.

Figure 2.1 illustrates the rationale of Lamb-wave-based damage evaluation for a plate which contains a defect at position B. An ultrasound transducer located at position A serving as an actuator generates ultrasonic waves when fed with an excitation. Upon propagating omni-directionally in the structure, the generated waves encounter the defect at B, consequently producing wave scattering including reflection and transmission. When the reflected and transmitted wave signals captured with sensors at positions C and D are examined, identification of the defect (including its location, size and shape) can be achieved through appropriate identification algorithms, in recognition of the fact that differences in the location and severity of abnormality in structures produce different wave scattering phenomena.

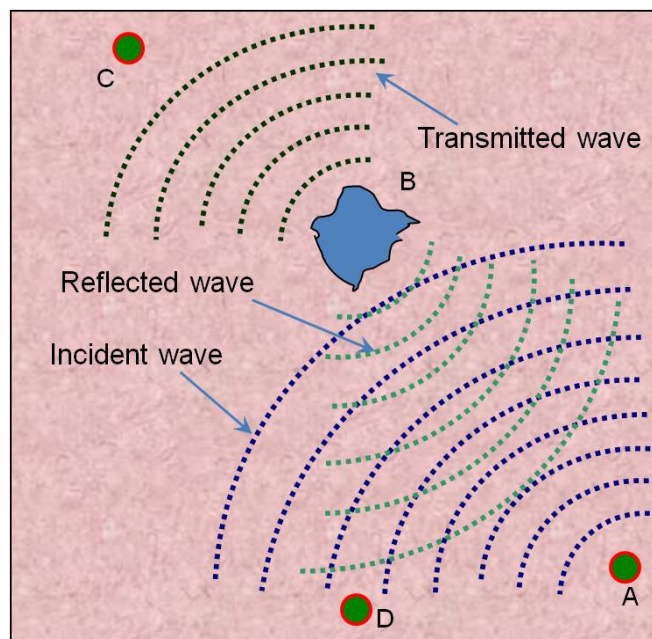


**Fig. 2.1.** Rationale of Lamb-wave-based damage evaluation (A: transmitter, B: defect, C: receiver, D: receiver)

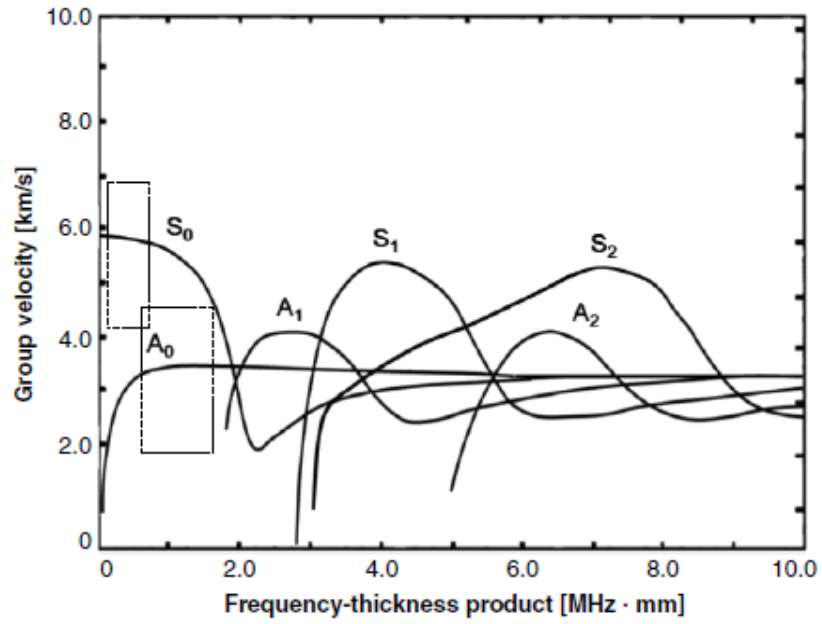
## **2.2 Lamb-wave-based Damage Identification: A Review of Methodology**

As a representative of traditional NDE techniques, the approach based on the use of ultrasonic bulk waves is widely used to examine the thickness of structures by measuring the time-of-flight (ToF), the time used for the wave to propagate a certain distance [39, 40]. However, its applications have been hitherto hampered due to the nature of point-by-point measurement when applied to inspection of a large area. In contrast, Lamb-wave-based detection has recently achieved great success in the development of NDE techniques [28-38, 41-46]. The major difference between a bulk wave and a Lamb wave is that the former propagates in a bulky structure and the latter in a thin plate, guided by the upper and lower surfaces of the plate. Due to the plate boundaries, multiple wave scatterings and mode conversions are possible as the wave propagates. As a result of superimpositions of scattered and mode-converted waves, complex Lamb wave packets are produced in the structures.

Various Lamb-wave-based damage identification approaches are here categorised into two groups according to the geometric characteristics of the structure under inspection: plate-like structures and tube-like structures.

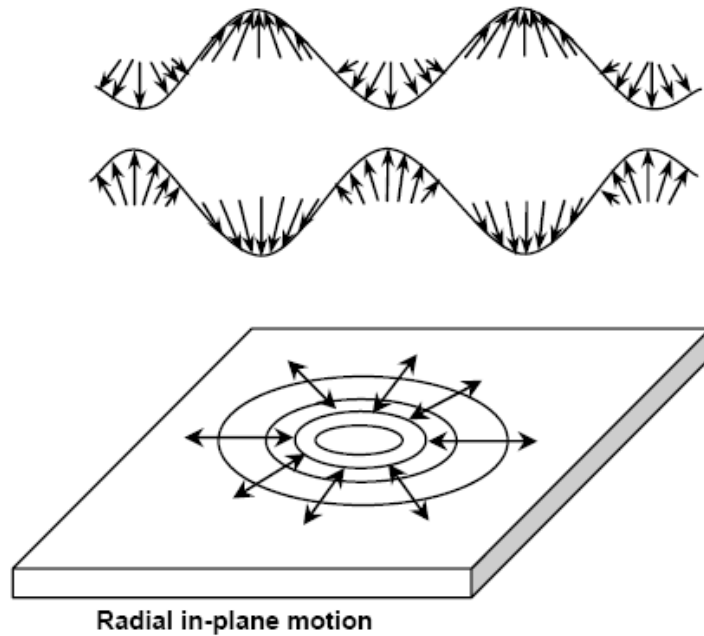
## 2.2.1 Plate-like Structures

Figure 2.2 shows the dispersion curves of Lamb waves in an aluminium plate (group velocity vs. product of excitation frequency and plate thickness (PFT)), illustrating the dispersive properties of Lamb waves (to be detailed in Section 3.2). It can be seen that the velocity of a specific Lamb wave mode varies as a function of excitation frequency and the thickness of the structure, and at least two Lamb modes (lowest-order symmetric Lamb mode,  $S_0$ , and anti-symmetric Lamb mode,  $A_0$ ) exist at each PFT. At a relatively low PFT, only  $S_0$  and  $A_0$  are available; as PFT increases, more Lamb modes of higher order develop, complicating a captured signal. Nevertheless a less dispersive region exists in the low frequency range where two fundamental modes travel at almost constant velocities, referred to as the *non-dispersion region* (indicated by rectangles in Fig. 2.2). Most Lamb-wave-based damage identification approaches employ  $S_0$  and  $A_0$  in the non-dispersion region. The schematics of particle motion in  $S_0$  and  $A_0$  are plotted in Fig. 2.3, indicating the displacement direction of particles and the resulting motion.  $S_0$  predominantly have radial in-plane displacement of particles, Fig. 2.3(a), while  $A_0$  mostly have out-of-plane displacement, Fig. 2.3(b). Therefore,  $S_0$  is often described as ‘compressional’, showing thickness bulging and contracting; and  $A_0$  is known as ‘flexural’, presenting constant-thickness flexing, though higher-order anti-symmetric modes have increasingly complex through thickness displacements. Under the same excitation condition, the magnitude of  $S_0$  (in-plane motion) is normally smaller than that of  $A_0$  (out-of-plane motion).



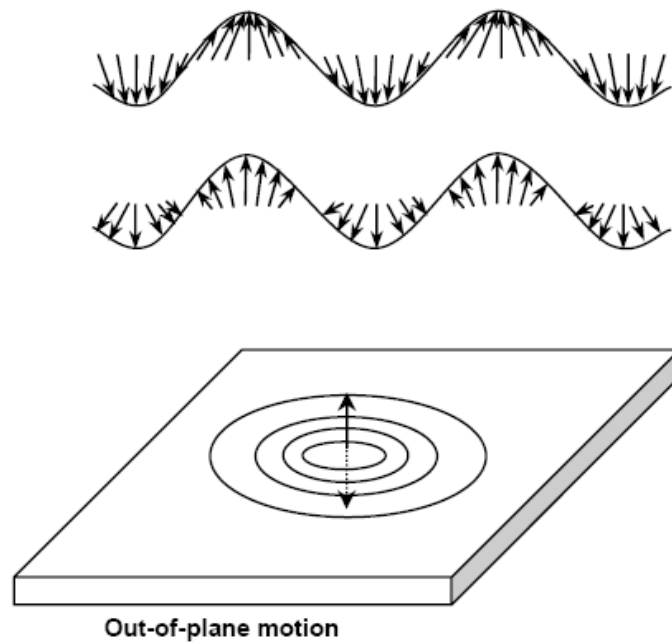
**Fig. 2.2.** Dispersion curves of Lamb waves in a free aluminium plate

( $C_L = 6500 \text{ m/s}$ ,  $C_T = 3150 \text{ m/s}$ ,  $C_L$ : velocity of longitudinal wave,  $C_T$ : velocity of transverse wave; dotted rectangle: non-dispersion region) [47]



(a)

**Fig. 2.3.** Particle motion in (a)  $S_0$  and (b)  $A_0$



(a)

**Fig. 2.3. Cont.**

### ***Using Lowest-order Symmetric Lamb Mode ( $S_0$ )***

In the majority of Lamb-wave-based studies [8, 9, 48], the  $S_0$  mode is selected for damage identification, because compared with the  $A_0$  mode it exhibits [49]:

- (i) lower attenuation ( $A_0$  usually displays higher attenuation during propagation because of the dominant out-of-plane movement of particles in that mode, which leaks partial energy to the surrounding medium; whereas  $S_0$  has mostly in-plane displacement and its energy is confined within the plate);
- (ii) faster propagation velocity, meaning that complex wave reflection from structural boundaries can be avoided in some cases; and

(iii) lower dispersion, facilitating signal interpretation.

In addition to its advantages already described, the  $S_0$  mode has been found to exhibit higher sensitivity to damage in structural thickness and to delamination in composites in terms of pulse-echo measurement in particular in terms of pulse-echo measurement [50, 51], compared to  $A_0$ . For the same defect in a structure, the  $S_0$  mode produces stronger reflections than  $A_0$ , implying that the  $S_0$  mode can be more suited to locating a defect than  $A_0$  if reflection of the wave is explored [52]. With all these advantages,  $S_0$  claims a wide application domain. However,  $S_0$  has a longer wavelength than the  $A_0$  mode at a given frequencies in the non-dispersion region. This undermines its sensitivity to damage of small dimension, since the half wavelength of a selected mode should ideally be shorter than or equal to the size of damage so as to allow the wave to interact with the damage phenomenally [53].

### ***Using Lowest-order Anti-symmetric Lamb Mode ( $A_0$ )***

There has been increasing awareness of using the  $A_0$  mode for damage identification [54-57]. The merits of this mode, in comparison with the  $S_0$  mode, include [49]:

- (i) shorter wavelength at a given excitation frequency and therefore greater sensitivity to small-sized damage (reiterating that the half wavelength of a

selected mode should ideally be shorter than or equal to the size of the damage to allow the wave to interact with it);

- (ii) greater signal magnitude (the  $A_0$  mode in a Lamb wave signal is usually much stronger than the  $S_0$  mode, presenting a high signal-to-noise ratio (SNR), though as mentioned earlier it attenuates more quickly); and
- (iii) easier means of activation (the out-of-plane motion of particles in a plate can be more easily activated by ultrasound transducers vibrating out-of-plane).

The  $A_0$  mode outperforms the  $S_0$  mode with higher sensitivity to surface damage such as cracks [55], corrosion [54, 56] or surface crack growth [57]. In recognition of the above observations and in particular of the fact that the  $A_0$  mode features a shorter wavelength than its symmetric counterparts and therefore enables scrutiny of damage of smaller dimension, the  $A_0$  mode has been employed for identification of a variety of defects, e.g., corrosion [53]. However, due to its out-of-plane vibration manner,  $A_0$  is particularly susceptible to conditions that exist on the surface of structures. For example,  $A_0$  has been reported to be very sensitive to the coupling effect of fluid [22, 53, 58]. Another drawback of  $A_0$  is its fast attenuation properties during propagation, especially when the structure is coupled with another kind of medium. Therefore,  $A_0$  may not be suitable for long-range NDE.

## 2.2.2 Tube-like Structures

The counterparts of Lamb waves propagating in a tube are *cylindrical Lamb waves*, which have received a great deal of attention in developing NDE techniques for tube-like structures such as pipework in the petro-chemical industry [35, 59-61]. Petro-pipework transfers oil from one place to another hundreds or even thousands of miles away, remaining in service for years. If damage occurs, it causes great economic loss. The NDE techniques for inspecting pipework are therefore of great significance.

Figure 2.4 shows the dispersion curves of cylindrical Lamb wave (group velocities vs. PFT) in a steel pipe. It can be observed that the characteristics of cylindrical Lamb waves are much more complex than those of Lamb waves in a plate. To further distinguish the wave modes in tubular structures, all cylindrical Lamb modes are defined as  $L(0,n)$ ,  $T(0,n)$  and  $F(m,n)$  (where  $m$  and  $n$  are two integers, and  $m,n=1, 2, 3, etc.$ ). The first integer of the integer pair in each mode label gives the harmonic order of circumferential variation. Despite the axially symmetric (zero-order) modes that propagate axially along the tube, other modes have harmonic variation of displacements and stresses around the circumference. For example, when  $m=1$ , this kind of mode, e.g.,  $F(1,2)$ , has one cycle of variation around the circumference; when  $m=2$ , it has two, and so on.

As a result of the complexity of cylindrical Lamb waves in tube-like structures, most

endeavours have focused on the means to generate a single mode, to mitigate the difficulty of dealing with multiple modes [62]. In practical applications, ring-type transducers are customarily employed to generate symmetric modes, such as  $L(0,n)$  [60].

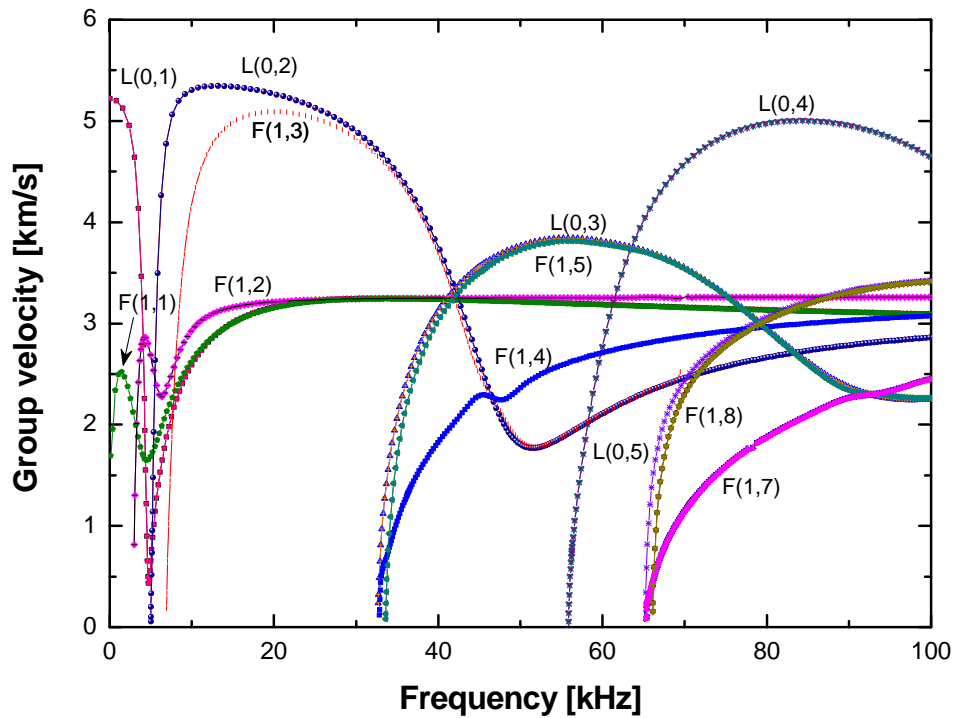


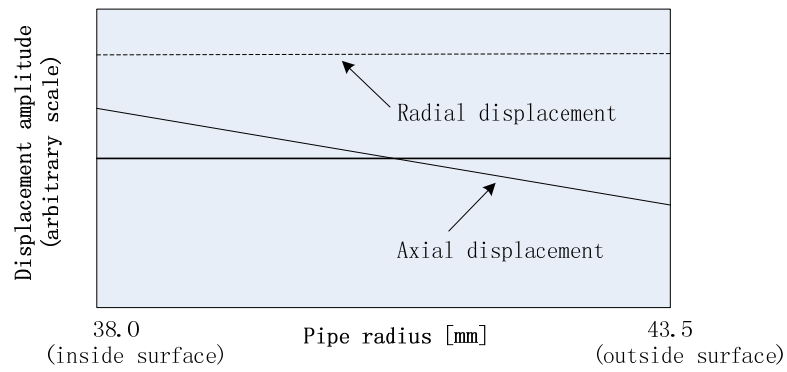
**Fig. 2.4.** Dispersion curves of cylindrical Lamb waves in a steel pipe (inner diameter: 150 mm, thickness: 50 mm)

### *Using Longitudinal Modes*

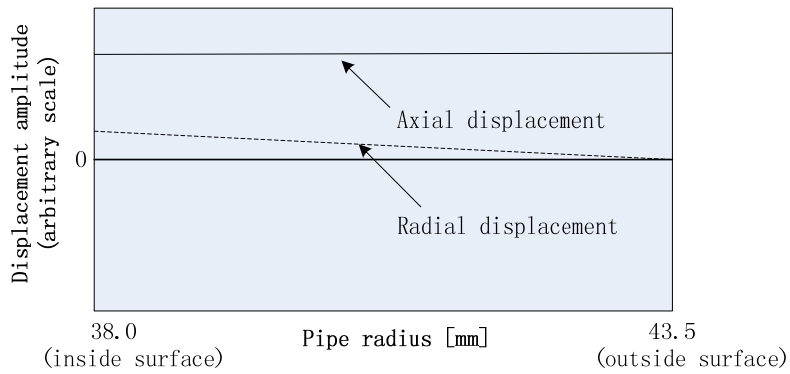
Longitudinal cylindrical Lamb modes,  $L(0,n)$ , have particle displacement only in the axial and radius directions, and there is no circumferential component of particle displacement. They are symmetric modes that travel axially along the pipe. It has

been documented that  $L(0,n)$  can be activated by a piezoelectric transducer system which comprises a ring of piezoelectric elements clamped individually to the pipe surface [60], and  $L(0,1)$  can be generated using two transmitter rings [63]. Figure 2.5(a) shows the mode shape of the  $L(0,1)$  mode in a steel pipe at an excitation frequency of 70 kHz. It can be seen that the radial displacement components dominate the particle vibration, which is similar to the out-of-plane vibration in the  $A_0$  plate mode at a low frequency [63].

On the other hand,  $L(0,2)$  has relatively uniform stress distribution over the cross-section of the pipe, and is therefore susceptible to abnormalities in the cross-section which emerges at either inner or outer surface of the pipe [60]. Because of its practical non-dispersive properties,  $L(0,2)$  is prevalent in use for pipe inspection, in particular long range inspections [62]. Figure 2.5(b) shows the mode shape of  $L(0,2)$ , which consists predominantly of axially symmetric uniform axial motions throughout the thickness of the pipe wall, and is therefore similar to the  $S_0$  mode in plate at a low frequency [63].  $L(0,2)$  is appealing in practice for several reasons: (i) it is almost non-dispersive over a wide range of excitation frequencies, resulting in fewer changes in waveform and attenuated signal intensity; (ii) it always has fast propagation velocity in practical applications, so that any unwanted wave modes arrive after the acquisition of  $L(0,2)$ , facilitating signal interpretation; and (iii) its mode shape (Fig. 2.5(b)) makes it equally sensitive to internal and external defects at any circumferential location.



(a)



(b)

**Fig. 2.5.** Mode shapes of (a)  $L(0,1)$  and (b)  $L(0,2)$  in a steel pipe (inner diameter: 76 mm, thickness: 5.5 mm) at an excitation frequency of 70 kHz

### ***Using Torsional Modes***

Torsional modes have only the circumferential components of particulate vibration. Figure 2.6 presents the dispersion curves of torsional Lamb modes in a steel pipe. It can be observed from the figure that multiple torsional modes exist in the frequency range from 0 to 3.0 MHz, and the lowest torsional mode  $T(0,1)$  is non-dispersive

whereas other higher modes are markedly dispersive. Figure 2.7 displays the mode shape of the  $T(0,1)$  mode in a 3-inch pipe. It can be seen that the tangential displacements are approximately constant throughout the pipe wall thickness, indicating that defects may be detectable anywhere in the cross-section of the pipe using  $T(0,1)$ . In general,  $T(0,1)$  has been an attractive candidate to develop NDE techniques for inspection of tube-like structures including circumferential and longitudinal defects [59], in that (i) its signal shape and intensity are retained as it propagates in the structures; and (ii) at all frequencies  $T(0,1)$  remains the fastest of the torsional modes.

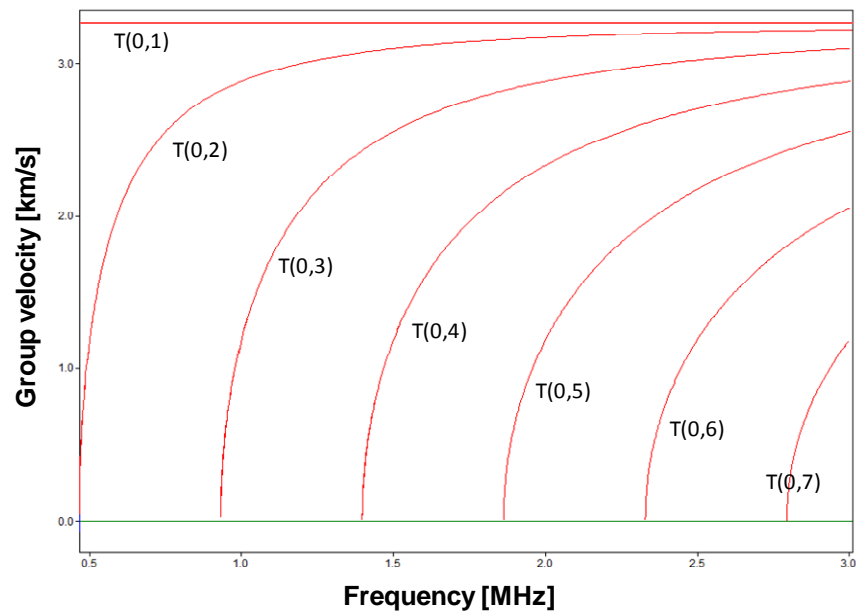


**Fig. 2.6.** Dispersion curves of torsional modes in a steel pipe (outer diameter: 60 mm, thickness: 3.5 mm) [64]

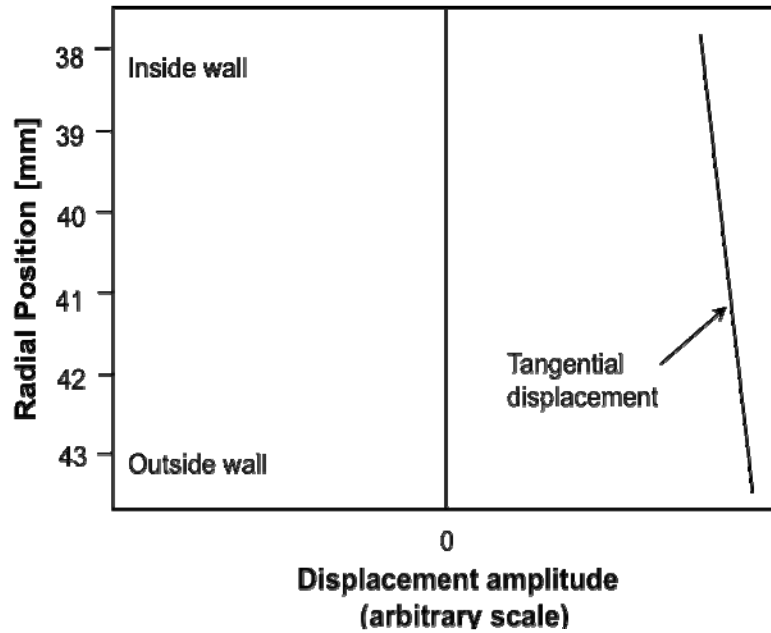


Fig. 2.7. Mode shape of  $T(0,1)$  in a 3-inch pipe at 45 kHz (radial and axial displacements being zero) [59]

## 2.3 QUS

### 2.3.1 Implementations

Osteoporosis, the consequence of asymptomatic bone loss earlier in cancellous and later in cortical bone, increases the risk of bone fracture especially in regions of dominant skeletal sites, e.g., spine, distal radius and hip, producing a significant public health threat to an estimated 55% of people over 50 years of age worldwide (80% are female). In the United States, about 34 million individuals suffer from osteoporosis and 10 million are at high risk of developing it in the near future [65]. In

Hong Kong, people over 60 account for 12% of the population, with a yearly increase of 5.1% contrasting with the global rate of 1.7%. These figures indicate that more and more Hong Kong citizens are likely soon to develop osteoporosis and associated problems [66].

Two major techniques in current use for assisting in the diagnosis of osteoporosis and monitoring of the healing progress of fractured bone are radiation-based bone mineral density (BMD) analysis (*i.e.*, *bone densitometry*, such as DXA, the ‘gold standard’ method for clinical diagnosis of osteoporosis), and quantitative ultrasound (QUS). QUS outperforms densitometry in some aspects, including (i) potential to render rich information including various elastic properties and geometric features of bone, contrasting with BMD which is inherently limited to bone density and geometry alone; (ii) absence of health risk to operators and patients by virtue of not using ionising radiation; and (iii) low energy consumption, good portability and inexpensive implementation. To clinically implement QUS, one can use (i) axial transmission, (ii) transverse transmission, or (iii) a pulse-echo scheme [12-21] (Fig. 1.1).

### ***Axial Transmission***

The axial transmission technique, using a pair of transducers placed in tandem on one side of the skeletal site, as illustrated in Fig. 1.1(a), can easily assess human long bones such as the tibia and radius. This technique has been reported to be able to

reflect multiple parameters of bone, such as geometric and mechanical properties [18, 25, 67-69]. The axial transmission technique is the most promising way to implement QUS in clinic.

As an example, in the technique proposed by Moilanen *et al.* [16, 70, 71] a device consisting of a wave transmitter and a wave receiver which could be perpendicularly positioned at a particular skeletal site was developed. With the transmitter fixed and the receiver moving at a constant step, signals captured at different measurement positions contribute to a distance-time diagram from which the velocities of waves propagating in the bone can be calculated. Bossy *et al.* [14, 72] developed a bidirectional axial transmission technique in which an ultrasonic probe with four integrated transducers (two transmitters at both ends and two receivers in the middle of the probe). Ultrasonic waves are activated by two transmitters to travel along the bone in opposite directions and then received by two receivers. This configuration was considered to offer enhanced precision of measurement. In addition to those two techniques, some techniques have been commercialised, and the Sunlight Omnisense™ (Sunlight Medical) is one such. It makes use of a set of transducers to measure the SOS along a fixed distance of the cortical layer of a bone (e.g., phalanges, radius, metatarsus and tibia [26, 73]), parallel to its long axis.

### ***Transverse Transmission***

The transverse transmission technique allows the pulse of ultrasound to propagate transversely through bones. BUA and SOS determined from ultrasound transmission measurements can be employed to evaluate the properties of the bone. In this technique, two transducers, one serving as transmitter and the other as receiver, are positioned in opposite directions on two sides of the skeletal site [74] (Fig. 1.1(b)).

It is suggested that the transverse transmission measurement provides information about bone density, bone elasticity and the characteristics of bone microstructure, which are of vital importance in determining bone strength [75-78]. Transverse transmission measurements are often conducted at the distal radius, heel pad, os calcis, tibia, phalanges, and patella [79-83]. For example, transverse transmission at the heel pad can be used (i) for prediction of fracture risk, and (ii) to assist in the diagnosis of osteoporosis [84].

### ***Pulse-echo***

As illustrated in Fig. 1.1(c), when a wavefront impinges at the interface of soft tissue and bone, reflection and refraction take place. The total incident energy is subsequently separated into reflected and refracted components, as well as that absorbed by surrounding tissues coupled to bones. The proportions of the reflected

and refracted energy are dependent on the properties of the interface, incident angle and wave frequency. Based on this, reflection-based ultrasonic measurements have been used for bone assessment. This technique can reflect the elastic and material properties of bone, as well as bone microstructure features [85, 86].

### **2.3.2 Hypotheses**

Among the above three means of implementing QUS, axial transmission has attracted the most attention. To perform axial transmission measurements, different hypotheses have been applied by considering the bone structure to be a plate or tube:

#### ***Plate Model***

The middle section of a long bone, where fracture often occurs, can be deemed locally flat [69, 87]. The theory of Lamb waves in flat plate can thus predict wave propagation well in a long bone [88, 89]. Nicholson *et al.* [24] evaluated elastic waves propagating in acrylic plates (a kind of bone-mimicking material), and described *in vivo* tibial measurements of the lowest-order Lamb modes. Results showed that the theory of Lamb wave in plate can predict wave propagation well in bone, indicating that Lamb-wave-based measurement might offer an enhanced approach to the ultrasonic characterisation of long bones. Lee and Yoon [89] identified the leaky Lamb modes and the excitation frequency that are most effective for bone assessment.

In their study, wave propagation in Lucite™ plates of different thicknesses (simulating bone) and a bovine tibia with a cortical thickness of 2 mm were examined at various excitation frequencies. Moilanen *et al.* [22] tested some bone-mimicking materials, both free and immersed in fluid, and captured the lowest-order Lamb modes and the first bilayer wave mode in the free and immersed plates, respectively.

### ***Tube Model***

Although the plate model achieves good prediction for Lamb waves propagating in long bone, it becomes unwieldy when used for examining waves propagating in cortical bones of great thickness [25]. In recognition of the fact that human long bone is actually not a plate-like but tube-like structure, the theory of cylindrical Lamb waves in tube has been attractive for describing wave propagation characteristics in bones [25]. Due to the circumferential curvature of long bones such as the radius, it is preferable to replace waves in plate with those in tube in order to enhance the accuracy of bone thickness prediction [25]. The work conducted by Moilanen *et al.* [90] has demonstrated that the approach based on the characteristics of a particular wave mode in tube provides a good estimate of cortical bone thickness. Experiments were conducted by ultrasonically examining a series of acrylic tubes with an outer radius of 10.0 mm and wall thicknesses of 2.0, 4.0, 6.0 and 8.0 mm [25]. The results indicated that the plate model was inapplicable for examining waves in tubular samples when the tube wall was thick. Bone thickness is overestimated using plate

mode where the bone has a thick wall, resulting in impaired measurement precision and accuracy.

## **2.4 Medium Coupling Effect**

### **2.4.1 Introduction**

The characteristics of elastic waves propagating at an interface of multiple media (such as that between soft and hard media, e.g., soft tissue and bone) have attracted the attention of many researchers [91-102]. Some pilot studies [11, 22, 23, 58, 103, 104] have shown that the propagation of waves in hard media can be influenced by the attached/coupled soft media (e.g., fluid and soft tissues). To summarise the knowledge concerning the coupling effect in Lamb-wave-based NDE for engineering structures and QUS for human bone assessment, this section is divided into two parts.

### **2.4.2 Coupling Issues in NDE**

A number of wave-based NDE techniques have been developed and applied to various engineering structures, including those submerged or buried. Under such circumstances the structures are coupled with another medium that may exert certain effects on waves propagating in the structures. The coupled medium can provide a

way for the wave in a structure to radiate outwards. When they meet the boundaries of a coupled medium, the waves are reflected, finally pervading the whole coupled system. Some studies have found that this coupling effect can be prominent [11, 58, 103, 104]. Cheeke *et al.* [11, 58] reported prominent decreases in the group velocity of some Lamb modes in a stainless steel thin-walled cylinder and an aluminium thin-walled cylinder when both the cylinders were filled with water, a finding that drew much attention to this coupling effect. In the work of Yapura and Kinra [103], an analytical fluid-solid-coupled bi-layer model was developed, and the calculated dispersion properties of Lamb waves in this bi-layer model were found to be much different from those in a free solid plate, indicating a strong coupling effect of fluid on the characteristics of Lamb waves. Wu and Zhu [104] studied a fluid-solid-fluid medium, with the numerical results showing that the phase velocity of Lamb waves changes with the thickness of the fluid layers. All the work abovementioned has raised an issue that the surround medium (e.g., fluid) can exert certain coupling effect on Lamb waves propagating in solid structures.

### **2.4.3 Coupling Issues in QUS**

The coupling issue encountered in NDE applications is also a concern in QUS for human bone assessment. Continual efforts have been made with a hope of eliminating the coupling effect arising from soft tissues on ultrasound waves by manipulating transducers in a deliberate manner. Representatively, a device comprised of a

transmitter and a receiver was invented [16, 22, 71]. By fixing the transmitter and then moving the receiver at a constant step, signals captured at each step form a distance-time diagram, from which the wave packets propagating in bone can be depicted and velocities can be determined by fitting lines to the wave packets. With such a means the calculated wave velocity is independent of the overlying soft tissues. In a bidirectional axial transmission technique [14], an ultrasonic probe with four integrated transducers (two transmitters at both ends and two receivers in the middle of the probe) was developed. Ultrasonic waves are activated by two transmitters to travel along the bone in opposite directions and then received by two receivers. By considering the time delays of waves propagating in opposite directions, errors resulted from the unequal thickness of coupled soft tissues and probe inclination can be avoided. Despite most of the current endeavours in this regard are aimed at minimising the coupling effect of soft tissues through ingenious design of transducers or novel calculation algorithms, insight into the mechanism of coupling effect of soft medium on ultrasonic waves in a solid medium principally accommodating wave propagation is lacking.

Soft tissues covering bones may exert a coupling effect on Lamb waves in bone, modulating the wave propagation. Although Lamb waves are mostly confined in bones, soft tissue can provide a way for the Lamb wave to reradiate into it, provided that their velocity in bone is greater than the longitudinal velocity in the soft tissue [69, 105]. As a result, the waves do not propagate separately in bone and soft tissue (Fig.

2.8(a)), but propagate through the entire soft tissue-bone medium (Fig. 2.8(b)). The characteristics of Lamb wave in bone can thus be influenced by soft tissue [22]. This indicates that it is highly necessary to systematically interrogate and calibrate such coupling effects when developing high precision QUS-based techniques for bone assessment. Quantitative calibration of this effect and compensation for it remain significant whereas challenging.

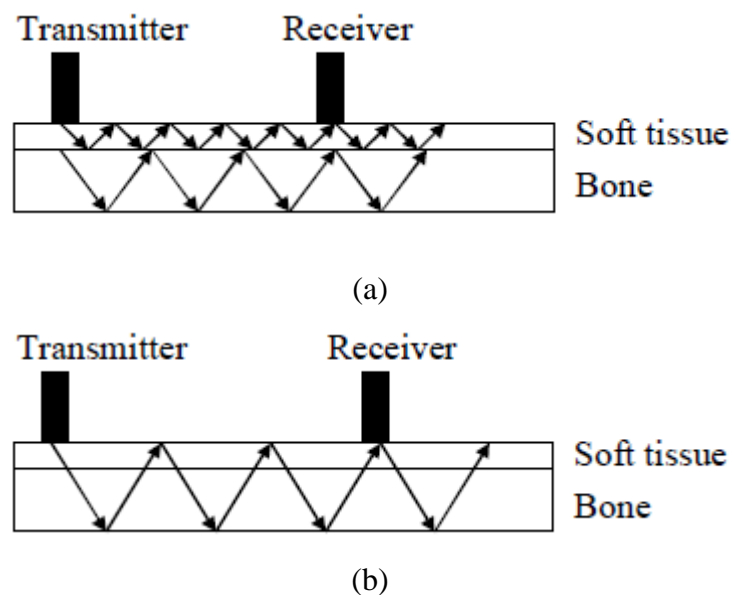


**Fig. 2.8.** Illustration of Lamb waves propagating either (a) separately in bone and soft tissue or (b) in the combination of bone and soft tissue [100]

## 2.5 Concluding Remarks

Lamb waves have been the core of intensive efforts in developing NDE techniques for engineering structures and QUS for human bone assessment. This chapter provides a

comprehensive review of the state of the art of Lamb-wave-based NDE and QUS, including the introduction of various applications of Lamb waves in NDE and QUS. Subsequently the effect of coupled media (fluid or soft tissue) on the propagation of Lamb wave is raised, with the understanding that such a coupling effect can modulate the propagation of Lamb wave in engineering structures and human bones. The significance of calibrating and rectifying this effect is emphasised.

# **CHAPTER 3            Fundamentals of Guided Waves**

## **3.1 Introduction**

Guided waves are elastic waves propagating along a waveguide, such as a plate, rod or cylinder. Lord Rayleigh in 1889 first explained wave propagation along a guided surface [106], and those waves are known as Rayleigh waves today. Following Rayleigh's work, Horace Lamb reported the waves discovered in plates in 1917, and the waves were named after him as Lamb waves. Lamb waves have been at the core of intensive research over decades with the aim of developing various NDE techniques for inspection of engineering structures and systems, mainly including theoretical development [107, 108], numerical simulation [109, 110], and experimental investigation [11, 53, 111-113]. The premise of Lamb-wave-based NDE is twofold: (i) propagation of Lamb waves can be modulated by damage existing in their propagation paths, accompanied by wave scattering such as reflection, transmission and mode conversion; and (ii) different locations and severities of damage cause different scattering phenomena of the waves.

Human bones (e.g., radius or femur) are complex 3D tubular structures with irregular cross-sections at different axial positions, which are overlaid by soft tissues (e.g., muscles and skin) and filled with marrow. But given that (i) as a result of the operation of QUS in an ultrasonic frequency range, the wavelength of a diagnostic wave is much shorter than the radius of curvature of a typical human long bone; and (ii) a transmitter and receiver placed in tandem (forming a transducer pair) for implementing axial transmission are often a short distance apart, the skeletal part covered by the transducer pair is often hypothesised to be locally flat by neglecting its curvature [69, 87]. Furthermore, when canvassing waves in human long bones in an ultrasonic frequency range [22, 24], the bone materials covered by the transducer pair can be considered to have a homogeneous and isotropic nature. Satisfactory precision has been demonstrated when using such an approximation for long bones [22, 24]. Under such a circumstance the bone-guided ultrasonic waves can be described using the theory of elastic waves in thin plates, *i.e.*, *Lamb waves*.

Although much relevant literature exists, it is incumbent here to recapitulate key aspects of Lamb waves relevant to the work.

## **3.2 Waves in Thin Plate Structures**

In a thin isotropic and homogeneous plate, an elastic wave, regardless of its mode, can generally be described in a form of *Cartesian* tensor notation as [114]:

$$\mu \cdot u_{i,jj} + (\lambda + \mu) \cdot u_{j,ji} + \rho \cdot f_i = \rho \cdot \ddot{u}_i \quad (i, j=1, 2, 3), \quad (3.1)$$

where  $u_i$  and  $f_i$  are respectively the displacement and the body force in the  $i$ -direction.  $\rho$  and  $\mu$  are the density and shear modulus of the plate, respectively.

$\lambda = \frac{2\mu \cdot \nu}{1-2\nu}$  ( $\lambda$  is Lamé constant, and  $\nu$  is the Poisson's ratio of the plate). Using the

*displacement potentials method* based on *Helmholtz decomposition* [114, 115],

assuming a plane strain condition, applying boundary conditions at both the upper and

lower surfaces, and considering the symmetric/anti-symmetric properties of

trigonometric function, Equation 3.1 can be decomposed into two uncoupled parts:

$$\frac{\tan(qh)}{\tan(ph)} = -\frac{4k^2 qp}{(k^2 - q^2)^2} \quad \text{for symmetric Lamb modes,} \quad (3.2a)$$

$$\frac{\tan(qh)}{\tan(ph)} = -\frac{(k^2 - q^2)^2}{4k^2 qp} \quad \text{for anti-symmetric Lamb modes,} \quad (3.2b)$$

where

$$p^2 = \frac{\omega^2}{c_L^2} - k^2, \quad q^2 = \frac{\omega^2}{c_T^2} - k^2, \quad k = \frac{2\pi}{\lambda_{wave}}, \quad c_L = \sqrt{\frac{E(1-\nu)}{\rho(1+\nu)(1-2\nu)}},$$

$$\text{and } c_T = \sqrt{\frac{E}{2\rho(1+\nu)}}.$$

In the above equations,  $h$ ,  $k$ ,  $\omega$  and  $\lambda_{wave}$  are respectively the half thickness of the plate, wavenumber, circular frequency and wavelength of a wave mode of interest.  $c_L$

and  $c_T$  are the velocities of longitudinal and transverse wave modes ( $E$ : Elastic modulus of the plate), respectively. Symbols  $S_i$  and  $A_i$  ( $i=0, 1, 2, \text{etc.}$ ) in what

follows stand for the symmetric and anti-symmetric Lamb modes, respectively, with

the subscript b7

ing the order. At any given frequency,  $S_0$  and  $A_0$  modes co-exist and higher-order modes appear as frequency increases (meaning that except for the  $S_0$  and  $A_0$  modes, each of the Lamb modes has a cut-off frequency where the phase velocity approaches infinity while the group velocity approaches zero). As indicated in Fig. 2.2 which shows the dispersion curves of different Lamb wave modes in a free aluminium plate [47], all modes are dispersive, manifesting as the dependence of propagation velocity on the algebraic product of excitation frequency and plate thickness, whereas a non-dispersion region exists at low frequency (less than  $1.0 \text{ MHz}\cdot\text{mm}$  for the plate under discussion) where  $S_0$  and  $A_0$  travel at almost constant velocities and higher-order modes are absent.  $S_0$  and  $A_0$  in the non-dispersion region are often employed for damage identification [28, 54] and bone assessment [23, 89, 90].

### **3.3 Waves in Tubular Structures**

As already described in Chapter 2, the counterparts of Lamb waves in plates propagating in a tubular structure such as a pipe are cylindrical Lamb waves (shown schematically in Fig. 3.1), which exhibit similar properties to those of Lamb waves in plates, but more complex.

Like Lamb waves in a flat plate that are grouped into symmetric or anti-symmetric modes, cylindrical Lamb waves can be categorised into three groups: longitudinal, torsional and flexural modes. At low frequencies, longitudinal, torsional and flexural

modes dominate in wave signals, whereas at high frequencies the waves in the pipe behave more and more like the normal Lamb modes in a thin plate or shell.

Zero-order cylindrical Lamb modes, represented by  $L(0,n)$ ,  $T(0,n)$  and  $F(0,n)$  (referring to Section 2.2.2 in Chapter 2) have attracted significant attention for the development of NDE techniques which can be used for pipe inspection. Three cylindrical, intermingled Lamb modes exist synchronously in tubular structures. In an axisymmetric tubular structure,  $L(0,n)$  modes are characterised by axisymmetric longitudinal and radial particle displacement;  $T(0,n)$  modes have only circumferential particle displacement;  $F(0,n)$  modes are non-symmetric and have displacement components in all directions. In particular,  $L(0,1)$  propagates similarly to the  $A_0$  mode in flat plates, and  $L(0,2)$  has properties similar to the  $S_0$  mode in flat plates, in terms of the vibration of particles [116]. Because their axisymmetric properties facilitate easy 360° inspection along the circumference of pipes, both  $L(0,1)$  and  $L(0,2)$  are preferable to other modes for damage identification [117].

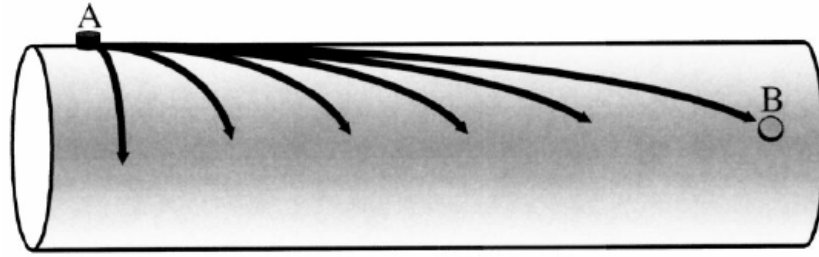


**Fig. 3.1.** Cylindrical Lamb waves in a pipe section, activated by an actuator at *A* and received by a sensor at *B*, showing six helical propagation paths [118].

### **3.4 Stoneley and Scholte Waves**

Stoneley and Scholte waves are the interface waves that propagate along solid-solid and liquid-solid interfaces, respectively. As illustrated in Fig. 3.2, when Medium 1 and Medium 2 are both solid, Stoneley waves emanates at the interface. They exist for two perfectly joined materials when specific conditions are satisfied [114]. Stoneley waves are not dependent on frequency, and therefore exhibit non-dispersive properties. In the scenario in which Medium 1 is fluid and Medium 2 is solid, Scholte waves exist at the interface. This wave type carries almost all of the energy in the liquid rather than in the solid, and its amplitude decreases slightly in the liquid but rapidly in the solid [114].

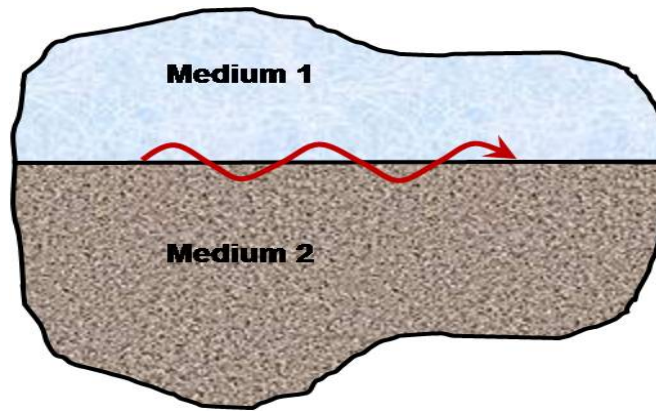


**Fig. 3.2.** Illustration of an interface wave travelling at an interface of two media

### 3.5 Waves in Fluid-solid-coupled Media

Many engineering structures, such as submarines and boat hulls, work in submerged environments where the outer structural surfaces are in contact with fluid. This phenomenon can be generalised into a fluid-solid-coupled issue. Likewise, human bone is covered with soft tissues which are a fluid-like medium. In these contexts, the characteristics of wave propagation in a fluid-solid-coupled medium become of great interest when carrying out wave-based NDE and QUS.

Figure 3.3 illustrates a 2D fluid-solid-coupled medium, considering the solid part as a homogeneous, isotropic and linear elastic plate of  $h$  in thickness which is coupled with a layer of fluid of  $h_f$  in thickness. Both solid and fluid parts have infinite in-plane dimensions. The mechanism governing the motions of elastic waves can be described using Equation 3.1. By applying the Helmholtz decomposition of the displacement vector [115], Equation 3.1 can be uncoupled as

$$u_i = \frac{\partial \phi}{\partial x_i} + e_{ijk} \frac{\partial \psi_k}{\partial x_j}, \quad (3.3)$$

where  $\phi$  is a scalar potential,  $\psi_j$  is a vector potential and  $e_{ijk}$  is the permutation symbol.

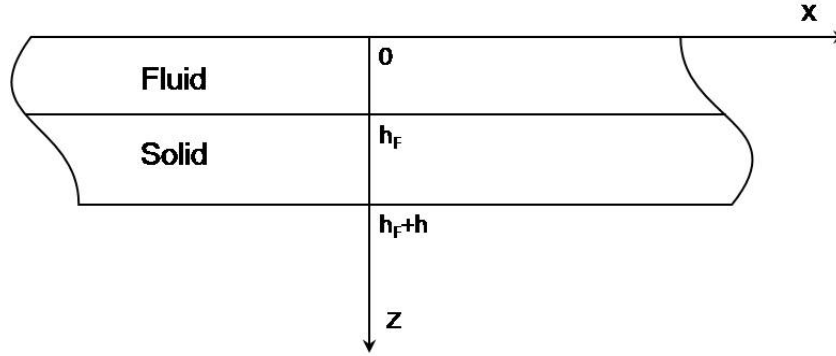


**Fig. 3.3.** Schematic of a fluid-solid-coupled medium

Considering a harmonic Lamb wave propagating along the  $x$ -direction under the plane strain hypothesis, the displacement potentials satisfy the wave equations (details can be found in [103]). Solutions to the wave equations are in form of a standing wave in the  $z$ -direction and a travelling wave in the  $x$ -direction. Finally, six unknown coefficients remain to be determined. Now considering a fluid-solid-coupled medium, the above discussion is also applicable. To achieve solutions for the six unknowns for this fluid-solid-coupled medium, the following boundary conditions should ideally be satisfied [103]:

- (i) as the upper surface of the fluid and lower surface of the plate are free, the normal stresses at both surfaces and the shear stress at the free surface of the solid remain zero,

$$\sigma_{zz} = 0, \text{ at } z = h_F + h \quad (3.4)$$

$$\sigma_{zz}^F = 0, \text{ at } z = 0 \quad (3.5)$$

$$\sigma_{xz} = 0, \text{ at } z = h_F + h \quad (3.6)$$

where  $\sigma_{zz}$  and  $\sigma_{zz}^F$  are the stress components in the  $z$ -direction in the solid and fluid, respectively.  $\sigma_{xz}$  is the shear stress component in the  $x$ - $z$ -plane in the solid;

- (ii) at the interface of the solid and fluid, the normal stresses are continuous, and therefore the stresses in the fluid and solid sides are equal,

$$\sigma_{zz} = \sigma_{zz}^F, \text{ at } z = h_F; \quad (3.7)$$

- (iii) the normal components of the displacements in the solid and fluid are the same at the fluid-solid interface,

$$u_{zz} = u_{zz}^F, \text{ at } z = h_F \quad (3.8)$$

where  $u_{zz}$  and  $u_{zz}^F$  are the displacement components in the  $z$ -direction in the solid and fluid, respectively; and

- (iv) as the fluid cannot sustain shear stresses, the tangential component of the stress tensor at the fluid-solid interface is discontinuous. As a result, the tangential stress tensor in the fluid side is zero,

$$\sigma_{xz}^F = 0, \text{ at } z = 0 \quad (3.9)$$

where  $\sigma_{xz}^F$  is the shear stress component in the  $xz$ -plane in the fluid.

With the above boundary conditions, the six unknown coefficients can be obtained, finally yielding the dispersion equations describing the characteristics of guided

waves in this fluid-solid-coupled medium [103],

$$\pi^2 \gamma p \Omega^4 (d^2 N + 4\xi^2 pqO) \sin 2\tau r + 16r(d^2 M + 4\xi^4 pqL)(d^2 L + 4\xi^2 pqM) = 0 \quad (3.10)$$

where

$$L = \cos p \sin q, \quad M = \cos q \sin p, \quad N = \cos 2p \sin 2q, \quad O = \cos 2q \sin 2p$$

$$p = \frac{1}{2} \pi \left( \frac{\Omega^2}{K^2} - \xi^2 \right)^{\frac{1}{2}}, \quad q = \frac{1}{2} \pi (\Omega^2 - \xi^2)^{\frac{1}{2}},$$

$$r = \frac{1}{2} \pi \left( \frac{\Omega^2}{K_F^2} - \xi^2 \right)^{\frac{1}{2}}, \quad d = \frac{1}{2} \pi \left( \frac{\Omega^2}{K_F^2} - 2\xi^2 \right),$$

$$K = \frac{c_L}{c_T}, \quad K_F = \frac{c_F}{c_T}, \quad \tau = \frac{h_F}{h}, \quad \gamma = \frac{\rho_F}{\rho}, \quad \Omega = \frac{2\omega h}{\pi c_T}, \quad \xi = \frac{2kh}{\pi},$$

$c_L$ ,  $c_T$  and  $c_F$  are the phase velocities of longitudinal and shear waves in the solid and bulk waves in the fluid, respectively.  $\rho_S$  and  $\rho_F$  are the densities of the solid and fluid, respectively.  $K$  and  $K_F$  are wavenumbers in the solid and fluid, respectively.  $k$  is the wavenumber that needs to be solved.

Noticing that the velocities calculated from Equation 3.10 are phase velocities, in an attempt to obtain the corresponding group velocities, the partial derivatives of Equation 3.10 were calculated with respect to  $\omega$  and  $\lambda$ , respectively. The group velocity can be obtained as

$$V_{group} = - \frac{A' + C' + D' + E' + F' + G'}{A + B + C + D + E + F + G} \quad (3.11)$$

where  $V_{group}$  is the group velocities of Lamb waves in the fluid-solid-coupled medium.

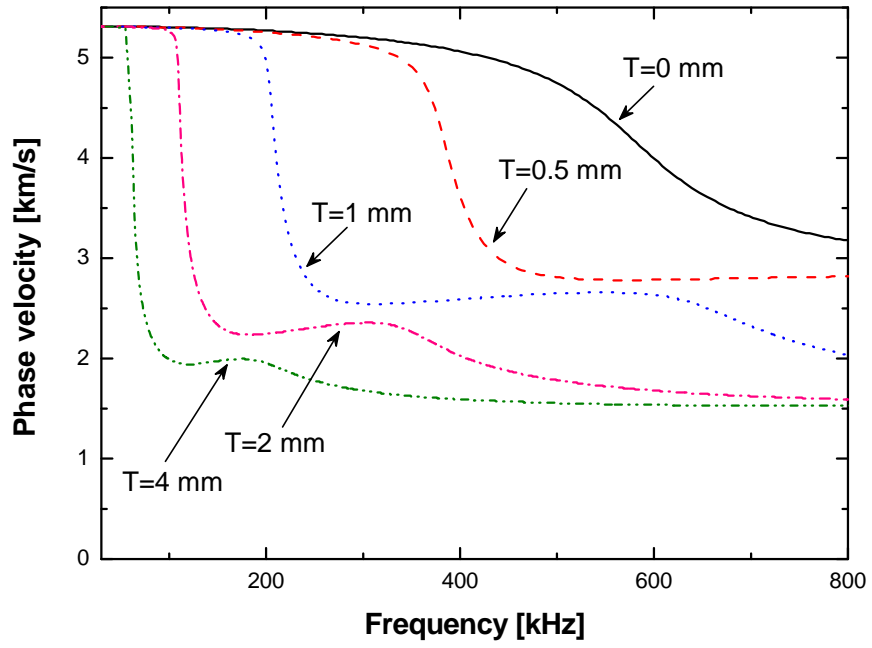
The summation of  $A - G$  is the derivative with respect to  $\omega$ , and that of  $A' - G'$  is the derivative with respect to  $\lambda$  (details can be found in Appendix A).

To obtain the solutions to Equation 3.10, *i.e.*, the dispersion curves of the discussed Lamb wave modes in terms of the phase velocity, an in-house code was developed in MATLAB<sup>®</sup> (Version 7.10 (R2010), the MathWorks) with a MATLAB function *fsolve*. To trace all the wave modes in a given frequency region, two steps were employed: (i) to trace solutions to the dispersion equation at selected frequencies using different pre-determined initial guesses (this operation was able to find all the modes at the given frequencies, indicating the number of the wave mode at these frequencies); and then (ii) to trace each mode in the whole frequency region starting from the frequency points where solutions had been achieved in step (i). It is noteworthy that in step (ii), because the velocities of most wave modes are dependent on frequencies, the initial guess at each selected frequency varied.

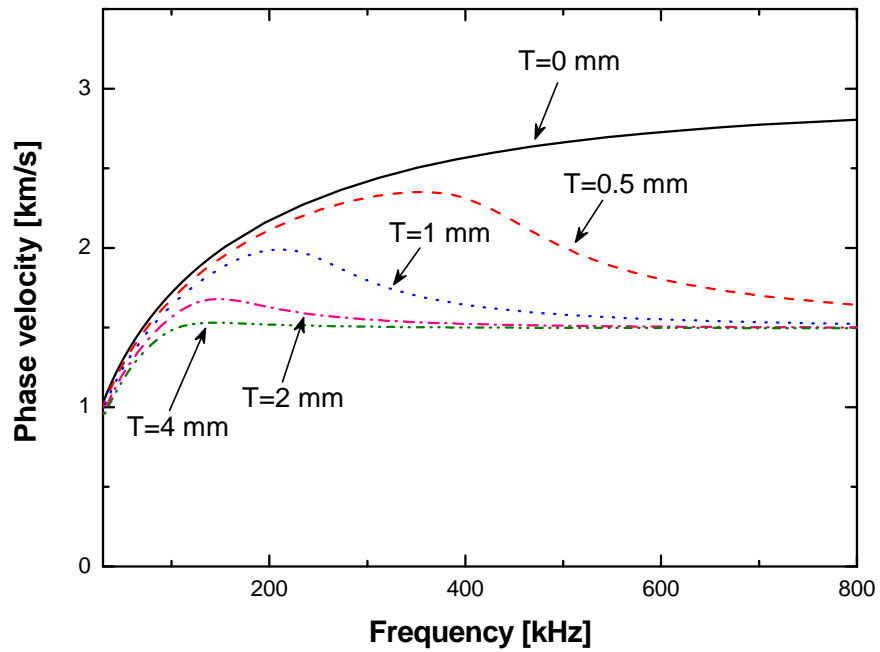
During the searching, the step in frequency had to be small, so as to find the modes whose velocities change sharply. Because of the complexity of Lamb wave propagation in a multi-phase medium a solution might not be achievable in some cases, for example, when two modes have very close propagation velocities. Moreover, except for the two lowest-order modes, most Lamb modes have cutoff frequencies, making it difficult to trace higher-order modes near their cutoff frequencies. In addition to the above difficulties, the cutoff frequencies for a fluid-solid-coupled scenario are unknown a priori. In such cases, tracing should be done both forward and backward (*i.e.*, from low frequencies to high frequencies and from high frequencies to low frequencies simultaneously) so as to obtain the complete

dispersion curve for the mode in the frequency region under investigation. With this code, solutions to Equation 3.10 were achieved, and were fed into Equation 3.11, which yielded the corresponding group velocities for the wave modes of interest.

As an application of the above code, Figs. 3.4 and 3.5 show the calculated dispersion curves of the  $S_0$  and  $A_0$  modes in a water-aluminium-coupled medium (thickness of the aluminium plate: 2 *mm*; thicknesses of water layers: 0, 0.5, 1, 2 and 4 *mm*). Marked influence of the water layer on the characteristics of Lamb waves in the coupled medium can be observed, showing (i) reduced propagating velocities of lowest-order Lamb waves in the presence of fluid; (ii) sensitivity of the velocity to the thickness of the fluid layer.

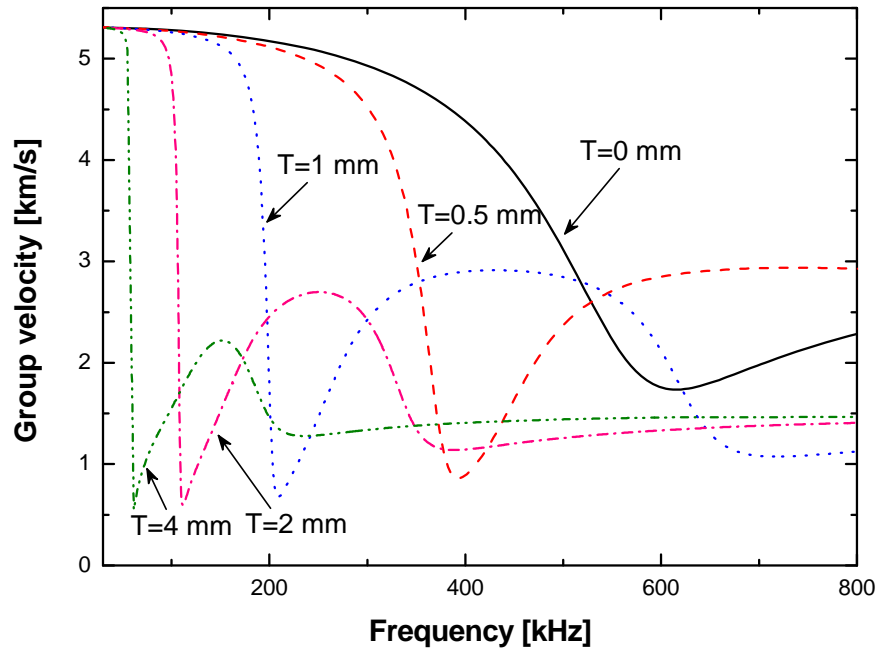


(a)

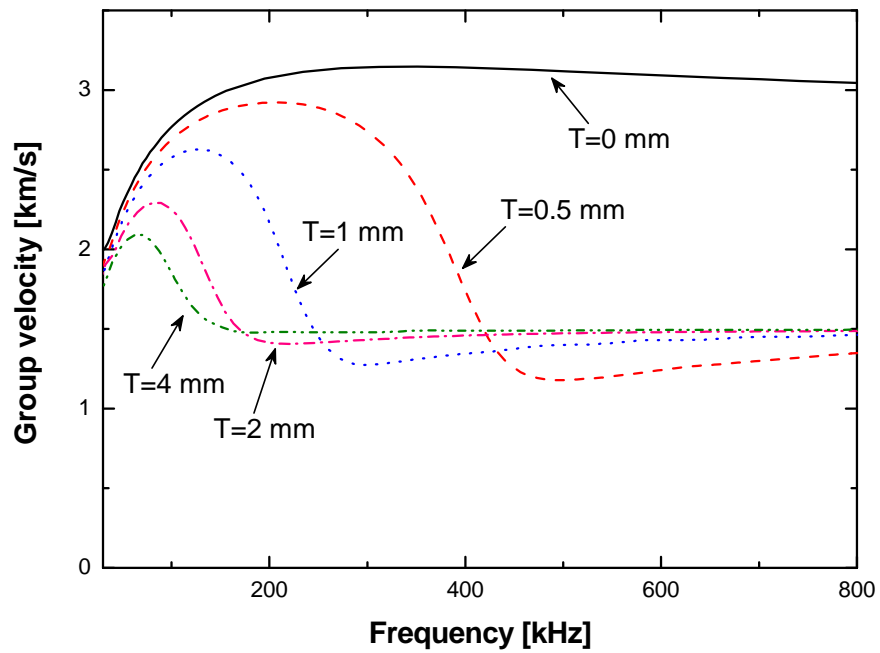


(b)

**Fig. 3.4.** Dispersion curves of (a)  $S_0$  and (b)  $A_0$  in water-aluminium-coupled medium (phase velocity vs. frequency) (T: thickness of water layer) calculated using the developed code



(a)



(b)

**Fig. 3.5.** Calculated dispersion curves of (a)  $S_0$  and (b)  $A_0$  in water-aluminium-coupled medium (group velocity vs. frequency) ( $T$ : thickness of water layer)

## 3.6 Leaky Lamb Waves

The above discussion is now extended to a scenario in which at least one surface of the plate is not free and is coupled with another medium, *viz.*, a multi-phase medium (e.g., a plate submerged in liquid or buried in soil). The coupling between two distinct phases introduces constraint confinements to the interface, and provides a way for Lamb waves to leak from the plate to the coupled medium by means of radiation, referred to as *leaky Lamb waves*. When leaky waves encounter boundaries of the different media they are scattered, accompanied by mode conversion and dissemination throughout the different phases. Because of such complexity, waves in coupled media often present great challenge in interpretation.

It is anticipated that with the modulation of medium coupling, Lamb waves in multi-phase media behave differently from those in free plates. The coupling effect may influence different Lamb wave modes to varying extent. In a preliminary estimate, considering a plate coupled with a fluid-like medium, the wave modes with radial in-plane displacement (predominantly in  $S_0$ ) were mostly retained in the plate because the fluid was unable to sustain shear (in-plane) loads, and as a result it was difficult for in-plane particle motion to cross the plate-liquid interface. In contrast, in a plate coupled with a medium that supported both in-plane and out-of-plane particle motion (e.g., a composite laminate or a plate adhered by silicon rubber), part of the energy of these modes could leak into the coupled medium through the interface. In both the

above cases, however, it is expected that obvious leakage of energy for modes dominating out-of-plane particulate vibration, e.g.,  $A_0$ , would travel across the interface, due to the continuity of out-of-plane strain and displacement at the interface. All the above surmises are investigated in the work that follows.

In particular, for an infinite fluid-solid-coupled medium with fluid thickness  $a$  and plate thickness  $b$ , the characteristic equation for this multi-phase medium can be described as [22], if both the solid and fluid media are deemed isotropic in nature but the latter is unable to sustain shear loads,

$$\det(G(\omega, k, c_F, c_L, c_T, a, b, \rho_F, \rho)) = 0, \quad (3.12)$$

Where  $G$  is the characteristic matrix for the coupled medium. Solutions to Equation 3.12 depict the dispersion curves of Lamb waves in a coupled medium. By way of illustration, Fig. 3.6 displays the dispersion curves of the  $A_0$  mode in an aluminium plate coupled with a layer of pure water [22], illustrating the prominent difference in the  $A_0$  mode when propagating in a free plate (Fig. 2.2) and in a plate coupled with fluid (Fig. 3.6).

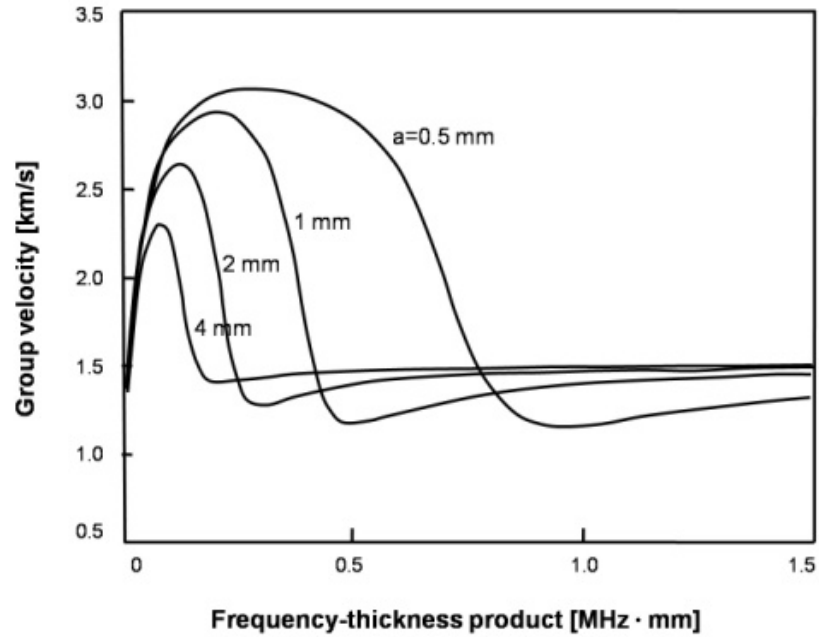


**Fig. 3.6.** Dispersion curves of the  $A_0$  mode in an aluminium plate coupled with a layer of pure water ( $a$ : thickness of water layer) [22]

### 3.7 Concluding Remarks

This chapter briefly outlines the theoretical bases for describing Lamb waves propagating in plate-like and tubular structures, and their counterparts coupled with fluid media. As the core of this thesis, the characteristics of Lamb waves propagating in fluid-solid-coupled media were investigated analytically. A code was developed to trace Lamb wave modes in such coupled media. As demonstrated by a case study (wave propagation in a water-aluminium-coupled medium), theoretical results demonstrate that coupled media can exert a prominent effect on the propagation

characteristics of Lamb waves, characterised by: (i) reduced propagating velocity of lowest-order Lamb waves in the presence of fluid; (ii) sensitivity of the velocity to the thickness of the fluid layer.

Although theoretical models exist, it is of great significance to explore such a coupling effect via FE simulation and experimental validation, allowing for the difference between real conditions and those that are assumed to be perfect during theoretical derivation and uncertainties in reality. Results from FE simulation and experimental validation can be then used to compensate for this effect in different coupling conditions (e.g., different thicknesses of coupled fluid layers and varied mechanical properties of coupled soft media) so as to achieve precision-enhanced identification and evaluation. Numerical and experimental investigations of such an effect in engineering and clinical scopes are to be described in the following chapters.

# **CHAPTER 4      Coupling Effect of Fluid on Lamb Waves and Application to Identification of Damage in Submerged Structures**

## **4.1 Introduction**

The anti-symmetric Lamb mode,  $A_0$ , featuring a shorter wavelength than its symmetric counterparts and therefore being able to pinpoint damage of smaller dimensions, has attracted much attention among those working to develop high-precision NDE techniques. However, as anticipated, the propagation of Lamb wave modes, and  $A_0$  in particular, is sensitive to the presence of coupled fluid, potentially leading to inaccurate identification results when applied in NDE for structures with coupled media, such as submerged structures. It is therefore highly necessary to calibrate and compensate for such coupling effects. In this chapter, the effect of a coupled medium on Lamb waves is systematically evaluated by ultrasonically interrogating wave propagation in an aluminium plate covered with a layer of fluid varying in thickness. As a prerequisite of implementing Lamb-wave-based

identification in submerged structures, the influence of the coupled fluid medium on Lamb wave propagation in solid structures is investigated and then calibrated quantitatively. An identification approach adjusted via consideration of medium coupling is numerically and experimentally validated by evaluating a through-thickness hole, as validation, and chemical corrosion, as an application, in submerged aluminium plates, with the assistance of a probability-based diagnostic imaging technique.

## **4.2 Coupling Effect of Fluid on Lamb Wave Propagation**

### **4.2.1 Three-dimensional (3D) Finite Element (FE) Modelling and Simulation**

Consider a square aluminium plate measuring  $600\text{ mm} \times 600\text{ mm} \times 1.6\text{ mm}$  and supported on its four edges. The upper surface of the plate is in contact with a fluid layer of the same planar area, with thickness varying from 0 to 10  $\text{mm}$  with an increment of 0.5  $\text{mm}$ , as shown schematically in Fig. 4.1. The material properties of the selected aluminium and fluid are briefly listed in Table 4.1. In this work the aluminium plate and fluid layer were simulated using 3D eight-node brick solid elements and 3D eight-node acoustic elements, respectively. To ensure simulation

accuracy, the largest dimension of elements was less than 1 *mm*, guaranteeing that at least ten elements were allocated per wavelength of the  $A_0$  mode (wavelength of the  $A_0$  mode at the frequency of 150 kHz is circa 15 *mm*). The numerical convergence of the computation was examined in terms of the element size and mesh density. It was found that the maximum dimension of the element of 1 *mm* provided a suitable balance between numerical accuracy and computational cost. Any further decrease in the element size does not cause any improvement in the simulation accuracy. In the acoustic elements, acoustic pressure was applied in the  $z$ -axis only (referring to Fig. 4.1 for the coordinate system), consistent with the fact that fluid cannot withstand shear loads within the  $x$ - $y$  plane.

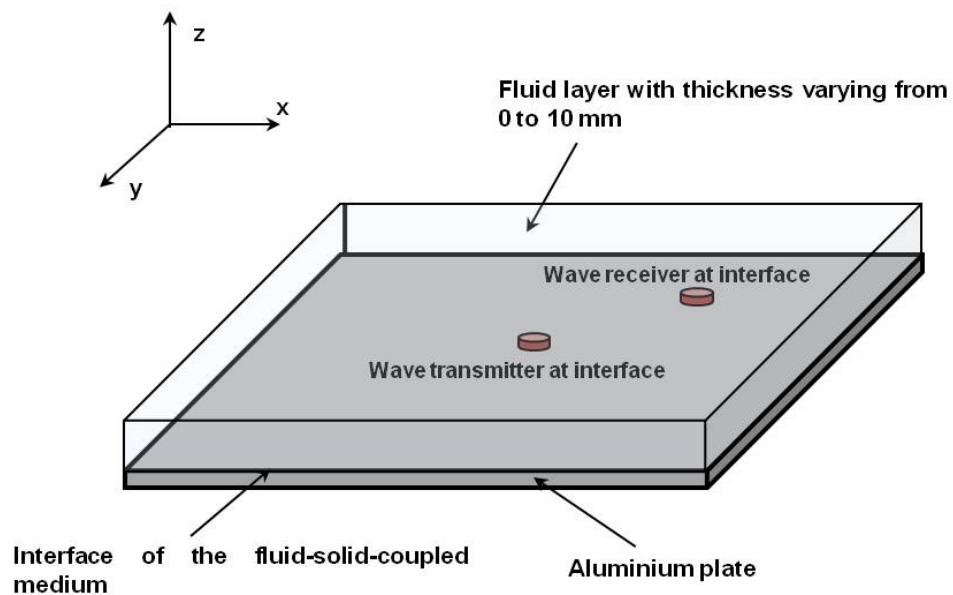


**Fig. 4.1.** Schematic of transmitter and receiver allocation for examining Lamb waves propagating in fluid-solid coupled medium (distance between transmitter and receiver: 175

*mm*)

**Table 4.1.** Material properties of aluminium and fluid for studying the coupling effect of fluid on Lamb wave propagation

<b>Materials</b>	<b>Density [kg/m<sup>3</sup>]</b>	<b>Elastic Modulus [GPa]</b>	<b>Poisson's Ratio</b>	<b>Bulk modulus* [GPa]</b>
<b>Aluminium</b>	2711	71	0.35	
<b>Fluid</b>	1000			2.2

\* Bulk modulus is used for defining fluid-like materials that cannot withstand tensile loadings, to be linked to Young's modulus approximately in terms of  $K_B = \frac{E}{3 \cdot (1 - 2\nu)}$  ( $K_B$ ,  $E$  and  $\nu$  are the bulk modulus, Young's modulus and Poisson's ratio of the material, respectively [119]).

The interface between the fluid layer and aluminium plate was simulated using a surface-based coupling constraint provided by ABAQUS<sup>®</sup>/EXPLICIT in terms of a node-to-surface formulation, called 'TIE'. This constraint allowed a mixture of rigid and deformable portions of a surface, as illustrated schematically in Fig. 4.2. The coupling constraints forced the degrees of freedom in the  $z$ -axis to be equal for a pair of surfaces, of which one was designated to be the master surface (solid surface) and the other the slave surface (fluid surface). Simulated by 'TIE', motions of particles at the interface were continuous in the out-of-plane direction but not in  $x$ - $y$  plane, as in reality.

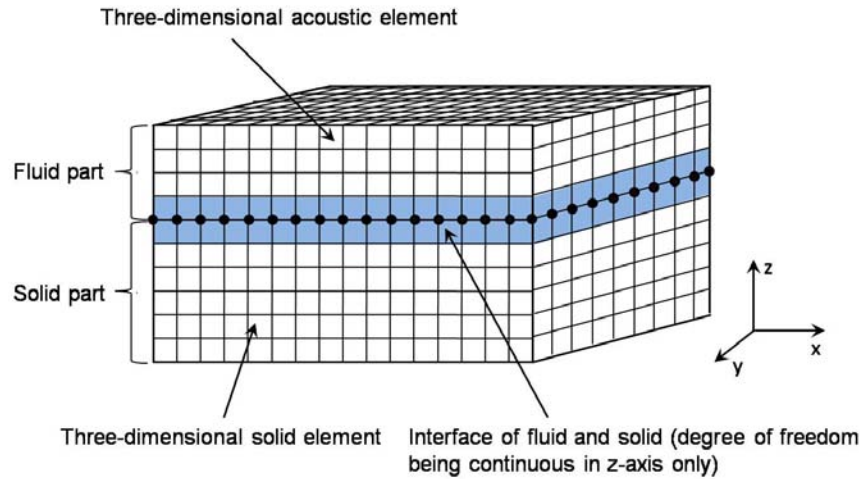


**Fig. 4.2.** Schematic of ‘*TIE*’ constraint for simulating the interface of fluid-solid-coupled media

To generate Lamb waves in the fluid-solid-coupled medium, a piezoelectric transmitter model [120] was employed and positioned at the planar centre of the interface, as shown in Fig. 4.1. Uniform vertical ( $z$ -axis) displacements were applied on FE nodes of the transmitter model to generate the  $A_0$  mode dominating the signal energy, in recognition of the fact that  $A_0$  mode has mostly out-of-plane displacement. With the transmitter model, five-cycle *Hanning* window-modulated sinusoid tonebursts at a central frequency of 150 kHz were activated [120] (Fig. 4.3). This frequency, in the given non-dispersion region, was lower than the cut-off frequencies of higher-order modes in the aluminium plate described, and as a consequence only the  $S_0$  and  $A_0$  modes co-existed. At this frequency, the  $A_0$  mode had greater magnitude in a captured signal than the  $S_0$  mode. Upon propagating in the coupled media, Lamb wave signals at the interface were captured with a piezoelectric receiver model [120], 175 mm from the transmitter.

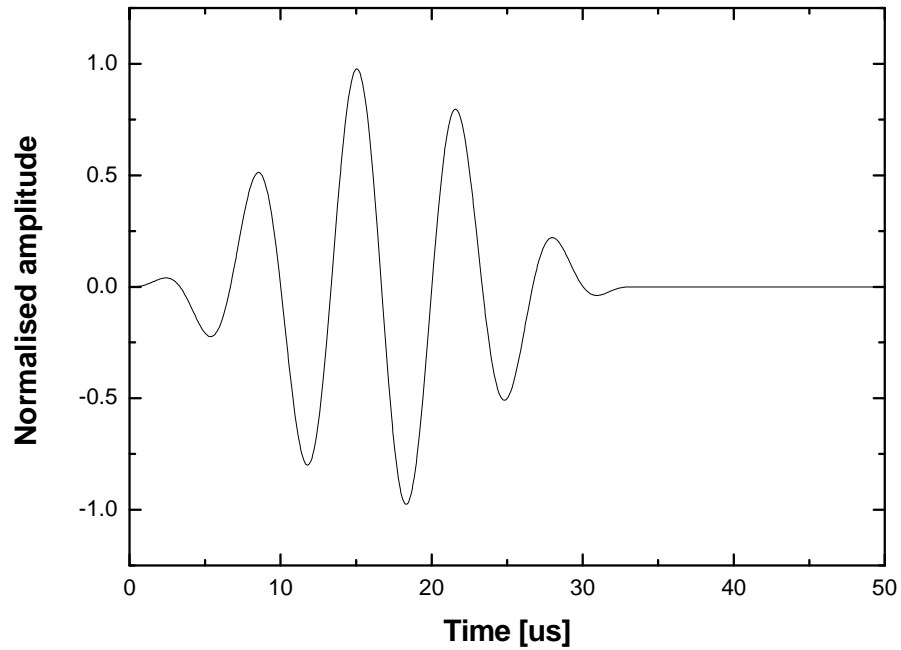


**Fig. 4.3.** A five-cycle *Hanning* window-modulated sinusoid toneburst at a central frequency of 150 kHz

Dynamic FE simulation was accomplished using the commercial FE package ABAQUS<sup>®</sup>/EXPLICIT. The step of calculation time was controlled to be less than the ratio of the minimum distance of any two adjoining nodes to the maximum velocity of wave mode involved, *viz.*, the  $S_0$  mode. The edges of the plate model were constrained using an “ENCASTRE” boundary condition which enforced the displacements and rotations of the nodes on plate edges to be zero in all the directions. The above modelling and simulation were repeated in the absence and presence of fluid layers of different thicknesses ranging from 0 to 10 *mm* with an increment of 0.5 *mm*. As an example, the FE model when the fluid layer was 4 *mm* in thickness is exhibited in Fig. 4.4.

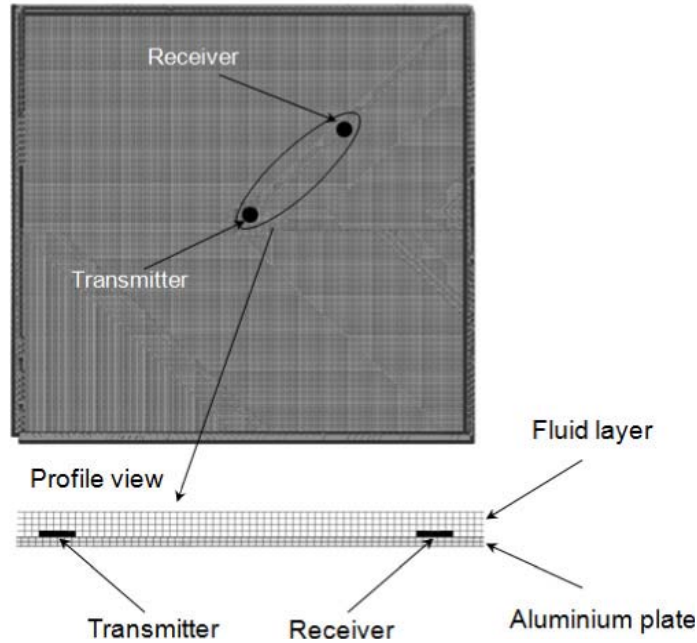
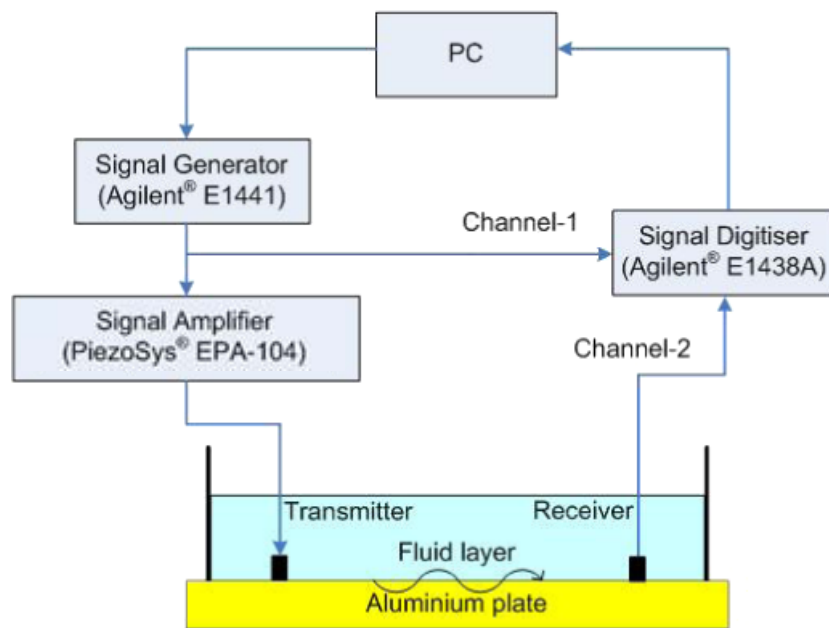


**Fig. 4.4.** FE model for fluid-solid-coupled medium containing a piezoelectric wave transmitter and receiver

## 4.2.2 Experimental Validation

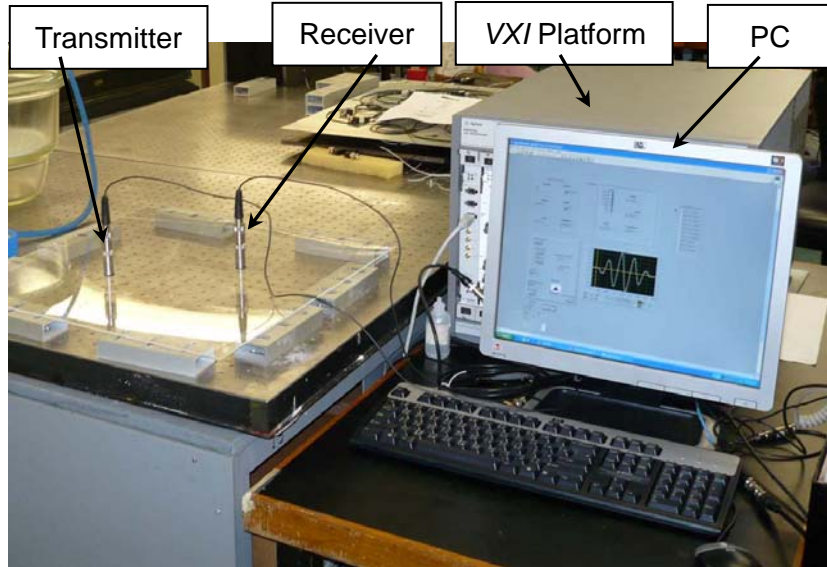
In parallel to the FE simulation, experimental validation was conducted at room temperature. All the material and geometric properties of the solid and fluid media, as well as the setup configurations, remained the same as those in the FE simulation. A pair of waterproof immersion transducers (Panametrics-NDT<sup>TM</sup>-V303-SU, central frequency: 1 MHz, diameter: 13 mm) was located in tandem at the interface, serving as the wave transmitter and receiver to generate and collect Lamb wave signals, respectively. The transmitter was positioned at the centre of the aluminium plate and the receiver was located 175 mm from the transmitter. Both transmitter and receiver were then instrumented with a signal generation/acquisition system developed on a

VXI platform [121], shown schematically in Fig. 4.5. Five-cycle *Hanning* window-modulated sinusoid tonebursts at a central frequency of 150 kHz were generated with a signal generation unit (Agilent® E1441), amplified to 180 V<sub>p-p</sub> with a linear signal amplifier (PiezoSys® EPA-104), and then applied to the transmitter. The Lamb wave signals were captured with a signal digitiser (Agilent® E1438A) at a sampling rate of 25 MHz. A fluid layer of thickness varying from 0 to 10 mm with an increment of 0.5 mm was introduced to be in contact with the upper surface of the aluminium plate, consistent with the FE simulation.



(a)

**Fig. 4.5.** (a) Setup and (b) photo of experimental validation



(b)

**Fig. 4.5.** *Cont.*

### 4.2.3 Signal Processing and Results

As representative results, raw Lamb wave signals captured at the interface (consisting of both the  $S_0$  and  $A_0$  modes) in the absence and presence of a fluid layer of 4 mm in thickness are compared in Fig. 4.6.

In consideration of the fact that wave propagation is actually the conveyance of energy, a Hilbert-transform (HT)-based signal processing technique [121, 122] was applied to all the numerically and experimentally obtained signals, to canvass the signals in terms of their energy distribution. The HT is defined as [7]

$$H(t) = \frac{1}{\pi} \int_{-\infty}^{+\infty} \frac{f(\tau)}{t - \tau} d\tau . \quad (4.1)$$

$H(t)$  is the HT of signal  $f(t)$ . Equation 4.1 performs a  $90^\circ$  phase-shift or quadrature filter to construct a so-called analytic signal  $F_A(t)$ :

$$F_A(t) = f(t) + iH(t) = e(t) \cdot e^{i\varphi(t)}, \quad (4.2a)$$

$$e(t) = \sqrt{f^2(t) + H^2(t)}, \quad \text{and} \quad \varphi(t) = \frac{1}{2\pi} \cdot \frac{d}{dt} \arctan \frac{H(t)}{f(t)}, \quad (4.2b)$$

where  $e(t)$  is the module of  $F_A(t)$  and its envelope depicts the energy distribution of  $f(t)$  in the time domain. For illustration, the HT-processed results of signals shown in Fig. 4.6 are shown in Fig 4.7. For comparison, Fig. 4.7 also includes the HT-processed signals when the thickness of the fluid layer was 1, 6 and 9 mm, respectively.

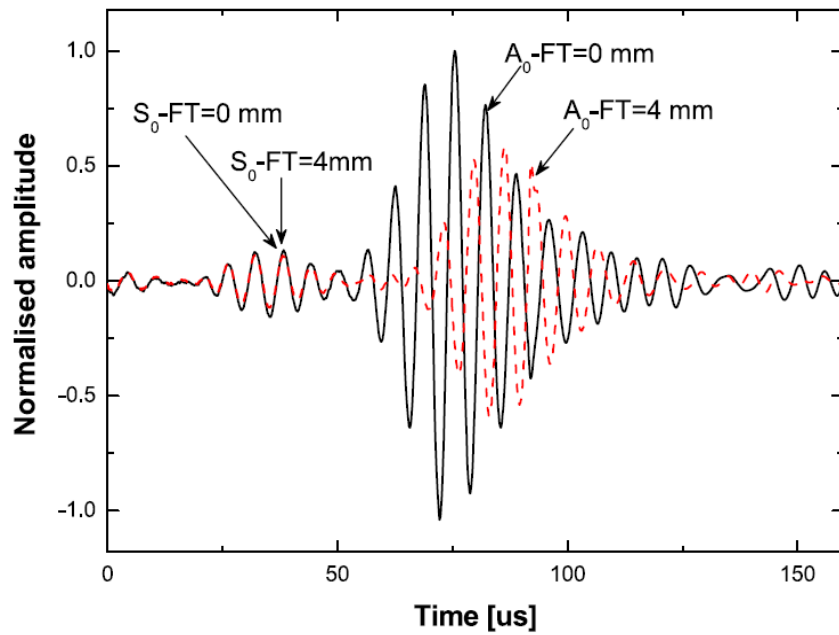


**Fig. 4.6.** Raw Lamb wave signals at the interface in the absence and presence of a fluid layer of 4 mm in thickness (FT: fluid layer thickness)

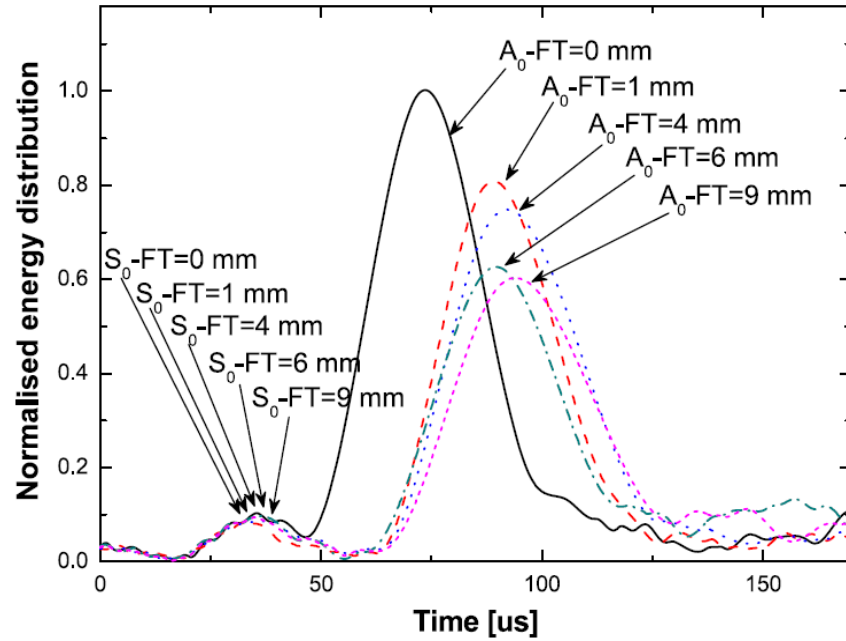
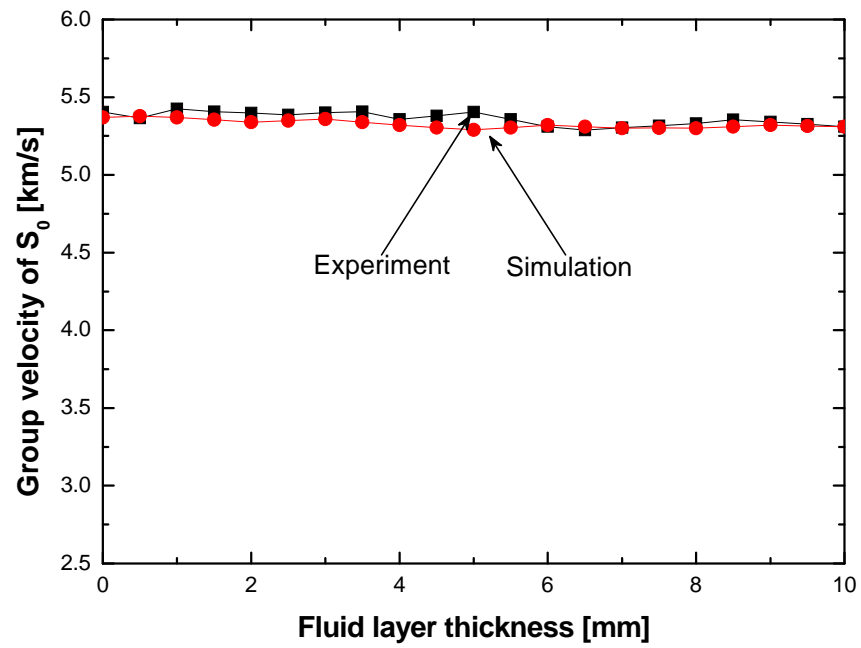


**Fig. 4.7.** HT-processed wave signals at the interface in the absence and presence of fluid layers of different thicknesses (FT: fluid layer thickness)

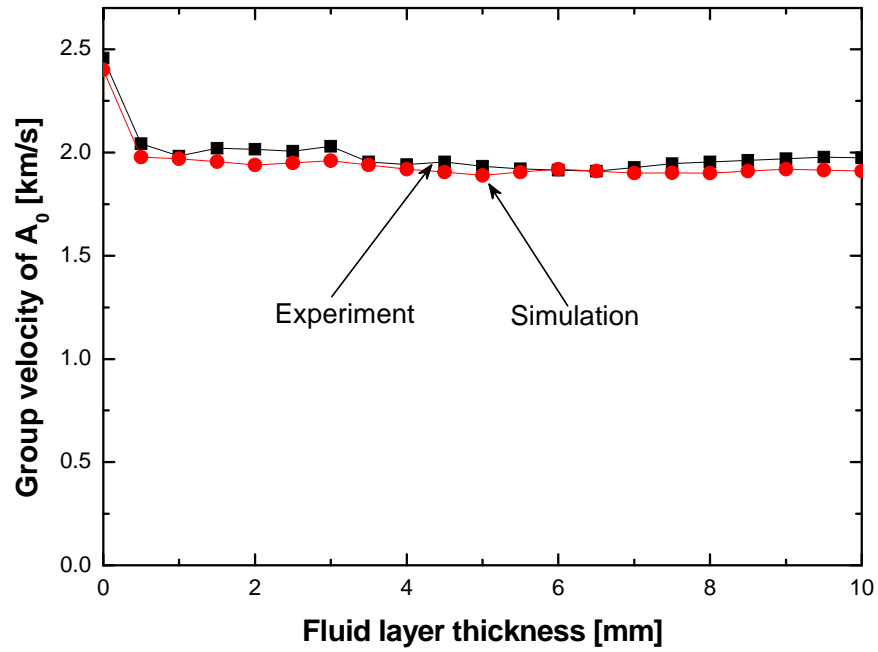
In Fig. 4.7, the first energy concentration is recognised as the  $S_0$  mode, which has the highest propagation velocity in the non-dispersion region; the second concentration is associated with the  $A_0$  mode that dominates the signal energy at the frequency of 150 kHz and therefore has greater magnitude than the  $S_0$  mode. It can be observed that the fluid layer does not exert a prominent influence on the  $S_0$  mode, whereas the  $A_0$  mode has a significant influence, manifesting in two ways: (i) a reduction in the signal magnitude; and (ii) a delay in the arrival time as a result of reduced propagation velocity, as illustrated in Fig. 4.8. Conclusion can also be drawn from Fig. 4.8 that the results from experiment and FE simulation match well, corroborating the modelling method including use of the “*TIE*” constraint. Although in some studies, a boundary layer between the fluid and solid layers was used, a satisfactory consistence between

the results from FE simulation and experiment in this study has proven that the “*TIE*” can simulate the coupling of fluid and solid parts with good acceptance. That is because such a boundary constraint is able to provide both the out-of-plane and in-plane (shear) continuities at the interface between the fluid and solid layers.



(a)

**Fig. 4.8.** Group velocities of (a)  $S_0$  and (b)  $A_0$  in aluminium plate coupled with a fluid layer versus thickness of fluid layer, obtained via FE simulation and experiment



(b)

**Fig. 4.8.** *Cont.*

In particular, the most noticeable changes in signal/energy magnitude and propagation velocity of the  $A_0$  mode take place when the fluid layer is initially introduced, and the changes fluctuate only slightly with further increases of the thickness of the fluid layer. The above observation underscores that the out-of-plane movement of particles in the  $A_0$  mode provides a way for Lamb waves to leak outwards into the surrounding coupled medium by radiation. The fluid loading, in turn, affects the wave propagation of the  $A_0$  mode. This is, however, not the case for the  $S_0$  mode, which dominates the in-plane vibration mode.

To facilitate understanding, Fig. 4.9 presents the energy distribution, obtained via FE simulation, of a Lamb wave signal propagating in a fluid-solid-coupled medium. In

the diagram, some energy of the  $A_0$  mode in the plate can be seen to leak into the fluid layer, whereas no significant energy leakage into the fluid layer is observed for the  $S_0$  mode. This simulation demonstrates the primary mechanism of greater signal attenuation of the anti-symmetric modes than the symmetric modes in a coupled medium.

It is worth mentioning that the above observation is not consistent with the theoretical calculated results in Fig. 3.5, which indicate that the velocities of both  $S_0$  and  $A_0$  are sensitive to the fluid layer thickness in a specific frequency range (for instance, 50-800 kHz for the  $S_0$  mode and 100-500 kHz for the  $A_0$  mode). This can be attributed to the discrepancy between the theoretical model and the experimental setup or FE simulation. That is because the theoretical model considers the water-aluminium-coupled medium, a two-layer system, as a whole in which waves are hypothesised to behave like those in a single-phase medium. However, in the latter case (experiment or FE simulation) the coupled system is deemed as multi-phases in which the transducers are in direct contact with the upper surface of the aluminium plate. The presence of a layer of fluid on the upper surface of the plate provides an additional boundary to the wave propagating in the plate. The latter case is in better agreement with reality.

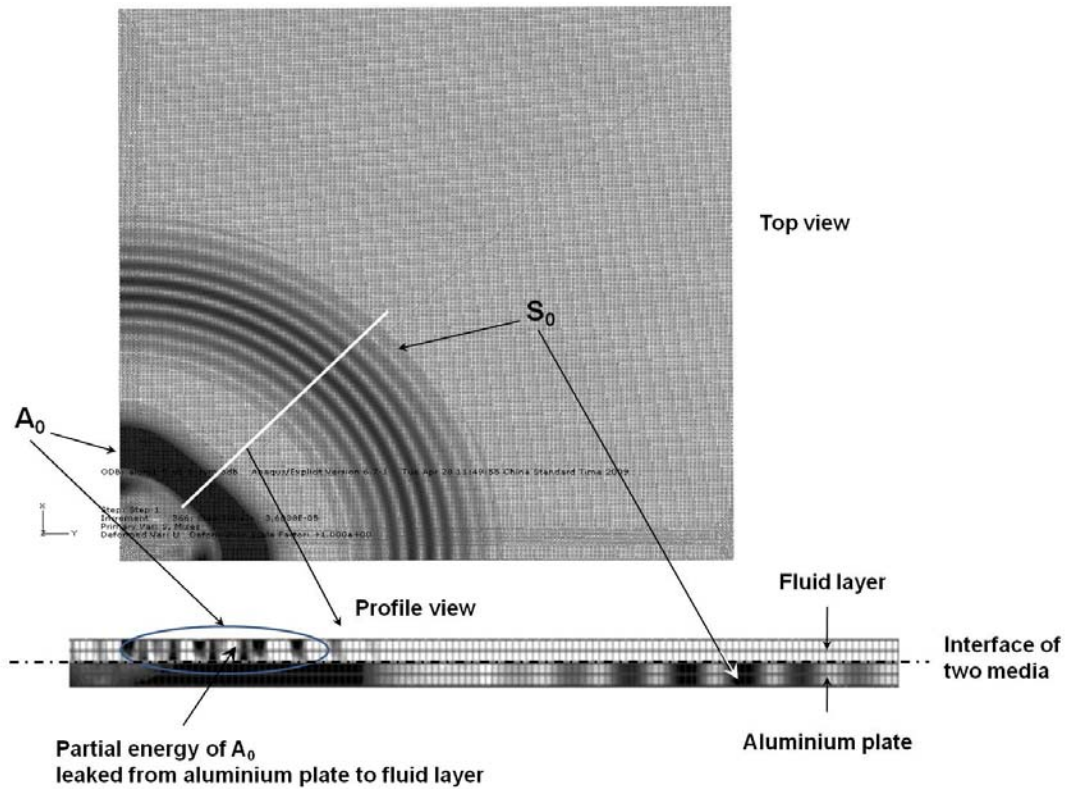
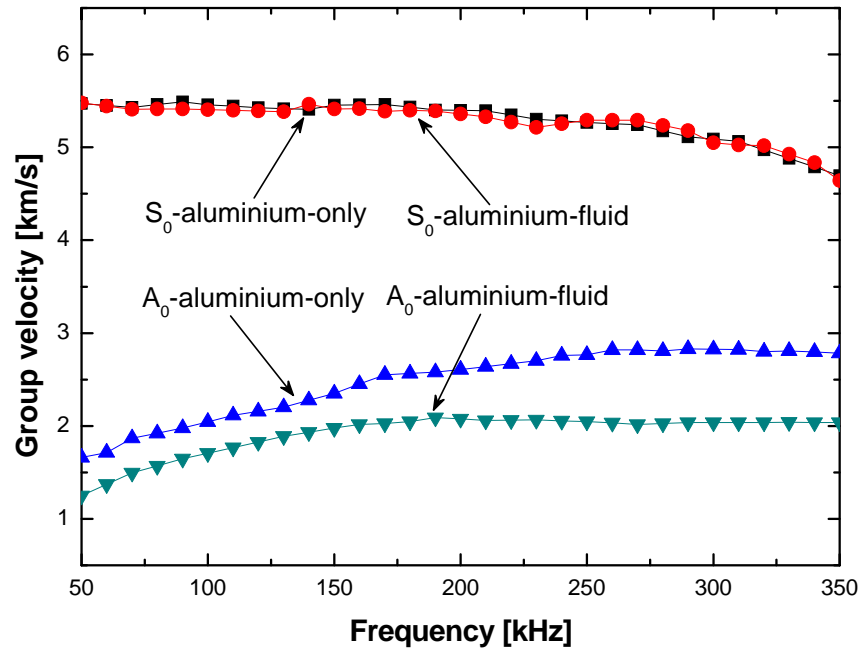
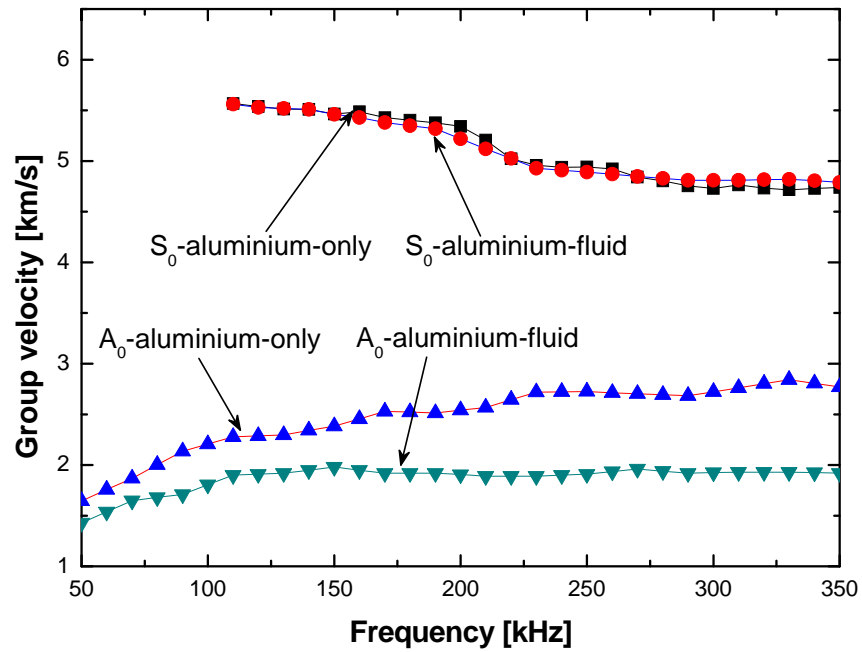


**Fig. 4.9.** Stress distribution of Lamb wave propagating in a fluid-solid-coupled medium, showing energy leakage of the  $A_0$  mode (for comparison, stress distributions displayed in the fluid layer and in the aluminium plate are not of the same scale; the darker the greyscale the higher the stress)

Extending the above examination by exciting Lamb waves in a sweep frequency range from 50 to 350 kHz, dispersion curves of the fundamental Lamb wave modes in the aluminium plate in the absence and presence of a fluid layer of 4 mm in thickness as an example were obtained experimentally and numerically, as displayed in Fig. 4.10. Based on the above results, the influence of the fluid coupling on the propagation of the  $A_0$  mode was quantitatively calibrated, subject to the thickness of the fluid layer.



(a)



(b)

**Fig. 4.10.** Dispersion curves of Lamb waves in an aluminium plate in the absence and presence of a fluid layer (4 mm in thickness) obtained via (a) FE simulation and (b) experiment

## **4.3 Application to Identification of Damage in Submerged Structures**

With the knowledge of the coupling effect of fluid on the propagation of Lamb waves as calibrated in Section 4.2, traditional Lamb-wave-based damage identification was modified when applied to the identification of damage in structures under the influence of medium coupling. In this work, to improve the identification procedure, a probability-based diagnostic imaging technique was introduced.

### **4.3.1 Probability-based Diagnostic Imaging**

There has been increasing interest in presenting results of damage identification intuitively in a two-dimensional image whose pixels correspond exclusively to spatial points of the structure under inspection, *i.e.*, diagnostic imaging [123-127]. This identification approach depicts damage using a greyscale image in which the field values at pixels indicate the probability of the presence of damage, and the region of pixels where the field values are above a threshold may further be assumed to represent the extent of the damage.

In this study, a probability-based diagnostic imaging approach was employed using ToF extracted from captured Lamb wave signals for establishing the probability at pixels [48]. ToF is here defined as the time lag from the moment at which a wave

receiver catches the damage-scattered wave to the moment at which the same receiver catches the incident wave [28]. Considering a transmitter-receiver pair, *i.e.*, a sensing path (in what follows *transmitter* is denoted by ‘*T*’, *receiver* by ‘*R*’ and *damage* by ‘*D*’), Fig. 4.11, we have

$$t_{T-D-R} - t_{T-R} = \left( \frac{L_{T-D}}{V} + \frac{L_{D-R}}{V} \right) - \frac{L_{T-R}}{V} = \Delta t, \quad (4.3)$$

where

$$L_{T-D} = \sqrt{(x_D - x_T)^2 + (y_D - y_T)^2}, \quad L_{D-R} = \sqrt{(x_D - x_R)^2 + (y_D - y_R)^2}, \quad \text{and}$$

$$L_{T-R} = \sqrt{(x_T - x_R)^2 + (y_T - y_R)^2}.$$

In the above equations,  $t_{T-D-R}$  is the ToF of the incident wave propagating from the transmitter to the damage and then to the receiver, and  $t_{T-R}$  is the ToF of the incident wave propagating directly from the transmitter to the receiver.  $\Delta t$  is the difference between the above two ToFs, which can be ascertained from a captured wave signal.  $L_{T-D}$  is the distance between the transmitter located at  $(x_T, y_T)$  and the damage centre presumed at  $(x_D, y_D)$  and to be determined;  $L_{D-R}$  is the distance between the damage centre and the receiver located at  $(x_R, y_R)$ ;  $L_{T-R}$  is the distance between the transmitter and receiver.  $V$  is the group velocity of the selected Lamb wave mode,  $A_0$  in this chapter, activated by the transmitter.

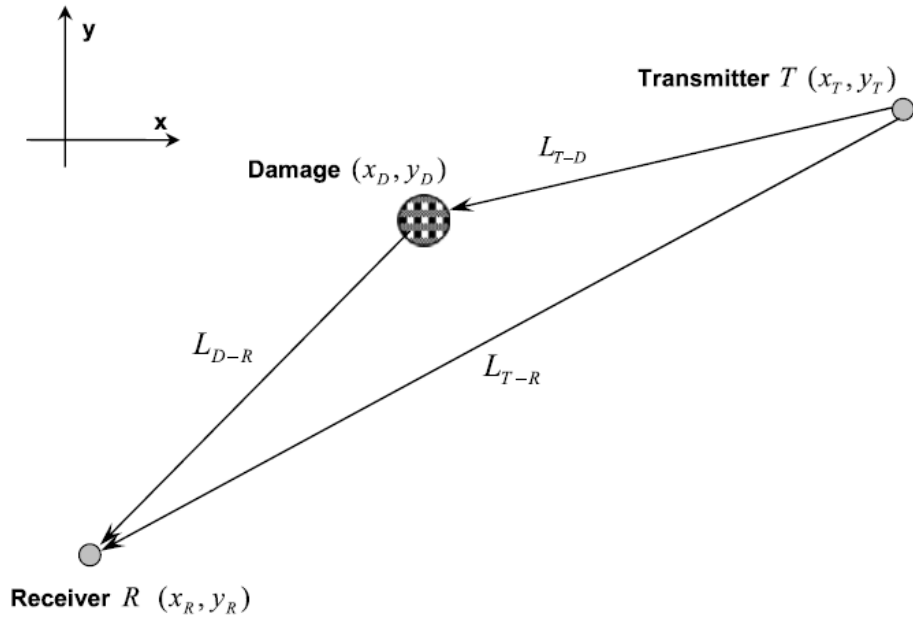


**Fig. 4.11.** Relative positions of transmitter, receiver and damage for a sensing path

Theoretically, solutions to Equation 4.3 configure a locus of root, the dotted ellipse in Fig. 4.12, indicating possible locations of the damage that reflects the perceptions as to damage in the structure from the perspective of the transmitter-receiver pair that creates such a locus. For a given transmitter-receiver pair, a greyscale image can be constructed in which the field value at a specific pixel is calibrated in terms of the shortest distance between that pixel and the locus established by the transmitter-receiver pair. This is driven by the hypothesis that the pixels exactly on the locus have the highest degree of probability (100%) as to the presence of damage, and for other pixels, the greater the distance to the locus, the lower the probability that damage exists there. To establish probabilities at pixels in relation to the loci created by different transmitter-receiver pairs, a *cumulative distribution function* (CDF) [128],  $F(z)$ , was introduced, defined as

$$F(z_{ij}) = \int_{-\infty}^z f(z_{ij}) \cdot dz_{ij}, \quad (4.4)$$

where  $f(z_{ij}) = \frac{1}{\sigma_{ij}\sqrt{2\pi}} \exp[-\frac{z_{ij}^2}{2\sigma_{ij}^2}]$  is the *Gaussian distribution function* representing the probability density function (PDF) of damage at pixel  $(x_m, y_m)$ , ( $m=1, 2, \dots, K$ , for the structure under inspection whose corresponding greyscale image has  $K$  pixels), perceived by the sensing path connecting transmitter  $T_i$  and receiver  $R_j$  ( $i=1, 2, \dots, N$ , and  $j=1, 2, \dots, M$  for the case that  $N$  transmitters and  $M$  receivers are considered).  $z_{ij} = \sqrt{(x_m - x_{ij})^2 + (y_m - y_{ij})^2}$ , where  $(x_{ij}, y_{ij})$  is the location on the locus established by sensing path  $T_i - R_j$  which has the shortest distance to pixel  $(x_m, y_m)$ .  $\sigma_{ij}$  is the standard variance. Given a distance  $z_{ij}$ , the probability of the presence of damage at pixel  $(x_m, y_m)$  established by sensing path  $T_i - R_j$ ,  $I(x_m, y_m)|_{ij}$  (*i.e.*, the field value of the greyscale image at pixel  $(x_m, y_m)$ ), is

$$I(x_m, y_m)|_{ij} = 1 - [F(z_{ij}) - F(-z_{ij})]. \quad (4.5)$$

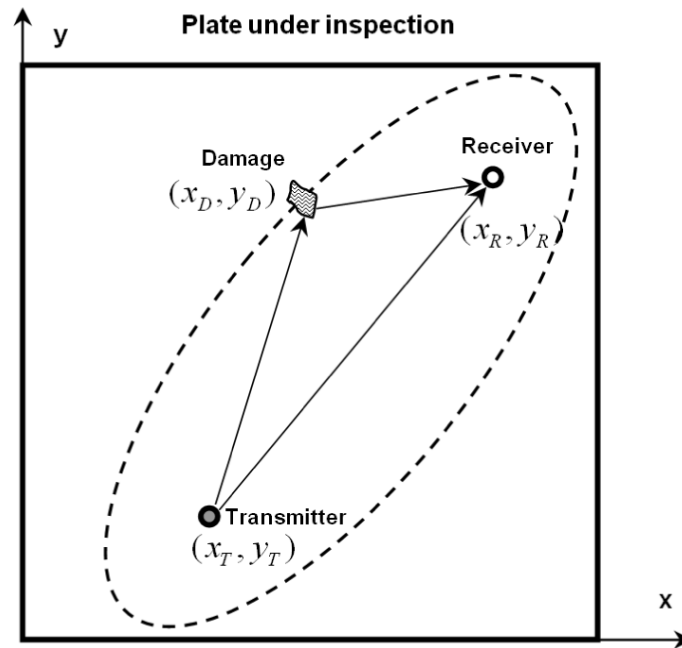


**Fig. 4.12.** Locus of roots to Equation 4.3 established by a sensing path, indicating possible locations of damage in the structure

Following the above steps, each sensing path contributes a greyscale image indicating the probability of the presence of damage at a specific pixel. Upon aggregation of such greyscale images contributed by all the available sensing paths via appropriate image fusion, damage in the structure, if any, can be highlighted at pixels where the field values (probabilities) are greater than a preset threshold. Details of this probability-based diagnostic imaging can be found elsewhere [28].

### 4.3.2 Identifying a Through-thickness Hole in a Submerged Aluminium Plate

For validation of the modified approach, the quantitatively calibrated influence of

fluid coupling on Lamb wave propagation was applied to evaluation of a through-thickness hole (15 mm in diameter) in a submerged aluminium plate ( 600 mm × 600 mm × 1.6 mm ) using the probability-based diagnostic imaging described above. The upper surface of the aluminium plate was in contact with a fluid layer varying in thickness. To prevent leakage of fluid through the hole, the hole was sealed with a thin film from the lower surface of the plate (opposite to the fluid layer). A pair of waterproof immersion transducers, the same as that described in Section 4.2.2, was employed to perform a pulse-echo measurement at different positions on the interface of the fluid layer and aluminium plate, providing three sensing paths,  $T_1$ - $R_1$ ,  $T_2$ - $R_2$  and  $T_3$ - $R_3$ , as indicated in Fig. 4.13. Signal generation/acquisition was accomplished with the system developed on a VXI platform (Fig. 4.4). Five-cycle *Hanning*-windowed sinusoid tonebursts at a central frequency of 150 kHz were excited and applied to the three transmitters in turn after being amplified to 180 V<sub>p-p</sub>. The Lamb wave signals were captured via three the sensing paths at a sampling rate of 25 MHz.

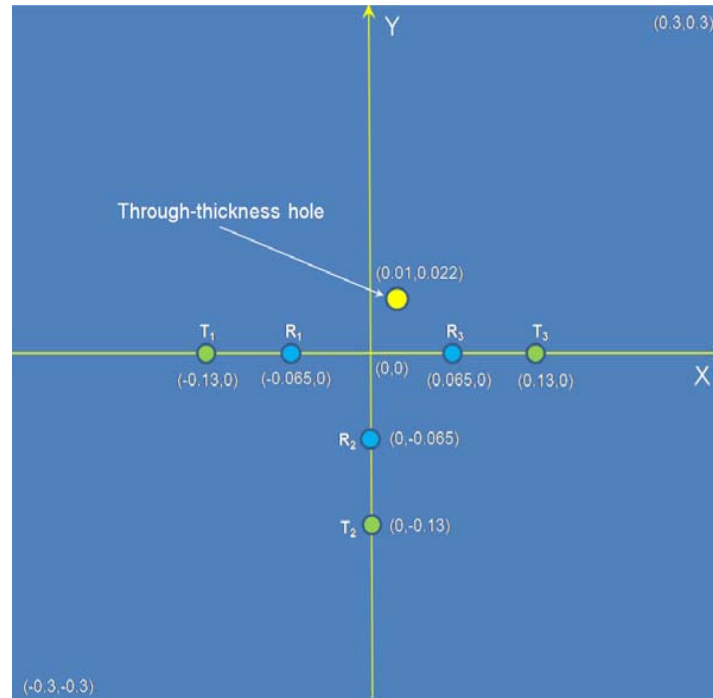
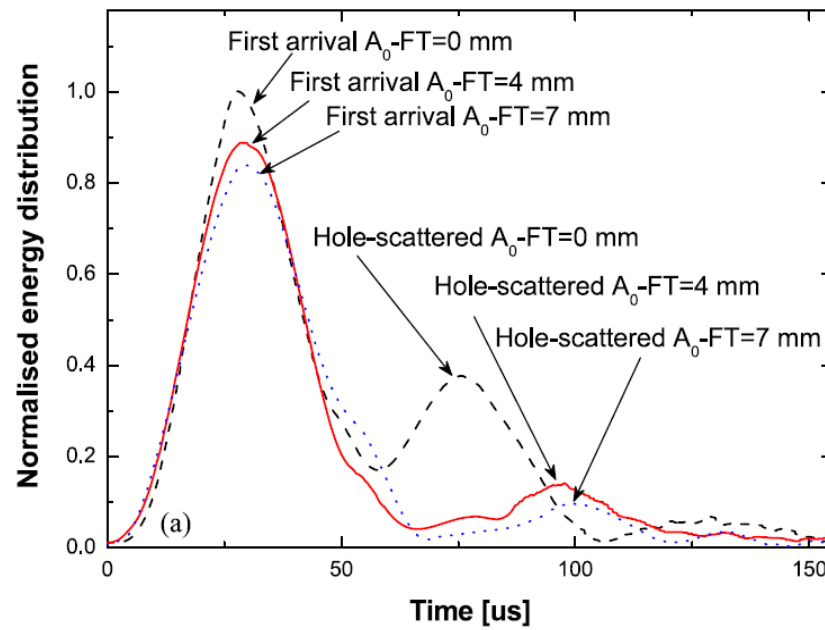


**Fig. 4.13.** An aluminium plate containing a through-thickness hole for validation of the approach (unit:  $m$ )

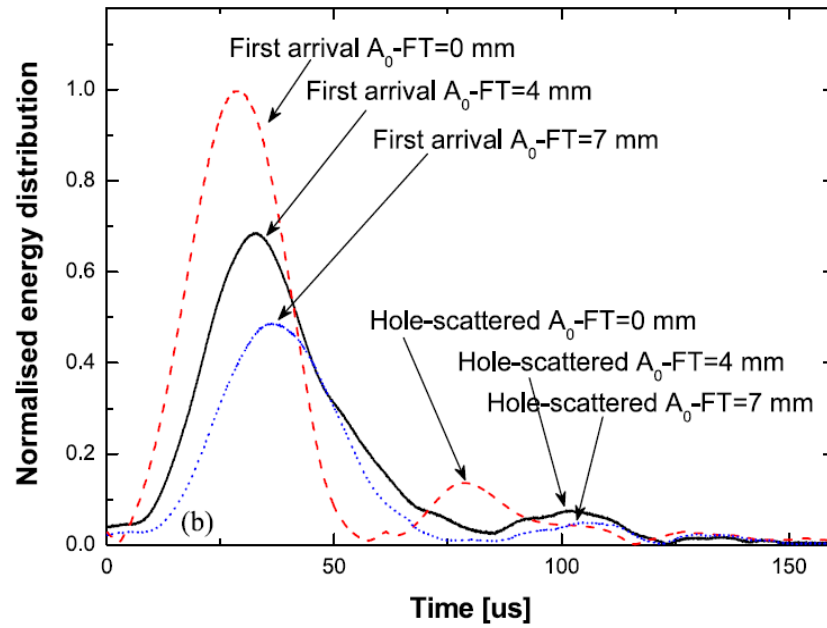
As demonstrated previously, the propagation characteristics of the  $A_0$  mode are significantly modulated when a fluid layer is initially introduced, but are then little affected with further increase in thickness of the fluid layer. Allowing for this, only fluid layers of 4 and 7  $mm$  in thickness were considered. Figure 4.14(a) shows the HT-processed signals experimentally captured via sensing path  $T_3$ - $R_3$ , as examples, in the absence and presence of fluid layers of different thicknesses (4 and 7  $mm$ ). For comparison, the signals via the same sensing paths obtained using the FE simulation technique introduced in Section 4.2.1 are presented in Fig. 4.14(b). Once the difference in ToFs between the incident and through-thickness hole-scattered  $A_0$  mode was ascertained, the probabilities of the presence of damage at pixels were calculated in terms of Equation 4.5 for individual sensing paths, to create probability

greyscale images. As an example, the image established by  $T_1-R_1$  when the fluid thickness was 4 mm is displayed in Fig. 4.15.



(a)

**Fig. 4.14.** HT-processed wave signals captured via sensing path  $T_3-R_3$  in the aluminium plate containing a through-thickness hole, in the absence and presence of fluid layers of different thicknesses, obtained via (a) experiment and (b) FE simulation (FT: fluid layer thickness)



(b)

**Fig. 4.14.** *Cont.*

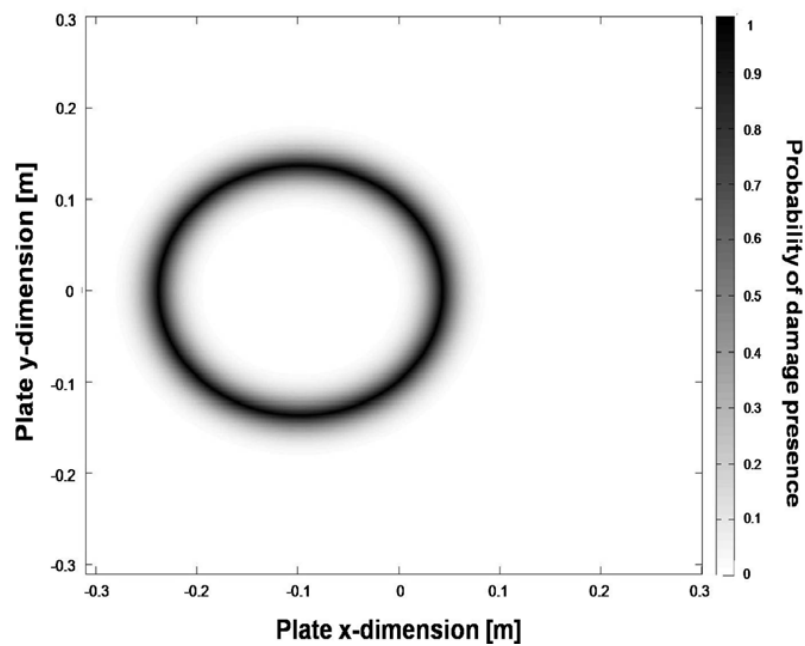
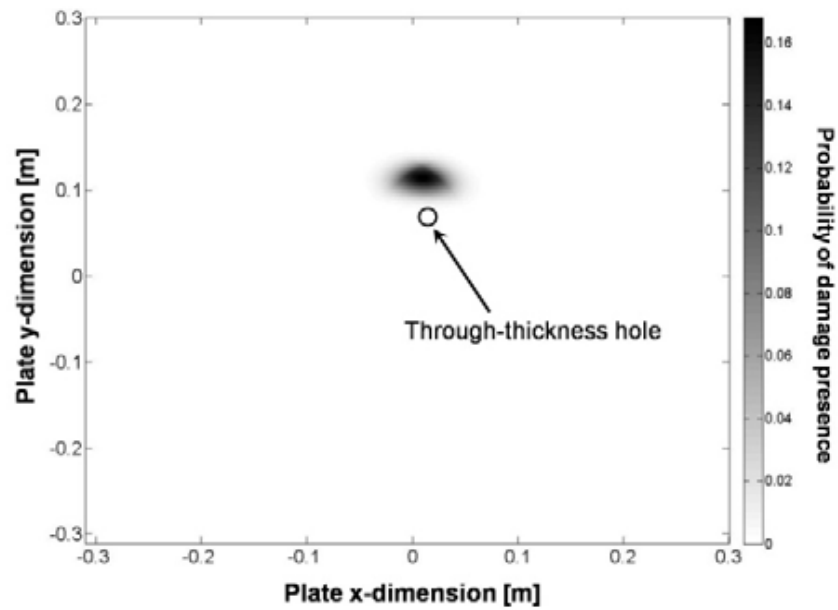


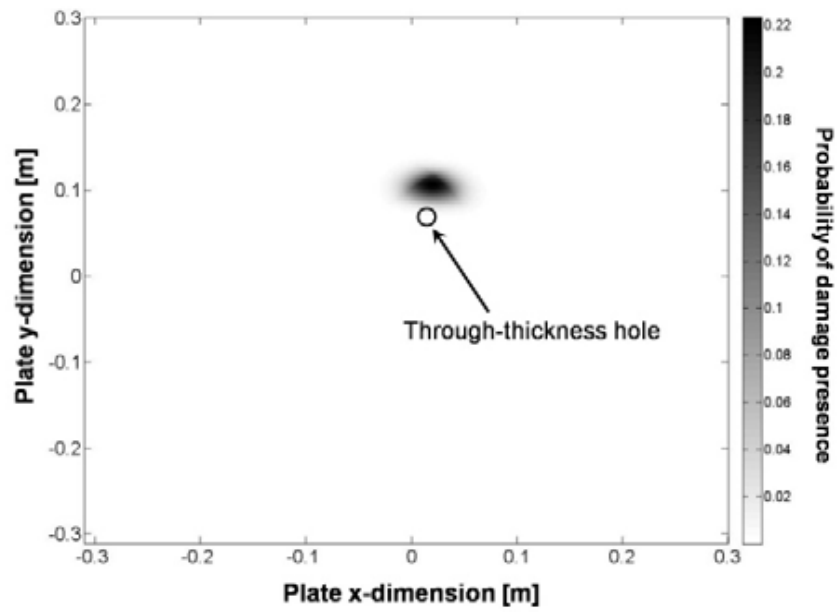
**Fig. 4.15.** A probability greyscale image of damage established by sensing path  $T_I$ - $R_I$  when the fluid layer was 4 mm in thickness (the darker the greyscale the higher the probability of the presence of damage)

The greyscale images formed by aggregating individual images contributed by three sensing paths are displayed in Fig. 4.16, without and with modification and compensation for the fluid coupling influence on Lamb wave propagation. When the same wave propagation velocity as that in the absence of fluid is used, ignoring the fluid coupling effect, a large discrepancy between the identification results and the actual position of the through-thickness hole can be observed, Fig. 4.16(a) and (b), regardless of the thickness of the fluid layer; in contrast, as observed in Fig. 4.16(c) and (d), using the modified wave propagation velocity to compensate for the fluid coupling, the identified damage matches the actual damage well (if 85% of the maximum of field values in the probability image was set as the threshold to draw an explicit conclusion that damage has occurred), regardless of the thickness of the fluid layer.

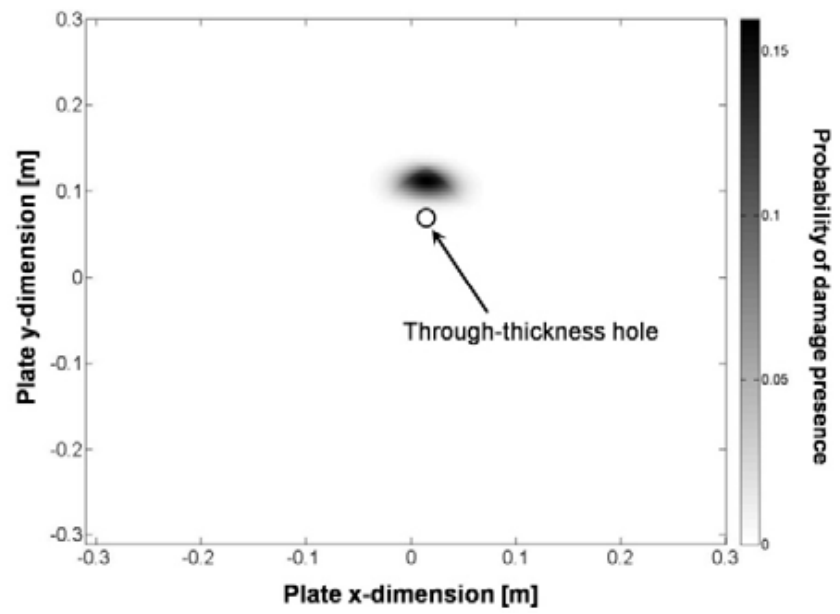


(a1)

**Fig. 4.16.** Identification results for a through-thickness hole in the aluminium plate coupled with fluid layers of different thicknesses: (a1 and a2) without rectification (a1: experimental result; a2: simulation result) when the fluid layer is 4 mm in thickness; (b1 and b2) without rectification (b1: experimental result; b2: simulation result) when the fluid layer is 7 mm in thickness; (c1 and c2) with compensation for the coupling effect (c1: experimental result; c2: simulation result) when the fluid layer is 4 mm in thickness; and (d1 and d2) with compensation for the coupling effect (d1: experimental result; d2: simulation result) when the fluid layer is 7 mm in thickness (white or black circle: actual damage)

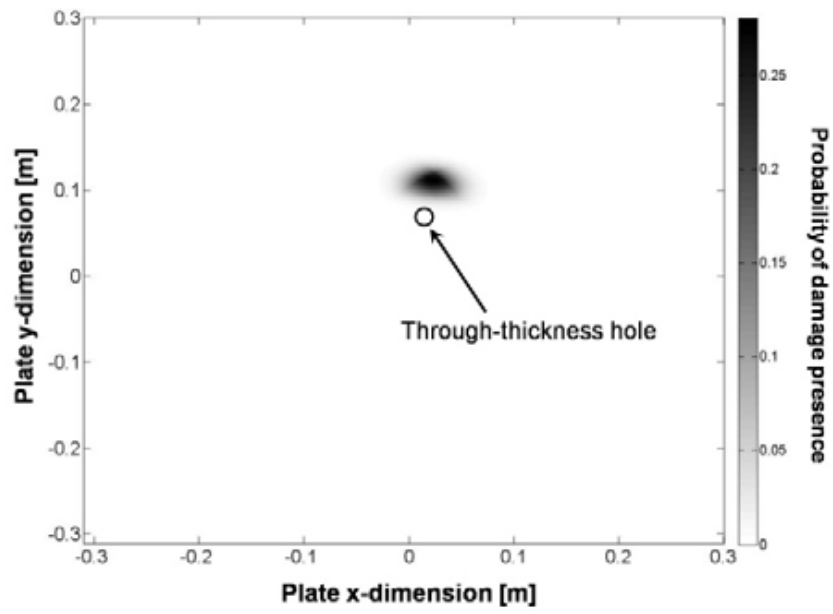


(a2)

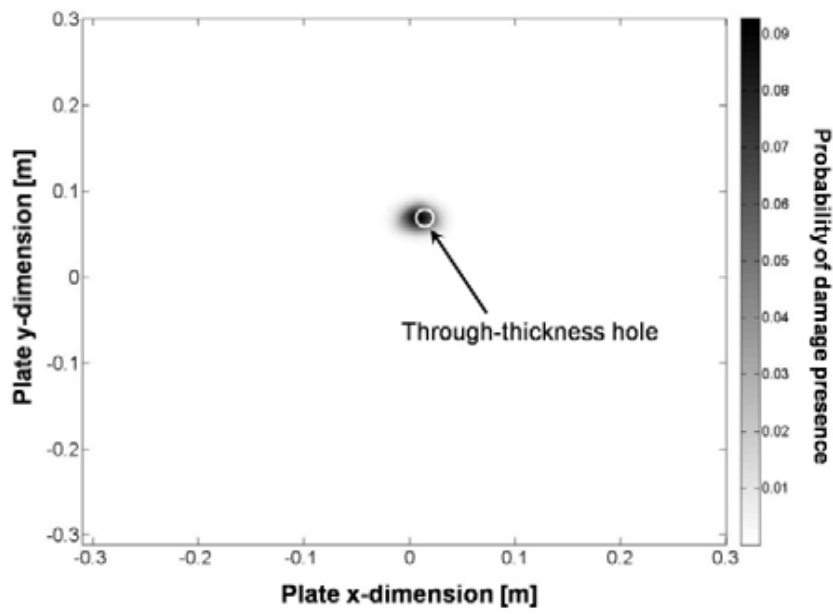


(b1)

**Fig. 4.16. Cont.**

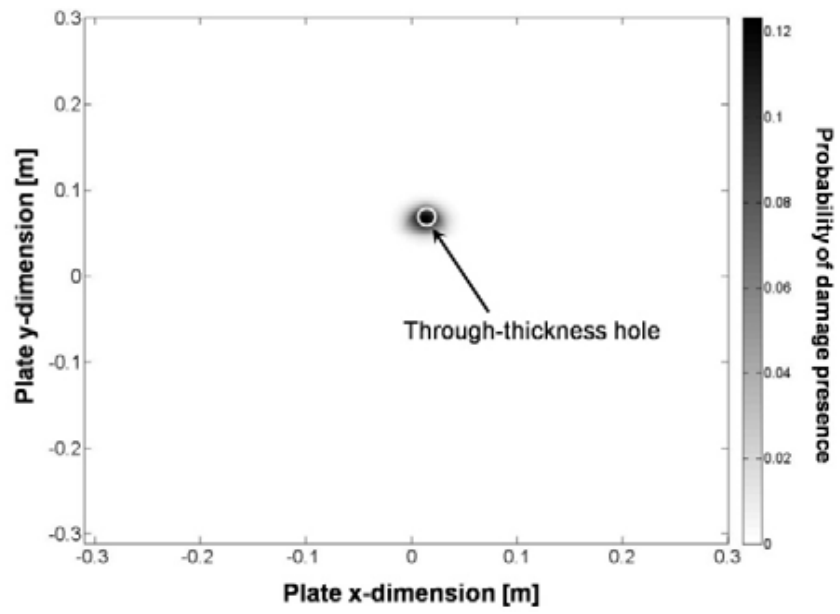


(b2)

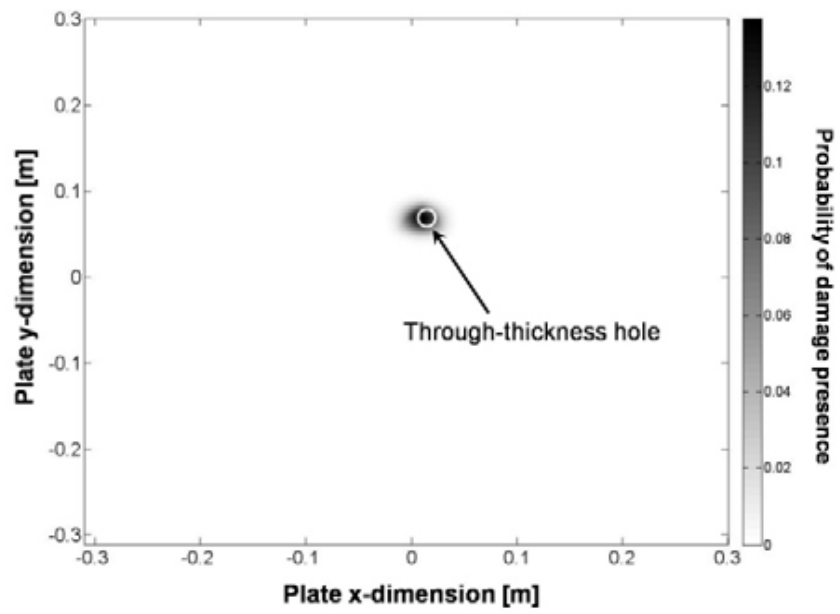


(c1)

**Fig. 4.16.** *Cont.*

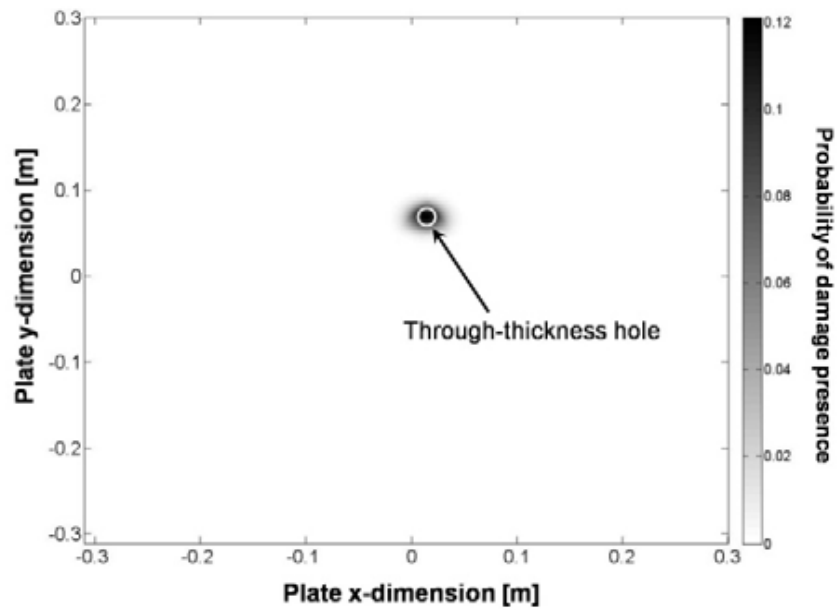


(c2)



(d1)

**Fig. 4.16.** *Cont.*

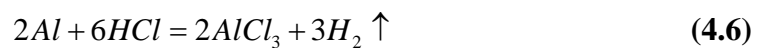


(d2)

**Fig. 4.16.** *Cont.*

### **4.3.3 Evaluating Corrosion Damage in a Submerged Aluminium Plate**

Following the validation of the approach developed by identifying a through-thickness hole in a submerged aluminium plate, the same approach was employed in this section to evaluate corrosion damage in a submerged aluminium plate as an application. Chemical corrosion was introduced into an aluminium plate ( $600\text{ mm} \times 600\text{ mm} \times 1.6\text{ mm}$ ) by exposing a roughly circular zone on the plate to 45% hydrochloric acid (Advanced Technology & Industrial Co., Ltd.), in the light of



After the chemical reaction was complete the chemical substances produced were removed and the surface of the corroded area was polished with sandpaper. This operation was repeated until a corroded area measuring roughly 15 mm in diameter and 1 mm in depth was formed, as shown in Fig. 4.17. The damage (drilled hole and corrosion) has a dimension comparable to the wavelength of  $A_0$  at the excitation frequency of 150 kHz (circa 15 mm), by considering the fact that the wavelength of selected mode must be comparable to the damage size to allow the wave to interact with damage. Though it is interesting to examine the sensitivity of the developed approach to dimension of the damage, the focus of this study is on the coupling effect of fluid on wave-based NDE. Thus the sensitivity of Lamb waves to damage of various dimensions is not a concern in the current study. The Lamb wave signals were excited and captured via three sensing paths,  $T_1-R_1$ ,  $T_2-R_2$  and  $T_3-R_3$ , respectively, with the same configurations as those used in the feasibility study.

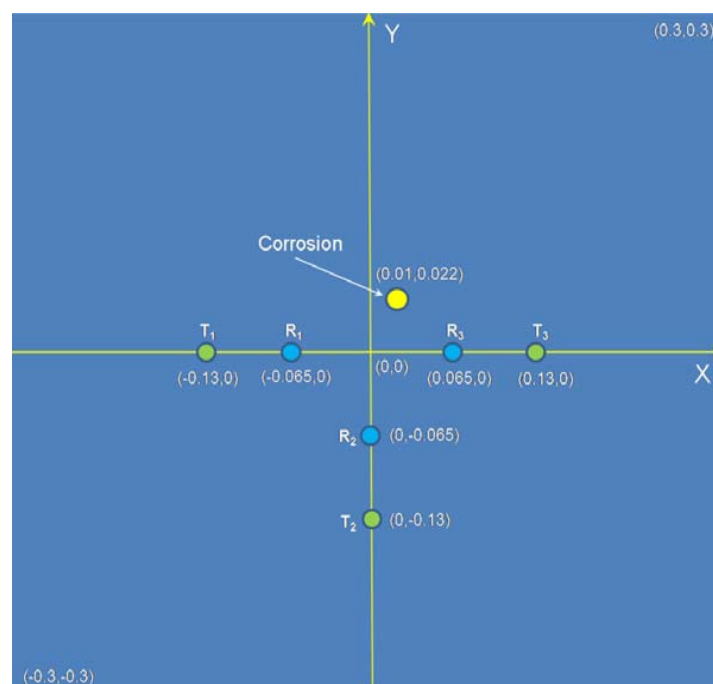


**Fig. 4.17.** Aluminium plate containing corrosion damage (unit:  $m$ )

Figure 4.18 shows the HT-processed signals experimentally captured via sensing path  $T_3-R_3$ , as example, in the absence and presence of fluid layers of different thicknesses (4 and 7  $mm$ , respectively). As in the observations in the feasibility study, the corrosion-scattered  $A_0$  mode can clearly be identified in the HT-processed signals.

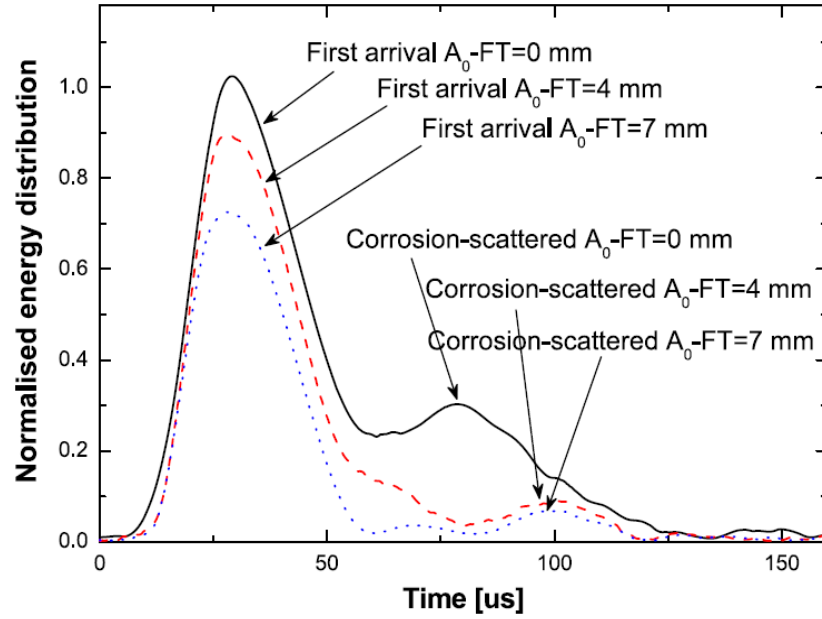
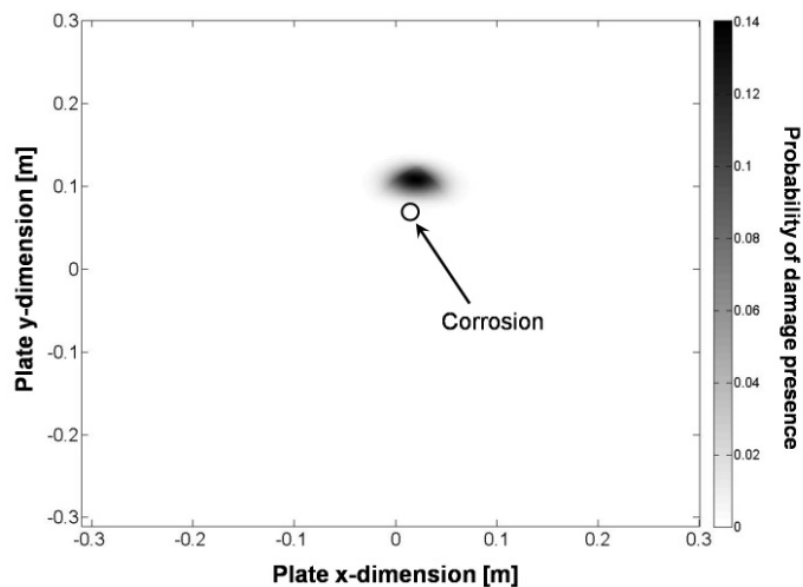


**Fig. 4.18.** HT-processed wave signals captured via sensing path  $T_3$ - $R_3$  in aluminium plate containing corrosion damage in the absence and presence of fluid layers of different thicknesses, obtained via experiment (FT: fluid layer thickness)

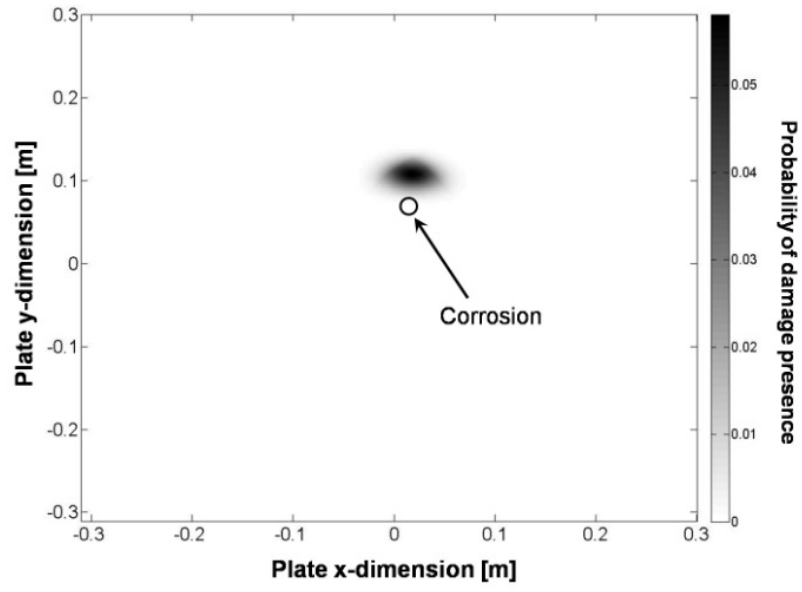
Following the procedure of probability-based diagnostic imaging, each sensing path contributed a probability image. On fusion of the images, the identification results are shown in Fig. 4.19, without and with the modification and compensation for the influence of fluid coupling on Lamb wave propagation. When the modified wave propagation velocity was used to compensate for the fluid coupling, it can be seen that the identification results for corrosion damage in the submerged aluminium plate were satisfactory regardless of the thickness of the fluid layer. For the sake of conciseness, only the results obtained via experiment are presented in Fig. 4.19, although good agreement between FE simulation and experiment was achieved.

As observed in both the experiment and simulation (Fig. 4.8(b)), there was no marked discrepancy in the degree of modulation of the  $A_0$  mode by fluid coupling regardless of differences in the thickness of the fluid layer. The most prominent modulation took place when the fluid layer was initially introduced, implying that the surrounding fluid medium exerted significant influence on Lamb wave propagation in a confined area only. This makes it possible to apply compensation for the coupling influence on Lamb wave propagation at a specific thickness of fluid to submerged structures regardless of differences in thickness of the coupled fluid media.

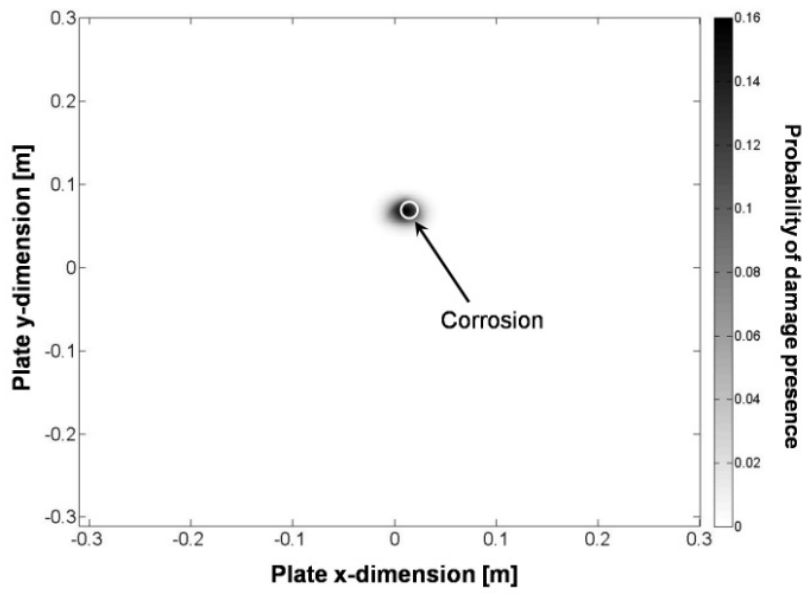


(a)

**Fig. 4.19.** Identification results for corrosion damage in aluminium plate coupled with fluid layer of different thicknesses: (a) without rectification when the fluid layer is 4 mm in thickness; (b) without rectification when the fluid layer is 7 mm in thickness; (c) with compensation for the coupling effect when the fluid layer is 4 mm in thickness; and (d) with compensation for the coupling effect when the fluid layer is 7 mm in thickness (white or black circle: actual corrosion)

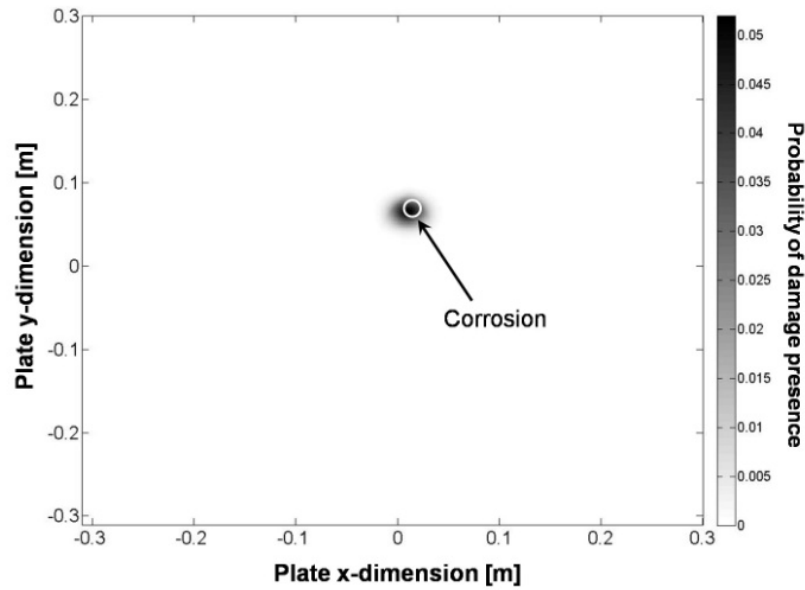


(b)



(c)

Fig. 4.19. *Cont.*



(d)

**Fig. 4.19.** *Cont.*

## 4.4 Concluding Remarks

The  $A_0$  mode was adopted to identify corrosion damage in submerged metallic structures, taking advantage of its shorter wavelength and therefore higher sensitivity to damage of small dimension compared with the  $S_0$  mode. However, the surrounding fluid medium noticeably modulates the propagation characteristics of the  $A_0$  mode in the structures, leading to erroneous identification without appropriate rectification. The effect of the coupled fluid medium on the  $A_0$  mode was investigated and calibrated quantitatively. With appropriate compensation for the coupling effect, structural damage including through-thickness hole and chemical corrosion in submerged aluminium plates was identified precisely with the assistance of a probability-based diagnostic imaging approach. The results demonstrate the necessity

of modification and compensation for medium coupling in practical applications of  
Lamb-wave-based damage identification to coupled media.

# **CHAPTER 5      Coupling Effect of Soft Tissues on Lamb Waves in Synthesised Soft Tissue-bone Phantoms (*Plate Model*)**

## **5.1 Introduction**

As addressed previously in Section 4.2.3, when applying QUS measurement in the clinic, soft tissues coupled with the cortical bone cause certain coupling effects on the propagation of Lamb waves. Although studies have been performed to eliminate the influence of such a coupling effect with the assistance of delicate design of transducers, as reviewed in Section 2.3.1 [14, 16, 72, 88], it is of vital significance to explore this coupling effect quantitatively, so as to achieve insight into the mechanism of the coupling effect of soft tissues on the characteristics of Lamb wave propagation.

In this chapter, comprehensive investigation is conducted of the coupling effect of soft tissues (of different thicknesses and elastic properties, in a range from normal to pathological conditions of human soft tissues) on lowest-order Lamb waves, *i.e.*, first-arrival signal (FAS) and second-arrival signal (SAS), propagating in synthesised bone

phantoms, through a series of parametric studies via 3D FE simulation and experiment. Herein the FAS is equivalent to the  $S_0$  mode in terms of propagation velocity, provided the skeletal part covered by a transducer pair in QUS measurement can be hypothesised to be locally flat by neglecting its curvature if QUS is operated in an ultrasonic frequency range [69, 87], as detailed in Section 3.1; while the SAS is equivalent to the  $A_0$  mode.

## **5.2 Fabrication of Synthesised Soft Tissue-bone Phantoms**

### **5.2.1 Sample Preparation**

A series of synthesised soft tissue-bone phantoms was fabricated, as listed in Table 5.1. Each phantom was comprised of a bone-mimicking medium (acrylic material) and a soft tissue-mimicking medium (either 98% glycerin or artificial silicon rubber (ASR)). Phantoms were grouped into two levels with increasing similarity to a real soft tissue-bone system.

**Table 5.1.** Description of synthesised soft tissue-bone phantoms

Level of evaluation	Sample No.	Thickness of bone phantom (acrylic) [mm]	Soft-tissue phantom	Thickness of soft-tissue phantom [mm]	Bulk/Elastic modulus of soft-tissue phantom* [kPa]
Level I	1#	2	Nil	0	$1.01 \times 10^2$ (air) (bulk modulus)
	2#	<i>ditto</i>	98% glycerin	1~10	$4.5 \times 10^6$ (bulk modulus)
	3#	3.2	Nil	0	$1.01 \times 10^2$ (air) (bulk modulus)
Level II	4#	<i>ditto</i>	ASR	0.8	11.96 (elastic modulus)
	5#	<i>ditto</i>	<i>ditto</i>	1.9	<i>ditto</i>
	6#	<i>ditto</i>	<i>ditto</i>	3.4	<i>ditto</i>
	7#	<i>ditto</i>	<i>ditto</i>	4.2	<i>ditto</i>
	8#	<i>ditto</i>	<i>ditto</i>	5.1	<i>ditto</i>
	9#	<i>ditto</i>	<i>ditto</i>	6.3	<i>ditto</i>
	10#	<i>ditto</i>	<i>ditto</i>	7.7	<i>ditto</i>
	11#	<i>ditto</i>	<i>ditto</i>	9.4	<i>ditto</i>
	12#	<i>ditto</i>	<i>ditto</i>	3.4	2.89
	13#	<i>ditto</i>	<i>ditto</i>	<i>ditto</i>	6.86
	14#	<i>ditto</i>	<i>ditto</i>	<i>ditto</i>	11.96
	15#	<i>ditto</i>	<i>ditto</i>	<i>ditto</i>	19.65
	16#	<i>ditto</i>	<i>ditto</i>	<i>ditto</i>	32.38
	17#	<i>ditto</i>	<i>ditto</i>	<i>ditto</i>	55.87
	18#	<i>ditto</i>	<i>ditto</i>	<i>ditto</i>	73.41
	19#	<i>ditto</i>	<i>ditto</i>	<i>ditto</i>	119.62
20#	<i>ditto</i>	<i>ditto</i>	<i>ditto</i>	181.23	
21#	<i>ditto</i>	<i>ditto</i>	<i>ditto</i>	336.87	
22#	<i>ditto</i>	<i>ditto</i>	<i>ditto</i>	536.51	

\* Elastic modulus is used for defining materials that can withstand both tensile and compressive loadings such as ASR.

- At a lower degree of evaluation (Level I), acrylic plates ( $460 \text{ mm} \times 240 \text{ mm} \times 2 \text{ mm}$ ) were chosen as the bone phantom (Samples No. 1#–2#). Acrylic is a sort of bone-mimicking material which has been widely used to simulate cancellous and cortical bone with demonstrated accuracy [22, 24], because of its similarity in material property to human cortical bone (density:  $\rho_{bone} = 1.5 \text{ g/cm}^3$  vs.  $\rho_{acrylic} = 1.2 \text{ g/cm}^3$ ; elastic modulus:  $E_{bone} = 1 \sim 14 \text{ GPa}$  [18,

129] vs.  $E_{acrylic} = 4.24 \text{ GPa}$  ; Poisson's ratio:  $\nu_{bone} = 0.37$  vs.  $\nu_{acrylic} = 0.39$  ). As a result, a wave mode propagates at very similar velocities in acrylic and human bone (e.g., the velocities of longitudinal and transverse wave modes in both materials are very similar:  $c_L = 2730 \text{ m/s}$  and  $c_T = 1325 \text{ m/s}$  , respectively [22]). Moreover, acrylic materials can easily be geometrically tailored to mimic various bone shapes. At this level, soft medium was simulated using a layer of 98% glycerin (density:  $\rho_{glycerin} = 1.26 \text{ g/cm}^3$  ; bulk modulus:  $K_{glycerin} = 4.52 \text{ GPa}$  ) of different thickness (0 ~ 10 mm, covering the thickness of human soft tissues at major skeletal sites). 98% glycerin has been used for mimicking soft tissues [130] for its morphologic similarity in many respects to human soft tissues, including very close ultrasonic attenuation ratio and bulky velocities of different waves in glycerin and in soft tissues.

- At a higher degree of evaluation (Level II), acrylic plates (460 mm × 240 mm × 3.2 mm) were selected as the bone phantom (Samples No. 3#–22#). Bearing in mind that real human soft tissues are not pure fluid but soft substances that support the propagation of shear waves, a layer of ASR was used to mimic soft tissues in this level (in-plane dimension: 160 mm × 60 mm). Different ASR layers were fabricated to have (i) different thicknesses (0.8 ~ 9.4 mm, covering the thickness of human soft tissues at major skeletal sites) but the same elastic properties ( $E_{ASR} = 11.96 \text{ kPa}$  , similar to those of typical healthy soft tissues [131]; density:  $\rho_{soft\ tissue} = 1.0 \text{ g/cm}^3$  [132] vs.  $\rho_{ASR} = 1.075 \text{ g/cm}^3$ ) (Samples No.

4#–11#), or (ii) different elastic properties (2.89 ~ 536 kPa, in a range from normal to pathological conditions of human soft tissues) but the same thickness (3.4 *mm*) (Samples No. 12#–22#). Sustaining continuous propagation of longitudinal and shear waves, ASR has high comparability with human soft tissues, and is deemed as a sort of tissue-equivalent material (TEM) [133].

ASRs of different elastic properties, for simulating soft tissues under different pathological conditions, were fabricated by controlling the ratios of silicon gel, firming agent and oil in the mixture in accordance to the following steps (Fig. 5.1):

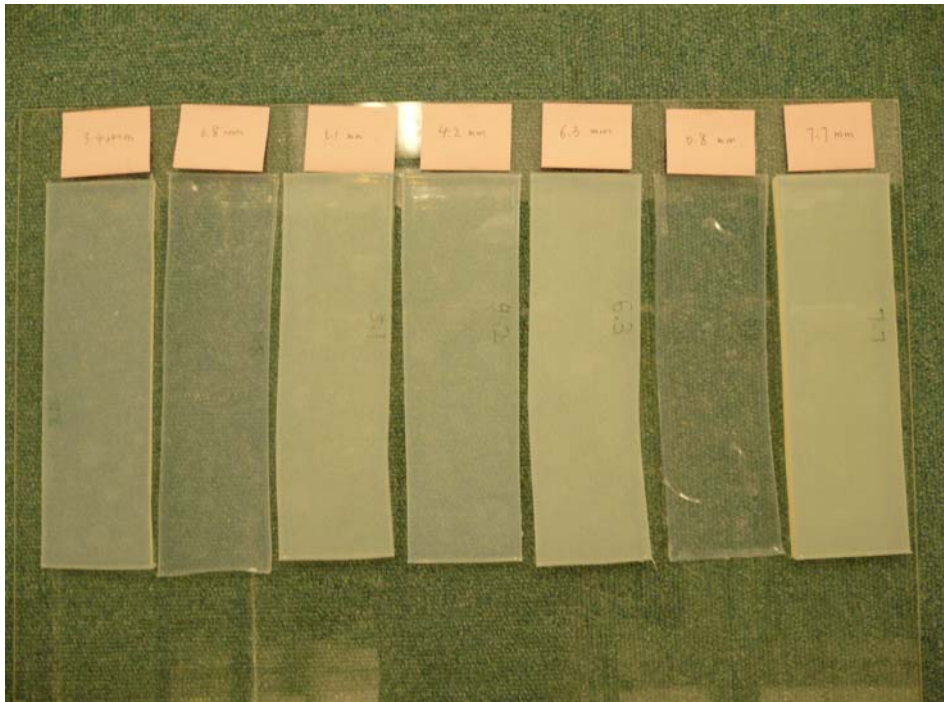
- (i) mixing silicon gel (Wacker M4600A, Wacker Chemicals (Hong Kong) Ltd.), firming agents (Wacker M4600B, manufacturer as the above) and oil (AK35, manufacturer as the above) at a specific ratio. The ratio of firming agent to silicon gel (RFS) was retained as 0.1 as recommended by the manufacturer, and the ratio of oil to silicon gel (ROS) varied from 0 to 2 with an increment of 0.2, leading to different elastic moduli ranging from 536 to 2.89 kPa (the lower the ROS the higher the elastic modulus);
- (ii) keeping the mixture in a desiccator (DURAN Productions GmbH & Co. KG) which was then vacuumed using a vacuum pump (FY-1c, Feiyue Electrical Machinery Co. Ltd.) to maintain an interior pressure less than 5 Pa. By such means, air bubbles in the mixture were removed;
- (iii) injecting mixtures (in the form of liquid) into two moulds, measuring 30 *mm* × 30 *mm* × 30 *mm* and 160 *mm* × 60 *mm* × 40 *mm* , respectively. ASRs

shaped with the former mould were used for determining their mechanical properties, and those shaped with the latter were used for mimicking soft tissues to be coupled with acrylic plates; and

- (iv) retaining all mixtures in moulds for 12 hours for the curing process.



**Fig. 5.1.** Photos of production of ASR: (a) mixing silicon gel, firm agents and oil; (b)  
produced ASR layers



(b)

**Fig. 5.1. Cont.**

To fabricate ASRs of different thicknesses, the procedures were similar to the above, in which RFS and ROS were set as 0.1 and 1.6, respectively, resulting in the elastic modulus of the fabricated ASR being 11.96 kPa.

Each fabricated ASR with the desired elastic property and geometry was adhered to an acrylic plate using a special adhesive, Type 460 (Boluo Yongqiang Chemical Co., Ltd.), to form a synthesised soft tissue-bone phantom. Nineteen phantoms were made by such means (Samples No. 4#–22#). Before adhering, the contacting surfaces of both media were cleaned and processed with a finishing agent, Type 330 (Boluo Yongqiang Chemical Co., Ltd.), to improve the agglutination between the two media. Prior to this, another four types of adhesive, Pattex<sup>®</sup> COMPACT (Henkel AG & Co.),

Pattex<sup>®</sup> CONTACT ADHESIVE (Henkel AG & Co.), Pattex<sup>®</sup> POWER EPOXY A-B (Henkel AG & Co.) and GEL GRIP<sup>™</sup> (Selleys Pty. Ltd.) had been tested against Type 460. It was observed that all the gluewater except 460 failed to glue rubber layer onto the plate. As shown in Fig. 5.2, the rubber layer could be easily removed after glued by COMPACT, CONTACT ADHESIVE, POWER EXPOXY A-B, GEL GRIP<sup>™</sup> about 1 hour after the gluing indicating a poor gluing condition, while the rubber layer was well glued by 460 which is a kind of gluewater specifically made for gluing rubber on solid structures. Type 460, a water-like glue specifically made for silicon rubber, features little viscosity and can provide even, firm and durable adhesion between ASR and hard materials with a very thin adhesive layer.

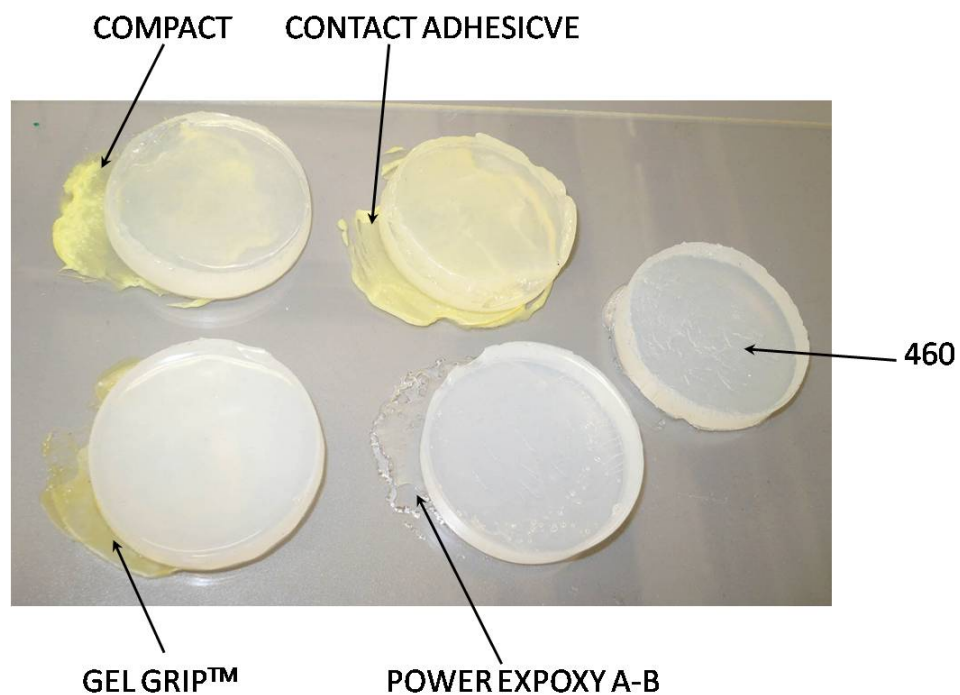


**Fig. 5.2.** Comparison of effects of different gluewater on gluing silicone rubber onto acrylic

plate

## **5.2.2 Mechanical Property Testing of Artificial Silicon Rubber (ASR)**

To ascertain the major mechanical properties of the fabricated ASR, a standard compression test was applied to the aforementioned ASR cubes ( $30\text{ mm} \times 30\text{ mm} \times 30\text{ mm}$ ) using a tensile testing platform (MTS<sup>®</sup> Alliance RT/50) as shown in Fig. 5.3. Each sample was axially fixed between a pair of crossheads 60 *mm* in diameter (the contact areas between the sample and crossheads were much smaller than those of the crossheads, allowing uniform compression to be applied to all samples). Testing was carried out at room temperature at a compression speed of 0.2 *mm/s*. Uniform compressive loads were applied to each sample until its axial strain reached 10%. Both surfaces of the two crossheads and the samples were pre-lubricated using a coupling gel (AQUASONIC<sup>®</sup>, Parker Laboratories, INC., The Netherlands) to minimise the friction between them.

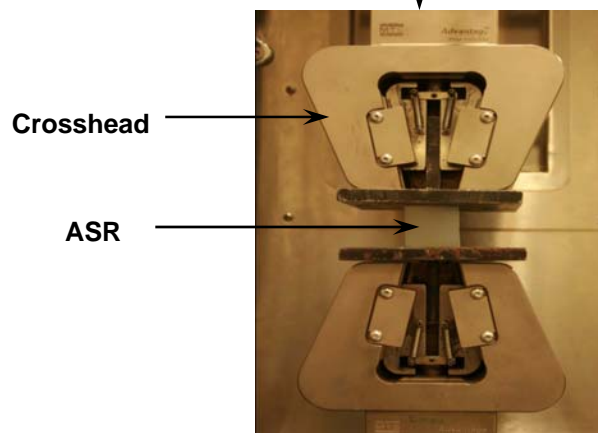


**Fig. 5.3.** Setup for compression testing of fabricated ASR (MTS® Alliance RT/50 platform)

The stress-strain relationship thus obtained when ROS was 1.6 as a representative example is shown in Fig. 5.4. It can be seen that the ASR exhibits approximately linear properties in the discussed strain range. The result demonstrates that the viscoelasticity and nonlinearity of silicon rubber is not of great concern for examining

ultrasonic waves in soft tissues at a relatively low frequency (<100 kHz), and under such a circumstance ASR can be treated as a linear, elastic and isotropic solid [132]. From the stress-strain relationships experimentally obtained at different ROSs, the elastic moduli of the fabricated ASR samples were determined, listed in Table 5.2.

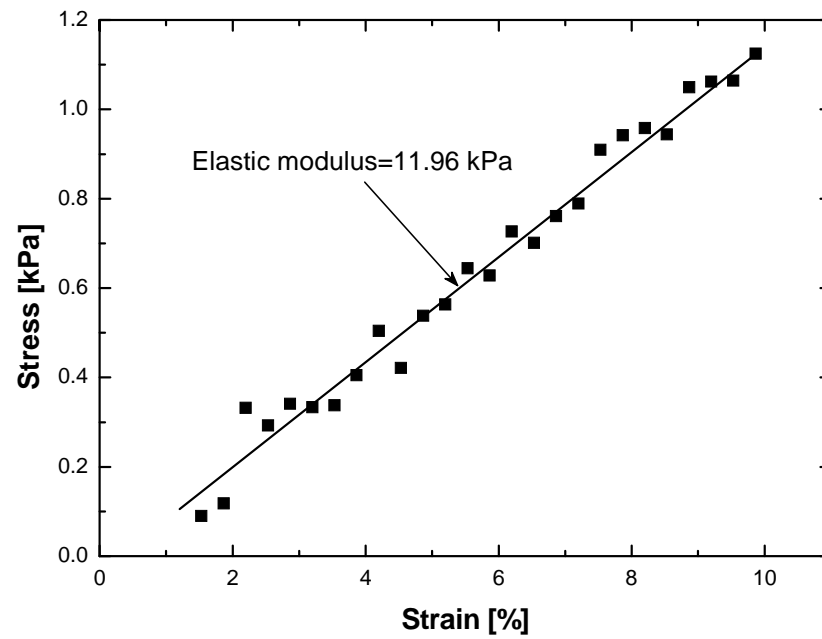


**Fig. 5.4.** Stress-strain relationship of the fabricated ASR (ROS: 1.6) obtained from compression testing

**Table 5.2.** Elastic moduli of synthesised ASR

Sample No.*	ROS	Elastic modulus [kPa]
12#	2.0	2.89
13#	1.8	6.86
14#	1.6	11.96
15#	1.4	19.65
16#	1.2	32.38
17#	1.0	55.87
18#	0.8	73.41
19#	0.6	119.62
20#	0.4	181.23
21#	0.2	336.87
22#	0	536.51

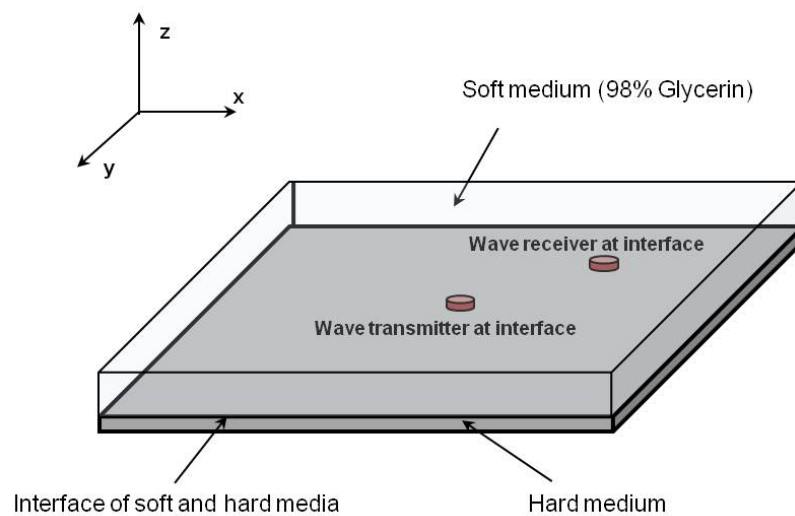
\* Sample numbers are consistent with those in Table 5.1.

## 5.3 Analysis Method

### 5.3.1 3D FE Modelling and Simulation

A 3D FE modelling and simulation technique was developed for analysing the synthesised soft tissue-bone phantoms. As mentioned, each phantom was comprised of a bone-mimicking, hard medium and a soft tissue-mimicking, soft medium. In the modelling, a transducer pair (including a transmitter and a receiver) was assumed to activate and receive Lamb waves at the interface, as shown schematically in Fig. 5.5. Both the transmitter and receiver were positioned at the interface between the two media, with the aim of exploring the influence of the coupled soft medium on Lamb wave propagation in the hard medium. For the 98% glycerin scenario, the transducers

were positioned directly on the upper surface of the acrylic plate, as seen in the setup photo in Fig. 5.6(a). With that measurement configuration, the captured wave signals are Lamb waves that propagate in the plate, rather than Scholte waves whose energy is most concentrated in fluid (refer to Section 3.4). For the ASR scenario, the transducer pair was placed on the upper surface of the hard medium just beside the edge of the soft medium (Fig. 5.6(b)). In this case, Stoneley waves exist at the interface between the two media, and dissipate quickly away from the interface, implying that the waves captured by the sensor are Lamb waves propagating in the hard medium rather than Stoneley waves. It is noteworthy that, aimed at exploring the medium coupling effect on Lamb wave characteristics in the hard medium, a transducer pair was positioned in tandem at the interface between the hard and soft media rather than atop the soft medium, which is different from real clinical applications of QUS.



(a)

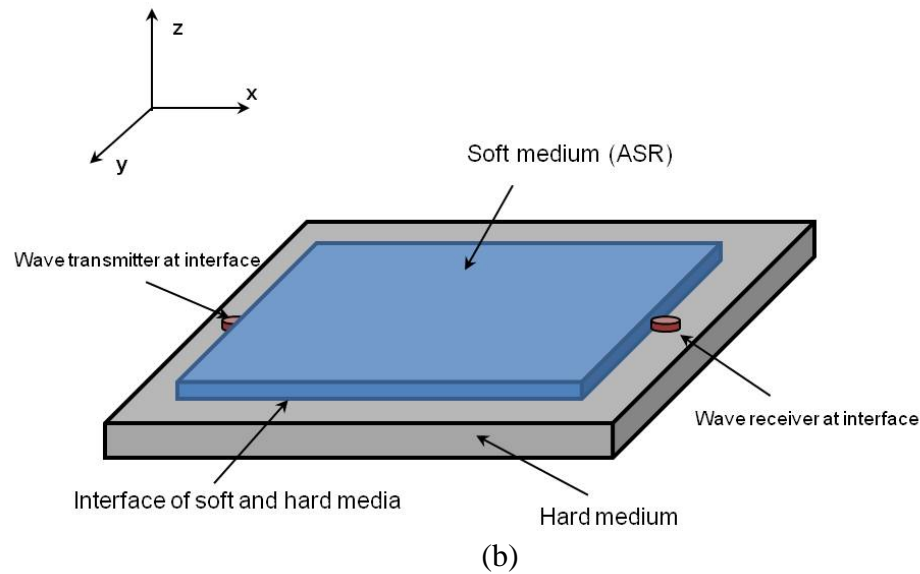


**Fig. 5.5.** Schematic of transmitter and receiver allocation in FEM for (a) glycerin and (b) ASR scenarios

In the modelling, the hard medium was modelled using 3D eight-node brick solid elements. The soft medium was modelled using 3D eight-node acoustic elements for glycerin or 3D eight-node brick solid elements for ASR. To simulate the soft tissue, for the glycerin scenario, acoustic pressure was applied in the  $z$ -axis only, consistent with the fact that fluid cannot sustain shear loads within the  $x-y$  plane (referring to Fig. 5.5 for the coordinate system); for the ASR scenario, it was demonstrated in Section 5.2.2 that, at relatively low excitation frequencies ( $<100\text{ kHz}$ ), the viscoelasticity and nonlinearity of soft tissue is not a great concern in the canvassing of wave propagation and can be simulated as elastic and isotropic.

The interface between the hard and soft media of each phantom was modelled using a specialised surface-based coupling constraint in terms of a node-to-surface

formulation provided by ABAQUS<sup>®</sup>/EXPLICIT and named ‘*TIE*’, which was described in Section 4.2.1. In particular, the displacement of particles at the interface between the soft and hard media was continuous in the out-of-plane direction only, due to the fact that fluid cannot sustain shear stress. However, that is not the case when soft tissue is considered as ASR: particles at the interface of the two media vibrate continuously in both the out-of-plane and in-plane directions, more closely mimicking real human bone covered with soft tissue than when fluid is used for simulation.

With the transmitter model presented in Section 4.2.1, the FAS and SAS of different waveforms at different central frequencies could be activated. Upon activation by the transmitter model, wave propagation at the interface was acquired using a receiver model (presented in Section 4.2.1) by capturing deformation (strain, stress and displacement) in three orthotropic directions. Dynamic FE simulation was accomplished using the commercial FE package ABAQUS<sup>®</sup>/EXPLICIT.

### **5.3.2 Experimental Validation**

In line with the above FE modelling and simulation, an experiment approach with supporting hardware and software for implementation was developed. A pair of waterproof ultrasound transducers (the same as those reported in Section 4.2.2) was collocated at the upper surface of the acrylic plate for the two scenarios discussed (Fig. 5.6), and driven by a signal generation and data acquisition system configured on a

VXI platform that was introduced in Section 4.2.2, as sketched in Fig. 5.7.

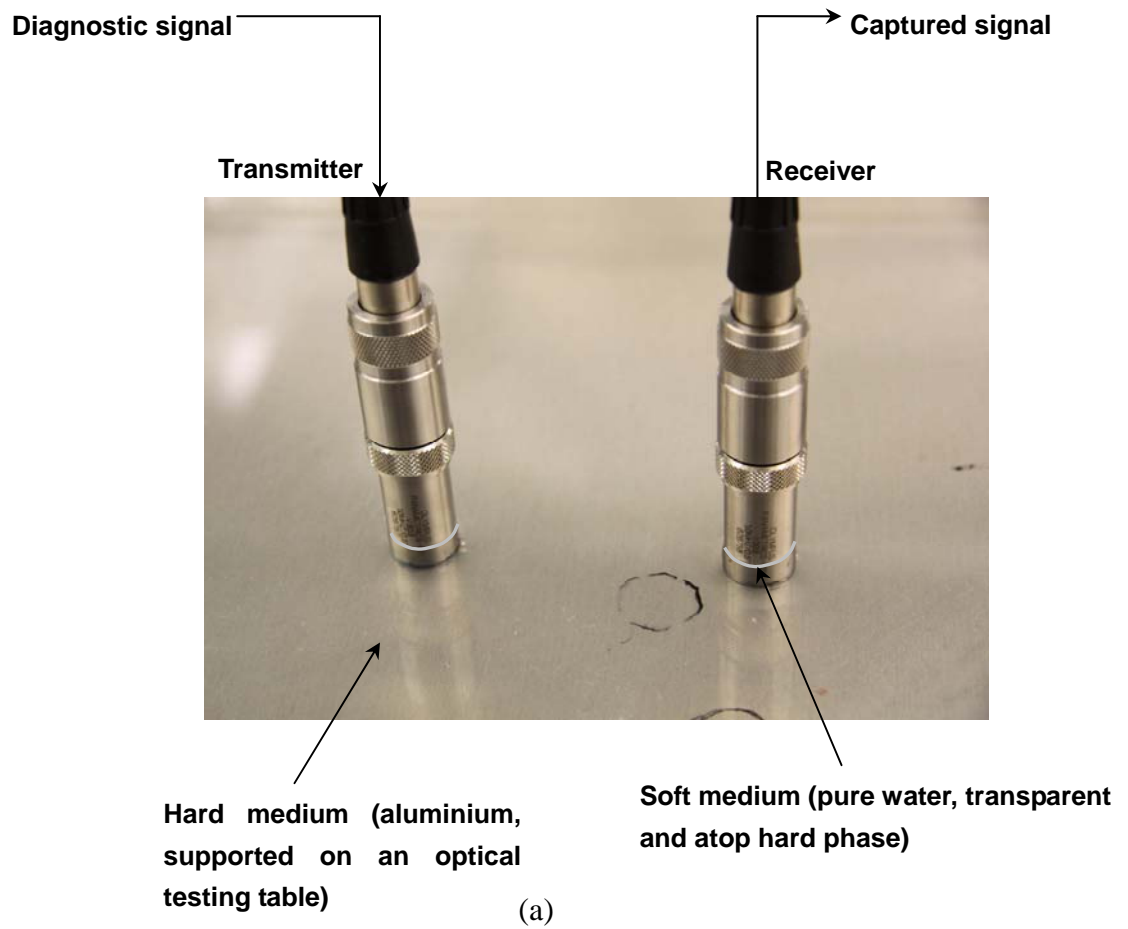
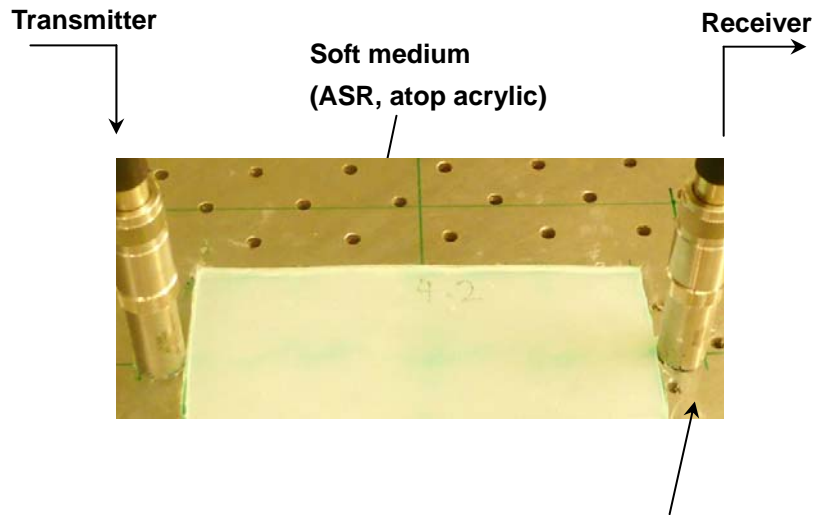


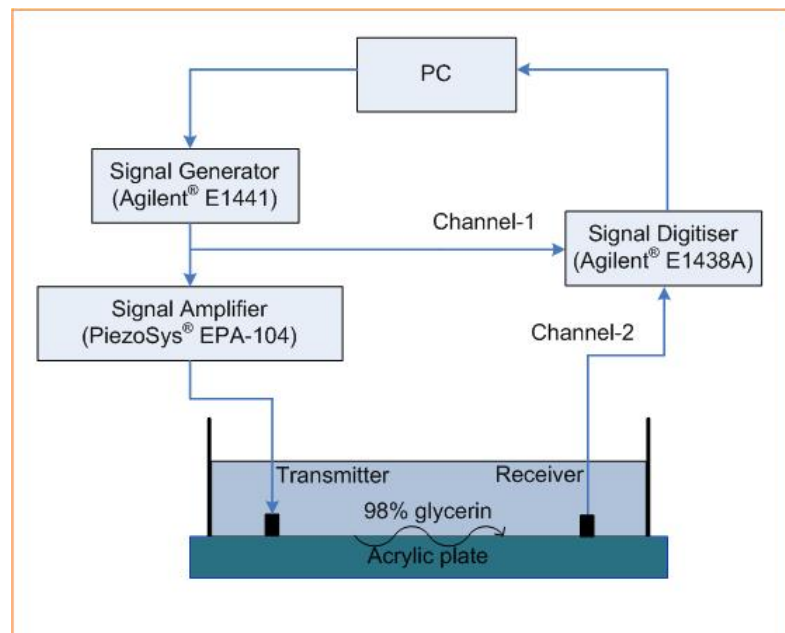
**Fig. 5.6.** Photos of experimental setup for (a) glycerin and (b) ASR scenarios



Hard medium (an acrylic plate, transparent and supported on an optical testing table)

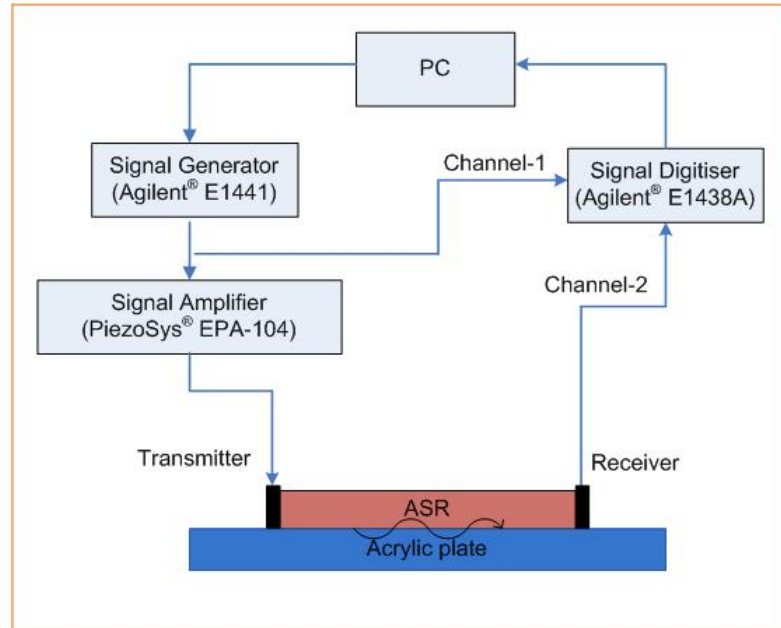
(b)

Fig. 5.6. Cont.



(a)

Fig. 5.7. Experimental setup for (a) glycerin and (b) ASR scenarios



(b)

**Fig. 5.7. Cont.**

### 5.3.3 Signal Processing

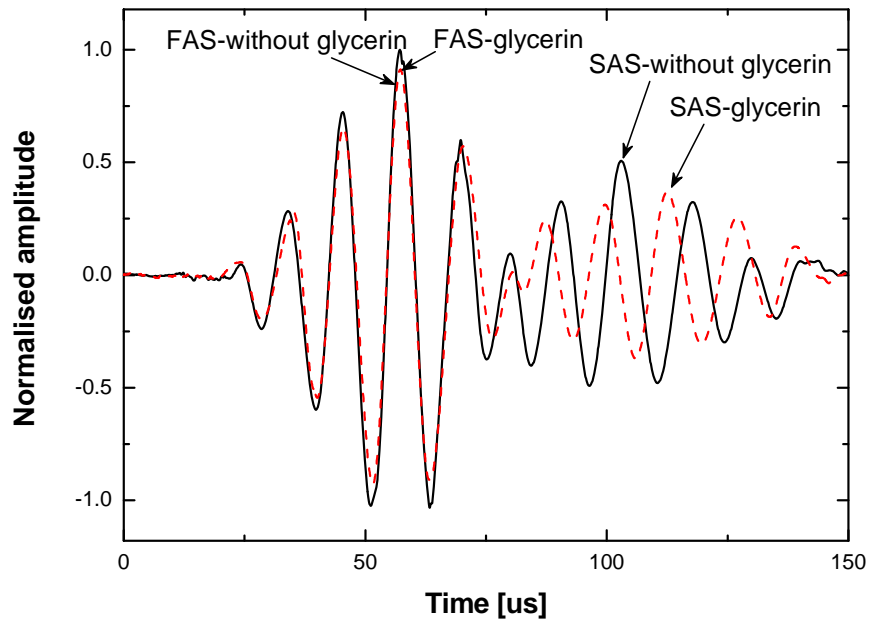
In practice, captured ultrasound signals are prone to various contaminations including random electrical/magnetic interference, mechanical noise, temperature/humidity fluctuation and measurement uncertainty. To minimise such contaminations, a series of signal processing endeavors was employed, including signal averaging, DC offset, smoothing and de-noising. The captured raw signals were finally processed by HT detailed in Section 4.2.3.

## 5.4 Results and Observations

### 5.4.1 Influence of Thickness of Coupled Soft Media

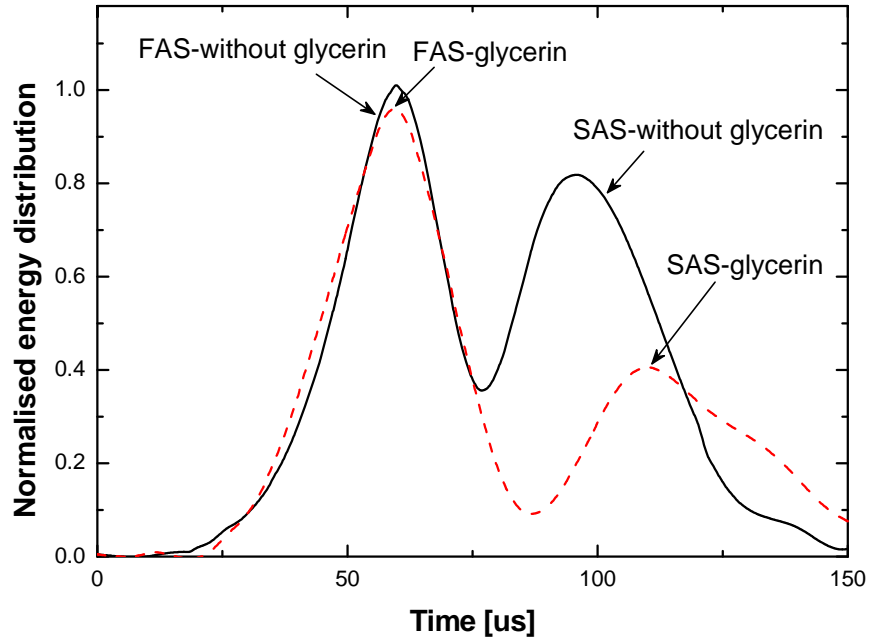
#### *98% Glycerin (Level I)*

Layers of 98% glycerin with different thicknesses (0 ~ 10 *mm* with an increment of 0.5 *mm*) (Samples No. 1#–2#) were canvassed. Five-cycle *Hanning*-window modulated sinusoid tonebursts at a central frequency of 100 kHz with a peak-to-peak magnitude of 180 V were activated as the diagnostic signal. Figure 5.8 presents a typical wave signal *in vitro* captured and pre-processed (signal averaging, DC offset, smoothing and de-noising) when the soft medium was 4 *mm* in thickness, and its corresponding HT-processed counterpart. For comparison the signal captured from a free acrylic plate in the absence of soft medium (Sample No. 1#) is also included.



(a)

**Fig. 5.8.** (a) Pre-processed *in vitro* signals in phantoms in the absence (Sample No. 1#) and presence of a layer of 98% glycerin 4 mm in thickness (Sample No. 2#) at an excitation frequency of 100 kHz; and (b) HT-processed results of signals shown in (a) (signal being normalised relative to amplitude extremum of the signal in No. 1# sample)



(b)

**Fig. 5.8.** *Cont.*

Figure 5.8(b) depicts the distribution of signal energy in the time domain, and the first and second energy concentrations are associated with FAS and SAS, respectively. It can clearly be seen that the soft medium exerts marked influence on SAS, manifesting as a reduction in energy magnitude and a delay in time of arrival as a result of reduced propagation velocity, whereas FAS is insensitive to the coupling effect. From comparison with the benchmarking signal in the free acrylic plate it can be concluded that the reduction in signal energy is attributable to the coupling effect rather than to wave attenuation with propagation distance. This coincides with the analysis in Section 4.2.3: in FAS ( $S_0$ ) particles predominantly have radial in-plane displacement, consistent with the wave propagation direction, and it is difficult for that motion pattern to cross the interface of fluid and solid because glycerin, a fluid medium, cannot sustain shear (in-plane) loads; in contrast, the SAS ( $A_0$ ), has mostly out-of-

plane particulate motion and a portion of the energy carried can leak from the hard to the soft medium. That is the primary mechanism of signal attenuation of a mode dominating out-of-plane vibration in the hard medium when coupled with another medium.

Illustrating variation in the thickness of the soft medium (0 ~ 10 mm), Fig. 5.9 shows the dependence of the propagation velocities of FAS and SAS on the thickness of the coupled 98% glycerin layer. A coincident modulation of SAS from the soft medium according to its thickness can be observed: both the energy magnitude and the velocity of SAS decrease prominently when the soft medium is first introduced, but no further change is noted as the thickness of the soft medium increases.

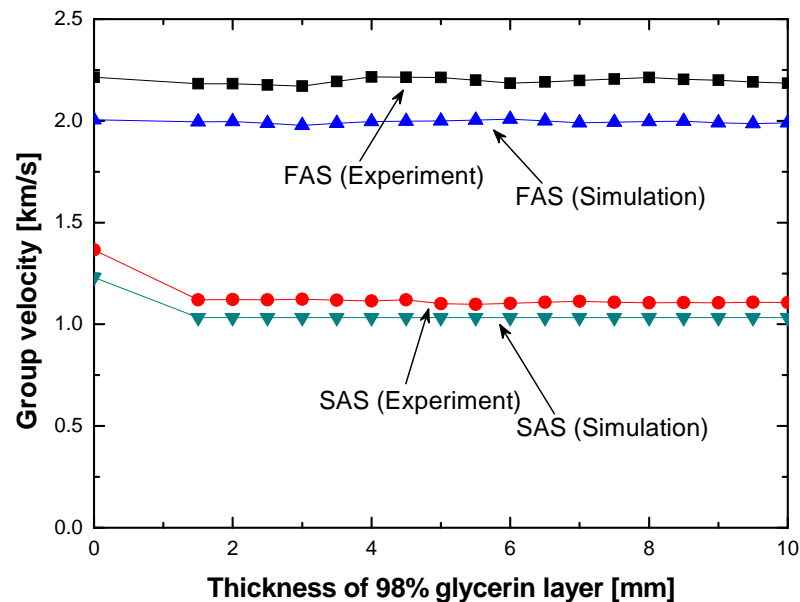


**Fig. 5.9.** Group velocities of FAS and SAS in phantoms (Samples No. 1#–2#) obtained through simulation and experiment vs. thickness of coupled 98% glycerin layer (excitation

frequency: 100 kHz)

To facilitate interpretation of this observation, the stress field across the thickness of the fluid-solid-coupled medium as a result of wave propagation (with the soft medium 2 mm in thickness as an example) was obtained with 3D FE simulation, and shown in Fig. 5.10. It is obvious that part of the energy associated with SAS leaks out from the hard to the soft medium, but the energy associated with FAS is confined in the hard medium.

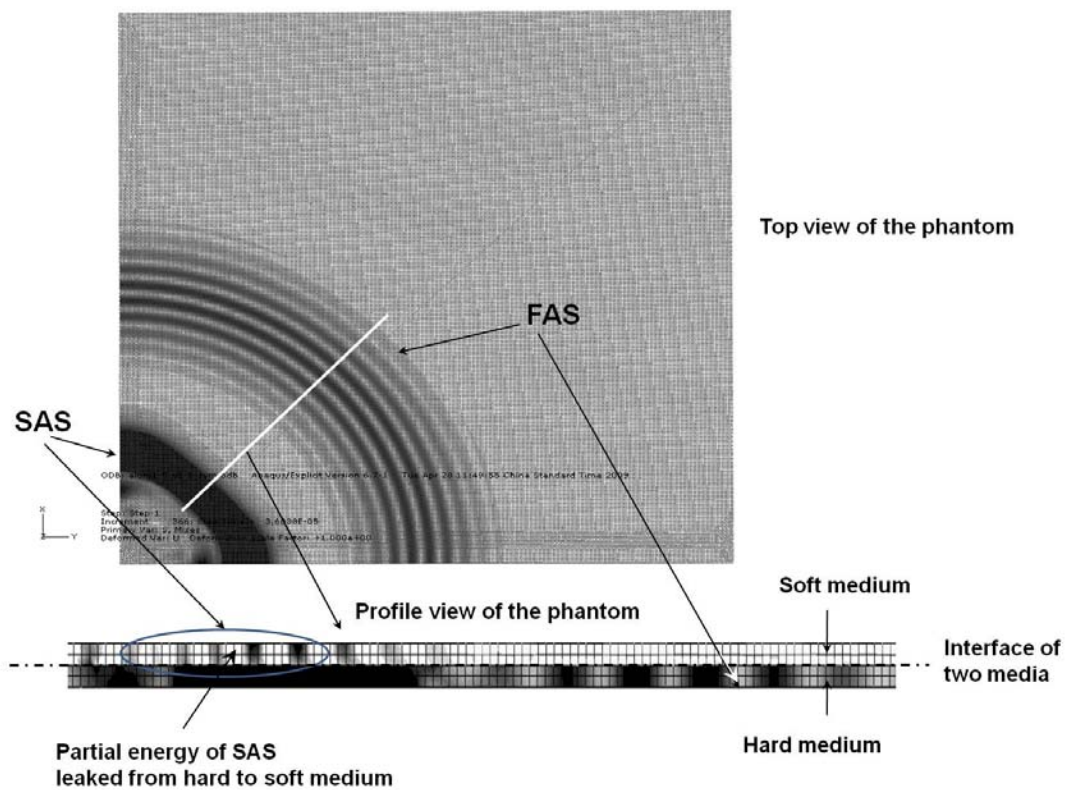


**Fig. 5.10.** Stress field as a result of wave propagation in phantom (Sample No. 2#) coupled with a layer of 98% glycerin 2 mm in thickness, showing that energy associated with SAS leaks from hard to soft medium but that associated with FAS is confined in hard medium (note: for convenience of comparison, the displayed stress fields in the soft and hard media

are not of the same scale; the darker the greyscale the higher the stress)

## ***ASR (Level II)***

Layers of ASR with different thicknesses (0 ~ 9.4 *mm*) but the same elastic properties ( $E_{ASR} = 11.96 \text{ kPa}$ ) were explored (Samples No. 3#–11#). Diagnostic signals with the same waveform as that in the above case were activated at a series of candidate frequencies ranging from 50 to 200 kHz, so as to ascertain the optimal excitation frequency. Captured signals under an excitation of 75 kHz showed the best recognisability for both FAS and SAS, and this frequency was therefore selected as the excitation frequency of the diagnostic signal in the parametric work.

As some representative results, HT-processed signals when the thickness of the ASR layer was 0.8 *mm* (Sample No. 4#), 3.4 *mm* (Sample No. 6#), 4.2 *mm* (Sample No. 7#), 7.7 *mm* (Sample No. 10#) and 9.4 *mm* (Sample No. 11#) are combined in Fig. 5.11. Further, including all the discussed thicknesses of the soft medium (0.8 ~ 9.4 *mm*), changes in the propagation velocities of FAS and SAS and changes in their peak energy magnitudes, subject to the thickness of the coupled ASR layer, are summarised in Figs. 5.12 and 5.13, respectively. The figures highlight the observations that the coupled ASR layer clearly exerts an influence on both FAS and SAS, both of which exhibit reductions in signal magnitude and decreases in propagation velocity, albeit to different degrees. The most significant changes occur when the ASR layer is first introduced, and the decrease in signal magnitude continues as the thickness of the ASR layer increases, but the propagation velocities of both modes fluctuate very slightly with further increase in ASR thickness. This result is different from the case

when a fluid layer serves as the soft medium (the effect of pure water was described in Section 4.2.3, and that of 98% glycerin was previously explored in this section), in which prominent modulation of ultrasonic waves due to existence of coupled medium is noticed for SAS only. As shown in Figs. 5.9 and 5.12, the results from experiment and FE simulation show satisfactory consistence, validating the methods adopted in FE simulation. However, in both figures, the consistency of velocities of FAS from experiment and simulation is not as good as that of SAS. This may be attributable to the '*TIE*' constraint which may not actually simulate the glycerin-acrylic and rubber-acrylic interfaces, because 98% glycerin has a little viscosity, and the silicon rubber can sustain shear stresses. Moreover, the particulate vibration of FAS is most in-plane, which may induce shear stresses in the soft part. As mentioned in Section 4.2.3, a bounded layer between the soft and hard parts may provide enhanced precision to simulate the coupling condition between soft and hard parts. Such a bounded layer will be considered in future studies.

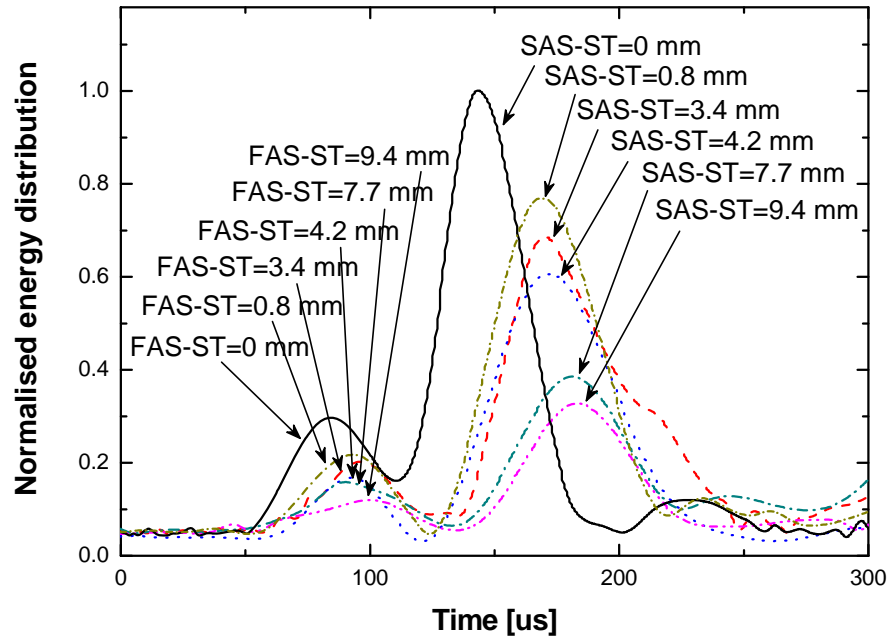


**Fig. 5.11.** HT-processed *in vitro* signals in phantoms in the absence (Sample No. 3#) and presence of a layer of ASR of different thicknesses (Samples No. 4#, 6#, 7#, 10# and 11#) at an excitation frequency of 75 kHz (ST: thickness of soft medium (ASR); signal normalised relative to amplitude extremum of the signal in No. 3# sample)

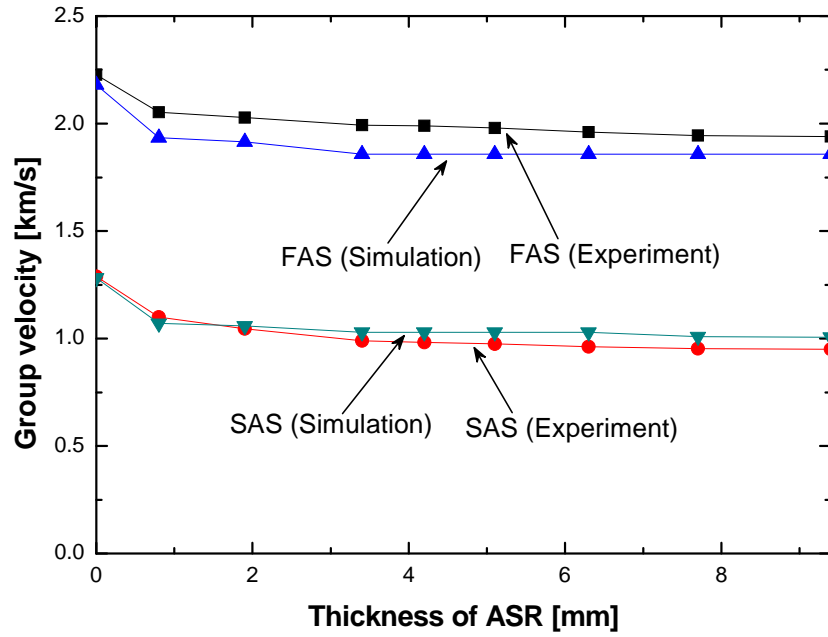


**Fig. 5.12.** Group velocities of FAS and SAS in phantoms (Samples No. 3#–11#) obtained through simulation and experiment vs. thickness of coupled ASR layer (excitation frequency: 75 kHz)

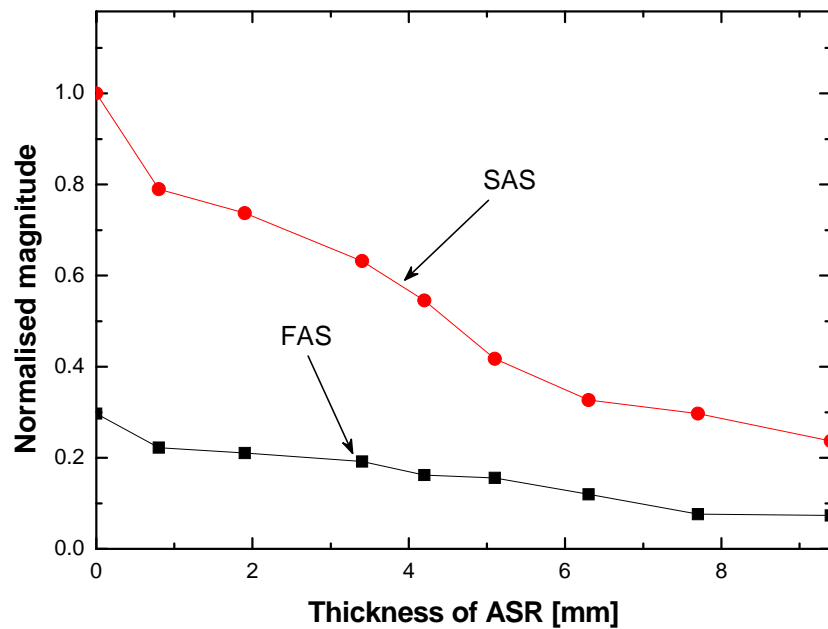


**Fig. 5.13.** Magnitudes of FAS and SAS in phantoms (Samples No. 3#–11#) vs. thickness of coupled ASR layer (excitation frequency: 75 kHz; signal magnitude normalised relative to amplitude extremum of the signal in No. 3# sample)

To visualise the wave leakage from the hard to the soft medium, the stress field throughout the thickness of the ASR-solid-coupled phantom (when the ASR layer is 3.4 *mm* in thickness as an example, Sample No. 6#) is shown in Fig. 5.14, displaying prominent leakage of energy from the hard to the soft medium for both modes. This result implies that because real human soft tissues can support both in-plane and out-of-plane particulate motion patterns, soft tissues provide means by radiation for Lamb waves (FAS and SAS) to leak into overlying soft tissues. When leaky Lamb waves encounter boundaries of different media they are scattered, accompanied by mode conversion, and then disseminate throughout the different media.

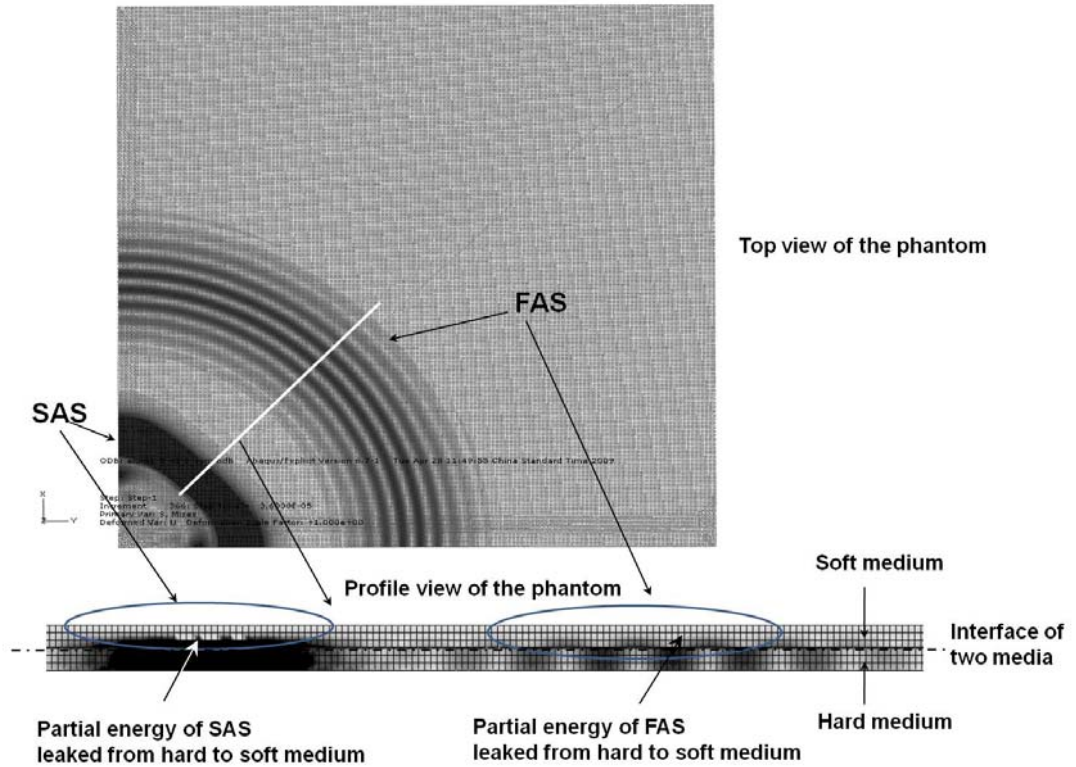


**Fig. 5.14.** Stress field as a result of wave propagation in phantom (Sample No. 6#) coupled with a layer of ASR 3.4 mm in thickness, showing that energies associated with both FAS and SAS leak from hard to soft medium (note: for convenience of comparison, the displayed stress fields in the soft and hard media are not of the same scale; the darker the greyscale the higher the stress)

## 5.4.2 Influence of Elastic Properties of Coupled Soft Media

Layers of ASR with different elastic moduli (2.89 ~ 536 kPa) but the same thickness (3.4 mm) were examined (Samples No. 12#–22#). Different elastic moduli of ASR were used with the aim of mimicking different pathological conditions of human soft tissues, such as scars and burns, which manifest different elastic properties. By

varying the elastic moduli of ASR, variations in the propagation velocities of FAS and SAS and variations in their peak energy magnitudes, subject to the elastic modulus of the coupled ASR layer, are diagrammed in Figs. 5.15 and 5.16, respectively. As observed, the existence of ASR modulates both wave modes: the propagation velocities of both drop immediately upon the introduction of ASR and then stabilise despite further increase in the elastic modulus of ASR; but the peak energy magnitudes of both modes are continuously attenuated as the modulus increases.

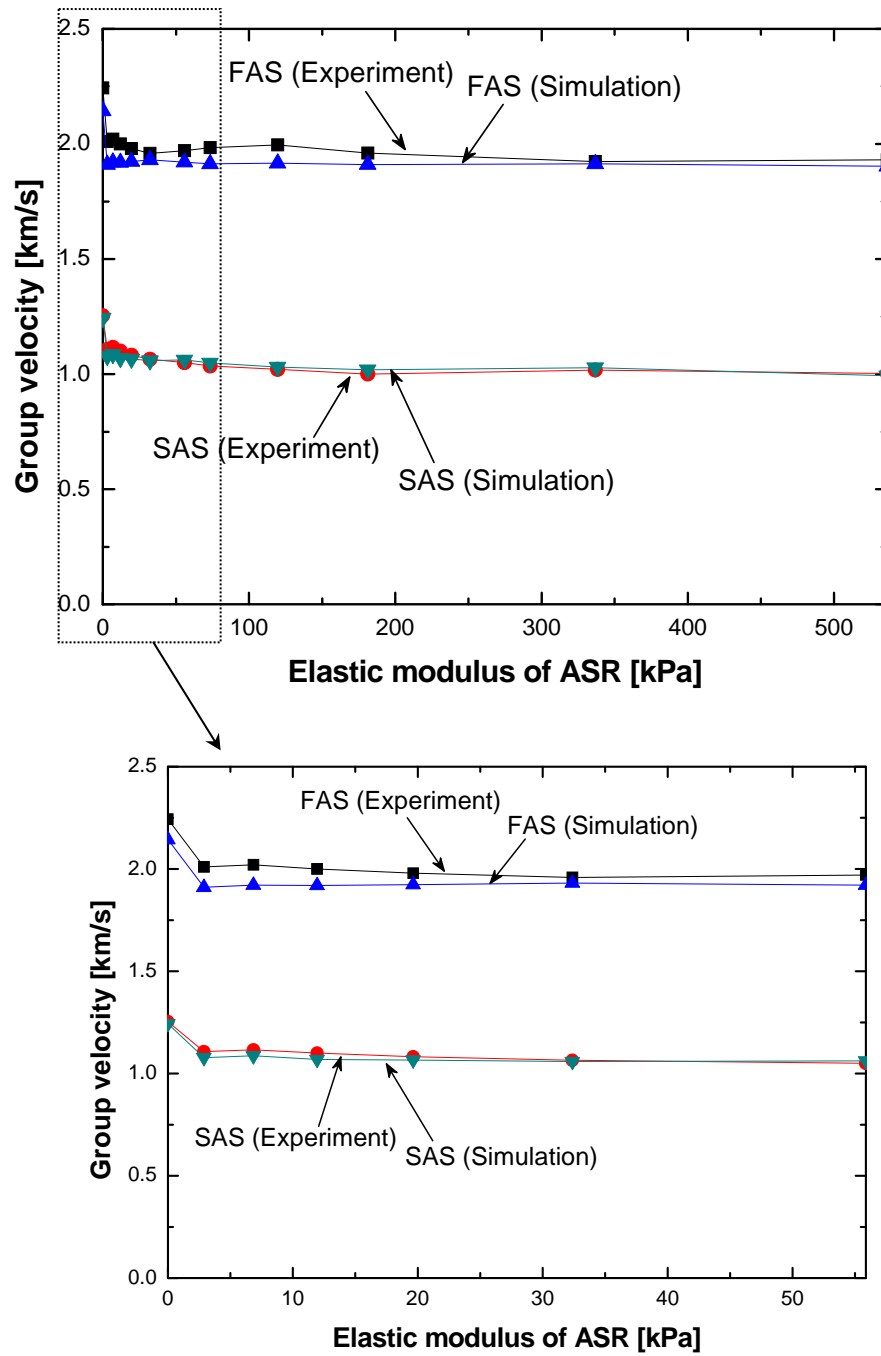


**Fig. 5.15.** Group velocities of FAS and SAS in phantoms (Samples No. 12#–22#) obtained through simulation and experiment vs. elastic modulus of the coupled ASR layer (excitation frequency: 75 kHz).

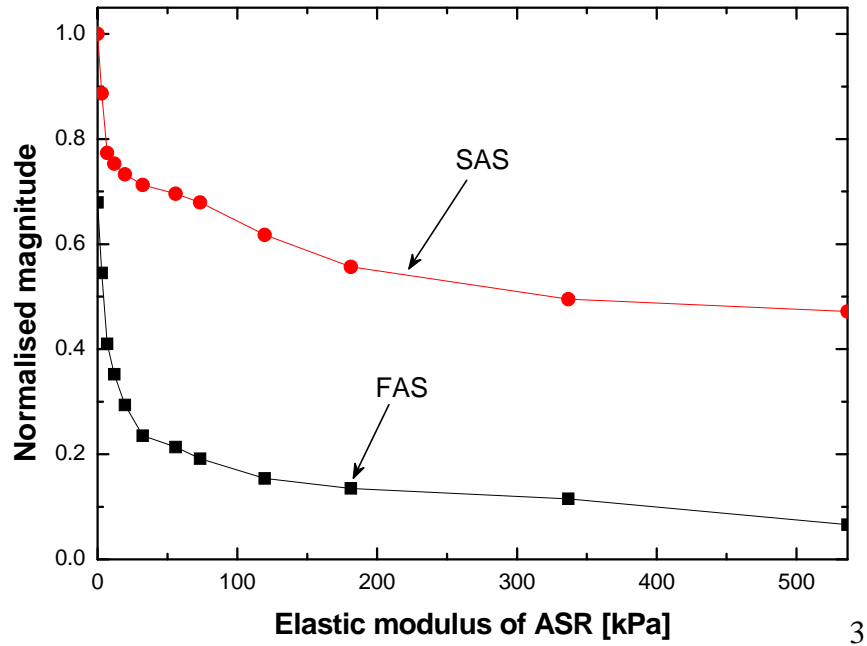
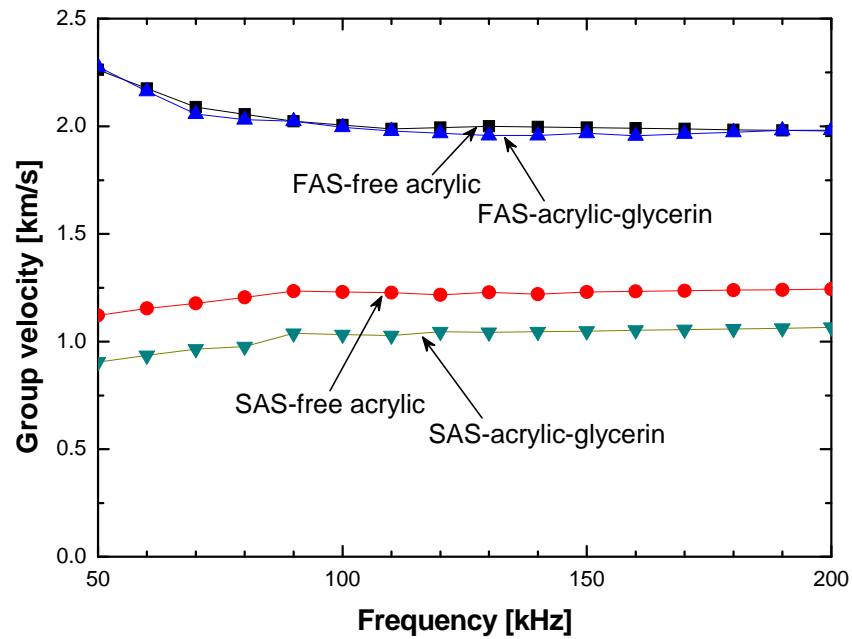


**Fig. 5.16.** Magnitudes of FAS and SAS in phantoms (Samples No. 12#–22#) vs. elastic modulus of coupled ASR layer (excitation frequency: 75 kHz; signal magnitude normalised relative to amplitude extremum of signal in No. 3# sample)

## 5.5 Discussion

To investigate the dependence of the propagation velocities of two wave modes on the excitation frequency of the diagnostic signal, FAS and SAS were activated in a sweep frequency range from 50 to 200 kHz to propagate in the synthesised bone phantoms. The dispersion curves of two modes obtained in the absence and presence of a soft medium (either a layer of 98% glycerin 4 mm in thickness or a layer of ASR 3.4 mm in thickness, as two typical cases) are plotted in Figs. 5.17 and 5.18. The results reiterate that the coupling effect of a soft medium on FAS and SAS exists across the whole frequency range measured: a fluid-like medium (98% glycerin) has little

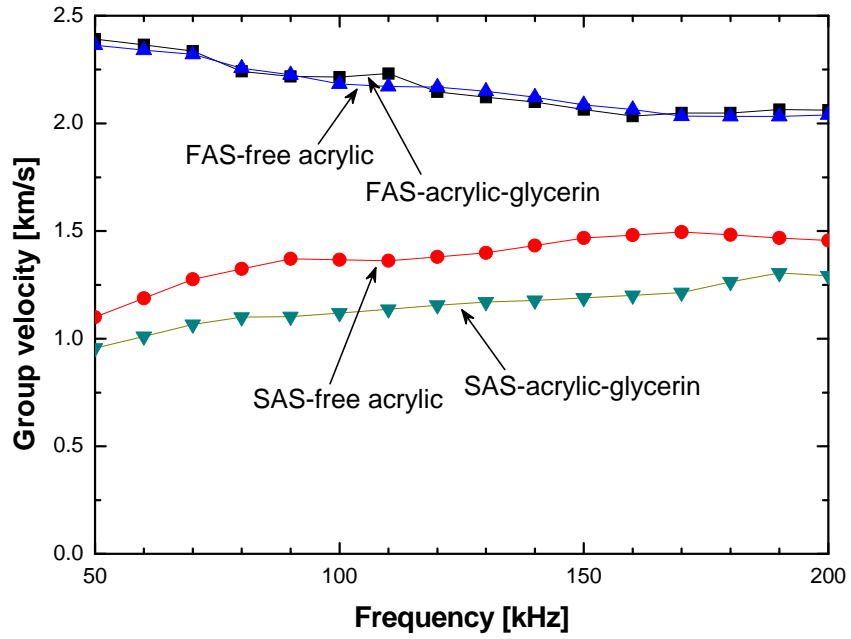
impact on FAS, but significant impact on SAS as a result of inability to sustain shear (in-plane) wave propagation; in contrast, ASR exerts a strong coupling influence on both wave modes.



(a)

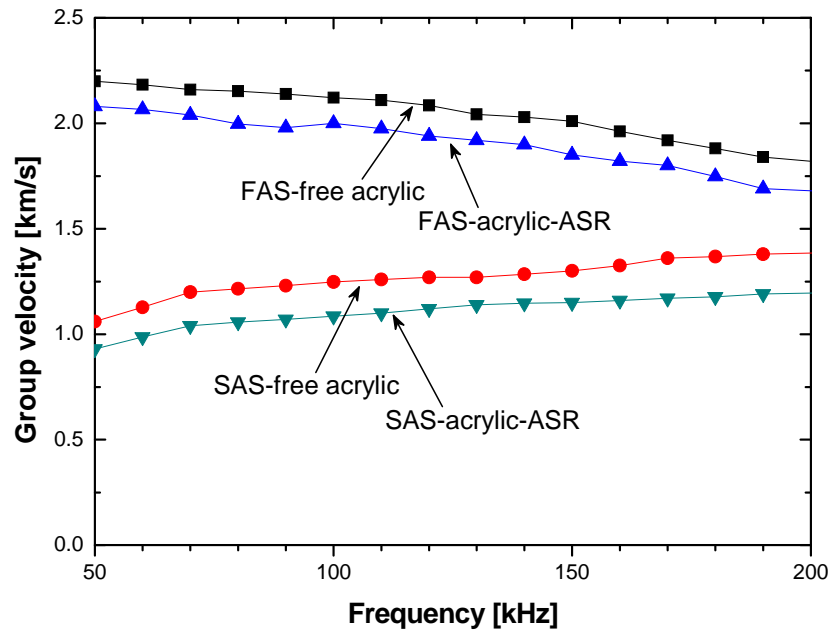
**Fig. 5.17.** Dispersion curves of FAS and SAS in phantoms in the absence (Sample No. 1#) and presence of a layer of 98% glycerin 4 mm in thickness (Sample No. 2#) obtained through

(a) 3D FE simulation and (b) experiment



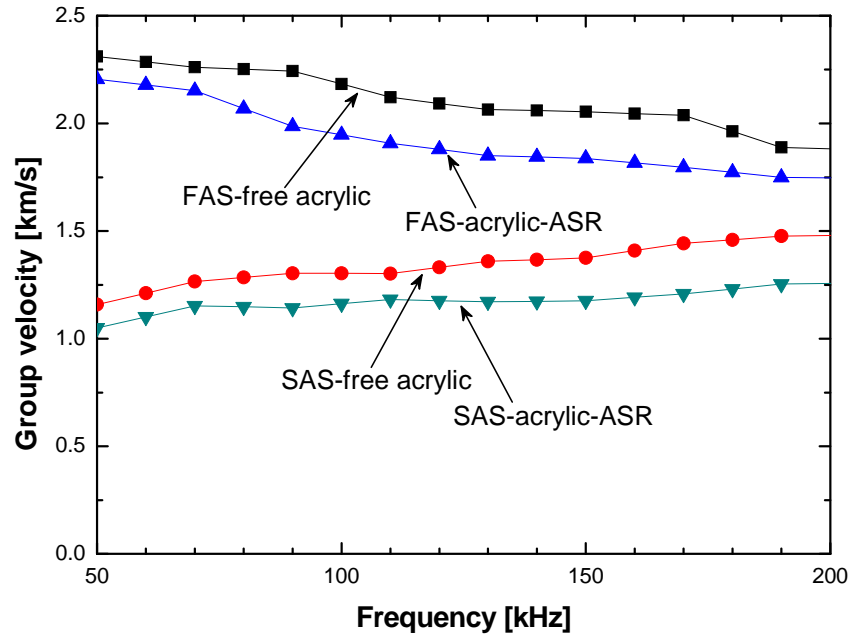
(b)

Fig. 5.17. Cont.



(a)

Fig. 5.18. Dispersion curves of FAS and SAS in phantoms in the absence (Sample No. 3#) and presence of a layer of ASR 3.4 mm in thickness (Sample No. 6#) obtained through (a) 3D FE simulation and (b) experiment



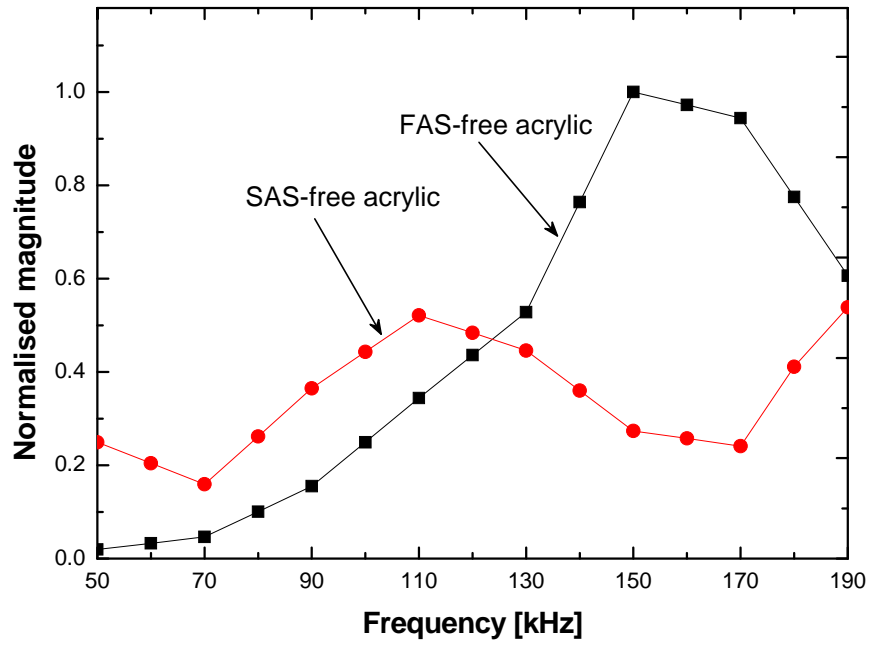
(b)

**Fig. 5.18.** *Cont.*

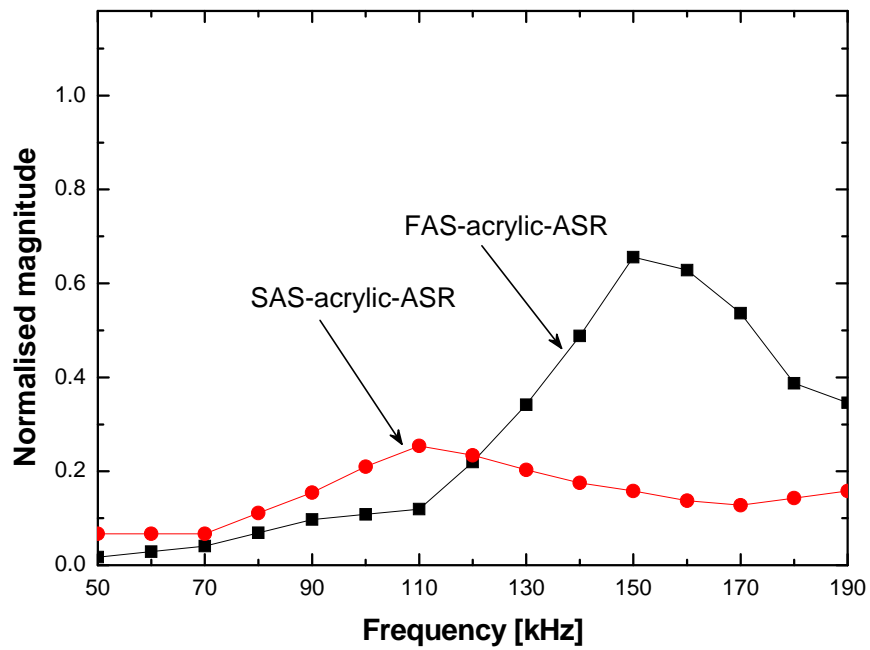
As discussed earlier when developing the 3D FE modelling simulation technique (Section 5.2.1), ASR, a sort of TEM, is often described as a linear, elastic and isotropic solid at relatively low excitation frequencies (<100 kHz), with the purpose of canvassing the characteristics of ultrasonic waves in it. In this work, the majority of the simulation was carried out at 75 kHz, with ASR simulated using brick elements having linear, isotropic and elastic properties. As seen in Figs. 5.17 and 5.18 in which higher frequencies up to 200 kHz were explored, the results from simulation and experiment were in good agreement, demonstrating the applicability and feasibility of the developed modelling and simulation technique for studying ultrasonic waves in a frequency range up to 200 kHz.

In the 3D FE simulation and experiment it was also found that FAS and SAS at

different excitation frequencies had different shares of the overall signal energy, *i.e.*, different wave mode dominance. The magnitudes of the two wave modes measured *in vitro* in synthesised phantoms in the absence and presence of a layer of ASR (3.4 mm in thickness as an example), subject to excitation frequency, are displayed in Fig. 5.19, in which it is observed that (i) FAS achieves dominance in the overall signal energy at 150 kHz, but SAS is dominant at 100 kHz; (ii) the existence of a coupled soft medium does not shift resonant frequencies (at which a particular wave mode reaches its maximum in signal magnitude), by comparing Figs. 5.19(a) and (b). This can be helpful in clinical practice to select the most optimal excitation frequency so as to achieve an improved SNR for a preferred wave mode.



(a)



(b)

**Fig. 5.19.** Magnitudes of FAS and SAS in (a) a phantom in the absence of soft medium (Sample No. 3#) and (b) a phantom in the presence of a layer of ASR 3.4 mm in thickness (Sample No. 6#) vs. excitation frequency (signal magnitude normalised relative to amplitude extremum of the signal in No. 3# sample at excitation frequency of 150 kHz)

Throughout the data the most prominent modulations arising from a coupled soft medium on the propagation velocities of FAS or SAS take place when the soft medium is initially introduced, and there is no marked discrepancy in that modulation with different thicknesses of the soft medium (Figs. 5.9 and 5.12). This implies that the surrounding soft tissues exert a perceptible influence on the speed of ultrasonic Lamb waves in a confined area only, making it possible to extend the compensation for such an influence at a specific thickness of the soft medium to general cases, if propagation velocity alone is of concern in bone assessment. Nevertheless, a continuous and increasing modulation of signal magnitude is seen with an increase in thickness (Fig. 5.13) or elastic properties (Fig. 5.16) of ASR. This result implies that rectification for such a coupling effect is case-dependent and compensation should be applied according to the calibrated relationships between changes in signal magnitude and changes in soft medium (Figs. 5.13 and 5.16) if signal magnitude is also a factor in bone assessment.

## 5.6 Concluding Remarks

Ultrasonic transverse wave modes, in particular the lowest anti-symmetric Lamb wave mode, SAS (*i.e.*,  $A_0$ ), have been increasingly preferred by the research and clinical communities to substitute for FAS for developing precision-enhanced QUS, due to their shorter wavelength in comparison with that of FAS and therefore their higher sensitivity to pathological degradation in bone. It is envisaged, however, that

these wave modes are sensitive to the presence and changes in surrounding soft tissues coupled with bone, manifesting characteristics distinct from those in free solids. This can impair the precision and accuracy of transverse wave-based QUS, potentially leading to erroneous diagnoses without appropriate rectification. This chapter sought a quantitative insight into the coupling effect of soft tissues on the characteristics of different ultrasonic wave modes in synthesised soft tissue-bone phantoms. The results revealed that the influence of coupled soft tissues can be reflected in reductions, to different degrees, in propagation velocities and signal energy intensities of FAS and SAS, and such reductions are subject to the thickness and elastic properties of the soft tissues. This work confirms that the coupling effect of soft tissues on ultrasonic waves should be quantitatively taken into account when developing high-precision QUS.

# **CHAPTER 6      Coupling Effect of Soft Tissues on Lamb Waves in Synthesised Soft Tissue-bone Phantoms (*Tube Model*)**

## **6.1 Introduction**

In the previous chapter the coupling effect of soft tissues on Lamb waves in synthesised bone phantoms was investigated using plate models (acrylic plates coupled with 98% glycerin or ASR). However, real human long bones (e.g., radius or femur) are actually complex 3D tubular structures with irregular cross-sections at different axial locations. Bones are wrapped with soft tissues (e.g., muscles and skin) and filled with marrow. Under such a circumstance, waves propagating in the bone are cylindrical Lamb waves, whose characteristics were briefly introduced in Section 3.3. Disregarding this reality, most studies have hypothesised long bones to be flat plates, neglecting the curvature, and have used the simple theory of Lamb waves in flat plates, as did the previous chapter. However, it has been recognised that this plate theory is too simple for describing waves in real bone structures [74, 75]. To achieve faithful depiction of Lamb waves in tubular bones, the theory of cylindrical Lamb

waves [76-79] is employed to re-visit the effect of coupled soft tissues on wave propagation in synthesised bone phantoms, so as to approximate the reality. By that means enhanced precision is anticipated compared with that using the plate model. The 3D FE modelling and simulation, experiment approach and signal processing as developed in Chapter 5 are used in this investigation.

## **6.2 Fabrication of Synthesised Soft Tissue-bone Phantoms**

A series of acrylic tubes (inner diameter: 26 *mm*; thickness: 2mm; length: 260 *mm*) was prepared, and each was wrapped with a layer of ASR varying in thickness (Samples No. 2# - 8#, with constant elastic modulus of 11.96 kPa) and elastic modulus (Samples No. 9# - 19#, with constant thickness of 3.2 *mm*), as listed in Table 6.1, serving as soft tissue-bone phantoms. The production procedure for the ASR layers remained the same as that described in Section 5.2.1 for fabricating plate phantoms, and the evaluation of the mechanical properties of the ASR was the same as that introduced in Section 5.22. Each produced ASR layer was glued onto the surface of an acrylic tube using the glue water (Type 460) introduced in Section 5.2.1, wrapping the tube.

**Table 6.1.** Description of synthesised soft tissue-bone phantoms

Sample No.	Bone phantom	Soft-tissue phantom	Thickness of soft-tissue phantom [mm]	Bulk/elastic modulus of soft-tissue phantom [kPa]
1#	acrylic	Nil	0	$1.01 \times 10^2$ (air) (bulk modulus)
2#	<i>ditto</i>	ASR	2.1	11.96
3#	<i>ditto</i>	<i>ditto</i>	3.2	11.96
4#	<i>ditto</i>	<i>ditto</i>	4.5	11.96
5#	<i>ditto</i>	<i>ditto</i>	5.4	11.96
6#	<i>ditto</i>	<i>ditto</i>	6.4	11.96
7#	<i>ditto</i>	<i>ditto</i>	7.6	11.96
8#	<i>ditto</i>	<i>ditto</i>	9.3	11.96
9#	<i>ditto</i>	<i>ditto</i>	3.2	2.89
10#	<i>ditto</i>	<i>ditto</i>	3.2	6.86
11#	<i>ditto</i>	<i>ditto</i>	3.2	11.96
12#	<i>ditto</i>	<i>ditto</i>	3.2	19.65
13#	<i>ditto</i>	<i>ditto</i>	3.2	32.38
14#	<i>ditto</i>	<i>ditto</i>	3.2	55.87
15#	<i>ditto</i>	<i>ditto</i>	3.2	73.41
16#	<i>ditto</i>	<i>ditto</i>	3.2	119.62
17#	<i>ditto</i>	<i>ditto</i>	3.2	181.23
18#	<i>ditto</i>	<i>ditto</i>	3.2	336.87
19#	<i>ditto</i>	<i>ditto</i>	3.2	536.51

## 6.3 Dispersion Properties of Lamb Waves in Tube

As stated in Section 2.2.2, the characteristics of cylindrical Lamb waves in tubes are complex and difficult to interpret. To assist in the recognition of different cylindrical Lamb modes, the commercial software package *DISPERSE*<sup>®</sup> developed at Imperial College London, UK, was employed to obtain the dispersion curves of cylindrical Lamb waves in the acrylic tube, *i.e.*, Sample No. 1# (Table 6.1). The dispersion properties obtained facilitated the understanding of cylindrical Lamb waves in the synthesised tubular soft tissue-bone phantoms.

Figure 6.1 shows the dispersion curves calculated by *DISPERSE*<sup>®</sup> for a tube (outer

diameter: 30 mm; thickness: 2 mm). The behaviour of cylindrical Lamb waves in the tube is remarkably different from that of their counterparts in a plate. In the frequency range from 80 kHz and 260 kHz there are five cylindrical Lamb modes,  $L(0,2)$ ,  $F(1,3)$ ,  $L(0,1)$ ,  $F(1,1)$  and  $F(1,2)$ . In terms of propagation velocity, these wave modes can be categorised into two groups: a high-velocity group, including  $L(0,2)$  and  $F(1,3)$ , and a low-velocity group, including  $L(0,1)$ ,  $F(1,1)$  and  $F(1,2)$ . In each group, the modes exhibit very similar propagation velocities. This can cause difficulty in mode recognition, and the observed signals might result from the contribution of more than one wave mode, for example, the FAS in a captured signal might be the superposition of  $L(0,2)$  and  $F(1,3)$ .

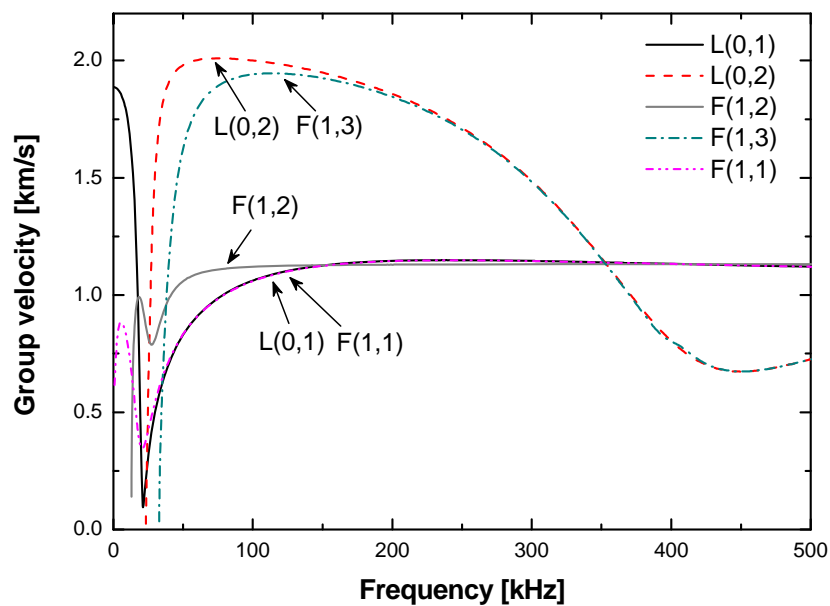
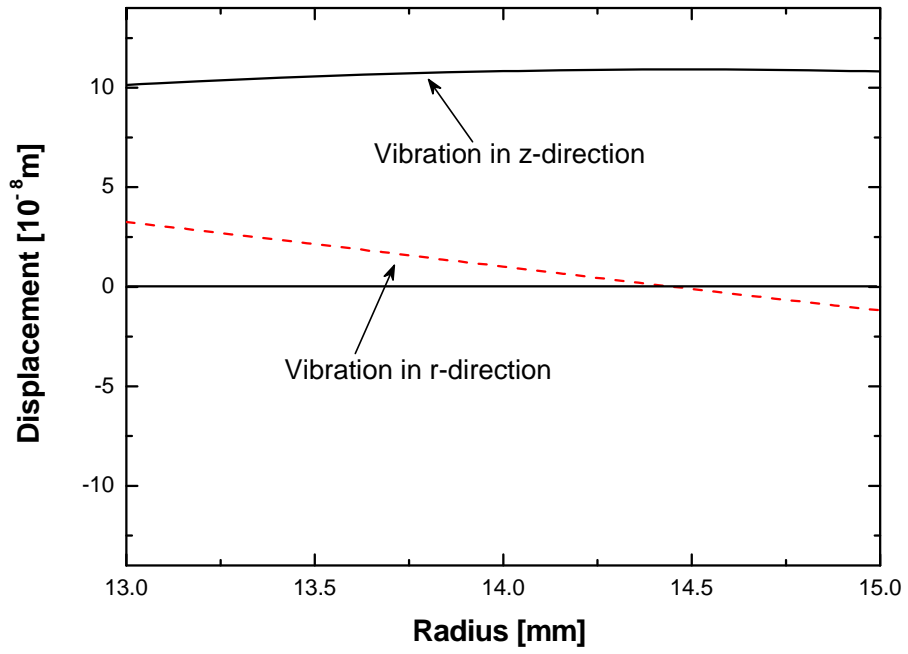


**Fig. 6.1.** Dispersion curves of cylindrical Lamb waves at frequencies from 0 to 500 kHz  
calculated by *DISPERSE*<sup>®</sup>

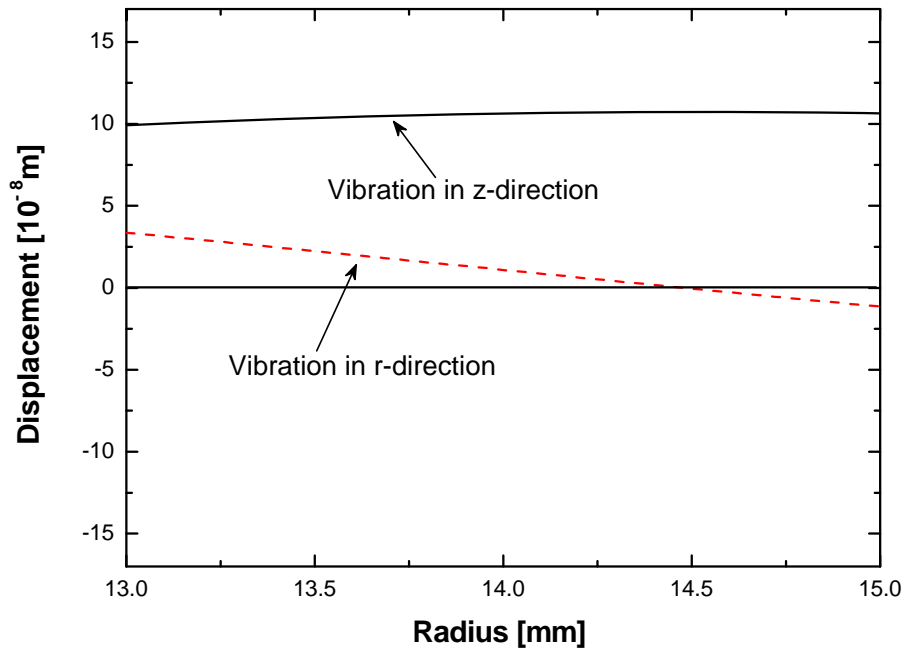
Figure 6.2 shows the calculated mode shapes of the abovementioned five cylindrical

Lamb modes at an excitation frequency of 100 kHz using the same software. As seen from Figs. 6.2(a) and (b), the modes in the high-velocity group have similar mode shapes, and their particles vibrate predominantly in the  $z$  – *direction*, *i.e.*, out-of-plane direction, referring to Fig. 6.3 for the coordinate system), like the  $S_0$  mode in a plate. This may indicate that the FAS is the contribution of both  $L(0,2)$  and  $F(1,3)$ . On the other hand, as seen in Figs. 6.2 (c) and (d),  $L(0,1)$  and  $F(1,1)$  have particulate vibrations predominantly in the  $r$  – *direction* (*i.e.*, in-plane direction, referring to Fig. 6.3 for the coordinate system), like the  $A_0$  mode in a plate ( $F(1,2)$  has much smaller particulate vibrations than those of  $L(0,1)$  and  $F(1,1)$ , and therefore may contribute little to SAS, as can be noticed from Figs. 6.2 (c), (d) and (e)).

The above results can help in the interpretation of observations in the following experiments and 3D FE simulations.



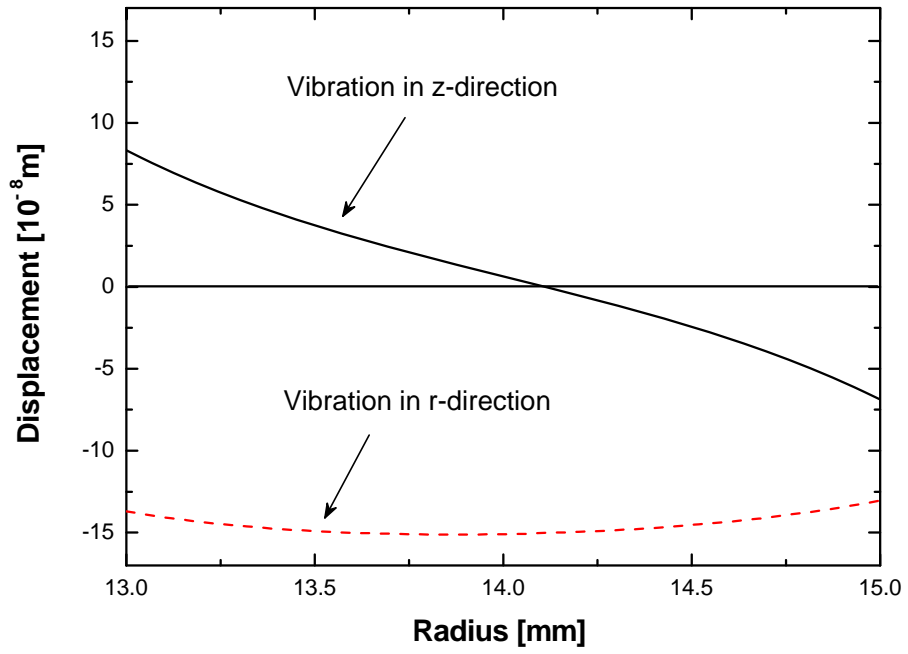
(a)



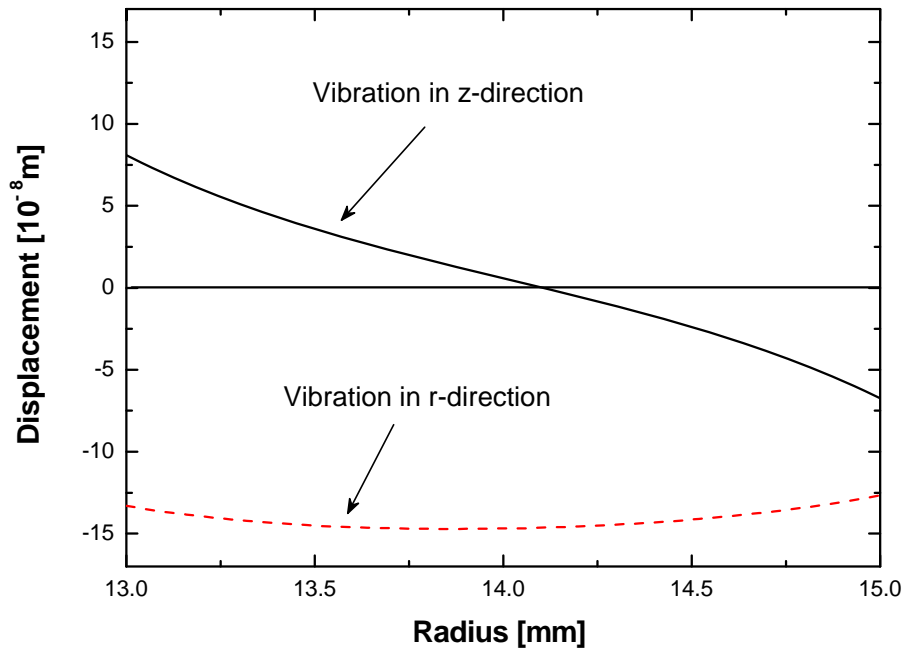
(b)

**Fig. 6.2.** Mode shapes of (a)  $L(0,2)$ , (b)  $F(1,3)$ , (c)  $L(0,1)$ , (d)  $F(1,1)$  and (e)  $F(1,2)$

calculated by *DISPERSE*<sup>®</sup>

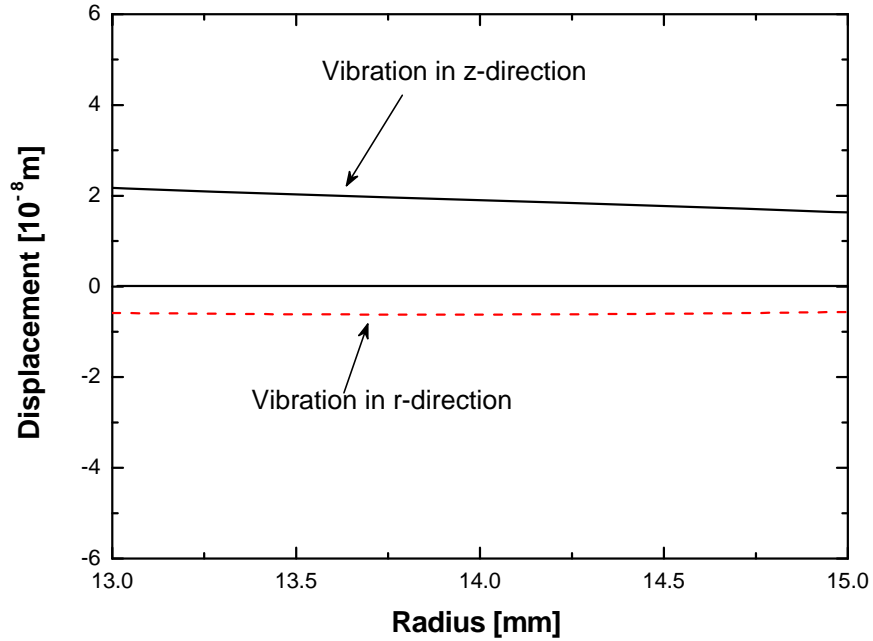


(c)



(d)

**Fig. 6.2.** *Cont.*



(e)

Fig. 6.2. Cont.

## 6.4 Analysis Method

The coupling effect of soft tissues on cylindrical Lamb waves propagating in synthesised phantoms was investigated via FE simulation and experiment.

### 6.4.1 3D FE Modelling and Simulation

Consider any sample from Samples 2#–19# listed in Table 6.1, supported on its two ends. Both the acrylic tube and ASR were simulated using 3D eight-node brick solid elements. Again, in a relatively low frequency range (<100 kHz), the ASR could be modelled as a linear elastic and isotropic solid, as described in Section 5.2.2. The interface between the ASR and acrylic tube was simulated using the ‘TIE’ constraint

introduced in Section 4.2.1. A series of five-cycle *Hanning* window-modulated sinusoid tonebursts at central frequencies from 100 kHz to 260 kHz was activated and captured with the transmitter model and the receiver model, respectively, as elaborated in Section 4.2.1. The above modelling and simulation were repeated for all the samples of different thicknesses and elastic moduli, as listed in Table 6.1.

## **6.4.2 Experimental Validation**

In parallel to FE simulation, experiment was conducted at room temperature for all the samples listed in Table 6.1. A pair of waterproof immersion transducers as described in Section 4.2.2, serving respectively as wave transmitter and receiver to generate and collect cylindrical Lamb wave signals, was collocated in tandem at the interface of the tube and the ASR, clamping the coupled ASR layer in the axial direction, as illustrated in Fig. 6.3. Note that in order to explore the medium coupling effect on Lamb waves in bone phantom, the transducer pair was positioned in tandem at the interface between the acrylic tube and ASR layer rather than on the ASR layer, which is different from real clinical applications of QUS. To obtain good mechanical and acoustical coupling between the ultrasonic transducers and acrylic tubes, each transducer was placed on a wedge made of acrylic (Fig. 6.3). One surface of the wedge had the same curvature as that of the tube, as seen in the insert of Fig. 6.3, enabling them to be in close contact with the curved surface of the tube. By that means, the transducer-generated waves could be transmitted efficiently into the tube

through the wedge. Both transducers were instrumented with a signal generation/acquisition system developed on a *VXI* platform [121] as introduced in Section 4.2.2.

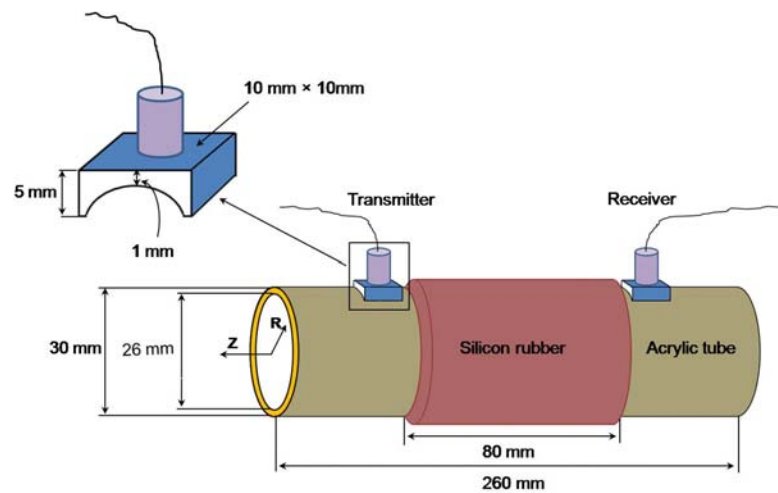


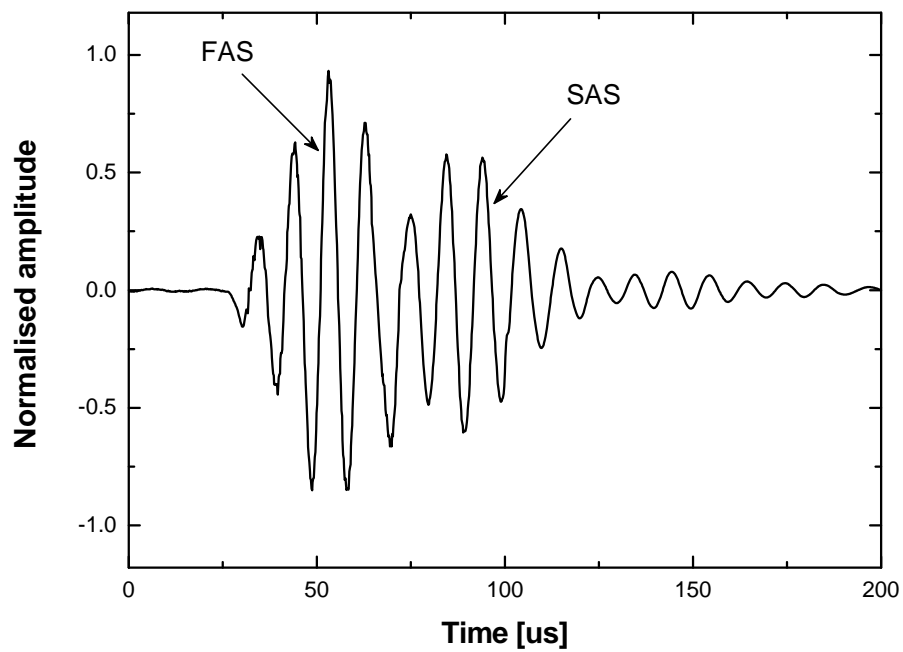
**Fig. 6.3.** Schematic of experimental setup (wedge between transducer and tube is zoomed in)

(distance of transmitter and receiver is 108 mm)

## 6.5 Results and Discussion

As a representative example, Fig. 6.4 presents a raw signal experimentally captured from the No. 1# sample at an excitation frequency of 100 kHz and its HT-processed result. From Figs. 6.4(a) and (b), two wave packages can clearly be observed, corresponding to the FAS and SAS, with velocities around 2010 m/s and 1100 m/s, respectively. By referring to the dispersion curves of cylindrical Lamb waves in a tube (Fig. 6.1) obtained previously, the FAS can be attributed to the superposition of  $L(0,2)$  and  $F(1,3)$ , whereas the SAS represents the combination of  $L(0,1)$  and

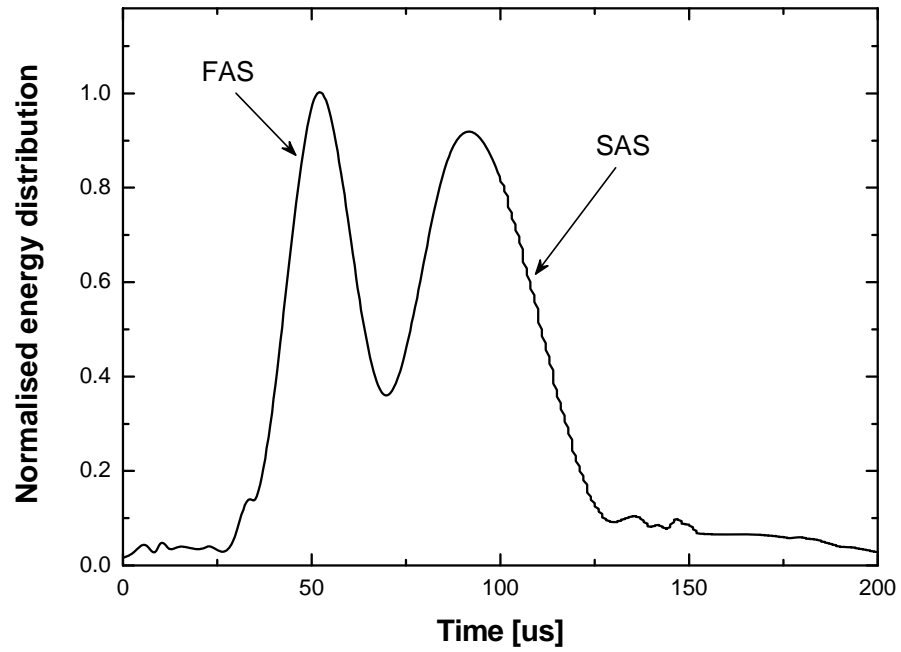
$F(1,1)$  (as discussed above,  $F(1,2)$  has much smaller particulate vibrations than those of  $L(0,1)$  and  $F(1,1)$ , and therefore contributes little to SAS). However, because of their very similar velocities it is extremely difficult to separate individual wave modes from the captured signal.



(a)

**Fig. 6.4.** Signals captured from a free acrylic tube at an excitation frequency of 100 kHz: (a)

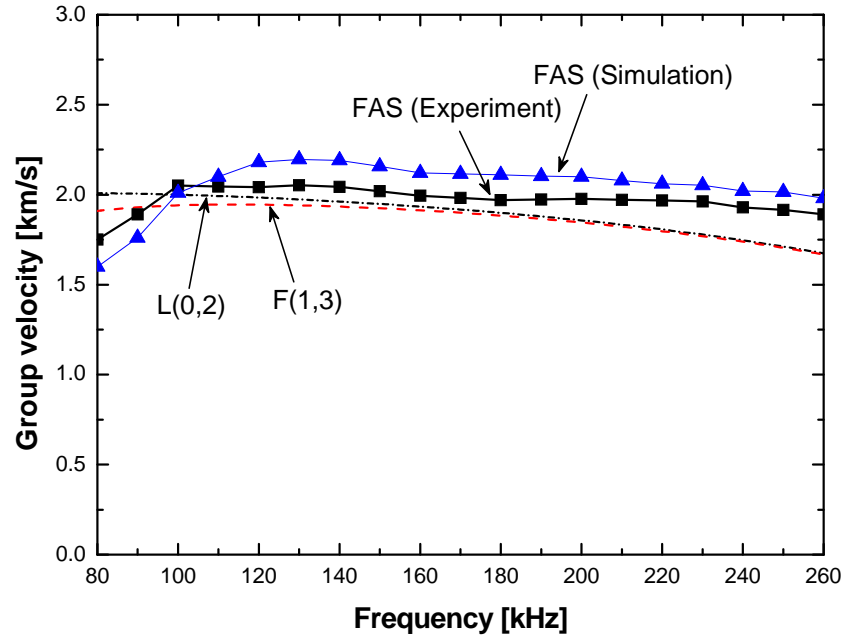
time domain signal and (b) HT-processed result of signal in (a)



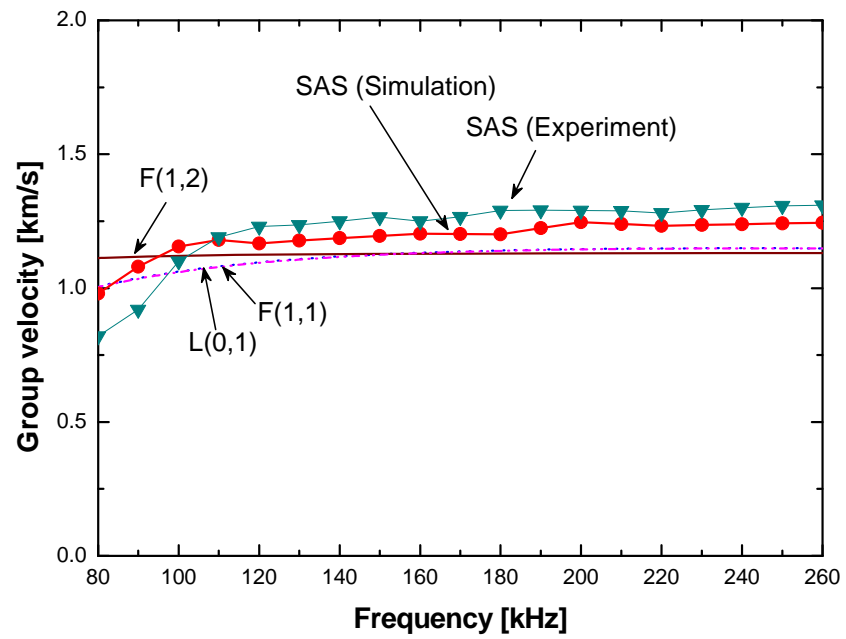
(b)

Fig. 6.4. *Cont.*

Figure 6.5 displays the experimentally and numerically obtained dispersion curves of cylindrical Lamb wave propagating in Sample No. 1#. The results of FE simulation and experiment in the frequency region concerned show satisfactory consistency. In addition, the results in Fig. 6.5 also include those calculated by *DISPERSE*<sup>®</sup>. It can be seen that the FAS obtained from experiment and FE simulation is comparable to  $L(0,1)$  and  $F(1,3)$  calculated by *DISPERSE*<sup>®</sup>, and the SAS is comparable to  $L(0,1)$ ,  $F(1,1)$  and  $F(1,2)$ .



(a)

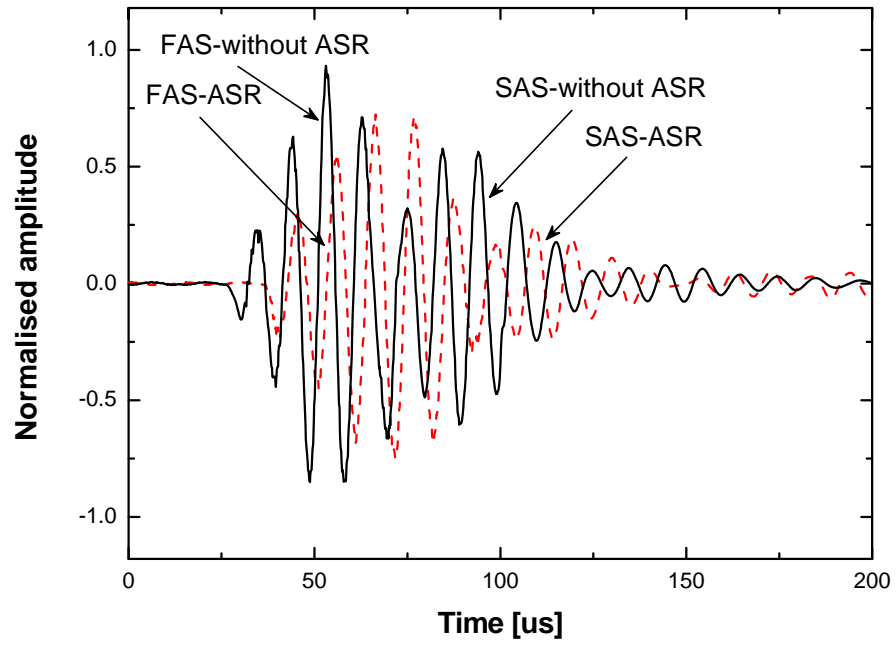


(b)

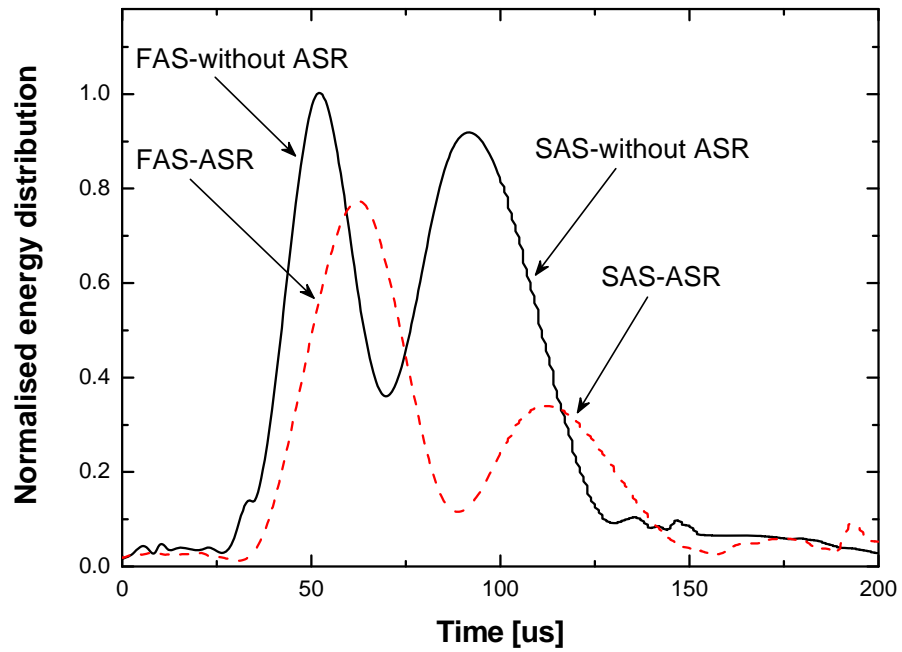
**Fig. 6.5.** Dispersion curves of (a) FAS and (b) SAS captured from No. 1# Sample via experiment and FE simulation (for comparison, wave modes calculated by *DISPERSE*<sup>®</sup> are also included in the figures, labelled  $L(0,2)$  and  $F(1,3)$  in (a);  $F(1,2)$ ,  $L(0,1)$  and  $F(1,1)$

in (b))

Figure 6.6 displays the raw and HT-processed signals captured from the synthesised samples in the absence (Sample No. 1#) and presence (Sample No. 3#) of a layer of ASR at an excitation frequency of 100 kHz. It can be seen that the presence of a layer of ASR has a significant effect on both FAS and SAS: (i) the arrival times of both modes are delayed in Sample No. 3# compared with their counterparts in Sample No. 1#, as a result of the reduced propagation velocity; (ii) the signal intensities of both FAS and SAS decrease when the ASR is introduced, and the amplitude of SAS has a greater reduction than that of FAS. This greater reduction can be attributed to the out-of-plane vibration pattern of  $L(0,1)$  and  $F(1,1)$  (main components of wave modes in SAS, as addressed in Section 6.3), which makes it easier for the energy associated with the SAS to leak across the ASR-acrylic interface in comparison with the FAS which has dominant in-plane particulate vibration.



(a)



(b)

**Fig. 6.6.** Signals captured from an acrylic tube in the absence and presence of a layer of ASR at an excitation frequency of 100 kHz: (a) time domain signal and (b) HT-processed result of signal in (a)

The group velocities of the FAS and SAS in all the samples in the absence and presence of a layer of ASR of different thicknesses were obtained using the same approach as above, and are summarised in Fig. 6.7. It can be observed that the most significant changes in propagation velocity of the FAS and SAS take place at the initial introduction of the ASR, and the velocities fluctuate slightly with increase of the thickness of the ASR layer.

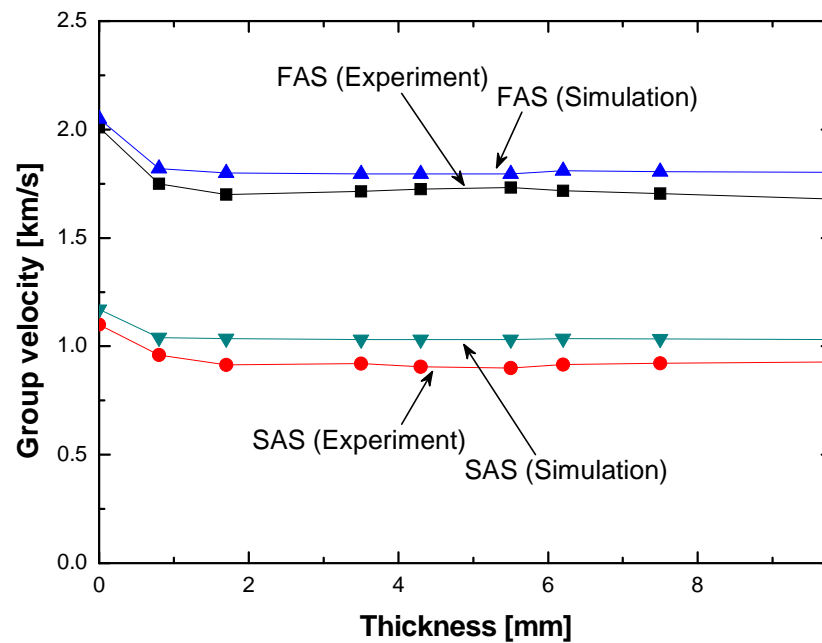


**Fig. 6.7.** Group velocities of FAS and SAS captured from an acrylic tube in the absence and presence of a layer of ASR of different thickness at an excitation frequency of 100 kHz

As elaborated in Section 5.4.2, apart from the thickness, changes in the properties (e.g., elastic modulus) of coupled media can also influence the propagation of Lamb waves in plate-like structures. This observation was checked again with tube-like structures. Using the same approach, the dependence of the group velocities of FAS

and SAS on elastic modulus of ASR was calibrated, and the results are shown in Fig. 6.8. Again, the most significant changes in the propagation velocities of the FAS and SAS occur upon the initial introduction of the ASR, whereas further change in the elastic modulus of the ASR does not prominently influence the characteristics of the FAS and SAS.

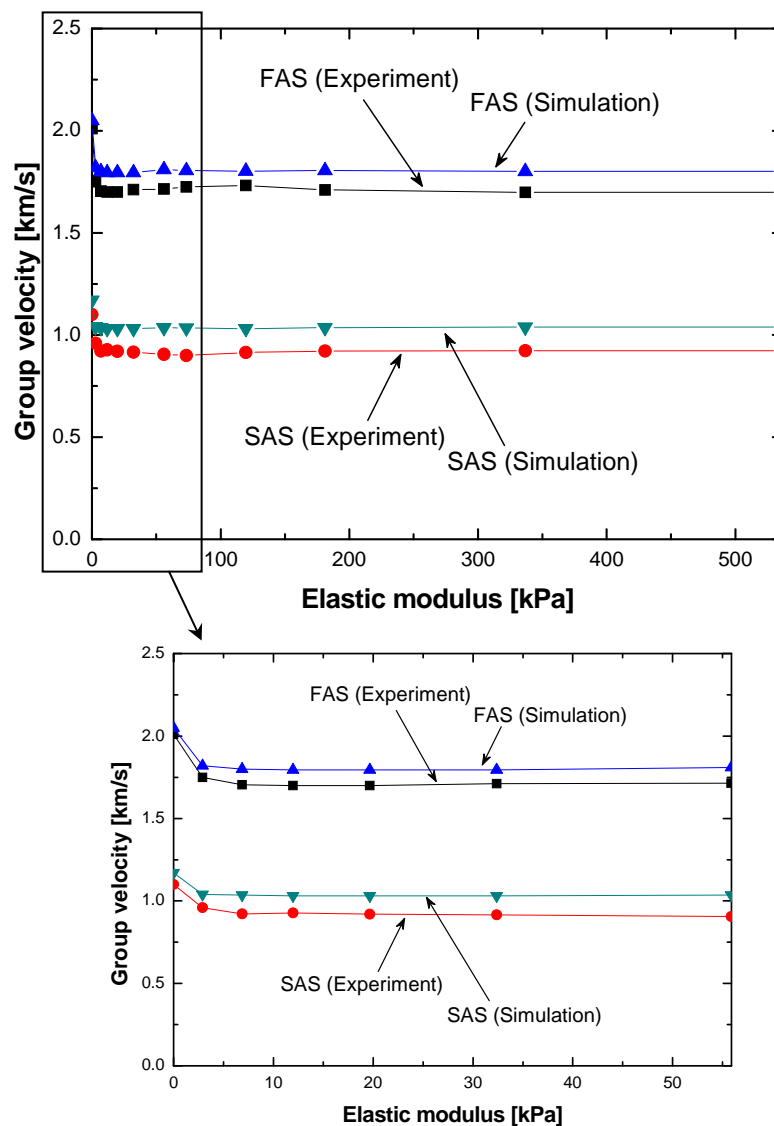
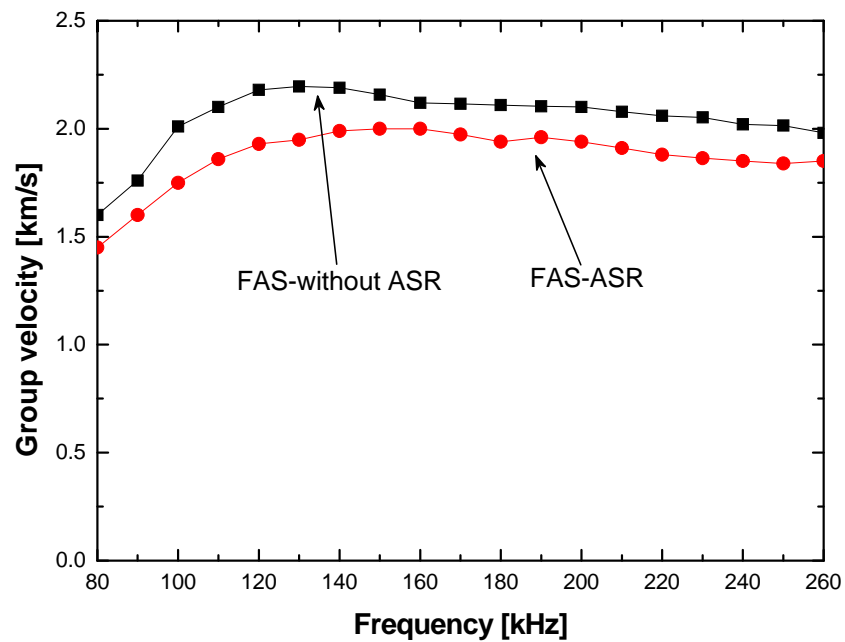


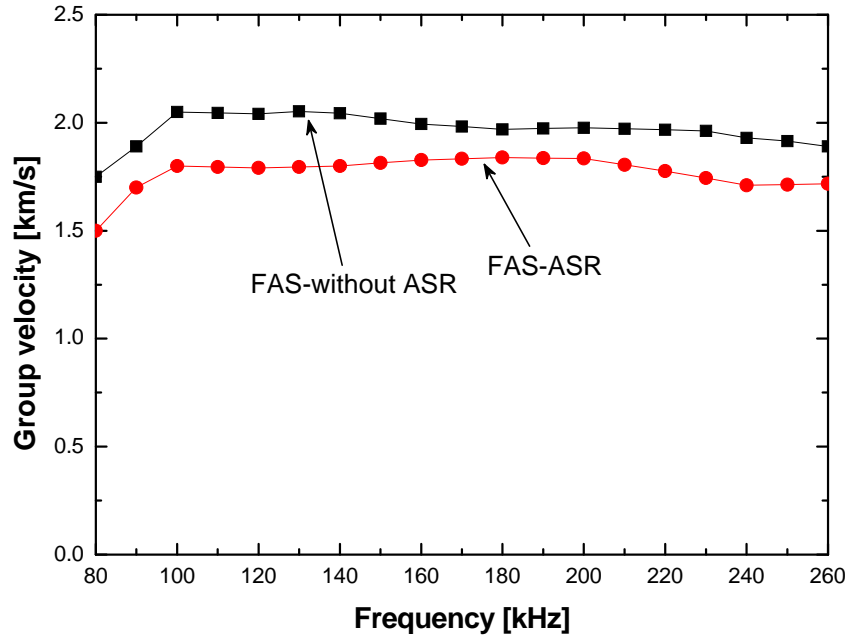
**Fig. 6.8.** Group velocities of FAS and SAS captured from an acrylic tube in the absence and presence of a layer of ASR of different elastic moduli at an excitation frequency of 100 kHz

By extending the above analysis to a frequency range from 80 to 260 kHz, Fig. 6.9 shows the numerically and experimentally captured dispersion curves in the absence and presence of a layer of ASR (Sample No. 3#). The same observation was achieved at all the discussed frequencies. Because the strain at the interface between the tube and the ASR is continuous in both out-of-plane and in-plane directions, the wave energy associated with the FAS and SAS in the tube can traverse the interface and leak into the ASR, pervading in the entire ASR-acrylic-coupled system. In turn, the propagation of both FAS and SAS can therefore be influenced.

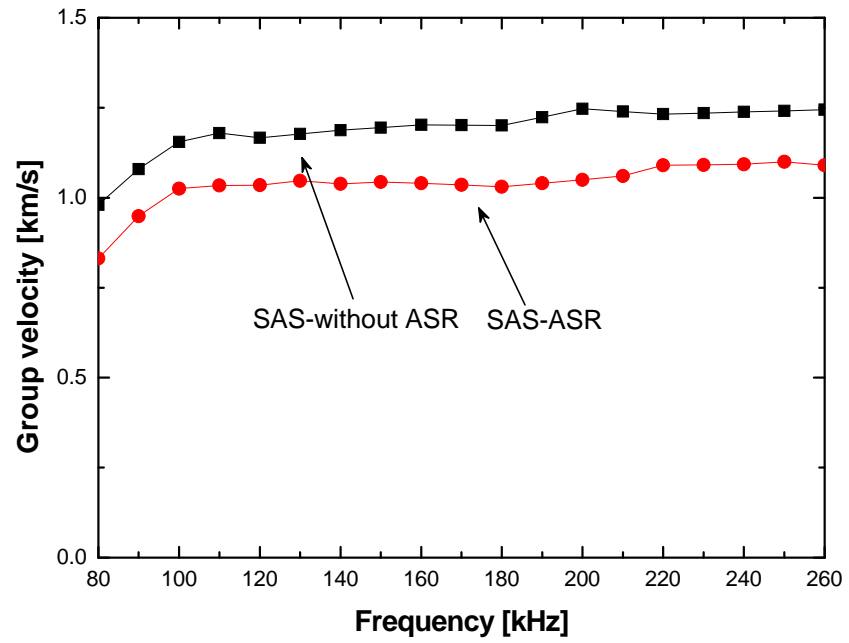


(a)

**Fig. 6.9.** Dispersion curves of ((a) and (b)) FAS and ((c) and (d)) SAS captured from an acrylic tube in the absence and presence of a layer of ASR ((a) and (c) FE simulation; (b) and (d) experiment)

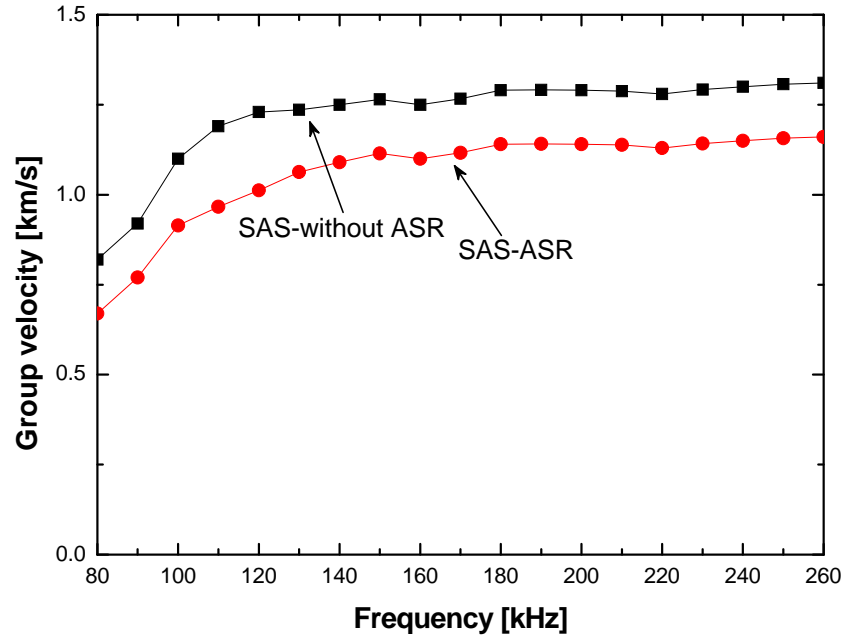


(b)



(c)

Fig. 6.9. Cont.

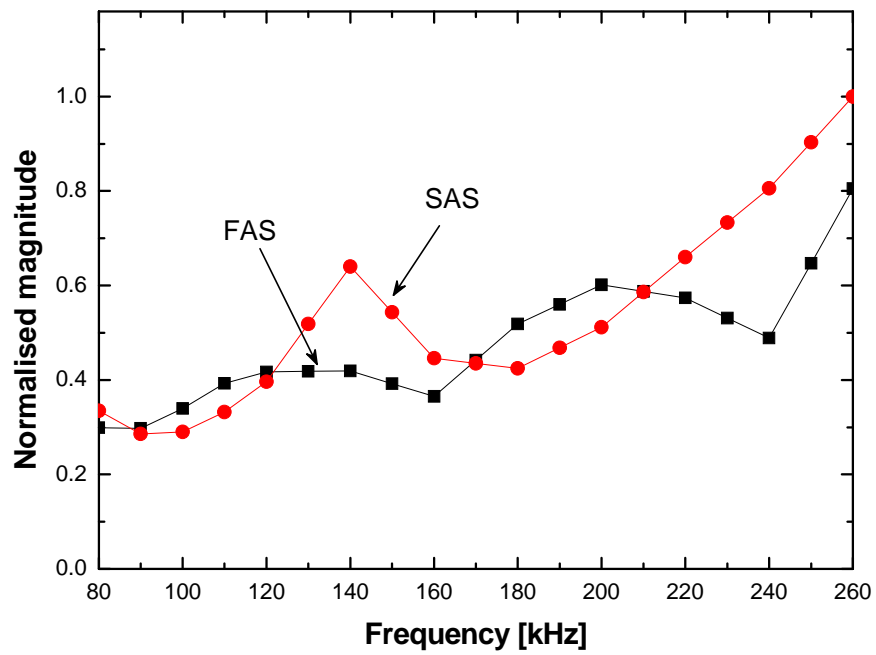


(d)

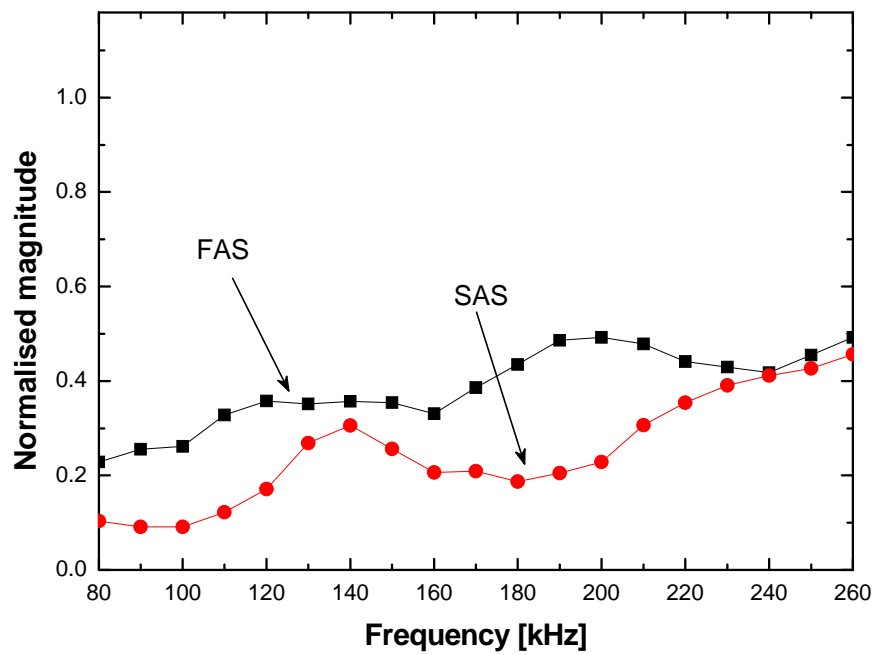
**Fig. 6.9.** *Cont.*

In the 3D FE simulation and experiment it was also found that the FAS and SAS at different excitation frequencies had different shares of the overall signal energy, *i.e.*, different wave mode dominance. The magnitudes of the two wave modes measured *in vitro* in synthesised phantoms in the absence and presence of a layer of ASR (Samples No. 1# and 3 #), subject to excitation frequency, are displayed in Fig. 6.10, in which it can be observed that (i) the energy peaks of the FAS and SAS change as the frequency increases; (ii) the presence of a layer of ASR significantly reduces the peak amplitudes of the FAS and SAS at each excitation frequency, as explicitly shown in Figs. 11(a) and (b); (iii) the existence of a coupled soft medium does not shift the characteristic frequencies (at which a particular wave mode reaches its maximum signal magnitude) (Fig. 11(a) and (b)). This last finding can be helpful in clinical practice to select the optimal excitation frequency so as to achieve an improved SNR

for a particular wave mode.

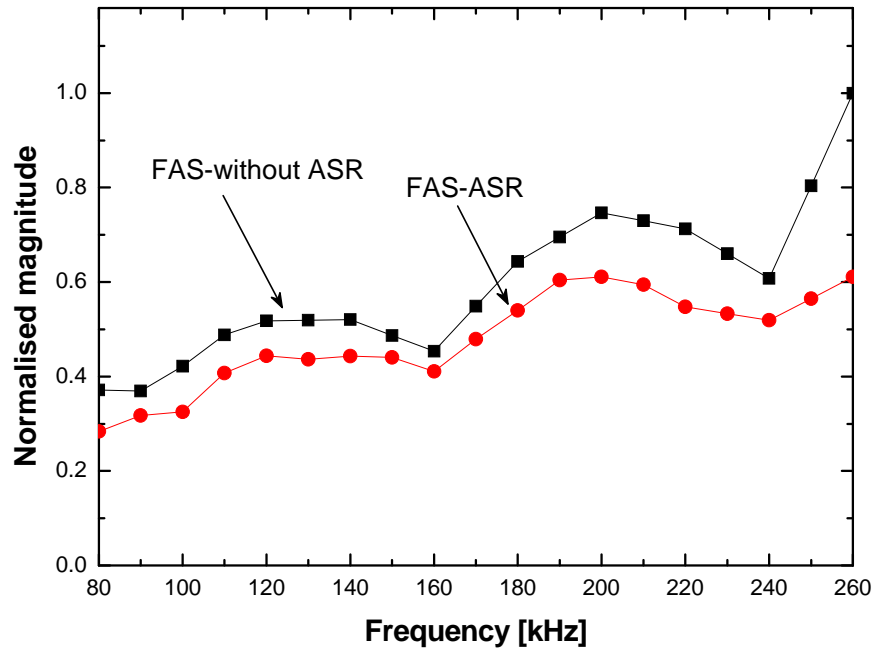


(a)

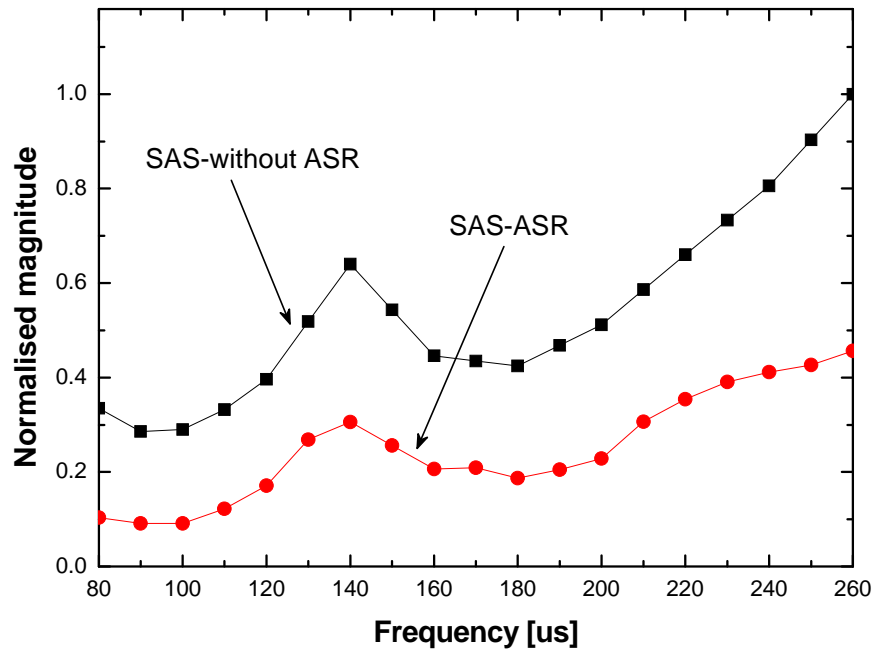


(b)

**Fig. 6.10.** Magnitudes of FAS and SAS captured from an acrylic tube in the (a) absence and (b) presence of a layer of ASR vs. excitation frequency



(a)



(b)

**Fig. 6.11.** Magnitudes of (a) FAS and (b) SAS captured from an acrylic tube in the absence and presence of a layer of ASR vs. excitation frequency

## 6.6 Plate Model vs. Tube Model

The effects of soft tissues on waves propagating in bone structures simulated using plate models and tube models were investigated in Chapter 5 and in this chapter, respectively. The results from both models highlighted that the effect imparted by surrounding soft tissues can modulate the propagation characteristics of ultrasonic waves in bones. The waves in both plate and tube exhibited prominent reductions in velocity when soft tissues were initially introduced, as observed in Figs. 5.16 and 6.9. Furthermore, the reductions in the velocities of the FAS and SAS were greater in the tube model than in the plate model, as shown in Table 6.2, indicating that the waves in the tube model were more sensitive to the coupling effect of soft tissue than those in the plate model. Such an observation in the current experimental configuration can be attributable to the difference in the thickness between the plate phantom and the tube phantom. The thickness of the plate is 3.2 mm, and that of the tube is 2 mm. Lamb waves in the tube are thus at a lower PFT comparing with those in the plate (both having the same excitation frequency of 100 kHz). Under such a circumstance, some wave modes, e.g., SAS, in the tube has stronger out-of-plane particulate vibration than that in the plate, which might result in higher sensitivity to the coupling effect on Lamb waves in the tube than that in the plate. In the future work, the issue concerning the coupling effect on waves in different structure models (e.g., plate, tube, *etc.*) will be explored.

**Table 6.2.** Relative reductions in velocities of FAS and SAS in phantoms coupled with ASR relative to those in free phantoms in terms of plate and tube models at excitation frequency of 100 kHz

Model	FAS	SAS
Plate	9.8%	11.7%
Tube	12.4%	16.8%

On the other hand, the FAS and SAS showed different wave mode dominance in signal intensity in the plate model and the tube model. For example, the FAS reached peak magnitude at 150 kHz in the plate model, compared with 120 kHz in the tube model, below 190 kHz. The peak magnitudes of the SAS in the plate and tube models were 110 kHz and 140 kHz, respectively. Compared with the results obtained from plate phantoms in Section 5.4, the above observations (obtained from tube phantoms) indicate a similar conclusion, namely that the coupling effect of soft tissues alters the characteristics (including velocity and amplitude) of Lamb waves. This finding also highlights the importance of choosing an appropriate model when the intensity of a particular wave is of interest. Considering that human bones are tube-like structures, it is recommended that the tube-like model described be used for the development of high-precision QUS.

## 6.7 Concluding Remarks

In this chapter, the coupling effects of soft tissues on the propagation of cylindrical Lamb waves in synthesised tube phantoms were investigated numerically and experimentally. The results showed that although variations in the thickness and elastic modulus of mimicked soft tissues did not prominently affect wave propagation, the initial introduction of mimicked soft tissues had a marked coupling effect on the characteristics of the FAS and SAS in the tube-like structure. These observations tally with those when a plate model was used, as reported in Chapter 5. Calibration and rectification of such a coupling effect therefore remain significant for clinical bone assessment, to be conducted in the next chapter.

# **CHAPTER 7      Application to Precision Enhancement of QUS-based Monitoring of Mimicked Healing Progress of Bone Fracture**

## **7.1 Introduction**

Bone fracture, a skeletal trauma, is common throughout populations of all ages, but particularly among the elderly. Monitoring of the healing progress of bone fracture at different stages is of vital importance to the application of appropriate therapy. In this regard, QUS using axial transmission measurement is one of the most cost-effective QUS implementations, by virtue of its intrinsic attributes such as being radiation-free and its capacity to provide rich information pertaining to bone properties, as introduced in Section 2.3.1. However, human bones have complex structures, in particular fractured bones, where the captured wave signals, whether FAS or SAS, encounter callus (a substance in the fractured region connecting bone fragments) when propagating across the fractured part. As a result the captured signals contain multiple wave components, making their interpretation a highly complex task. Under

such circumstances, most existing studies exploit the FAS which propagates the fastest in bone structures, because of the ease in differentiating it from other wave modes that arrive subsequently, and in linking changes in characteristics of the FAS to the healing progress of bone fracture. Studies have shown that the velocity of the FAS can reflect changes in the properties of callus at different bone healing stages [87, 129, 134]. As commented earlier, however, there has been increasing use of the SAS rather than the FAS for developing QUS techniques. The SAS has the advantage of higher sensitivity than the FAS to pathological degradation in bone, as a result of its shorter wavelength [16, 23-25].

It is envisaged that the coupling effect of surrounding tissues on ultrasonic waves is often ignored in clinical practice during QUS-based bone assessment, resulting in compromised accuracy of the assessment. This effect was systematically interrogated and quantitatively calibrated in Chapters 5 and 6, with the results having the potential to improve the diagnosis accuracy of QUS.

In this chapter, the feasibility of using the FAS and SAS for predicting different healing stages of bone fracture is demonstrated. Secondly, the role of the coupling effect of surrounding soft tissues in QUS when used for monitoring the healing progress of fracture is explored. The calibrated results of the effect achieved in Chapter 5 is then applied to enhance the precision of QUS when used to predict a particular healing stage of a mimicked fracture phantom under the influence of

overlying soft tissues.

## **7.2 Monitoring of Healing Progress of Mimicked Bone Fracture**

### **7.2.1 Preparation of Fractured Bone Phantoms**

The healing progress of bone fracture is customarily mimicked by dividing the progress into several stages, at each of which the callus features different material properties and geometric features in numerical simulation [19, 134]. A gap between two plates simulating two pieces of the fractured bone, with water filling the gap to mimic callus, is often used for simplicity in experimental work [133, 135, 136]. That procedure may be questionable, however, when applied to examining wave propagation in fractured bone, since the callus is not a pure fluid medium but a solid substance with the ability to sustain shear stress. In this chapter, to achieve a closer approximation of reality, ASR, as elaborated in Section 5.2.1, a type of *tissue equivalent material* (TEM), is used to replace the pure water used in conventional studies [9, 11], due to its close mechanical properties to the real substance in the fractured region, *i.e. callus*.

The fractured bone during the healing progress was imitated with a synthesised

phantom fabricated in accordance to the following steps:

- (i) two identical acrylic plates ( $230\text{ mm} \times 240\text{ mm} \times 3.2\text{ mm}$  each) were connected via an ASR strip. The ASR strip varied from 1 to 6 mm with an increment of 1 mm in width (the direction along the axial direction of the phantom), to mimic different healing stages of bone fracture, as shown schematically in Fig. 7.1. The ASR was prepared in line with the manufacturing procedures introduced in Section 5.2.1. The elastic modulus of the ASR strip was 2.8 MPa, close to that of the callus (initial connective tissue (ICT)) in a real fractured bone during its early healing stage (density:  $\rho_{ICT} = 1.05\text{ g/cm}^3$ , elastic modulus:  $E_{ICT} = 3\text{ MPa}$  [19, 87]).
- (ii) another intact acrylic plate ( $460\text{ mm} \times 240\text{ mm} \times 3.2\text{ mm}$ , without any mimicked callus) was benchmarked; and a pair of transducers was placed on the upper surface of the bone phantoms, as shown in Fig. 7.1.

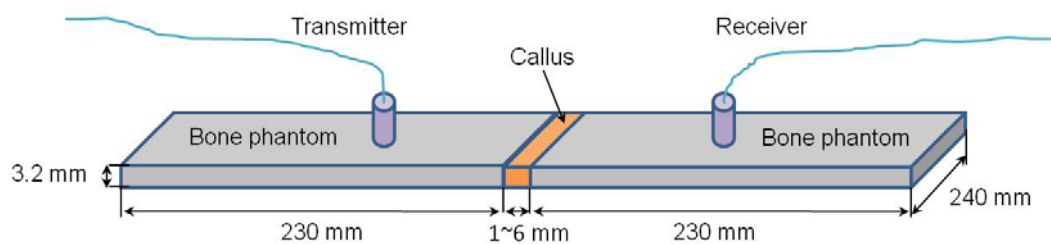


**Fig. 7.1.** Schematic of ultrasonic measurement of mimicked fractured bone phantom

The procedures of the fabrication and mechanical testing of the ASR for mimicking the callus were in accordance with those introduced in Sections 5.2.1 and 5.2.2,

respectively. The stress-strain relationship obtained from the mechanical test is shown in Fig. 7.2, indicating that the ASR fabricated for mimicking callus demonstrated approximately linear mechanical properties in the strain range of 0 - 10%.

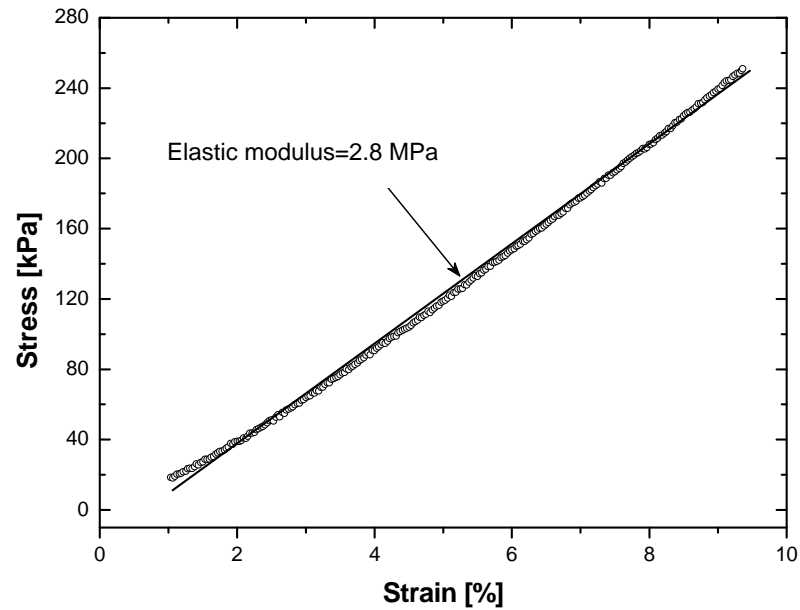
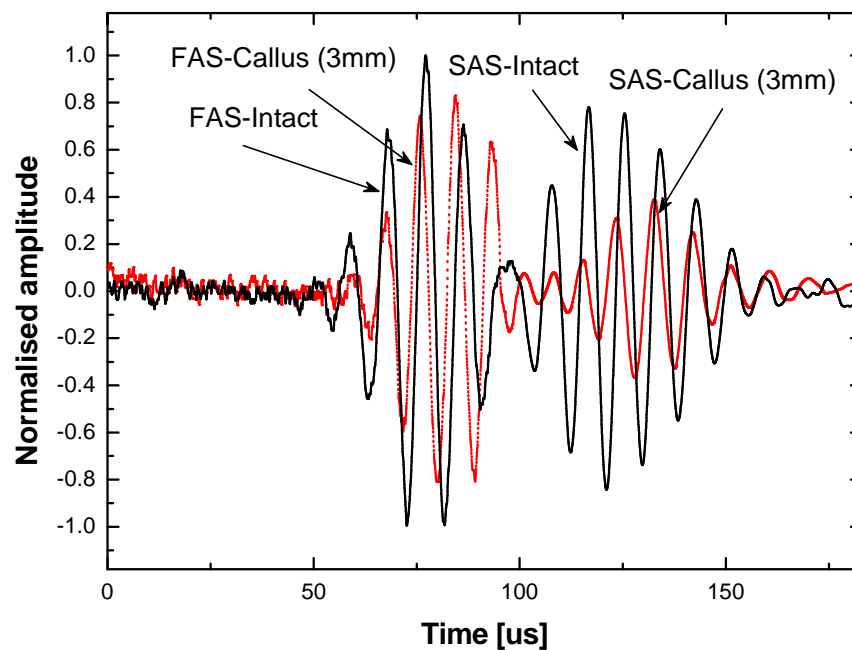


**Fig. 7.2.** Stress-strain relationship of ASR obtained from a mechanical compression test (open circles: experimental data; solid line: linear regression of experimental data)

## 7.2.2 Results and Discussion

Following application of the analysis methods developed and detailed in previous chapters (including 3D FE modelling and simulation, experiment and signal processing techniques), Fig. 7.3 presents as an example a raw signal captured in the bone fracture phantom when the width of the ASR strip (mimicking callus) is 3 mm at an excitation frequency of 100 kHz, and its HT-processed result. For comparison, its

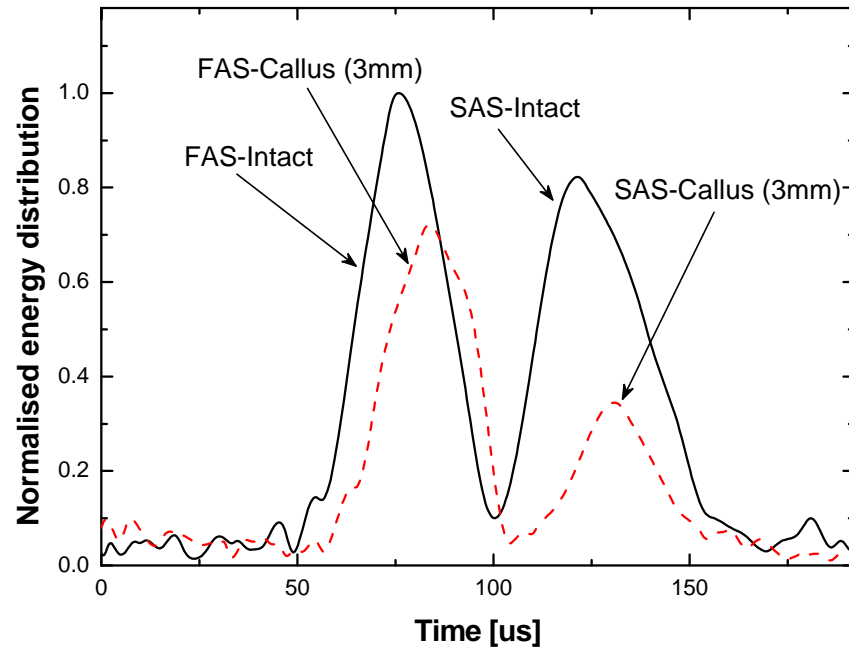
counterpart in an intact bone phantom (without callus) is also included in Fig. 7.3. The characteristics of both the FAS and SAS can be seen to be clearly different in the fractured phantom from those in the intact phantom. The signals (FAS and SAS) captured from the fractured bone phantom manifest a delay in arrival time (due to reduced propagation velocity) and a relative reduction in signal intensity when compared to those in the intact phantom. These changes can be attributed to the existence of callus (mimicked by ASR), which has significantly different acoustic properties from those of bone (mimicked by acrylic materials). As a result, the transmitted signals are substantially attenuated.



(a)

**Fig. 7.3.** Wave signals captured from an intact phantom and a fractured phantom with callus

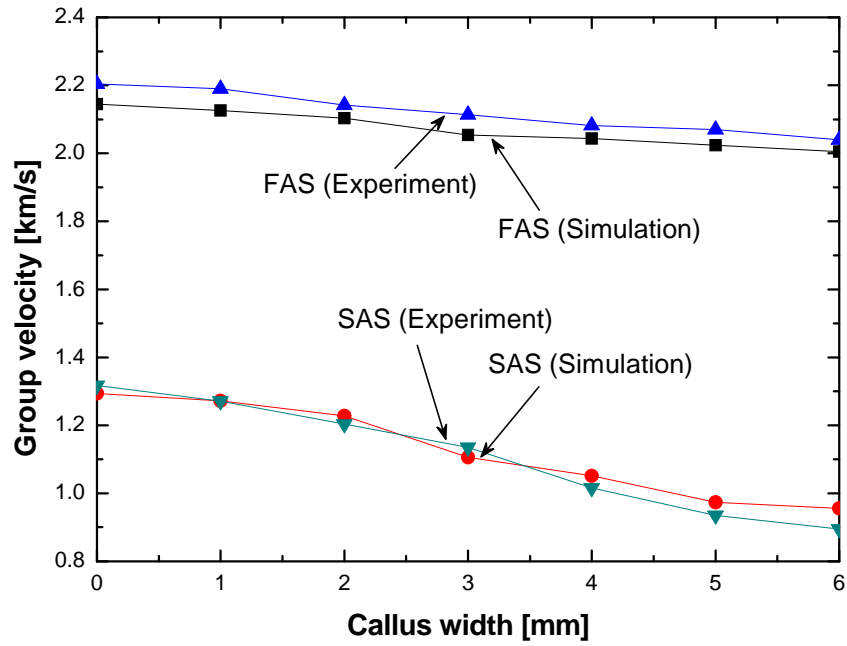
width 3 mm: (a) raw signals and (b) their HT-processed results



(b)

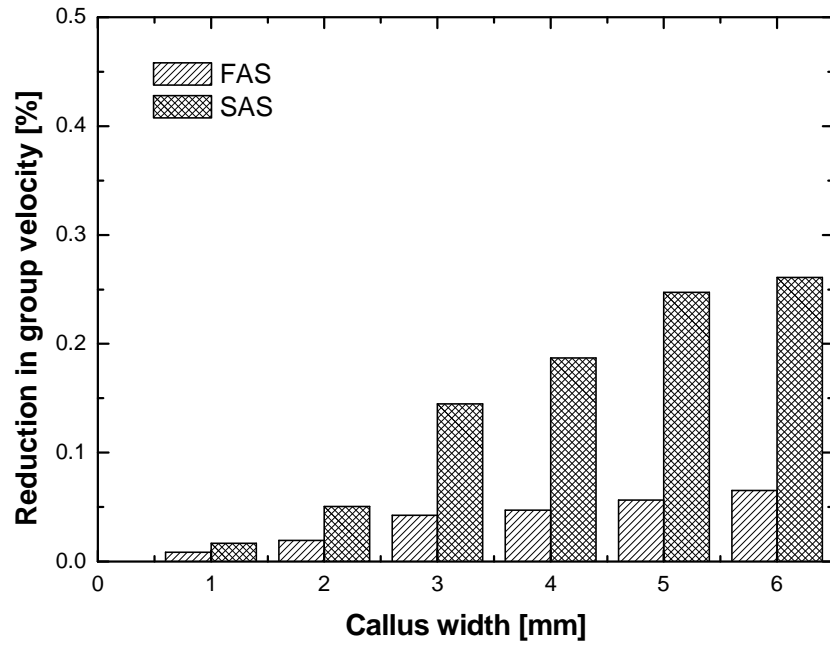
**Fig. 7.3. Cont.**

Figure 7.4 displays the propagation velocities of FAS and SAS at each mimicked bone healing stage from both experiment and FE simulation (excitation frequency was kept at 100 kHz). When the callus is of large width (indicating early healing stage), the FAS and SAS have greater reductions in velocity compared with the intact bone phantom (callus width 0 mm). As the width of callus decreases (implying progressive healing), the velocities of the FAS and SAS increase accordingly, gradually approximating those in the intact bone phantom. This is consistent with observations in studies [129, 133, 136] in which the FAS was employed to monitor the healing progress of bone fracture.

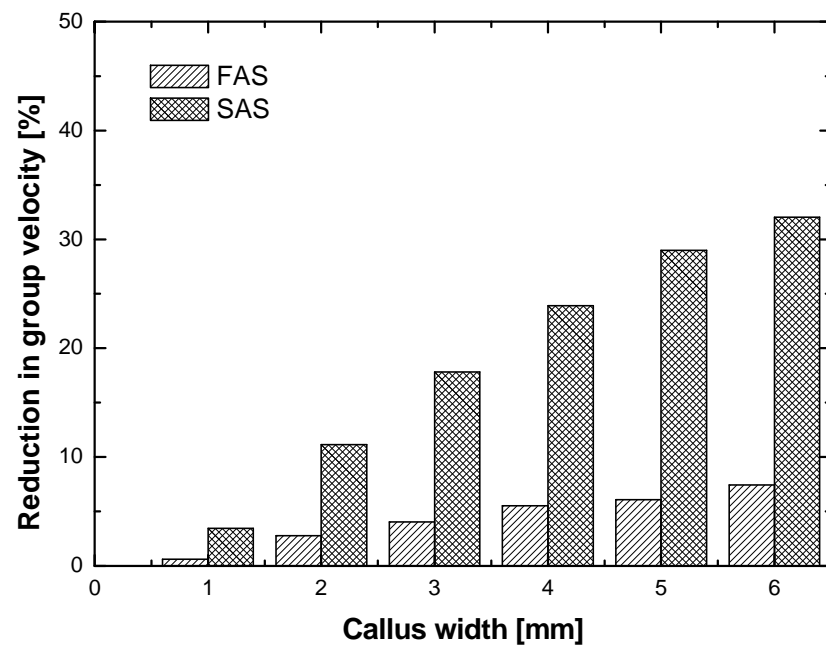


**Fig. 7.4.** Velocities of FAS and SAS at different healing stages from both experiment and FE simulation (at 100 kHz)

It was also observed that the SAS shows more significant changes in velocity than the FAS at different healing stages of mimicked bone fracture, as displayed in Figs. 7.5(a) and (b), indicating a greater sensitivity to variation in callus than the FAS. This can be attributed to the fact that the SAS has smaller wavelength than the FAS. The SAS therefore has the potential to develop precision-enhanced monitoring of bone fracture healing.



(a)



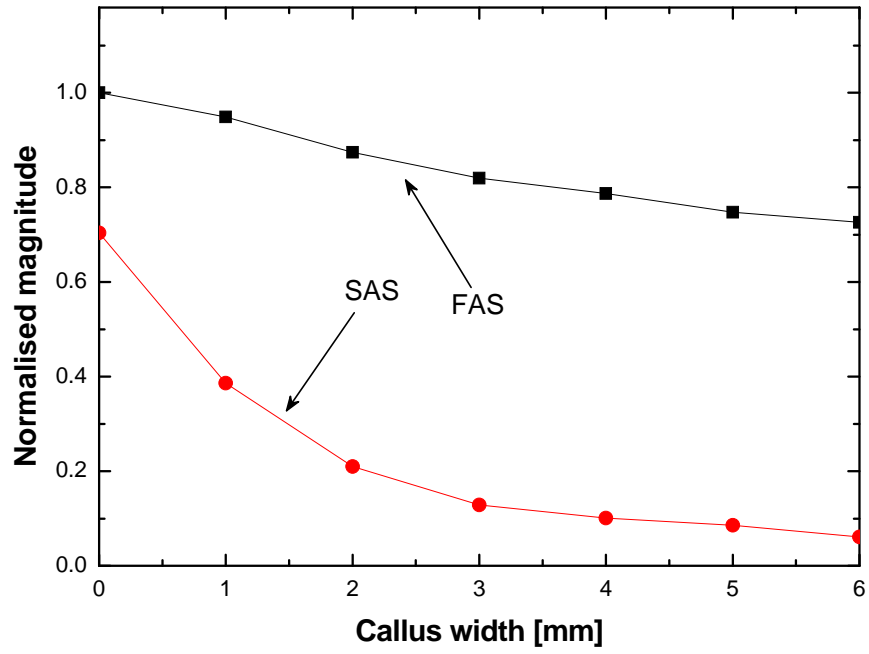
(b)

**Fig. 7.5.** Relative reductions in velocities of FAS and SAS at different healing stages of mimicked bone fracture via (a) FE simulation (b) experiment

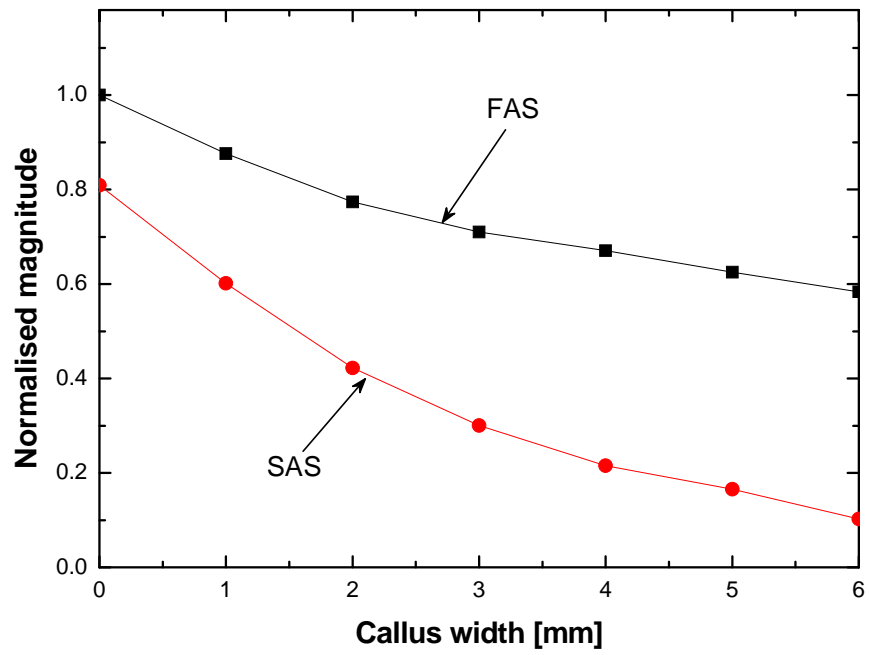
During the initial stage of the healing progress of bone fracture, callus is comprised of connective tissue. As demonstrated in Section 5.2.2, soft tissues, at low excitation

frequencies (<100 kHz), can be described as linear, elastic, isotropic solids. Under the current excitation frequency of 100 kHz, the callus was simulated in FE modelling by solid elements that were linear, elastic and isotropic. In Fig. 7.4, the results from FE simulation and experiment exhibit satisfactory consistency, which further complements the abovementioned hypothesis.

As well as the signal velocities customarily measured in the clinic, the signal magnitude can sometimes render supplementary information. Figure 7.6 presents the magnitude variation subjected to different callus widths from both experiment and FE simulation. The results demonstrate that the magnitudes of both FAS and SAS increase with the decrease of callus width (from the early healing stage to the intact stage). This phenomenon can be used to assist in predicting different healing stages of bone fracture.



(a)



(b)

**Fig. 7.6.** Magnitudes of FAS and SAS vs. callus width via (a) FE simulation and (b) experiment (excitation frequency of 100 kHz)

Furthermore, the magnitude of the SAS showed higher sensitivity to the change in callus width than that of the FAS, as demonstrated in Fig. 7.7 in which the SAS has greater reduction in magnitude than the FAS at each healing stage of mimicked bone fracture. This again reinforces the good potential of the SAS for monitoring the healing progress of bone fracture, with enhanced precision compared to FAS.

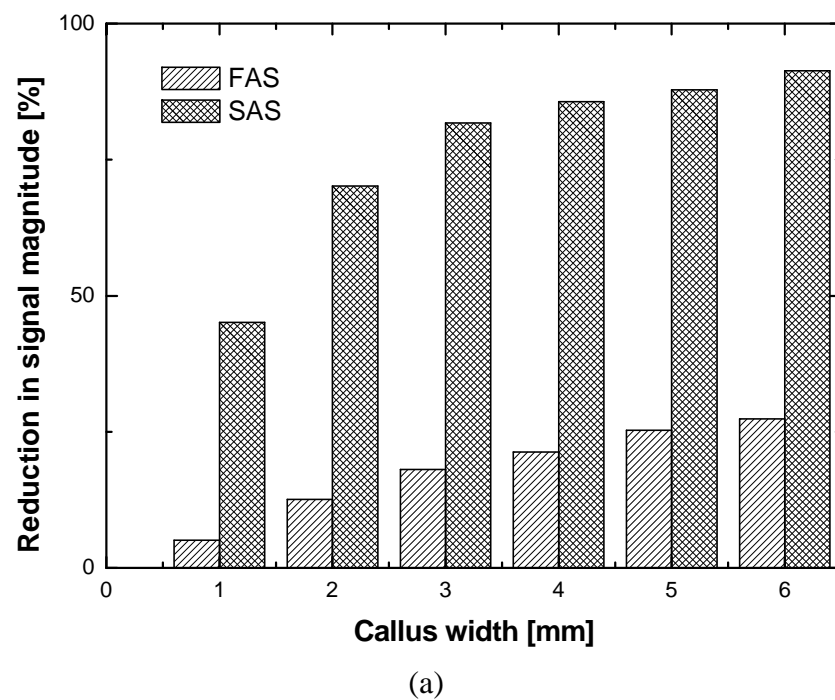
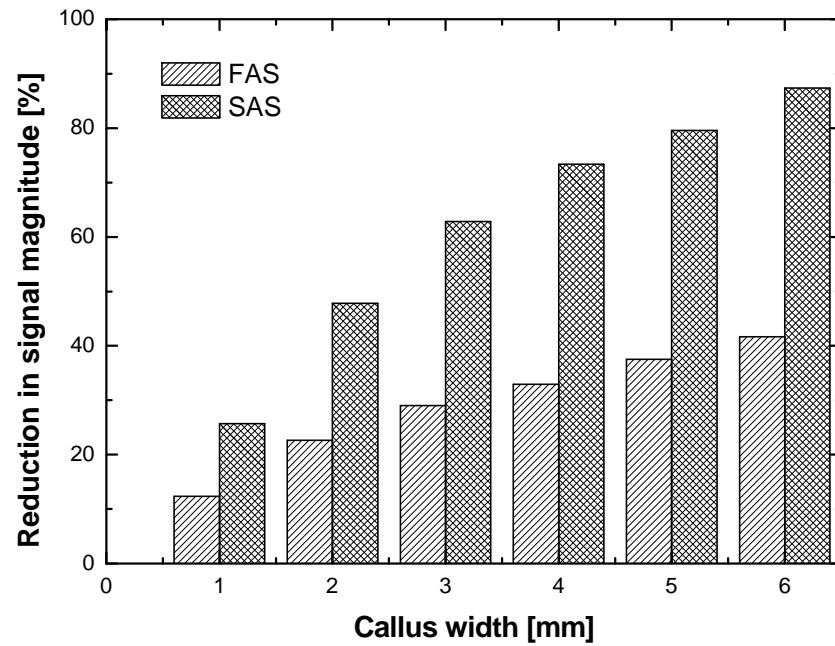


**Fig. 7.7.** Relative reductions in magnitude of FAS and SAS at different healing stages of mimicked bone fracture via (a) FE simulation and (b) experiment



(b)

Fig. 7.7. Cont.

### 7.3 Effect of Soft Tissues on Monitoring of Healing Progress of Mimicked Bone Fracture

In the previous section, the feasibility of using SAS to predict the healing stages of mimicked bone fracture was canvassed, in the absence of any overlying soft tissues.

In clinical practice, however, the presence of overlying soft tissues coupled with the bone cannot be avoided. In the following part, the influence of coupling soft tissue in monitoring the healing progress of bone fracture is explored.

### 7.3.1 Sample Preparation

The bone fracture phantoms described in Section 7.2.1 were used again. Moreover, to introduce the coupling effect of overlying soft tissues, a layer of ASR (dimensions:  $160\text{ mm} \times 60\text{ mm} \times 3.4\text{ mm}$ , elastic modulus: 11.96 kPa) was glued to the upper surface of each phantom with Type 460 adhesive, with the callus immediately under the middle of the ASR, as illustrated in Fig. 7.8. The sample was then instrumented with the signal generation/acquisition system developed on a VXI platform [121] introduced in Section 4.2.2.

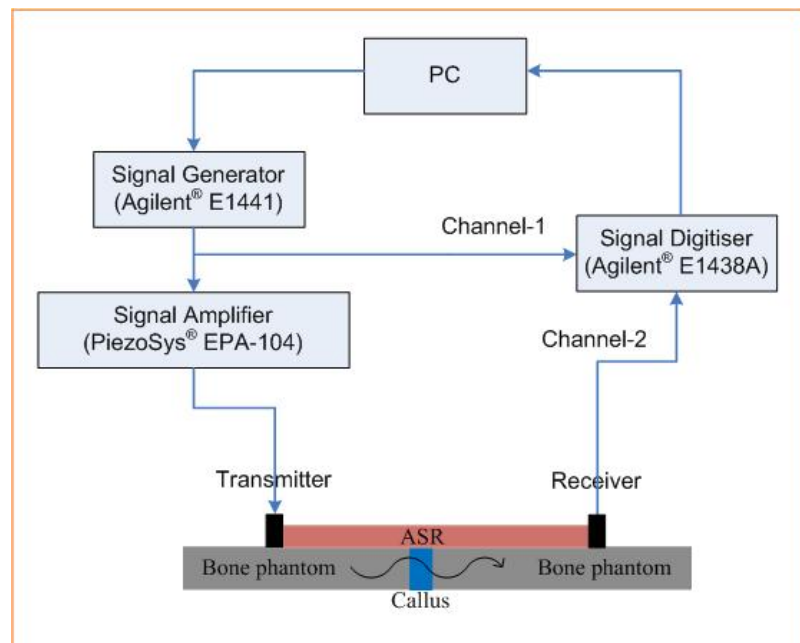
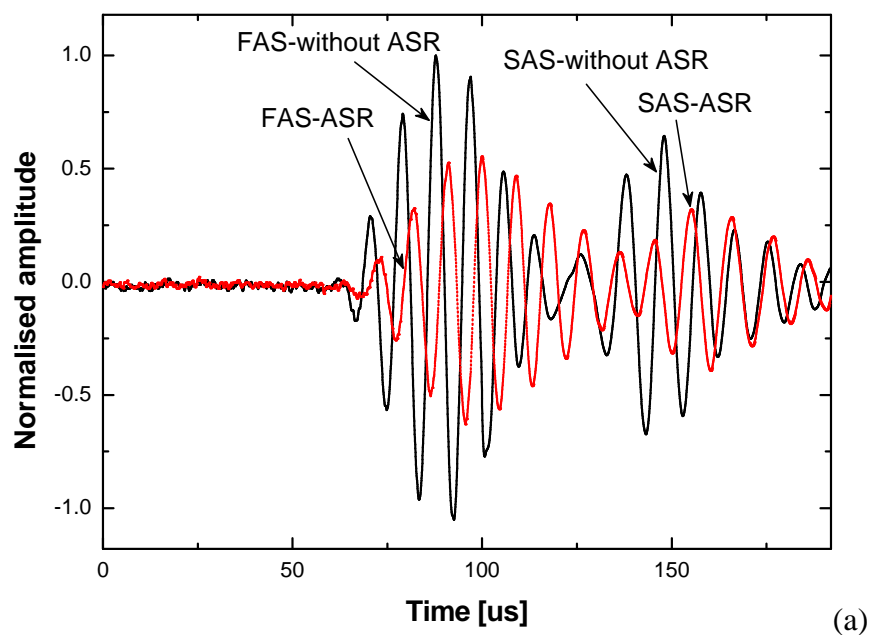


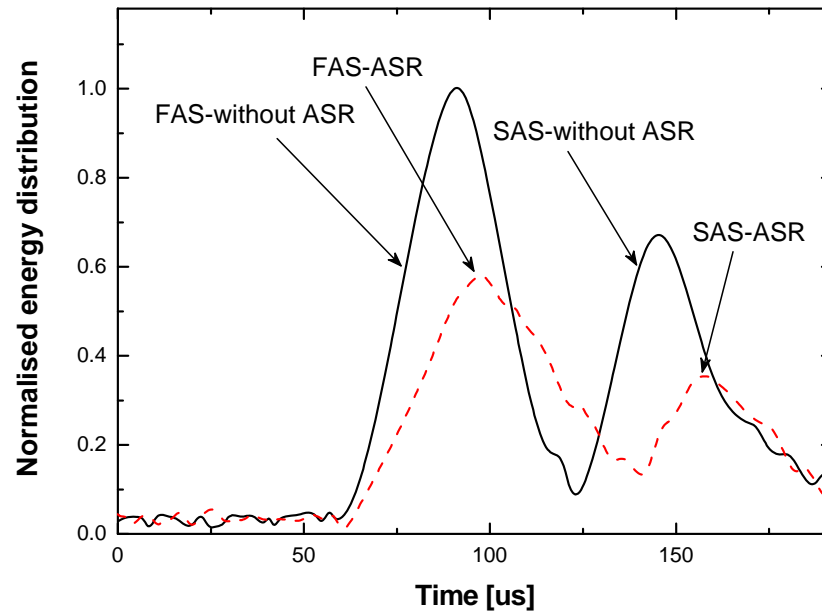
Fig. 7.8. Experimental setup

### 7.3.2 Results and Discussion

Two representative raw wave signals captured from the above phantoms when the callus width was 2 mm, in the absence and presence of ASR, and their HT-processed results, are presented in Figs. 7.9(a) and (b). It can be noticed that the presence of ASR changes the characteristics of both the FAS and the SAS, evidencing an increased propagation time because of the reduced propagation velocities and attenuated signal magnitude.



**Fig. 7.9.** Signals captured from bone fracture phantom with callus 2 mm in width in the absence and presence of ASR: (a) raw signals and (b) their HT-processed results



(b)

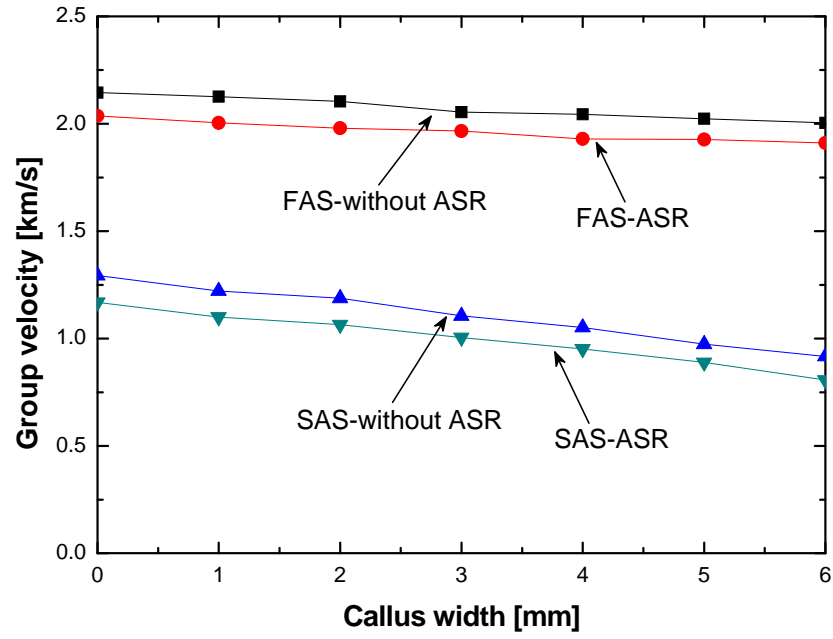
**Fig. 7.9. Cont.**

To further interrogate this effect on ultrasonic wave propagation in fractured bone phantoms, Figs. 7.10 and 7.11 respectively present the velocities and signal intensities of both FAS and SAS subject to callus width (varying from 1 to 6 *mm* with an increment of 1 *mm*) in the absence and presence of ASR. It is obvious that the presence of ASR causes further reductions in the velocity and magnitude of both the FAS and the SAS at each callus width compared with those in fractured bone phantoms in the absence of ASR. Without differentiating such reductions caused by the coupling effect from those due to the existence of callus, the accuracy of monitoring can be compromised. Furthermore, the coupled ASR layer with fixed thickness and elastic properties seemed to have a consistent effect on both the FAS and SAS in terms of propagation velocity, regardless of the different healing stages of mimicked fracture. That is because the callus width was much smaller than the axial

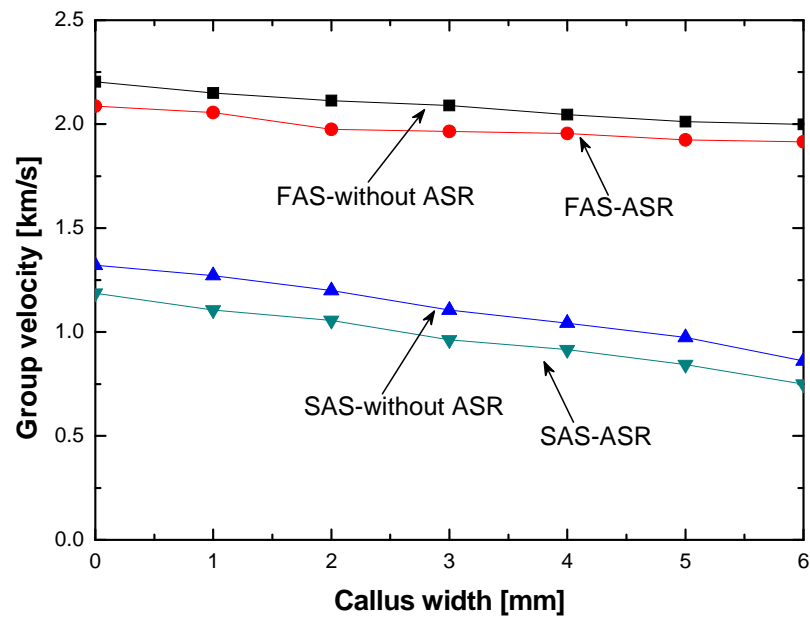
dimension of the bone phantom, and under such a circumstance waves propagating in the callus along its width would not be influenced by the surrounding soft tissues. This observation implies that the overall influence of coupled soft tissues on waves propagating in the fractured bone phantom with callus can be hypothesised to be the same as that in the same phantom but without callus. On the other hand, this effect also influenced the signal intensity of the captured waves, as seen in Fig. 7.11 in which the magnitudes of the FAS and the SAS at each healing stage decrease at different rates before and after the introduction of the ASR, and the greatest reductions take place during early healing stages in the whole course of the healing progress.

As discussed in Section 5.4.1, the most prominent modulations from a coupled soft medium on propagation velocities of FAS and SAS take place when the soft medium is initially introduced, and there is no evident discrepancy in such a modulation when the soft medium has different thickness (Fig. 5.12). This implies that the surrounding soft tissues exert perceptible influence on the velocity of FAS or SAS only in a confined area, making it possible to apply the calibration at a specific thickness of the soft tissues to compensate for the coupling effect, regardless of the difference in thickness of the coupled soft tissues, if only variations in the wave velocity is referred to in QUS. This conclusion indicates that the calibrated results in Fig. 7.10 which is obtained from mimicked fractured bones in the presence of a layer of soft tissue of constant thickness can be used to compensate for velocities of FAS and SAS in the

fractured bones in which the soft tissue is of different thickness. Nevertheless, modulation from the soft medium on signal magnitudes of both FAS and SAS is continuous and increasing, with increase in the thickness of ASR (Fig. 5.13), articulating that rectification of such a coupling effect is case-dependent and compensation should be applied in terms of the calibrated relationships between signal magnitudes and properties of soft tissues (Figs. 5.13), if variations in the signal magnitude is also a parameter to be relied on in QUS. The results shown in Fig. 7.11 therefore cannot be directly applied to compensate for magnitudes of FAS and SAS in the fractured bone with soft tissue of other thinness. If signal intensity is concerned in the bone fracture monitoring, calibration of magnitudes of FAS and SAS in the fractured bone is of necessity for each case (at different healing stages and with the soft tissue of different thicknesses). The above concern on compensating for the coupling effect of the soft tissues of different thicknesses can be extended to the case in which soft tissues are of different elastic moduli.

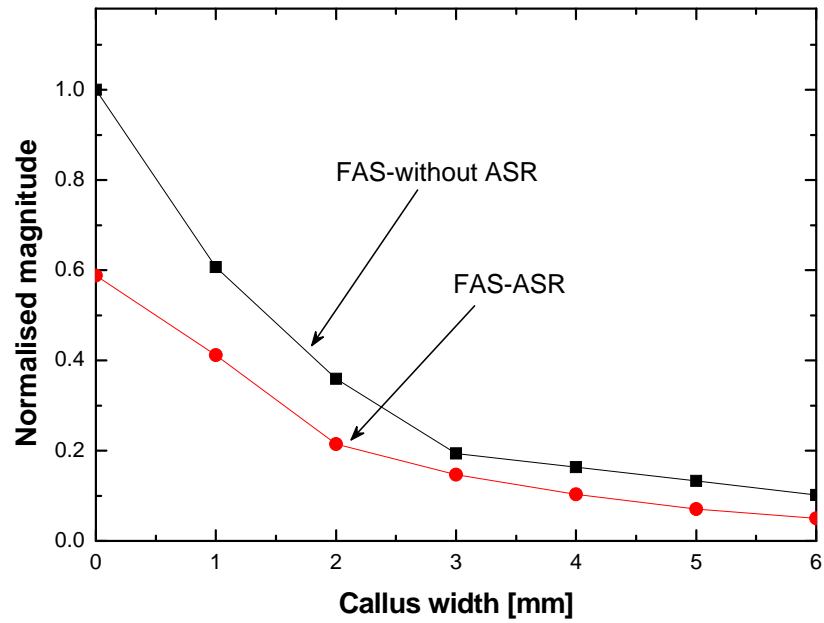


(a)

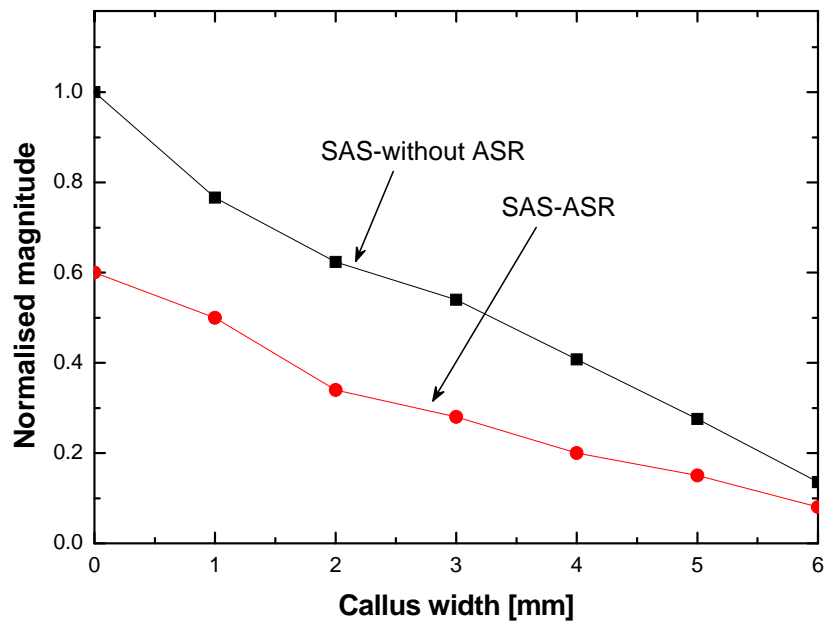


(b)

**Fig. 7.10.** Group velocities of FAS and SAS captured from fractured bone phantoms of different callus widths in the absence and presence of ASR via (a) FE simulation and (b) experiment



(a)



(b)

**Fig. 7.11.** Signal intensities of (a) FAS and (b) SAS captured from fractured bone phantoms of different callus widths in the absence and presence of ASR

The relative reductions in the velocities of the FAS and SAS experimentally obtained at different mimicked healing stages in the presence of ASR compared to those in the

absence of ASR are shown in Fig. 7.12, from which the relative reductions in the velocities of the FAS and SAS can be seen subject to callus width at each healing stage, being around 5% and 12%, respectively.

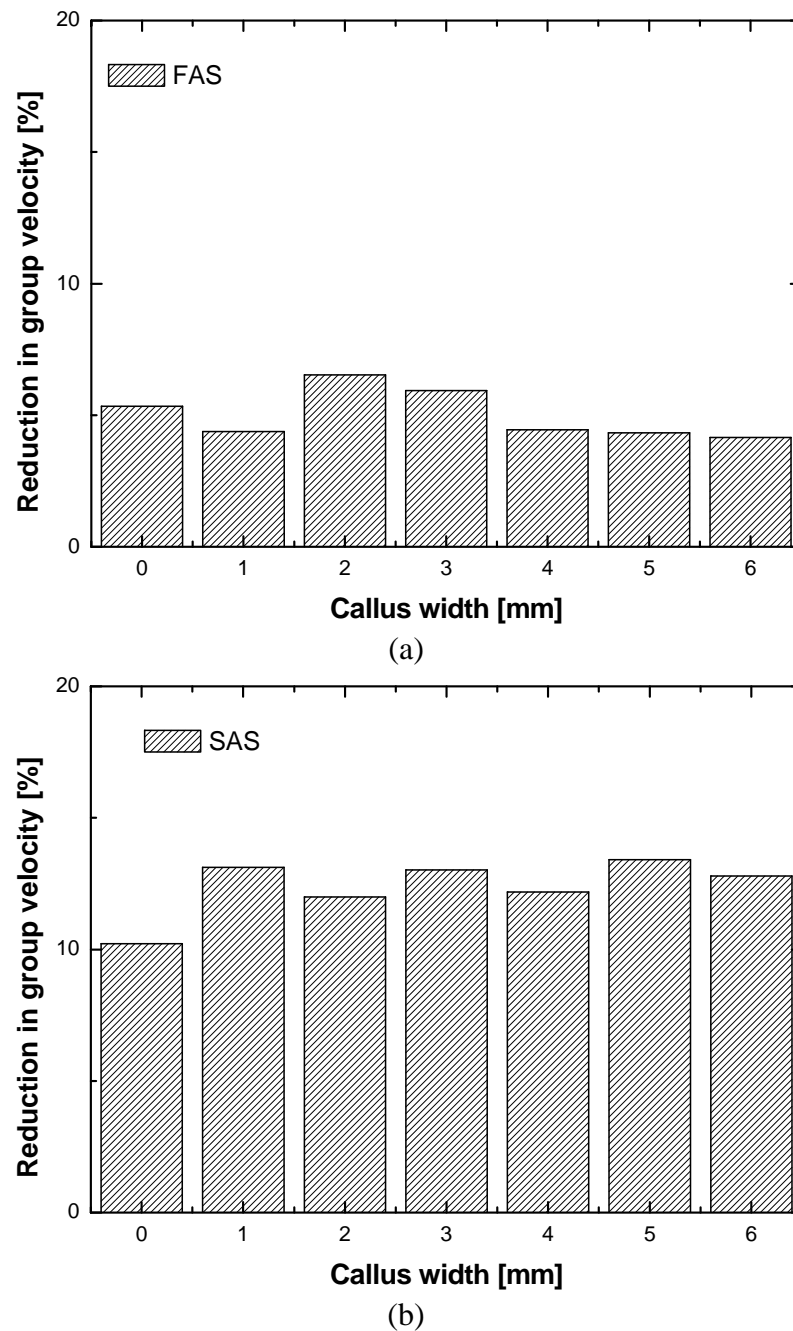


**Fig. 7.12.** Influence of coupled ASR on (a) FAS and (b) SAS with callus of different widths

## 7.4 Application to Prediction of Mimicked Bone Healing by Considering Coupling Effect

In this section, the previously calibrated coupling effect of soft tissues on the propagation of ultrasound waves is applied to enhance the precision of prediction for bone healing. For the convenience of interpretation, four cases are considered, as illustrated schematically in Fig. 7.13:

- (i) an intact bone phantom (an acrylic plate with the dimensions  $460\text{ mm} \times 240\text{ mm} \times 3.2\text{ mm}$ , without coupled ASR), henceforth called Phantom-1 (Fig. 7.13(a));
- (ii) two identical acrylic plates (each  $230\text{ mm} \times 240\text{ mm} \times 3.2\text{ mm}$ ) connected via an ASR strip (prepared in line with the manufacturing steps of ASR introduced in Section 5.2.1) with width  $2\text{ mm}$  to mimic a particular healing status, as sketched schematically in Fig. 7.13 (b), called Phantom-2. As described previously, the ASR strip was intended to mimic callus in bone. In fractured bone, the size and elastic properties of callus vary at different healing stages, and therefore its geometric features can be used to indicate the healing progress of the fractured bone. In this case soft tissues were not introduced;
- (iii) to introduce the coupling effect of soft tissue, a layer of ASR (  $160\text{ mm} \times 60\text{ mm} \times 3.4\text{ mm}$  ,  $E_{ASR} = 11.96\text{ kPa}$  ) was glued atop a sample identical to Phantom-2, as illustrated in Fig. 7.13 (c), called Phantom-3. The elastic modulus of  $11.96\text{ kPa}$  was selected, very close to that of normal human

soft tissues. A transducer pair was positioned at the interface between the bone phantom and ASR layer, clamping the coupled ASR layer in the axial direction, as shown in Fig. 7.13 (c). Note that as explained earlier, the transducer pair was positioned at the interfaces rather than above the soft tissue, to explore the medium coupling effect on the SAS in the bone phantom; this is different from real clinical applications of QUS. Signals captured from this sample (with both callus and coupled soft tissues) were therefore deemed equivalent to *in vitro* signals from a fractured bone; and

- (iv) an intact bone phantom, the same as Phantom-1, but coupled with a layer of ASR, denoted by Phantom-4 (Fig. 7.13(d)).

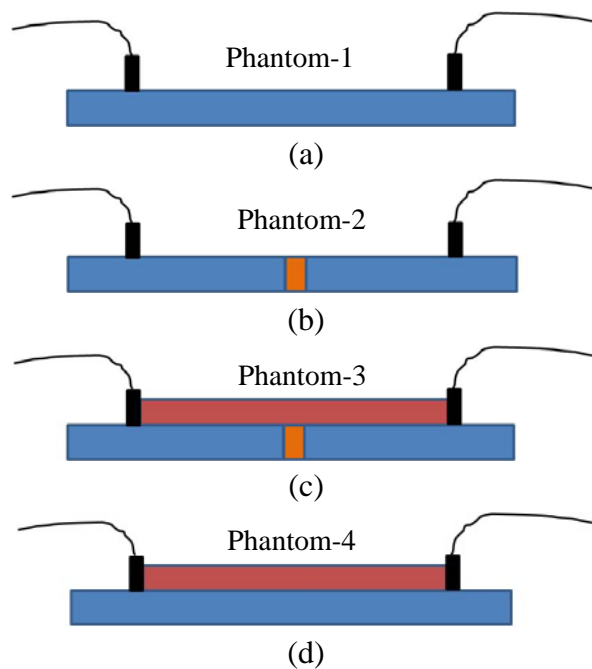


**Fig. 7.13.** Different configurations of bone fracture phantoms: (a) An intact bone phantom; (b) a fractured bone phantom with callus width 2 mm; (c) a fractured bone phantom as in (b) but with a layer of ASR and (d) an intact phantom as same as that in (a) with a layer of ASR

First, Phantom-3 was ultrasonically evaluated (five-cycle *Hanning*-window modulated sinusoidal tonebursts at 100 kHz with a magnitude of  $180 V_{p-p}$  being used as the diagnostic signal).

### 7.4.1 Prediction Without Consideration of Coupling Effect

For Phantom-3 (with callus 2 mm and coupled soft tissues), the relative reduction in the velocity of the SAS measured *in vitro* (denoted henceforth by  $V_{fracture-with\ ASR\ (in\ vitro)}$ ) with regard to that in the intact phantom (containing neither callus nor coupled overlying soft tissues) (denoted by  $V_{intact}$  in what follows),  $R_{in\ vitro-intact}$

( $R_{in\ vitro-intact} = \frac{V_{intact} - V_{fracture-with\ ASR\ (in\ vitro)}}{V_{intact}}$ ) was determined to be 23%, as seen in Fig.

7.14. Without consideration of the coupling effect of soft tissues, this reduction was attributed entirely to the existence of callus. In this case, by linking  $R_{in\ vitro-intact}$  with the previously calibrated relative reductions in the velocity of the SAS at different healing stages, as displayed in Fig. 7.5(b), the healing stage in Phantom-3 was determined to be 4 mm in width, deviating considerably from the actual callus width (2 mm). This inaccurate determination of healing stage can be attributed to the disregard of the effect of the coupled ASR, which produced an additional reduction in the velocity of the SAS. Note that the velocity of SAS shown in Fig. 7.5(b) was measured from the fractured bone sample without any coupled soft tissues, and it is hereinafter denoted by  $V_{fracture-without\ ASR}$ .

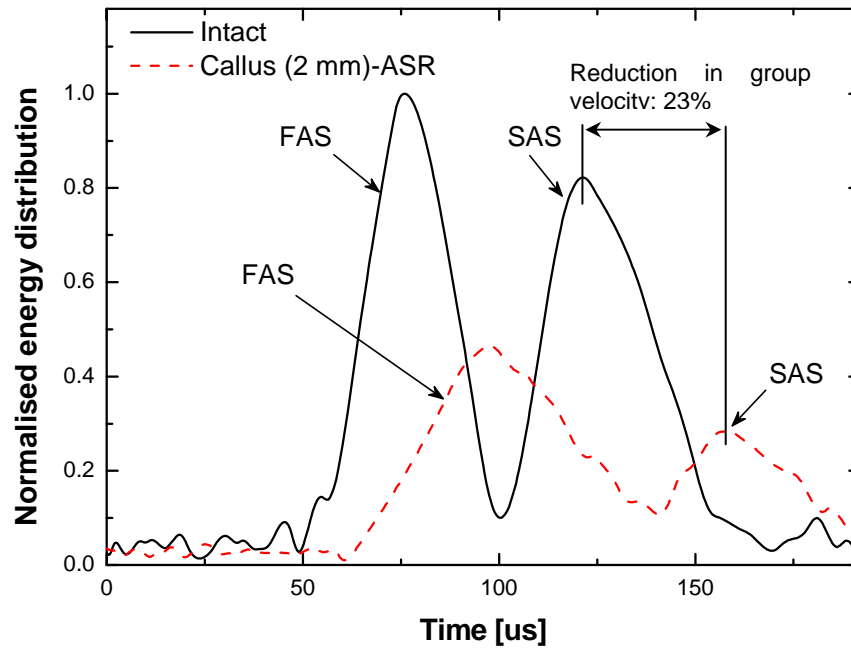


**Fig. 7.14.** HT-processed results of wave signals captured from Phantom-1 and Phantom-3

## 7.4.2 Prediction With Consideration of Coupling Effect

Conclusions obtained from previous parametric studies indicate that, apart from degradation in bone including callus, the coupling effect of overlying soft tissues also causes reduction in the velocity of SAS. Such an effect should be appropriately removed before using Fig. 7.5(b) to predict the callus width, because the correlation in Fig. 7.5(b) was established in the absence of any overlying soft tissues.

As already mentioned, because the callus width was much smaller than the axial dimension of the fractured bone sample, waves propagating within callus along its width would not be affected by the surrounding soft tissues. This means that the overall influence of coupled soft tissues on waves propagating in the entire fractured

bone (with coupled ASR layer and callus) can be hypothesised to be the same as that in a healthy bone (with the same coupled ASR layer but without any callus, shown in Fig. 7.13(d)), namely,

$$\frac{V_{fracture-without\ ASR} - V_{fracture-with\ ASR\ (in\ vitro)}}{V_{fracture-without\ ASR}} = \frac{V_{no\ fracture-without\ ASR} - V_{no\ fracture-with\ ASR}}{V_{no\ fracture-without\ ASR}}, \quad (7.1)$$

where  $V_{no\ fracture-with\ ASR}$  is the velocity of SAS in Phantom-4 shown in Fig. 7.13(d). The right term of Equation 7.1,  $\frac{V_{no\ fracture-without\ ASR} - V_{no\ fracture-with\ ASR}}{V_{no\ fracture-without\ ASR}}$  indicates the reduction

rate in the velocity of SAS, fully due to the coupling effect of ASR layer, propagating in a healthy bone without fracture, therefore denoted by  $R_{coupling}$  (*i.e.*,

$$R_{coupling} = \frac{V_{no\ fracture-without\ ASR} - V_{no\ fracture-with\ ASR}}{V_{no\ fracture-without\ ASR}}). \text{ Then we have}$$

$$\frac{V_{fracture-without\ ASR} - V_{fracture-with\ ASR\ (in\ vitro)}}{V_{fracture-without\ ASR}} = R_{coupling}. \quad (7.2)$$

On the other hand, referencing the calibrated coupling effect of ASR on SAS shown in Fig. 5.16(b), which was obtained using the same sample as Phantom-4 in Fig.

7.13(d),  $R_{coupling}$  was determined to be 12% at the current excitation frequency of 100 kHz (*i.e.*,  $\frac{V_{fracture-without\ ASR} - V_{fracture-with\ ASR\ (in\ vitro)}}{V_{fracture-without\ ASR}} = R_{coupling} = 12\%$ ). In addition, with

knowing

$$R_{in\ vitro-intact} = \frac{V_{no\ fracture-without\ ASR} - V_{fracture-with\ ASR\ (in\ vitro)}}{V_{no\ fracture-without\ ASR}}, \quad (7.3)$$

we have

$$\frac{V_{no\ fracture-without\ ASR} - V_{fracture-without\ ASR}}{V_{no\ fracture-without\ ASR}} = \frac{R_{in\ vitro-intact} - R_{coupling}}{1 - R_{coupling}}. \quad (7.4)$$

Observing the subscript of all variables in the left term of Equation 7.4, it can be seen that this defined reduction in the velocity of SAS had been compensated by considering the coupling effect from soft tissues (*i.e.*, the coupling effect of overlying soft tissues had been removed), which can be now directly used to predict the callus width in terms of Fig. 7.5(b).

Substituting the measured relative reduction rates (  $R_{in\ vitro-intact} = 23\%$  and  $R_{coupling} = 12\%$  ) from captured signals into Equation 7.4, it has

$$\frac{V_{no\ fracture-without\ ASR} - V_{fracture-without\ ASR}}{V_{no\ fracture-without\ ASR}} = \frac{R_{in\ vitro-intact} - R_{coupling}}{1 - R_{coupling}} = \frac{23\% - 12\%}{1 - 12\%} = 12.5\% .(7.5)$$

Using the reduction in the velocity of SAS of 12.5% rather than 23% (used in Section 7.4.1), the predicted callus width is circa 2 mm, tallying with the real callus width.

## 7.5 Concluding Remarks

This chapter first demonstrated the feasibility of using the FAS and SAS to monitor the healing progress of bone fracture. The results show that the velocities and signal magnitudes of both the FAS and SAS reduced as the callus width increased; in particular, the SAS evidenced higher sensitivity than the FAS to width variation of the callus, indicating its good potential for monitoring the healing progress of bone fracture. With the concern that soft tissues coupled with bone could influence the

precision of the prediction of bone healing stages, mimicked fractured bone phantoms at various healing stages were ultrasonically interrogated in the absence and presence of soft tissues. The results showed that the presence of soft tissues influenced both the FAS and SAS in the mimicked fractured bone phantoms at each healing stage, but without compensation the precision of QUS-based evaluation for human bones could be compromised. In an application, the previously achieved understanding of the coupling effect was incorporated when predicting the healing stage of a particular fractured bone phantom. It was found that without considering this coupling effect, the predicted healing stage deviated considerably from the actual one, whereas after compensating for the effect, the current healing stage was accurately determined, highlighting the necessity of systematic calibration of and compensation for such an effect.

# **CHAPTER 8      Conclusions and Future Research Recommendations**

## **8.1 Concluding Remarks**

The coupling effect of soft media (fluid, soft tissue, *etc.*) on the propagation of ultrasonic elastic waves in solid structures (petroleum pipelines, offshore platforms, boat/submarine hulls, human bones, *etc.*) is the core subject of this thesis. This issue was systematically and quantitatively investigated in this study with the purpose of enhancing the precision of traditional NDE for engineering structures and QUS for clinical bone assessment. Various materials, including aluminium, acrylic, water, 98% glycerin, and silicon rubber were chosen to form different samples and phantoms, simulating different engineering structures and mimicking soft tissue-bone systems. Analyses were conducted on these phantoms via 3D FE simulation and experiment. A series of signal processing endeavours was applied to captured ultrasonic signals, including signal averaging, DC offset, smoothing and de-noising and Hilbert transform.

The coupling effect was first explored using a water-aluminium coupled medium. It was observed that the presence of fluid exerted prominent modulation on the  $A_0$  mode; the most notable effect occurred when the fluid was initially introduced. This phenomenon might create difficulty in delivering correct identification of damage without appropriate rectification if such a wave mode was used for developing NDE techniques for the inspection of structures coupled with fluid, for example submerged objects. The coupling effect on Lamb waves propagating in aluminium plates was quantitatively calibrated in the work. As an application, this quantitatively calibrated coupling effect of the surrounding fluid medium on the characteristics of Lamb waves was used to amend traditional Lamb-wave-based NDE in detecting corrosion damage in a submerged aluminium plate. The results exhibited precision-enhanced identification of damage when rectification and compensation for the coupling effect were applied.

The above study was then extended to a bio-medical scenario: QUS-based bone assessment under the influence of coupled soft tissues. For this purpose, a series of synthesised soft-tissue bone phantoms was fabricated, and the influence of soft tissues on ultrasonic waves propagating in bone was investigated. At a lower level imitation, a layer of 98% glycerin (mimicking soft tissue) was introduced to the upper surface of an acrylic plate (bone phantom). The results from ultrasonic tests indicated that the propagation of the  $A_0$  mode could be substantially affected in the presence of fluid, whereas its velocity did not change greatly as the thickness of the fluid further

increased. At a higher level of imitation, considering the reality that soft tissue is not pure fluid, but a soft substance that sustains shear stresses, a layer of ASR varying in thickness and elastic modulus (mimicking the variety of soft tissues from normal to pathological conditions) was introduced to mimic soft tissues. It has been observed that the presence of a layer of ASR exerted a prominent coupling effect on the characteristics of both the FAS and SAS in acrylic plates, manifesting as: (i) reduced propagation velocities and (ii) attenuated signal intensity.

Although the plate model (detailed in Chapter 5) achieves good prediction for Lamb waves propagating in long bone, it can become unwieldy to the examination of waves propagating in cortical bones of great thickness or small radii as a result of the ignorance of bone curvature [25]. In this aspect, the tube-like model (studies in Chapter 6) provides a good estimate of wave propagation characteristics in cortical bone of great thickness [90]. In recognition of the fact that human long bone is actually not a plate-like but tube-like structure, as a more advanced step to simulate it, acrylic tubes were selected and a layer of ASR (varying in thickness and elastic modulus) was circumferentially adhered onto the tube to mimic the soft tissue-bone system, with closer similarity to real bone systems. Similar effects of the ASR layer on the FAS and SAS to those in acrylic plates were observed. Furthermore, the coupling effect of soft tissues is more prominent in tube than that in plate, indicating the necessity for rectification of this coupling effect when developing QUS for bone assessment based on the tube model.

As an application, the previously calibrated relationship between manifestations of the captured signals and variations in the coupled soft tissues was used to enhance the precision of QUS-based prediction for bone fracture healing. It was found that without compensation for the coupling effect of soft tissues inaccurate identification of the healing stage of bone fracture was obtained; with compensation for the effect, satisfactory accuracy in identifying the current healing status was achieved.

In summary, the presence of fluid/soft tissues can affect the propagation of Lamb waves in engineering structures/bones to different extents for different wave modes. It is essential to calibrate and rectify such coupling effects when implementing both NDE for engineering structures submerged and QUS for human long bone assessment.

## **8.2 Research Recommendations**

Despite the encouraging results obtained from the work using the analysis tools developed here, several points call for improvement in future work, summarised as follows:

First, the bone phantoms in this study were created using acrylic plates or tubes, which were deemed homogeneous and isotropic. However, bones are actually anisotropic and heterogeneous in nature, as reflected by directionality in their microstructure. To depict real bone structures authentically, anisotropy should ideally

be taken into account in future studies, using anisotropic material properties. For cancellous bone, porosity should also be taken into account, which can be modelled for example using cylindrical inclusions embedded in a bony matrix with their axis parallel to the longitudinal axis of the bone. In addition, further improvement on the simulation of the interface between two media should be considered, such as using a boundary layer, with a hope of enhancing the simulation accuracy and precision.

Second, the coupling effect of soft tissues on the FAS and SAS when used for QUS-based bone fracture assessment was investigated using acrylic plates. Bearing in mind that real bones are tube-like structures, acrylic tubes should continue to be used in future studies to produce fractured bone phantoms, but mimicked callus should be introduced possessing not only different geometric features but also different elastic properties to imitate different healing statuses of the fractured bone. It is intended that the coupling effect of soft tissues on the FAS and SAS will be examined in the cylindrical modality.

Third, in the current configuration of simulation and testing, the transducer pair was placed at the interface between the mimicked bone and soft tissues, rather than atop the soft tissues. It was acknowledged that this configuration was different from real clinical applications, in which transducer surfaces are in contact with soft tissues in terms of axial transmission measurement. With the comprehensive understanding of the mechanism of the coupling effect of soft tissues on the FAS and SAS, it is

intended that the improved configuration of locating transducers atop mimicked soft tissues will be explored in future work.

Last but not least, in recognition that there is still a large difference between the *in vitro* model developed in this study and real soft tissue-bone system, *in vitro* and *in vivo* tests on real animal bone samples will be conducted in future work. In this connection, the tibia and radius from bovine, sheep or human cadavers with soft tissues will be used to investigate the coupling effect of soft tissues on the propagation characteristics of ultrasound waves *in vitro* and *in vivo*.

## APPENDIX

$$\frac{\partial p}{\partial \omega} = \frac{1}{4} \pi \left( \frac{2\Omega}{k^2} \frac{\partial \Omega}{\partial \omega} - \xi^2 \right) \left( \frac{\Omega^2}{k^2} - \xi^2 \right)^{-\frac{1}{2}},$$

$$\frac{\partial p}{\partial k} = -\frac{1}{4} \pi \left( \frac{\Omega^2}{k^2} - 2\xi \frac{\partial \xi}{\partial k} \right) \left( \frac{\Omega^2}{k^2} - \xi^2 \right)^{-\frac{1}{2}},$$

$$\frac{\partial q}{\partial \omega} = \frac{1}{4} \pi \left( 2\Omega \frac{\partial \Omega}{\partial \omega} - \xi^2 \right) \left( \Omega^2 - \xi^2 \right)^{-\frac{1}{2}},$$

$$\frac{\partial q}{\partial k} = -\frac{1}{4} \pi \left( \Omega^2 - 2\xi \frac{\partial \xi}{\partial k} \right) \left( \Omega^2 - \xi^2 \right)^{-\frac{1}{2}},$$

$$\frac{\partial r}{\partial \omega} = \frac{1}{4} \pi \left( \frac{2\Omega}{k_F^2} \frac{\partial \Omega}{\partial \omega} - \xi^2 \right) \left( \frac{\Omega^2}{k_F^2} - \xi^2 \right)^{-\frac{1}{2}},$$

$$\frac{\partial r}{\partial k} = -\frac{1}{4} \pi \left( \frac{\Omega^2}{k_F^2} - 2\xi \frac{\partial \xi}{\partial k} \right) \left( \frac{\Omega^2}{k_F^2} - \xi^2 \right)^{-\frac{1}{2}},$$

$$\frac{\partial d}{\partial \omega} = \pi \frac{\Omega}{k_F^2} \frac{\partial \Omega^2}{\partial \omega}, \quad \frac{\partial d}{\partial k} = -2\pi \xi \frac{\partial \xi}{\partial k},$$

$$K = \frac{c_L}{c_T}, \quad K_F = \frac{c_F}{c_T}, \quad \tau = \frac{a}{h}, \quad \gamma = \frac{\rho_F}{\rho}, \quad \Omega = \frac{2\omega h}{\pi c_T}, \quad \xi = \frac{2kh}{\pi}, \quad \frac{\partial \Omega}{\partial \omega} = \frac{2h}{\pi c_T}, \quad \frac{\partial \xi}{\partial k} = \frac{2h}{\pi}$$

$$\frac{\partial L}{\partial \omega} = \frac{\partial q}{\partial \omega} \cos p \cos q - \frac{\partial p}{\partial \omega} \sin p \sin q,$$

$$\frac{\partial L}{\partial k} = \frac{\partial q}{\partial k} \cos p \cos q - \frac{\partial p}{\partial k} \sin p \sin q, \quad \frac{\partial M}{\partial \omega} = \frac{\partial p}{\partial \omega} \cos q \cos p - \frac{\partial q}{\partial \omega} \sin q \sin p,$$

$$\frac{\partial M}{\partial k} = \frac{\partial p}{\partial k} \cos q \cos p - \frac{\partial q}{\partial k} \sin q \sin p, \quad \frac{\partial N}{\partial \omega} = 2 \frac{\partial q}{\partial \omega} \cos 2p \cos 2q - 2 \frac{\partial p}{\partial \omega} \sin 2p \sin 2q,$$

$$\frac{\partial N}{\partial k} = 2 \frac{\partial q}{\partial k} \cos 2p \cos 2q - 2 \frac{\partial p}{\partial k} \sin 2p \sin 2q$$

$$\frac{\partial O}{\partial \omega} = 2 \frac{\partial p}{\partial \omega} \cos 2q \cos 2p - 2 \frac{\partial q}{\partial \omega} \sin 2q \sin 2p,$$

$$\frac{\partial O}{\partial k} = 2 \frac{\partial p}{\partial k} \cos 2q \cos 2p - 2 \frac{\partial q}{\partial k} \sin 2q \sin 2p$$

$$A = \pi^2 \gamma \frac{\partial p}{\partial \omega} \Omega^4 (d^2 N + 4\xi^2 pqO) \sin 2\tau r$$

$$B = 4\pi^2 \gamma p \Omega^3 (d^2 N + 4\xi^2 pqO) \sin 2\tau r$$

$$C = \pi^2 \gamma p \Omega^4 \left( 2d \frac{\partial d}{\partial \omega} N + d^2 \frac{\partial N}{\partial \omega} + 4\xi^2 \frac{\partial p}{\partial \omega} qO + 4\xi^2 p \frac{\partial q}{\partial \omega} O + 4\xi^2 pq \frac{\partial O}{\partial \omega} \right) \sin 2\tau r$$

$$D = 2\tau \pi^2 \gamma p \Omega^4 \frac{\partial r}{\partial \omega} (d^2 N + 4\xi^2 pqO) \cos 2\tau r$$

$$E = 16 \frac{\partial r}{\partial \omega} (d^2 M + 4\xi^4 pqL)(d^2 L + 4\xi^2 pqM)$$

$$F = 16r \left( 2d \frac{\partial d}{\partial \omega} M + d^2 \frac{\partial M}{\partial \omega} + 4\xi^4 \frac{\partial p}{\partial \omega} qL + 4\xi^2 p \frac{\partial q}{\partial \omega} L + 4\xi^2 pq \frac{\partial L}{\partial \omega} \right) (d^2 L + 4\xi^2 pqM)$$

$$G = 16r (d^2 M + 4\xi^4 pqL) \left( 2d \frac{\partial d}{\partial \omega} L + d^2 \frac{\partial L}{\partial \omega} + 4\xi^2 \frac{\partial p}{\partial \omega} \cdot qM + 4\xi^2 p \frac{\partial q}{\partial \omega} M + 4\xi^2 pq \frac{\partial M}{\partial \omega} \right)$$

$$A' = \pi^2 \gamma \frac{\partial p}{\partial k} \Omega^4 (d^2 N + 4\xi^2 pqO) \sin 2\tau r$$

$$C' = \pi^2 \gamma p \Omega^4 \left( 2d \frac{\partial d}{\partial k} N + d^2 \frac{\partial N}{\partial k} + 4\xi^2 \frac{\partial p}{\partial k} qO + 4\xi^2 p \frac{\partial q}{\partial k} O + 4\xi^2 pq \frac{\partial O}{\partial k} \right) \sin 2\tau r$$

$$D' = 2\tau \pi^2 \gamma p \Omega^4 \frac{\partial r}{\partial k} (d^2 N + 4\xi^2 pqO) \cos 2\tau r$$

$$E' = 16 \frac{\partial r}{\partial k} (d^2 M + 4\xi^4 pqL)(d^2 L + 4\xi^2 pqM)$$

$$F' = 16r \left( 2d \frac{\partial d}{\partial k} M + d^2 \frac{\partial M}{\partial k} + 16\xi^3 \frac{\partial \zeta}{\partial k} pqL + 4\xi^4 \frac{\partial p}{\partial k} qL + 4\xi^4 p \frac{\partial q}{\partial k} L + 4\xi^4 pq \frac{\partial L}{\partial k} \right) (d^2 L + 4\xi^2 pqM)$$

$$G' = 16r (d^2 M + 4\xi^4 pqL) \left( 2d \frac{\partial d}{\partial k} L + d^2 \frac{\partial L}{\partial k} + 16\xi^3 \frac{\partial \zeta}{\partial k} pqM + 4\xi^2 \frac{\partial p}{\partial k} \cdot qM + 4\xi^2 p \frac{\partial q}{\partial k} M + 4\xi^2 pq \frac{\partial M}{\partial k} \right)$$

$$V_{group} = - \frac{A' + C' + D' + E' + F' + G'}{A + B + C + D + E + F + G}$$

## REFERENCE

1. M. Bayliss, D. Short and M. Bax. 1988. *Underwater Inspection*: London: E. & F. N. Spon.
2. H. Nordb. 1986. NDE-overview and legal requirements, in *Proceedings of the Submersible Technology*, Graham & Trotman, Limited, pp. 183-187.
3. L. Upda, S. Mandayam, S. Upda, Y. Sun and W. Lord. 1996. Development in gas pipeline inspection technology, *Material Evaluations*, **54**(4):467-471.
4. K. Mandal, D. Dufour, T.W. Krause and D.L. Atherton. 1997. Investigations of magnetic flux leakage and magnetic Barkhausen noise signals from pipeline steel, *Journal of Physics D-Applied Physics*, **30**(6):962-973.
5. W.B. Na and T. Kundu. 2002. Underwater pipeline inspection using guided waves, *Journal of Pressure Vessel Technology*, **124**(2):196-200.
6. R. Mijarez, P. Gaydecki and M. Burdekin. 2007. Flood member detection for real-time structural health monitoring of sub-sea structures of offshore steel oilrigs, *Smart Materials and Structures*, **16**(5):1857-1869.
7. W.J. Staszewski, C. Boller and G.R. Tomlinson. 2004. *Health Monitoring of Aerospace Structures: Smart Sensor Technologies and Signal Processing*, New York: John Wiley & Sons, Inc.
8. R.A. Badcock and E.A. Birt. 2000. The use of 0-3 piezocomposite embedded Lamb wave sensors for detection of damage in advanced fibre composites, *Smart Materials and Structures*, **9**(3):291-297.
9. N. Guo and P. Cawley. 1993. The interaction of Lamb waves with delaminations in composite laminates, *The Journal of the Acoustical Society of America*, **94**(4):2240-2246.
10. G. Maze, J.D.N. Cheeke, X. Li and Z. Wang. 2001. Coupled guided acoustic modes in water-filled thin-walled tubes, *The Journal of the Acoustical Society of America*, **110**(5):2295-2300.
11. J.D.N. Cheeke, K. Shannon and Z. Wang. 1999. Loading effects on  $A_0$  Lamb-like waves in full and partially filled thin-walled tubes, *Sensors and Actuators B*, **59**(2-3):180-183.
12. S.H. Prins, H.L. Jørgensen, L.V. Jørgensen and C. Hassager. 1998. The role of quantitative ultrasound in the assessment of bone: A review, *Clinical Physiology*, **18**(1):3-17.
13. K.A. Wear. 2003. Autocorrelation and cepstral methods for measurement of tibial cortical thickness, *IEEE Transactions on Ultrasonics, Ferroelectrics, and Frequency Control*, **50**(6):655-660.
14. E. Bossy, M. Talmant, M. Defontaine, F. Patat and P. Laugier. 2004. Bidirectional axial transmission can improve accuracy and precision of ultrasonic velocity measurement in cortical bone: A validation on test materials, *IEEE Transactions on Ultrasonics, Ferroelectrics, and Frequency Control*, **51**(1):71-79.

15. S.P. Dodd, J.L. Cunningham, A.W. Miles, S. Gheduzzi and V.F. Humphrey. 2006. Ultrasonic propagation in cortical bone mimics, *Physics in Medicine and Biology*, **51**(18):4635-4647.
16. P. Moilanen, P.H.F. Nicholson, T. Kärkkäinen, Q. Wang, J. Timonen and S. Cheng. 2003. Assessment of the tibia using ultrasonic guided waves in pubertal girls, *Osteoporosis International*, **14**(12):1020-1027.
17. C.F. Njeh, I. Saeed, M. Grigorian, D.L. Kendler, B. Fan, J. Shepherd, M. McClung, W.M. Drake and H.K. Genant. 2001. Assessment of bone status using speed of sound at multiple anatomical sites, *Ultrasound in Medicine and Biology*, **27**(10):1337-1345.
18. V.C. Protopappas, D.I. Fotiadis and K.N. Malizos. 2006. Guided ultrasound wave propagation in intact and healing long bones, *Ultrasound in Medicine and Biology*, **32**(5):693-708.
19. M.G. Vavva, V.C. Protopappas, D.I. Fotiadis and D. Polyzos. 2006. Two-dimensional modeling of guided ultrasound wave propagation in intact and healing bones immersed in fluid, in *Proceedings of the International Special Topics Conference on Information Technology in Biomedicine (IEEE-ITAB)*, Oct., Ioannina, Greece.
20. X.S. Guo, D. Yang, D. Zhang, W.G. Li, Y. Qiu and J.R. Wu. 2009. Quantitative evaluation of fracture healing process of long bones using guided ultrasound waves: A computational feasibility study (L), *The Journal of the Acoustical Society of America*, **125**(5):2834-2837.
21. F. Lefebvre, Y. Deblock, P. Campistron, D. Ahite and J.J. Fabre. 2002. Development of a new ultrasonic technique for bone and biomaterials in vitro characterization, *Journal of Biomedical Materials Research*, **63**(4):441-446.
22. P. Moilanen, P.H.F. Nicholson, V. Kilappa, S. Cheng and J. Timonen. 2006. Measuring guided waves in long bones: Modeling and experiments in free and immersed plates, *Ultrasound in Medicine and Biology*, **32**(5):709-719.
23. M. Muller, P. Moilanen, E. Bossy, P. Nicholson, V. Kilappa, J. Timonen, M. Talmant, S. Cheng and P. Laugier. 2005. Comparison of three ultrasonic axial transmission methods for bone assessment, *Ultrasound in Medicine and Biology*, **31**(5):633-642.
24. P.H.F. Nicholson, P. Moilanen, T. Karkkainen, J. Timonen and S. Cheng. 2002. Guided ultrasonic waves in long bones: Modelling, experiment and in vivo application, *Physiological Measurement*, **23**(4):755-768.
25. P. Moilanen, P.H.F. Nicholson, V. Kilappa, S. Cheng and J. Timonen. 2007. Assessment of the cortical bone thickness using ultrasonic guided waves: Modelling and in vitro study, *Ultrasound in Medicine and Biology*, **33**(2):254-262.
26. D. Hans, S.K. Srivastav, C. Singal, R. Barkmann, C.F. Njeh, E. Kantorovich, C.C. Gluer and H.K. Genant. 1999. Does combining the results from multiple bone sites measured by a new quantitative ultrasound device improve discrimination of hip fracture, *Journal of Bone and Mineral Research*, **14**(4):644-651.
27. X.S. Guo, D. Zhang, D. Yang, X.F. Gong and J.R. Wu. 2008. Comment on

- "Three-dimensional finite element modeling of guided ultrasound wave propagation in intact and healing long bones," [J. Acoust. Soc. Am. 121(6), 3907-3921 (2007)], *The Journal of the Acoustical Society of America*, **123**(6):4047-4050.
28. N. Guo and P. Cawley. 1992. Lamb waves for the NDE of composite laminates, *Review of Progress in Quantitative Nondestructive Evaluation*, **11B**:1443-1450.
  29. Y. Zou, L. Tong and G.P. Steven. 2000. Vibration-based model-dependent damage (delamination) identification and health monitoring for composite structures a review, *Journal of Sound and Vibration*, **230**(2):357-378.
  30. W. Zhu. 2002. An FEM simulation for guided elastic wave generation and reflection in hollow cylinders with corrosion defects, *Journal of Pressure Vessel Technology-Transactions of the ASME*, **124**(1):108-117.
  31. Z. You and W. Lord. 1991. A 3-D finite element formulation for ultrasonic NDE, in *Proceedings of the the 17th Annual Review of progress in quantitative nondestructive evaluation*, Jul., New York, USA, pp. 233-240.
  32. L.Q. Yao, J.G. Zhang, L. Lu and M.O. Lai. 2004. Nonlinear extension and bending of piezoelectric laminated plate under large applied field actuation, *Smart Materials and Structures*, **13**(2):404-414.
  33. J.L. Rose, D. Jiao and J.S. Jr. 1996. Ultrasonic guided wave NDE for piping, *Materials Evaluation*, **54**(11):1310-1313.
  34. J.L. Rose. 2000. Guided wave nuances for ultrasonic nondestructive evaluation, *IEEE Transactions on Ultrasonics, Ferroelectrics, and Frequency Control*, **47**(3):575-583.
  35. J.L. Rose. 1995. Recent advances in guided wave NDE, in *Proceedings of the IEEE Ultrasonics Symposium*, Nov., Seattle, USA, pp. 761-770.
  36. S.G. Pierce, W.R. Philp, B. Culshaw, A. Gachagan, A. McNab, G. Hayward and F. Lecuyer. 1996. Surface-bonded optical fibre sensors for the inspection of CFRP plates using ultrasonic Lamb waves, *Smart Materials and Structures*, **5**(6):776-787.
  37. N. Guo and P. Cawley. 1994. Lamb wave reflection for the quick nondestructive evaluation of large composite laminates, *Materials Evaluation*, **52**(3):404-411.
  38. J.D. Achenbach. 2000. Quantitative nondestructive evaluation, *International Journal of Solids and Structures*, **37**(1-2):13-27.
  39. J. Krautkramer and H. Krautkramer. 1983. *Ultrasonic Testing of Materials*, New York: Springer-Verlag.
  40. L. Lynnworth. 1989. *Ultrasonic Measurements for Process Control: Theory, Techniques, Applications*, Boston: Academic Press.
  41. H.D.V. Sergio and S. Costas. 2002. Real-time nondestructive evaluation of fiber composite laminates using low-frequency Lamb waves, *The Journal of the Acoustical Society of America*, **111**(5):2026-2033.
  42. S. Legendre, D. Massicotte, J. Goyette and T.K. Bose. 2000. Wavelet-transform-based method of analysis for Lamb-wave ultrasonic NDE signals, *IEEE Transactions on Instrumentation and Measurement*, **49**(3):524-530.
  43. F.L. Degertekin and B.T. Khuri-Yakub. 1997. Lamb wave excitation by Hertzian

- contacts with application in NDE, *IEEE Transactions on Ultrasonics, Ferroelectrics, and Frequency Control*, **44**(4):769-779.
44. D.E. Chimenti and R.W. Martin. 1991. Nondestructive evaluation of composite laminates by leaky Lamb waves, *Ultrasonics*, **29**(1):13-21.
  45. W.B. Na and T. Kundu. 2002. Underwater pipeline inspection using guided waves, *Journal of Pressure Vessel Technology - Transactions of the ASME*, **124**(2):196-200.
  46. Y. Cho and J.L. Rose. 1996. Guided waves in a water loaded hollow cylinder, *Nondestructive Testing and Evaluation*, **12**(5):323 - 339.
  47. R.S.C. Monkhouse, P.D. Wilcox and P. Cawley. 1997. Flexible interdigital PVDF transducers for the generation of Lamb waves in structures, *Ultrasonics*, **35**(7):489-498.
  48. M. Lemistre and D. Balageas. 2001. Structural health monitoring system based on diffracted Lamb wave analysis by multiresolution processing, *Smart Materials and Structures*, **10**(3):504-511.
  49. Z. Su and L. Ye. 2009. *Damage Identification Using Lamb Waves - From Fundamentals to Applications*, London: Springer-Verlag GmbH & Co.
  50. V. Giurgiutiu and A. Cuc. 2005. Embedded non-destructive evaluation for structural health monitoring, damage detection, and failure prevention, *The Shock and Vibration Digest*, **37**(2):83-105.
  51. L. Wang and F.G. Yuan. 2007. Group velocity and characteristic wave curves of Lamb waves in composites: Modeling and experiments, *Composites Science and Technology*, **67**(7-8):1370-1384.
  52. V. Giurgiutiu, J. Bao and W. Zhao. 2003. Piezoelectric wafer active sensor embedded ultrasonics in beams and plates, *Experimental Mechanics*, **43**(4):428-449.
  53. J. Chen, Z. Su and L. Cheng. 2010. Identification of corrosion damage in submerged structures using fundamental anti-symmetric Lamb waves, *Smart Materials and Structures*, **19**(1):015004(12pp).
  54. S. Grondel, C. Paget, C. Delebarre, J. Assaad and K. Levin. 2002. Design of optimal configuration for generating  $A_0$  Lamb mode in a composite plate using piezoceramic transducers, *The Journal of the Acoustical Society of America*, **112**(1):84-90.
  55. T. Ghosh, T. Kundu and P. Karpur. 1998. Efficient use of Lamb modes for detecting defects in large plates, *Ultrasonics*, **36**(7):791-801.
  56. V. Giurgiutiu. 2005. Tuned Lamb wave excitation and detection with piezoelectric wafer active sensors for structural health monitoring, *Journal of Intelligent Material Systems and Structures*, **16**:291-305.
  57. X.P. Qing, H.-L. Chan, S.J. Beard and A. Kumar. 2006. An active diagnostic system for structural health monitoring of rocket engines, *Journal of Intelligent Material Systems and Structures*, **17**:619-628.
  58. J.D.N. Cheeke, X. Li and Z. Wang. 1998. Observation of flexural Lamb waves ( $A_0$  mode) on water-filled cylindrical shells, *The Journal of the Acoustical Society of America*, **104**(6):3678-3680.

59. A. Demma, P. Cawley, M. Lowe and A.G. Roosenbrand. 2003. The reflection of the fundamental torsional mode from cracks and notches in pipes, *The Journal of the Acoustical Society of America*, **114**(2):611-625.
60. D.N. Alleyne, B. Pavlakovic, M.J.S. Lowe and P. Cawley. 2001. Rapid long-range inspection of chemical plant pipework using guided waves, *Review of Progress in Quantitative Nondestructive Evaluation*, **20**:180-187.
61. J.L. Rose. 2002. A baseline and vision of ultrasonic guided wave inspection potential, *Journal of Pressure Vessel Technology*, **124**(3):273-282.
62. D.N. Alleyne and P. Cawley. 1997. Long range propagation of Lamb waves in chemical plant pipework, *Materials Evaluation*, **55**(4):504-508.
63. M.J.S. Lowe, D.N. Alleyne and P. Cawley. 1998. Defect detection in pipes using guided waves, *Ultrasonics*, **36**(1-5):147-154.
64. Z.H. Liu, C.F. He, B. Wu, X.Y. Wang and S.M. Yang. 2006. Circumferential and longitudinal defect detection using T(0,1) mode excited by thickness shear mode piezoelectric elements, *Ultrasonics*, **44**(s1):E1135-E1138.
65. <http://www.iofbonehealth.org/facts-and-statistics.html>.
66. <http://www.censtatd.gov.hk/home/index.jsp>.
67. C.F. Njeh, N. Shaw, J.M. Gardner-Medwin, C.M. Boivin and T.R. Southwood. 2000. Use of quantitative ultrasound to assess bone status in children with juvenile idiopathic arthritis: A pilot study, *Journal of Clinical Densitometry*, **3**(3):251-260.
68. M. Muller, P. Moilanen, M. Talmant, V. Kilappa, P. Nicholson, J. Timonen, S. Cheng and P. Laugier. 2004. Axial transmission techniques for bone assessment: An in vitro comparative study, in *Proceedings of the IEEE Ultrasonics Symposium*, pp. 557-560.
69. E. Bossy, M. Talmant and P. Laugier. 2004. Three-dimensional simulations of ultrasonic axial transmission velocity measurement on cortical bone models, *The Journal of the Acoustical Society of America*, **115**(5):2314-2324.
70. P. Moilanen, M. Talmant, V. Bousson, P.H.F. Nicholson, S. Cheng, J. Timonen and P. Laugier. 2007. Ultrasonically determined thickness of long cortical bones: Two-dimensional simulations of in vitro experiments, *The Journal of the Acoustical Society of America*, **122**(3):1818-1826.
71. P. Moilanen, Ultrasonic guided wave measurements in bone. Doctor of Philosophy, Jyväskylä, Finland: University of Jyväskylä, 2004.
72. E. Bossy, M. Talmant, F. Peyrin, L. Akrouf, P. Cloetens and P. Laugier. 2004. An in vitro study of the ultrasonic axial transmission technique at the radius: 1-MHz velocity measurements are sensitive to both mineralization and intracortical porosity, *Journal of Bone and Mineral Research*, **19**(9):1548-1556.
73. R. Barkmann, E. Kantorovich, C. Singal, D. Hans, H.K. Genant, M. Heller and C.C. Glüer. 2000. A new method for quantitative ultrasound measurements at multiple skeletal sites first results of precision and fracture discrimination, *Journal of Clinical Densitometry*, **3**(1):1-7.
74. C.F. Njeh, C.M. Boivin and C.M. Langton. 1997. The role of ultrasound in the assessment of osteoporosis: A review, *Osteoporosis International*, **7**(1):7-22.

75. R.B. Ashman, S.C. Cowin, W.C. Van Buskirk and J.C. Rice. 1984. A continuous wave technique for the measurement of the elastic properties of cortical bone, *Journal of Biomechanics*, **17**(5):349-361.
76. J.J. Kaufmann and T.A. Einhorn. 1993. Perspectives: Ultrasound assessment of bone, *Journal of Bone and Mineral Research*, **8**(5):517-525.
77. M.B. Tavakoli and J.A. Evans. 1992. The effect of bone-structure on ultrasonic-attenuation and velocity, *Ultrasonics*, **30**(6):389-395.
78. T.A. Einhorn. 1992. Bone strength - the bottom line, *Calcified Tissue International*, **51**(5):333-339.
79. A.J. Foldes, A. Rimon, D.D. Keinan and M.M. Popovtzer. 1995. Quantitative ultrasound of the tibia: A novel approach for assessment of bone status, *Bone*, **17**(4):363-367.
80. S. Gnudi, N. Malavolta, C. Ripamonti and R. Caudarella. 1995. Ultrasound in the evaluation of osteoporosis - a comparison with bone-mineral density at distal radius, *British Journal of Radiology*, **68**(809):476-480.
81. P. Kann, U. Schulz, D. Klaus, B. Piepkorn and J. Beyer. 1995. in-vivo investigation of material quality of bone tissue by measuring apparent phalangeal ultrasound transmission velocity, *Clinical Rheumatology*, **14**(1):26-34.
82. M.R. Stegman, R.P. Heaney, D. Travers-Gustafson and J. Leist. 1995. Cortical ultrasound velocity as an indicator of bone status, *Osteoporosis International*, **5**(5):349-353.
83. C.H. Turner, M. Peacock, L. Timmerman, J.M. Neal and C.C. Johnston. 1995. Calcaneal ultrasonic measurements discriminate hip fracture independently of bone mass, *Osteoporosis International*, **5**(2):130-135.
84. D. Hans and M.A. Krieg. 2007. The clinical use of quantitative ultrasound (QUS) in the detection and management of osteoporosis, in *Proceedings of the IEEE Ultrasonics Symposium*, Oct., New York, USA, pp. 1529-1538.
85. S. Lees and F.R. Rollins Jr. 1972. Anisotropy in hard dental tissues, *Journal of Biomechanics*, **5**(6):557-566.
86. B.K. Hoffmeister, S.A. Whitten and J.Y. Rho. 2000. Low-megahertz ultrasonic properties of bovine cancellous bone, *Bone*, **26**(6):635-642.
87. V.C. Protopappas, I.C. Kourtis, L.C. Kourtis, K.N. Malizos, C.V. Massalas and D.I. Fotiadis. 2007. Three-dimensional finite element modeling of guided ultrasound wave propagation in intact and healing long bones, *The Journal of the Acoustical Society of America*, **121**(6):3907-3921.
88. P. Moilanen, M. Talmant, V. Bousson, P.H.F. Nicholson, S. Cheng, J. Timonen and P. Laugier. 2007. Ultrasonically determined thickness of long cortical bones: Two-dimensional simulations of in vitro experiments, *The Journal of the Acoustical Society of America*, **122**(3):1818-1826.
89. K.I. Lee and S.W. Yoon. 2004. Feasibility of bone assessment with leaky Lamb waves in bone phantoms and a bovine tibia, *The Journal of the Acoustical Society of America*, **115**(6):3210-3217.
90. P. Moilanen, M. Talmant, P.H.F. Nicholson, S.L. Cheng, J. Timonen and P. Laugier. 2007. Ultrasonically determined thickness of long cortical bones: Three-

- dimensional simulations of in vitro experiments, *The Journal of the Acoustical Society of America*, **122**(4):2439-2445.
91. S.Y. Hsia, S.M. Chiu and J.W. Cheng. 2006. Wave propagation at the human muscle-compact bone interface, *Theoretical and Applied Mechanics*, **33**(3):223-243.
  92. D. Komatitsch, C. Barnes and J. Tromp. 2000. Wave propagation near a fluid-solid interface: A spectral element approach, *Geophysics*, **65**(2):623–631.
  93. S.K. Tomar and M. Garg. 2005. Reflection and transmission of waves from a plane interface between two microstretch solid half-spaces, *International Journal of Engineering Science*, **43**(1-2):139-169.
  94. B. Singh. 2001. Reflection and refraction of plane waves at a liquid/thermo-microstretch elastic solid interface, *International Journal of Engineering Science*, **39**(5):583-598.
  95. B. Singh and R. Kumar. 2007. Wave reflection at viscoelastic-micropolar elastic interface, *Applied Mathematics and Computation*, **185**(1):421-431.
  96. A. Khurana and S.K. Tomar. 2007. Propagation of plane elastic waves at a plane interface between two electro-microelastic solid half-spaces, *International Journal of Solids and Structures*, **44**(11-12):3773-3795.
  97. B. Singh. 2002. Reflection of plane micropolar viscoelastic waves at a loosely bonded solid-solid interface, *Sadhana*, **27**:493-506.
  98. B. Singh. 2000. Reflection and transmission of plane harmonic waves at an interface between liquid and micropolar viscoelastic solid with stretch, *Sadhana*, **25**:589-600.
  99. A. Lakhtakia, V.K. Varadan and V.V. Varadan. 1990. Reflection of elastic plane waves at a planar achiral–chiral interface, *The Journal of the Acoustical Society of America*, **87**(6):2314-2318.
  100. P. Moilanen, P.H.F. Nicholson, V. Kilappa, Q. Wang, J. Timone and S. Cheng. 2003. The role of soft tissue in ultrasonic guided wave measurement in bone, in *Proceedings of the 5th World Congress on Ultrasonics (WCU)*, Sep., Paris, France, pp. 899-902.
  101. M.R. Myers. 2004. Transient temperature rise due to ultrasound absorption at a bone/soft-tissue interface, *The Journal of the Acoustical Society of America*, **115**(6):2887-2891.
  102. P. Moilanen, M. Talmant, V. Kilappa, P. Nicholson, S.L. Cheng, J. Timonen and P. Laugier. 2008. Modeling the impact of soft tissue on axial transmission measurements of ultrasonic guided waves in human radius, *Journal of the Acoustical Society of America*, **124**(4):2364-2373.
  103. C.L. Yapura and V.K. Kinra. 1995. Guided waves in a fluid-solid bilayer, *Wave Motion*, **21**(1):35-46.
  104. J. Wu and Z. Zhu. 1992. The propagation of Lamb waves in a plate bordered with layers of a liquid, *The Journal of the Acoustical Society of America*, **91**(2):861-867.
  105. E. Bossy, M. Talmant and P. Laugier. 2002. Effect of bone cortical thickness on velocity measurements using ultrasonic axial transmission: A 2D simulation

- study, *The Journal of the Acoustical Society of America*, **112**(1):297-307.
106. L. Rayleigh. 1885. On waves propagated along the plane surface of an elastic solid, *Proceedings of the London Mathematical Society*, **s1-17**(1):4-11.
  107. D.C. Gazis. 1958. Exact analysis of the plane-strain vibrations of thick-walled hollow cylinders, *Journal of the Acoustical Society of America*, **30**(8):786-794.
  108. I.A. Viktorov. 1967. *Rayleigh and Lamb Waves*, New York: Plenum Press.
  109. E. Moulin, J. Assaad, C. Delebarre, S. Grondel and D. Balageas. 2000. Modeling of integrated Lamb waves generation systems using a coupled finite element-normal modes expansion method, *Ultrasonics*, **38**(8):522-526.
  110. J.M. Galan and R. Abascal. 2002. Numerical simulation of Lamb wave scattering in semi-infinite plates, *International Journal for Numerical Methods in Engineering*, **53**(5):1145-1173.
  111. K.S. Tan, N. Guo, B.S. Wong and C.G. Tui. 1995. Experimental evaluation of delaminations in composite plates by the use of Lamb waves, *Composites Science and Technology*, **53**(1):77-84.
  112. Y.-H. Kim, D.-H. Kim, J.-H. Han and C.-G. Kim. 2007. Damage assessment in layered composites using spectral analysis and Lamb wave, *Composites Part B*, **38**(7-8):800-809.
  113. Z. Guo, J.D. Achenbach and S. Krishnaswamy. 1997. EMAT generation and laser detection of single Lamb wave modes, *Ultrasonics*, **35**(6):423-429.
  114. J.L. Rose. 1999. *Ultrasonic Waves in Solid Media*, Cambridge: Cambridge University Press.
  115. J.D. Achenbach. 1973. *Wave Propagation in Elastic Solids*, Amsterdam: North-Holland.
  116. P.S. Tua, S.T. Quek and Q. Wang. 2005. Detection of cracks in cylindrical pipes and plates using piezo-actuated Lamb waves, *Smart Materials and Structures*, **14**(6):1325-1342.
  117. K.R. Leonard and M.K. Hinders. 2003. Guided wave helical ultrasonic tomography of pipes, *The Journal of the Acoustical Society of America*, **114**(2):767-774.
  118. M. Hinders. 2003. Guided wave helical ultrasound tomography of pipes and tubes, Applied Science Department, The College of William & Mary in Virginia.
  119. E. Sapin-de Brosse, J.L. Gennisson, M. Pernot, M. Fink and M. Tanter. 2010. Temperature dependence of the shear modulus of soft tissues assessed by ultrasound, *Physics in Medicine and Biology*, **55**(6):1701-1718.
  120. Z. Su and L. Ye. 2005. Lamb wave propagation-based damage identification for quasi-isotropic CF/EP composite laminates using artificial neural algorithm, Part I: Methodology and database development, *Journal of Intelligent Material Systems and Structures*, **16**:97-111.
  121. Z. Su, X.M. Wang, Z.P. Chen, L. Ye and D. Wang. 2006. A built-in active sensor network for health monitoring of composite structures, *Smart Materials and Structures*, **15**(6):1939-1949.
  122. H.G. Chen, Y.J. Yan, W.H. Chen, J.S. Jiang, L. Yu and Z.Y. Wu. 2007. Early damage detection in composite wingbox structures using Hilbert-Huang

- transform and genetic algorithm, *Structural Health Monitoring: An International Journal*, **6**:281-297.
123. H.W. Park, H. Sohn, K.H. Law and C.R. Farrar. 2007. Time reversal active sensing for health monitoring of a composite plate, *Journal of Sound and Vibration*, **302**(1-2):50-66.
  124. G. Konstantinidis, B.W. Drinkwater and P.D. Wilcox. 2006. The temperature stability of guided wave structural health monitoring systems, *Smart Materials and Structures*, **15**:967-976.
  125. X. Zhao, H. Gao, G. Zhang, B. Ayhan, F. Yan, C. Kwan and J.L. Rose. 2007. Active health monitoring of an aircraft wing with embedded piezoelectric sensor/actuator network: I. Defect detection, localization and growth monitoring, *Smart Materials and Structures*, **16**(4):1208-1217.
  126. J.-B. Ihn and F.-K. Chang. 2008. Pitch-catch active sensing methods in structural health monitoring for aircraft structures, *Structural Health Monitoring: An International Journal*, **7**(1):5-19.
  127. C.H. Wang, J.T. Rose and F.-K. Chang. 2004. A synthetic time-reversal imaging method for structural health monitoring, *Smart Materials and Structures*, **13**(2):415-423.
  128. A.H.S. Ang and W. Tang. 1975. *Probability Concepts in Engineering Planning and Design, Volume 1: Basic Principles*, New York: John Wiley & Sons, Inc.
  129. V. Protopappas, I. Kourtis, D.I. Fotiadis, C.V. Massalas, G.R. Greece and G. Ioannina. 2003. Finite element modelling of ultrasound propagation in fractured long bones, in *Proceedings of the IASTED International Conference on Biomechanics*, Jun., pp. 54-58.
  130. E. Bossy, M. Talmant, M. Defontaine, F. Patat, C. Roux, S. Kolta and P. Laugier. 2003. A new probe dedicated to cortical bone strength assessment, in *Proceedings of the 5th World Congress on Ultrasonics (WCU)*, Sep., Paris, France, pp. 891-894.
  131. V. Egorov, S. Tsyuryupa, S. Kanilo, M. Kogit and A. Sarvazyan. 2008. Soft tissue elastometer, *Medical Engineering and Physics*, **30**(2):206-212.
  132. M.L. Palmeri, A.C. Sharma, R.R. Bouchard, R.W. Nightingale and K.R. Nightingale. 2005. A finite-element method model of soft tissue response to impulsive acoustic radiation force, *IEEE Transactions on Ultrasonics, Ferroelectrics, and Frequency Control*, **52**(10):1699-1712.
  133. C.F. Njeh, J.R. Kearton, D. Hans and C.M. Boivin. 1999. The use of quantitative ultrasound to monitor fracture healing: A feasibility study using phantoms, *Medical Engineering and Physics*, **20**(10):781-786.
  134. M.G. Vavva, V.C. Protopappas, L.N. Gergidis, A. Charalambopoulos, D.I. Fotiadis and D. Polyzos. 2008. The effect of boundary conditions on guided wave propagation in two-dimensional models of healing bone, *Ultrasonics*, **48**(6-7):598-606.
  135. S.P. Dodd, J.L. Cunningham, A.W. Miles, S. Gheduzzi and V.F. Humphrey. 2008. Ultrasound transmission loss across transverse and oblique bone fractures: An in vitro study, *Ultrasound in Medicine and Biology*, **34**(3):454-462.

136. G. Lowet and G. Van der Perre. 1996. Ultrasound velocity measurement in long bones: Measurement method and simulation of ultrasound wave propagation, *Journal of Biomechanics*, **29**(10):1255-1262.